IMPERIAL

Imperial College London

Department of Chemical Engineering

Exploring dispersion dynamics in agitated mixers via numerical simulations and machine learning

Author:
Fuyue Liang

Supervisor:
Prof. Omar K. Matar

September, 2024

Submitted in part fulfilment of the requirements for the degree of
Doctor of Chemical Engineering of Imperial College London
and the Diploma of Imperial College London

Declaration of Originality

The content presented herein is original material produced by the author. Citations have been provided to all the references used.

Copyright Statement

The copyright of this thesis rests with the author. Unless otherwise indicated, its contents are licensed under a Creative Commons Attribution-Non Commercial-No Derivatives 4.0 International Licence (CC BY-NC-ND).

Under this licence, you may copy and redistribute the material in any medium or format on the condition that; you credit the author, do not use it for commercial purposes and do not distribute modified versions of the work.

When reusing or sharing this work, ensure you make the licence terms clear to others by naming the licence and linking to the licence text.

Please seek permission from the copyright holder for uses of this work that are not included in this licence or permitted under UK Copyright Law.

Abstract

This thesis employs three-dimensional simulations combined with a hybrid front-tracking/level-set method to elucidate the complex interplay between flow dynamics and interfacial behaviours in a practical operational unit. Specifically, it examines the mixing of immiscible oil and water by a pitched blade turbine in a cylindrical vessel. The study focuses on the effects of impeller rotation frequency, the presence of surface active agents (surfactants) and their physiochemical properties on the evolution of interface and mixing performance, including interfacial area, dispersed drop number, and drop size distribution within the system.

Furthermore, due to the high computational cost of high-fidelity simulations, several data-driven models based on recurrent neural network are constructed using the simulation data and evaluated as an alternative approach for predicting dispersion performance metrics over multiple future time-steps based on their initial observations.

The results from this thesis provide a detailed picture of the underlying physics and interfacial dynamics within mixing systems as influenced by impeller speed, surfactant elasticity and solubility. This work bridges the gap in understanding of liquid-liquid dispersion process. Moreover, this thesis examines the applicability of several popular machine learning techniques in the field of multiphase flow mixing, highlighting the challenges and critical considerations involved in this process.

Acknowledgements

I would like to express my deepest gratitude to my great supervisor Prof. Omar K. Matar and my life-saving co-supervisor Dr. Lyes Kahouadji, for their invaluable guidance, support, and encouragement throughout the entire journey of my PhD degree. I thank Prof. Sibo Cheng for the guidance and support during my exploration of machine learning. Special appreciation to Dr. Damir Juric, Dr. Jalel Chergui, and Dr. Seungwon Shin for their contribution to the simulation code.

I would like to extend my thanks to my colleagues, Juan P. Valdés and Paula Pico, for their unwavering emotional and technical support. It has been my great fortune and pleasure to have your company during this adventure. I thank my other MFG colleagues for creating an encouraging and supportive environment: Dr. Alessio Lavino, Dr. Andrius Patapas, Dr. Assen Batchvarov, Dr. Gabriel F.N. Goncalves, Dr. Konstantinos Zinelis, Dr. Morgan Kerhouant, Dr. Nausheen M. Basha and Dr. Usman Rana.

I am also grateful to my badminton gangs: Annabelle Lu, Cherizza Choi, Karen Li, Yuqi Shi, Xinwei Zhou, and Lih Chern Hiew.

I extend my deepest gradtitude to my parents, Jian Liang and Yingling Fu, for their unwavering support throughout this journey. Your encouragement and love, through the moment of sadness, stress, and joy, have made this work possible.

Special thanks go to Dr. Ruiao Hu for his love, patience and companionship, and his cosy office in the Huxley building, which graciously adopted me every time there was a fire alarm in the chemical engineering building, providing me a much-needed sanctuary to continue working on this thesis without interruption.

I acknowledge the use of ChatGPT 3.5 (OpenAI, https://chat.openai.com/) for occasional assisting with the polishing and grammar checking of this thesis. I confirm that no content generated by AI has been presented as my own work.

Finally, well done, Fuyue!

Publications and repositories

The results presented in Chapter 4, 5 and 6 have been published in the following journal paper, respectively:

- **Liang, F.**, Kahouadji, L., Valdes, J. P., Shin, S., Chergui, J., Juric, D., & Matar, O. K. (2022). Numerical study of oil–water emulsion formation in stirred vessels: effect of impeller speed. Flow, 2, E34
- **Liang, F.**, Kahouadji, L., Valdes, J. P., Shin, S., Chergui, J., Juric, D., & Matar, O. K. (2023). Numerical simulation of surfactant-laden emulsion formation in an un-baffled stirred vessel. Chemical Engineering Journal, 472, 144807.
- **Liang, F.**, Valdes, J. P., Cheng, S., Kahouadji, L., Shin, S., Chergui, J., Juric, D., & Matar, O. K (2024). Liquid–Liquid Dispersion Performance Prediction and Uncertainty Quantification Using Recurrent Neural Networks. Industrial & Engineering Chemistry Research, 63(17), 7853-7875

In addition, I contributed to the development and have been one of the primary authors of the following Python repositories, which have been used to produce corresponding results presented in Chapter 6:

- Valdes, J. P., **Liang, F.**, & Pico, P. (2024). HAMPPSterS: Hybrid PC-HPC Automated Monitoring and Post-processing: Parametric Study Scheduler for Simulations (Version 6.1) [Computer software].
  https://github.com/jpv219/HAMPPSterS
- Valdes, J. P., & **Liang, F.** (2024). LSTMIX: Multivariate multistep RNN predictive framework for multidimensional mixing performance metrics. (Version 2.0) [Computer software].
  https://github.com/jpv219/LSTMIX

Besides, I participated in the publications listed below during this PhD:

- Barsha, N., Matar, O. K. & *et. al.*. (2024) Machine learning and physics-driven modelling and simulation of multiphase systems. International Journal of Multiphase Flow (In revision)
- Valdes, J. P., Kahouadji, L., **Liang, F.**, Shin, S., Chergui, J., Juric, D., & Matar, O. K. (2023). On the dispersion dynamics of liquid–liquid surfactant-laden flows in a SMX static mixer. Chemical Engineering Journal, 475, 146058.

- Valdes, J. P., Kahouadji, L., **Liang, F.**, Shin, S., Chergui, J., Juric, D., & Matar, O. K. (2023). Direct numerical simulations of liquid–liquid dispersions in a SMX mixer under different inlet conditions. Chemical Engineering Journal, 462, 142248

- Kahouadji, L., **Liang, F.**, Valdes, J. P., Shin, S., Chergui, J., Juric, D., & Matar, O. K. (2022). The transition to aeration in turbulent two-phase mixing in stirred vessels. Flow, 2, E30

Conferences and talks

I have attended and delivered talks in the following conferences during this PhD:

- **76th Annual Meeting of the APS Division of Fluid Dynamics** Nov 2023
  On drop dispersion and mixing performance in a stirred vessel: effect of surfactant solubility
- **2023 AIChE annual meeting** Nov 2023
  Machine Learning for Prediction and Optimization in Surfactant-Laden Liquid Dispersions
- **11th International Conference on Multiphase Flow** Apr 2023
  Numerical simulation of surfactant-laden emulsion formation in a stirred vessel
- **75th Annual Meeting of the APS Division of Fluid Dynamics** Nov 2022
  Numerical Simulation of Surfactant-Laden Emulsion Formation in a Stirred Vessel
- **2022 AIChE annual meeting** Nov 2022
  Numerical Simulation of Surfactant-Laden Emulsion Formation in a Stirred Vessel
- **14th European Fluid Mechanics Conference** Sep 2022
  A numerical vinaigrette: A myriad of interfacial singularities with surfactants
- **Mixing XXVII, the North American Mixing Forum** Jun 2022
  A numerical vinaigrette: A myriad of interfacial singularities with surfactants
- **ECCOMAS CONGRESS 2022** Jun 2022
  8th European Congress on Computational Methods in Applied Sciences and Engineering
  A Numerical Vinaigrette: Effect of Surfactants on Oil-water Emulsification
- **74th Annual Meeting of the APS Division of Fluid Dynamics** Nov 2021
  Effect of Impeller Rotation on Oil-water Emulsion Formation in Stirred Vessels

Awards

I have received the following awards during this PhD:

- Winner of UK Fluids Network Video Competition — Oct 2021
  https://sms.cam.ac.uk/media/3664840
  Oil-water Emulsion Formation in a Stirred Vessel

Notation

All symbols used in this thesis are defined where they are first introduced. For the reader's convenience, the meanings of the commonly used notations are presented below. Though many of the symbols are specific to the chapter where they are introduced, in some cases, symbols introduced in previous chapters might be used with the same meaning in following chapters.

Abbreviations

AL	Active Learning
CFD	Computational Fluid Dynamics
CMC	Critical Micelle Concentration
DSD	Drop Size Distribution
DES	Detached Eddy Simulation
DNS	Direct Numerical Simulation
DT	Decision Tree
FC	Fully-connected layer
GRU	Gated Recurrent Unit
GSx	Greedy Sampling on input (x) space
IA	Interfacial Area
KNN	K-Nearest Neighbours
LES	Large Eddy Simulation
LCRM	Level-Contour Reconstruction Method
LSTM	Long Short-Term Memory
MAE	Mean Absolute Error
MLP	Multi-Layer Perceptron
MRF	Multiple Referecen Frame
MSE	Mean Squared Error
PBT	Pitched Blade Turbine
RANS	Reynolds Averaged Navier-Stokes
RF	Random Forest
RPS	Revolution per Second
RMSE	Root Mean Squared Error
RNN	Recurrent Neural Network
RT	Rushton Turbine
ND	Number of Drops
S2S	Sequence-to-Sequence
SM	Sliding Mesh
SVM	Support Vector Machine
XGBoost	eXtreme Gradient Boosting

Roman letters

b	offset term, trainable parameter of LSTM unit
Bi	Biot number
$\mathbf{C}_t$	cell state storing long-term memory up to time t
C	bulk surfactant concentration
C_0	initial bulk surfactant concentration
C_s	Smogorinsky-Lilly coeffiecient
Ca	Capillary number
d_{32}	Sauter mean diameter
d_{max}	maximum drop diameter
D	impeller diameter, [m]
D_b	surfactant diffusivity in the bulk
D_s	surfactant diffusivity along the interface
Fr	Froude number
$\dot{G}$	deformation rate
h	desorption depth
$\mathbf{h}_t$	hidden state storing short-term memory up to time t
H	agitated tank height
$\mathbf{I}$	identity tensor
J	fluxes
$\mathbf{J}_D$	diffusive flux along the interface
k	adsorption parameter
M	number of bins representing DSD
$\mathbf{n}$	normal unit tensor
N	impeller rotating speed (frequency), [Hz] or [RPS]
Oh	Ohnesorge number
p	pressure
$\mathbf{p}$	perpendicular unit tensor
Pe	Peclét number
R^2	the coefficient of determination
Re	Reynolds number
$\boldsymbol{\mathcal{S}}$	rate-of-strain or rate-of-deformation tensors
$\mathbf{t}$	tangential unit tensor
T	agitated tank diameter
u'	turbulent velocity fluctuation
$\mathbf{u}$	velocity tensor
$\mathbf{u}^*$	velocity field where the effect of pressure is ignored
$\mathbf{u}_s$	interface velocity tensor
V_d	dispersed drop volume
V_{cap}	volume of a spherical drop whose diameter is the capillary length scale
$\mathbf{W}$	weight vector, trainable parameter of LSTM unit
We	Weber number
$\mathbf{x}$	Cartesian coordinate vector, $\mathbf{x} = [x, y, z]^T$
$\mathbf{x}_t$	input observations, $[x_0, x_1 ... x_t]^T$

Greek letters

β_s	surfactant elasticity
ϵ_T	turbulent dissipation rate
Γ	interfacial surfactant concentration
Γ_∞	maximum packing of surfactant species on the interface
δ	delta function
θ	azimuthal displacement of impeller
λ_c	Capillary length scale
μ	fluid viscosity
ρ	fluid density
σ	interfacial tension
σ_s	surfactant-free interfacial tension
τ	Marangoni stress
τ_{def}	deformation stress
τ_μ	viscous stress
τ_σ	interfacial tension stress
ϕ	phase volume fraction
φ	vector distance function

Subscripts

a	aqueous phase
b	bulk phase
c	continuous phase
d	dispersed phase
max	maximum
o	oil phase
def	deformation
diff	diffusion
a/d	adsorption and desorption process
s	interface
sub	sub-phase

Contents

1 Introduction **1**

1.1 Background and Motivation 1

1.2 Thesis Overview 2

2 Literature Review **4**

2.1 Mechanical Mixing 4

2.1.1 Agitated mixers in process industry 4

2.1.2 Parameters characterising liquid-liquid dispersion 7

2.1.3 Drop breakage in agitated vessels 13

2.1.4 Effect of surfactants 24

2.1.5 Computational fluid mixing 33

2.2 Machine learning in fluid dynamics 37

2.2.1 Machine learning in CFD 37

2.2.2 Sequential predictions with RNNs 38

2.3 Concluding remarks 38

3 Methodology **40**

3.1 CFD Simulations 40

3.1.1 Simulation Configuration 40

3.1.2 Governing Equations 42

3.1.3 Numerical technique for interface localisation 51

3.1.4 Solutions procedures 55

3.1.5 Validation 63

3.2 ML applications 67

3.2.1 RNNs: LSTM and GRU 67

3.2.2 Procedure for time-series prediction 70

4 Oil-water emulsion formation in stirred vessels: the effect of impeller speed **84**

4.1 Results and Discussion 84

4.1.1 Flow evolution 85

4.1.2 Interfacial behaviours 88

4.1.3 Drop count and their size distribution 92

4.2 Concluding Remarks 96

5 Oil-water emulsion formation in stirred vessels: the effect of surfactant 98
5.1 Adopted Values of Dimensionless Parameters . . . 98
5.2 Results and Discussion . . . 100
5.2.1 Surfactant effect on interface evolution . . . 100
5.2.2 Comparative statistics . . . 108
5.2.3 Effect of surfactant elasticity, β_s . . . 111
5.2.4 Effect of surfactant solubility, Bi . . . 114
5.3 Concluding Remarks . . . 117

6 Dispersion performance prediction and uncertainty quantification using RNNs 119
6.1 Results and discussion . . . 120
6.1.1 Comparative RNN unit performances: LSTM vs. GRU . . . 120
6.1.2 Model generalisation: performance on training and validation data . . . 123
6.1.3 Model performance: prediction via rollout . . . 124
6.1.4 Uncertainty quantification . . . 129
6.2 Concluding remarks . . . 130

7 Conclusions and future work 132
7.1 Conclusions . . . 132
7.2 Future Work . . . 133

Bibliography 134

List of Figures

2.1 An general overview of typical impeller designs in industry. 5

2.2 Schematic diagrams of flow fields generated by different impeller types: (a) radial; (b) axial; (c) mixed; (d) tangential. 6

2.3 Vertical velocity profile adjacent to a impeller blade. Reproduced from Paul et al. [2003]. 9

2.4 (a) Flow at a rotating disk; (b) Rotating flow over an infinite ground. Both figures are from Schlichting and Kestin [1961]. 9

2.5 Schematic representation of interaction between turbulent structures and drops, adapted from [Paul et al., 2003]. (a) Transport with large eddy; (b) shear by co-rotating eddies; (c) stretching by counter-rotating eddies; (d) multiple combined interactions. 15

2.6 (a) Elongational flow in the vicinity of the blade [Kumar et al., 1998];(b) Deformation and breakage of a drop in the boundary layer of the blade [Shimizu et al., 1999]. 16

2.7 The drop breakage cell for simulating breakage phenomena in stirred vessels Maaß et al. [2007] 21

2.8 Image sequence of drop breakage events from Solsvik and Jakobsen [2015]. (a) Equally-sized binary breakup; (b) multiple fragmentation. 22

2.9 (a) A schematic structure of generic surfactant molecules. The remaining three diagrams show the surfactant distribution at equilibrium with increasing concentration in the bulk, wherein (b) interface is partly covered; (c) interface is completely occupied; (d) micelles formed in the bulk. 25

2.10 Schematic diagrams illustrating the surfactant transport in oil-water system. (a) $-$ (b) display the convection and diffusion of surfactants along the interface, respectively. The red dotted arrows in (a) represent the induced Marangoni stresses; the light blue arrows refer to the fluid motion in the water phase. (c) presents surfactant adsorption and desorption between the interface and sub-phase, along with the surfactant diffusion from the bulk towards the sub-phase. (d) $-$ (e) show the two limiting cases with regard to the surfactant adsorption: kinetics-controlled and diffusion-controlled. Particularly, in figure (c) $-$ (e), the intensity of the background colour corresponds to the concentration of surfactants, where darker blue indicating a higher surfactant concentration. 28

2.11 (Top panel) Schematic diagram of drop deformation and corresponding surfactant distribution for a surfactant-covered drop subject to (a) non-axisymmetric shear flow and (b) axisymmetric extensional flow. (Bottom panel) Schematic of tip streaming, adapted from Bruijn [1993]. 30
2.12 Classification of modelling methods in the literature. 35

3.1 (a) Details of impeller geometry and physical properties of the two liquid phases. (b) Schematic illustration of the computational domain for the oil-water mixing system: a stirred vessel, filled with oil in the upper-half (coloured in gold) and water below (coloured in blue) is equipped with a 4-pitched-blade-turbine; the impeller blades have length l, width h, and thickness w, and are inclined at an angle α to the horizontal. The computational domain is divided into $4 \times 4 \times 6$ subdomains. The number of the Cartesian structured grids per subdomain is 64^3, which gives a total grid number of $256 \times 256 \times 384$; $(c) - (d)$ display side- and top-views of the turbine, respectively. Figures are reproduced from Liang et al. [2022]. 41
3.2 Schematic representation of a stationary control volume V subjected to a velocity field $\mathbf{u}(\mathbf{x}, t)$, which is enclosed by a surface S. dv and ds denote the infinitesimal volume and surface, respectively; $\mathbf{n}$ represents the normal vector to the interface. This figure is reproduced based on [Tryggvason et al., 2011]. 43
3.3 Schematic representations of (a) a thin control volume δv enclosed by interface δs consisting of a portion of both phases and their interface S, wherein the label $u_n, \mathbf{u}_i$ denote the normal velocity of the interface and velocities for phase i; (b) a small element of the interface, s_e, with its boundary annotated as a contour C, and $\mathbf{n}, \mathbf{t}$ and $\mathbf{p}$ represent the vector at the interface to the direction of normal, tangential and perpendicular, respective;y. Both figures are reproduced based on [Tryggvason et al., 2011]. 45
3.4 Schematic representations of interface in (a) front tracking method, wherein Lagrangian markers are advected with velocity from fixed grids; (b) level-set method, wherein the interface is computed as contour level of a distance function. say φ. 52
3.5 Schematic diagram of the interface reconstruction process in LCRM, (a) for two-dimensional simulation; $(b), (c)$ for three-dimensional simulations. 53
3.6 Schematic diagrams for an individual interface element with element area of A_e. The element is composed of three edge line ab, bc, and ca. (a) Geometrical information on the element: surfactant interface concentration Γ_s is stored at the element center $\mathbf{x}_c$, and Γ_{ab}, Γ_{bc}, and Γ_{ca} are the interpolated values at the mid point of the three edges, respectively; relevant vectors for this element are annotated, including the normal vector at the center of element, and vectors at the element edges including normal (yellow), tangent (blue), binormal (green). (b) Exemplified implementation of probing technique in the directions of $\mathbf{p}$ (edge ab) and $\mathbf{t}$ (edge bc). 59

3.7 Schematic representation of the ghost points near the interface. The two red dots are the defined ghost nodes in the dispersed phase, storing the extrapolated values of bulk concentrations. Diagram is adapted from Shin and Choi [2016], Shin et al. [2018]. 61

3.8 (a) Details of mixer geometry and (b) schematic configuration for the single-drop breakup validation against experimental data [Hančil and Rod, 1988]; (c) initial drop position and (d) the predicted emergent number of daughter drops n_{dd} following breakup. 65

3.9 Mesh stability test with three resolutions and the corresponding predicted n_{dd}. 66

3.10 (a) The simulation configuration reproduced from the experimental work of [Liu et al., 2017]; (b) the curve-fitting (black dotted line) using our simulation data (coloured in blue) and the experimental data (coloured in red) from [Liu et al., 2017]. The green triangles in the zoom panel represents the sample data reproduced from the prediction model, which is represented in Fig.10 in [Liu et al., 2017], and the inset image shows the state of simulated system at $t = 0.6s$. . . . 67

3.11 (a) Circuit diagram of a RNN with no output layers; (b) circuit diagram (left) and its unrolled version (right) until a final time-step labelled as sequence length (SL) of a LSTM network. This figure is reproduced from Liang et al. [2024]. . . . 68

3.12 Diagram of different gates in (a) *standard* LSTM unit and (b) GRU unit. This figure is reproduced from Liang et al. [2024]. 69

3.13 Flowchart that illustrates the architecture of the overall framework designed for training and deploying a multivariate multi-step RNN model with two-phase mixing performance data from high-fidelity CFD simulations. Colour-coded blocks denote general data pre-processing (teal) and model operations and exploration (violet). 71

3.14 Schematic detailing DSD binning transformation. Top diagram showcases the drop size sorting and counting process in each size range, while the bottom tables show the transition from variable-sized volume lists (s = ND_t) to discrete drop counts in a fixed number of bins (s = M). This figure is reproduced from Liang et al. [2024] 73

3.15 Schematic representation of the time-domain S2S windowing procedure implemented in Chapter 6. Top part provides a tabular representation of the windowed datasets, while bottom figures illustrate the rolling window procedure on top of a generic feature. Here, the window size is set to $s_w = 6$, where the number of input and target steps is $n_i = 4$ and $n_k = 2$, respectively. The window is shown to be rolled with a stride of $s = 1$. This figure is reproduced from Liang et al. [2024]. 77

3.16 Diagram of an RNN-FC neural network architecture, where each unit can be either an LSTM or GRU. This figure is reproduced from Liang et al. [2024]. . . . 78

3.17 Diagram of an RNN Encoder-decoder (ED) architecture, implementing mixed teacher forcing training. As with Figure 3.16, the RNN units can either be LSTM or GRU. This figure is reproduced from Liang et al. [2024]. 78

3.18 Diagram showcasing the procedure of ensemble-based uncertainty quantification. Take ND as an example, perturbations are introduced to the input sequence by adding noises, ϵ, drawn from a Gaussian distribution, $\mathcal{N}(0, 0.04^2)$, at each time-step, giving rise to the ensemble of perturbed inputs. All of the ensemble members are fed into the trained model which progressively produces the ensemble of predicted sequences (with a sequence length of $\tau_f + 1 - n_i$). r is the number of iterations determined by the target sequence length, $r = (\tau - n_i)/n_k$. This figure is reproduced from Liang et al. [2024]. 82

4.1 Flow field prior to the interface deformation ($t = 8 \times Rev.$) for $N = 5$ RPS, $(Re, We) = (9013, 55)$, represented by streamlines drawn on a $x - z$ plane at $y = 4.25$ cm. The inset of the three-dimensional vessel is coloured by the velocity magnitude; the blue arrows displayed in the close-up view are scaled by the velocity magnitude, indicating the velocity orientation. This figure is reproduced from Liang et al. [2022]. 85

4.2 Spatio-temporal evolution of the vortical structures for $N = 1$ RPS, $(Re, We) = (1802, 2.19)$ from an initial static state (a) until $t = 20 \times Rev.$ (l). In this and subsequent figures, the results are displayed in the $x - z$ plane at $y = 4.25$ cm, and cyan and gold are used to designate the aqueous and oil phases, respectively, while the red solid line represents the interface location. Enlarged snapshots of the vortical structures with corresponding annotations are shown for $t = 6 \times Rev.$ and $t = 9.5 \times Rev.$ in (m) and (n), respectively. This figure is reproduced from Liang et al. [2022]. 86

4.3 Vortical flow structures for $N = 1 - 5$ RPS corresponding to (Re, We) combinations of (1802,2.19), (3605,8.76), (5408,19), (7210,35), and (9013,55) are shown in $(a) - (e)$, respectively, at $t = 25 \times Rev.$ when the flow has reached a statistical steady-state. This figure is reproduced from Liang et al. [2022]. 87

4.4 Spatio-temporal evolution of the vortical structures for $N = 7$ and 10 RPS, corresponding to $(Re, We) = (12618, 107)$ and $(Re, We) = 18026, 219$ at $t = 2 - 9 \times Rev.$ shown in $(a) - (f)$, respectively. This figure is reproduced from Liang et al. [2022]. 88

4.5 Interface shape at a statistical steady-state for $N = 1 - 5$ RPS corresponding to (Re, We) combinations of (1802,2.19), (3605,8.76), (5408,19), (7210,35), and (9013,55) shown in $(a) - (e)$, respectively, at $t = 25 \times Rev.$ This figure is reproduced from Liang et al. [2022]. 89

4.6 Spatio-temporal evolution of interface for $N = 4$ RPS, $(Re, We) = (7210, 35)$ from a state where the interface starts to deform (a) until $t = 20 \times Rev.$ (l). This figure is reproduced from Liang et al. [2022]. 90

4.7 Close-up view of single ligament breakup into drops for $N = 5$ RPS, $(Re, We) = (9013, 55)$ during time frame $t = 16.375 - 16.625 \times Rev.$ This figure is reproduced from Liang et al. [2022]. 91

4.8 Vorticity in the ligament surroundings for $N = 5$ RPS, $(Re, We) = (9013, 55)$. Four horizontal planes generated at $z[\text{cm}] = 0.82, 0.70, 0.65, 0.58$, corresponding to the red-, blue-, green-, and yellow-labelled planes, are coloured according to the vorticity magnitude. The side- and top-view of the ligament are presented in the middle, and parts of the ligament are highlighted by white solid lines in the vorticity panels. This figure is reproduced from Liang et al. [2022]. 91

4.9 Spatio-temporal evolution of the interface toward the development of an oil-in-water emulsion for $(Re, We) = (12618, 107)$ and (18026, 219) shown in the top and bottom panels, respectively, for $t = 8 - 25 \times Rev.$ in $(a) - (f)$, respectively. This figure is reproduced from Liang et al. [2022]. 93

4.10 Temporal evolution of the number of dispersed drops for frequencies $N = 5, 6, 7, 8, 9, 10$ RPS, which correspond to $Re = 9013 - 18026$ and $We = 55 - 219$. Snapshots of the interface shapes at $t = 25 \times Rev.$ are also presented for each frequency. The black arrow indicates the earlier drop occurrence and the steeper increase from a zero drop count when the impeller speed is increased. This figure is reproduced from Liang et al. [2022]. 94

4.11 (a) Number of drops (blue line, inverted triangle markers) and interfacial area (red line, cross-shaped markers) of dispersed oil phase. (b) Box plot distribution of the drop size (outliers are not shown here), at $t = 25 \times Rev.$ for frequencies $N = 5, 6, 7, 8, 9, 10$ RPS, which correspond to $Re = 9013 - 18026$ and $We = 55 - 219$. Here, the median value of V_d/V_{cap} is indicated by the horiztonal red lines. This figure is reproduced from Liang et al. [2022]. 95

4.12 Drop size distribution of the dispersed oil phase at $t = 25 \times Rev.$ for $N = 5, 6, 7, 8, 9, 10$ RPS ($Re = 9013 - 18026$ and $We = 55 - 219$). The attached image shows a drop size map for $N = 7$ RPS at $t = 25 \times Rev.$ where all the dispersed phases are coloured by red, yellow and blue according to their size as small, moderate and large, respectively. This figure is reproduced from Liang et al. [2022]. 96

5.1 Comparative evolution of interfacial shapes for the surfactant-free (top), surfactant-laden I ($|\tau| > 0$, middle) and surfactant-laden II ($|\tau| = 0$, bottom) systems for $t = 8.5 - 12 \times Rev.$ The interface is coloured by the magnitude of Γ. The values of surfactant-related parameters correspond to the "base" case (see Section 5.1). This figure is reproduced from Liang et al. [2023]. 101

5.2 (a) Temporal evolution of the interfacial deformation for the three studied cases for $t = 7 - 10 \times Rev.$ regarding the minimum position of the deforming interface ($\tilde{z}$ shown by symbols) and the magnitude of the velocity of the vertical interface deformation ($|u_z|$ shown by lines); (b) the interplay between the flow field (streamlines in blue along with black arrows representing their directions) at the vessel center and the induced Marangoni stresses (red arrows) at the deforming interface for $t = 9 \times Rev.$ The interface is coloured by the magnitude of Γ. The surfactant-related parameter values remain unchanged from Figure 5.1. This figure is reproduced from Liang et al. [2023]. 103

5.3 Probability density function of parameter $\mathcal{Q}$ for surfactant-free and surfactant-laden I interfaces at $t = 11.5 \times Rev.$ The interfaces are coloured by $\mathcal{Q}$. The surfactant-related parameters are the same as in Figure 5.1. This figure is reproduced from Liang et al. [2023]. 103

5.4 Close-up visualisations of drop breakup mechanisms observed in surfactant-free system (left) at $t = 16.375 \times Rev.$, and surfactant-laden I system, at $t = 11.625, 12.375, 15.4 \times Rev.$ (from second left to right, respectively). The presented breakup events are via the capillary instability (left two columns), and surfactant-enhanced tip-streaming (right two columns). Two scenarios for tip-streaming are given, one initiated from the deforming interface and another from an elongated ligament. The surfactant-related parameters remain unchanged from Figure 5.1. This figure is reproduced from Liang et al. [2023]. 104

5.5 Visualisations of Marangoni stresses under different scenarios: (a) ligament elongation prior to its fragmentation towards multiple drops; (b) drop deformation where the evolving drops are coloured using σ; and (c) evolution of the deforming interface shape. The insets consist of two identical interfacial states coloured in Γ and τ, respectively; the negative sign of τ represents its direction, and the grey arrows refers to the direction of Marangoni stresses. The surfactant-related parameters remain unchanged from Figure 5.1. This figure is reproduced from Liang et al. [2023]. 106

5.6 (a) Interfacial shapes for the three studied systems at $t = 25 \times Rev.$, along with a similar inset showing the direction and magnitude of Marangoni stress as in Figure 5.5; (b) exemplified interfacial evolution in the surfactant-laden I system presenting the different outcomes depending on dispersed drop behaviours: (i) coalescence: ligament formation from consequent larger drop (circled in blue) elongation; (ii) merging back with the deforming interface: recurring ligament formation (circled in red) from the deforming interface. The surfactant-related parameters remain unchanged from Figure 5.1. This figure is reproduced from Liang et al. [2023]. 107

5.7 (a) Temporal evolution of dispersed entities number for surfactant-free, surfactant-laden I, and surfactant-laden II systems for a time frame of $t = 7 - 30 \times Rev.$, along with the representative interfacial shapes corresponding to the four steps of liquid dispersion (at $t = 9, 13, 15, 23.5 \times Rev.$, exemplified by the surfactant-free case). This profile is divided into three stages: (A) no dispersed drop, (B) dramatic increase and (C) gentle fall-off, which are respectively shown by dashed, solid, and dotted lines; (b) fitted drop size distribution (Probability Density Function with respect to log-scale of normalised drop volume) at $t = 26 \times Rev.$ for the three cases. The surfactant-related parameters remain unchanged from Figure 5.1. This figure is reproduced from Liang et al. [2023]. 109

5.8 A general quantitative insight into the mixing process for the systems with Marangoni stress turned on (a) and off (b), with regard to the evolution of interfacial area (lines) and dispersed entities count (symbols). Profiles of both metrics are displayed for varying surfactant elasticity numbers $\beta_s = 0.5, 0.7, 0.9$ during $t = 7-30 \times Rev$. Except for the variations in β_s, the rest of the surfactant-related parameters remain unchanged from Figure 5.1. This figure is reproduced from Liang et al. [2023]. 112

5.9 The averaged surfactant properties along the interface at $t = 9 \times Rev.$, (a) the averaged surfactant concentration, $\bar{\Gamma}$; (b) the averaged interfacial tension ($\bar{\sigma}$, lines) and the averaged magnitude of Marangoni stresses ($\bar{\tau}$, symbols). Here, $\tilde{z}$ refers to the dimensionless height on the interface, scaled using the minimum position of the deforming interface as in Figure 5.2; here, negative τ represents its direction pointing downward; (c) a comparison of the interfacial shapes for the three systems in the presence of Marangoni stress at $t = 17 \times Rev$. Except for the β_s variations, the rest of the surfactant-related parameters remain unchanged from Figure 5.1. This figure is reproduced from Liang et al. [2023]. 113

5.10 Temporal evolution of interfacial area (a) and dispersed drop number (b) for the cases with varying Bi and β_s during $t = 7 - 22 \times Rev.$ 114

5.11 Evolution of interfacial shapes for the case $Bi = 0.001$ for $t = 8.5 - 25 \times Rev.$ The interface is coloured using the same colour map as in Figure 5.1. Except for the Bi variation (and therefore k_d), the rest of the surfactant-related parameters remain unchanged from Figure 5.1. 116

5.12 Evolution of surfatcant concentration on the interface, in terms of the ratio between the concentration and its initial value, for $t = 0 - 10 \times Rev.$ Several insets are displayed to exemplify the interfacial surfactant concentration profiles by the cases of $Bi = 0.001$ and $Bi = 0.1$ at $t = 1, 2$ and $3 \times Rev.$ These insets present the top view of interface and are coloured by Γ. 117

6.1 LSTM-FC (top panel) and LSTM-ED (bottom panel) predicted vs. true data error dispersion plots for all 12 features considered in this work. A ± 20 % deviation area is included. Sub-figures to the left ((*a*), (*c*)) showcase training data, while those to the right ((*b*), (*d*)) illustrate validation data for the mixer respectively. 123
6.2 LSTM-FC (*a*) and -ED (*b*) predicted vs true data error dispersion plots for testing datasets, with a ±20% deviation region included. 124
6.3 Plots comparing the model target sequences (lines) and predicted sequences via rollout procedure (dots) of LSTM-FC ((*a*), (*c*)) and LSTM-ED ((*b*), (*d*)), with features ND and IA in the top and bottom, respectively. The results of predicted drop size distribution are exemplified using B_3, B_5, B_6 and B_8 for both network architectures $((e), (f))$. 127
6.4 $(a), (c)$: Exemplified histograms presenting the predicted drop size distribution via LSTM-FC and LSTM-ED; three test cases are shown for time-step $t = 280$: $Bi = 1, Bi = 0.002$ and Cl: 8 Hz, with the numeric labels in the figure denoting the corresponding bins (B_3, B_5, B_6, and B_8). $(b), (d)$: Temporal plots presenting the divergence between targeted and predicted drop size distribution via LSTM-FC and LSTM-ED, using metrics, Wasserstein distance. 128
6.5 Uncertainty quantification plots, comparing the model target (represented by solid lines), model predictions from unperturbed input (dotted line) and the ensemble prediction interval region (coloured bands), for LSTM-FC (*a*) and LSTM-ED (*b*). The dots cloud displayed at the early times represents the ensemble of perturbed input sequences. 128
6.6 Plots comparing the evolution of spread size and model performance (i.e., absolute residual between model prediction and target at each time-step, $|\widehat{y}_t - y_t|$) for LSTM-ED. 130

List of Tables

2.1 Studies surrounding flow patterns in stirred vessels. 10
2.2 Studies regarding drop size of other impeller types apart from Rushton turbine. 20
2.3 Experimental studies on single drop breakup. In this table, D is the impeller diameter, T the vessel diameter, d_m the mother drop diameter, P the Power number, V_m the volume of mother drop, N the impeller rotation speed, μ the drop viscosity, $\bar{\epsilon}$ the average energy dissipation rate and u_{flow} stands for the flow velocity of continuous fluid in channel. 22
2.4 Relevant studies that explore the deformation of single drop in the presence of surfactants, categorised by the flow types the drops subjected to and the solubility of surfactant under investigation. 32

3.1 Size (in volume [m^3]) of daughter drops in the tested computational resolutions from smallest (Drop 1) to largest (Drop 5). *Abs. Dev.* is the absolute deviation of drop size calculated using the log-scale volumes based on the fine resolution as reference (*Ref.*). 65
3.2 Simulation cases considered in this study, categorised into two groups according to the focus of each study: varying surfactant properties and modification of impeller speeds. 72
3.3 Hyperparameter search space and best-performing network configuration for each correpsonding architecture and RNN unit type. * *batch size range lies between 8 and 40, with a step of 4 for RNN-FC and 8 for RNN-ED, rendering 9 and 5 parameter values for each case, respectively.* 81

5.1 Parameter values used in the two parametric studies surrounding β_s and Bi. . . 99

6.1 Volumes of the dispersed entities corresponding to the size ranges presented in Figure 6.3. 120
6.2 Model accuracy and computational performance metrics of all combinations between RNN architectures and units. R^2 and RMSE values presented in brackets correspond to the training, validation and testing sets, respectively. *values marked with* * *and* + *correspond to the highest and lowest time taken for model tuning/training, repsectively.* 122

Chapter 1

Introduction

Contents

1.1 Background and Motivation 1

1.2 Thesis Overview 2

1.1 Background and Motivation

Mixing operations are prevalent throughout various industries, particularly in processes that involve physical and chemical transformations. Specially, mixing processes in mechanically agitated vessels are encountered widely in industry applications for various purposes: for blending of miscible liquids; to suspend solid particles in a low-viscosity liquid; to disperse gas bubbles or liquid droplets into a continuous phase. Among these applications, liquid-liquid immiscible mixing plays a crucial role in producing and increasing essential interfacial area for mass and heat transfer between phases [Paul et al., 2003], and thus is applicable for special processes, for instance, solvent extraction. Another widespread process involving immiscible liquids is emulsification, which is frequently observed in productive industries (e.g., food, pharmaceuticals, cosmetics, paint, detergent and etc.) when tiny drops are formed within a second liquid phase. However, this type of mixing is the most challenging process [Nienow et al., 1997] as it introduces several layers of complexities to the mixing systems [Ghotli et al., 2013] such as mean flow pattern and turbulence, drop breakup and coalescence, drop suspension, interfacial area, drop size distribution, potential phase inversion and the influence of additives or undesired impurities.

The extensive use and complexity of liquid dispersion in industry have motivated the multiphase research community to seek optimal mixing strategies tailored to specific applications for achieving desired product specifications [Nienow et al., 1997]. For example, in preparation of emulsion products like cosmetics, ensuring consistent and stable product properties is crucial. This guarantees that the product functions as expected, such as maintaining a specific shelf life without undergoing physical changes. In the context of agitated mixers, the associated solutions are often found by adopting empirical approaches [Gallo-Molina et al., 2017] since no widely-accepted design code is available for mixing, unlike the case of shell and tube heat-exchangers.

However, a naive implementation of empirical strategies without a ground understanding of mixing processes could potentially results in poor mixing, and thereby financial losses to stakeholders [Paul et al., 2003]. In addition, there is no simple way to detect over-design in mixing systems [Nienow et al., 1997], leading to unnecessary capital and operational costs. Therefore, optimising overall mixing performance requires a fundamental understanding of the underlying physical processes within the operating system, i.e., the phenomena listed above.

However, the inherent complexity of liquid dispersion, characterised by the interaction of multiple fluid phases and dynamic behaviours of dispersed entities within the system, poses significant challenges to both experimental observation and theoretical analysis. Thus, the multiphase research community has increasingly turned to leveraging growing computational resources. This shift aims to employ numerical simulations as a tool to uncover and understand the intricate physics underlying those complex phenomena, herein induced by agitators. In particular, by solving fundamental equations of flow motion, Computational Fluid Dynamics (CFD) provides detailed insights into flow patterns, turbulence characteristics and interfacial dynamics within agitated mixers. Furthermore, numerical simulations grant the access to the exploration of parameters that is not easily replicated or even practically impossible under experimental conditions due to equipment and measurement limitations.

Nevertheless, high-fidelity simulations, such as Direct Numerical Simulations (DNS), often demand substantial computational resources, making them less applicable for industrially relevant mixing systems. Consequently, there are few studies that offer detailed insights into the physical mechanisms governing the dispersion within practical mixing units. Meanwhile, advancements in Machine Learning (ML) have opened new avenues for enhancing CFD simulations and interpreting complex datasets. ML techniques, such as deep learning, hold the potential to augment CFD models by providing data-driven insights, accelerating simulation processes, and improving predictive accuracy. However, the high computational cost of CFD simulations leads to data scarcity for ML-model training as simulating industrial systems could take days to weeks on high-performance computing clusters, which hinders the application of ML in this area. Consequently, the total number of simulations available for ML-model training in a given study is limited. This necessitates developing a framework for constructing cost-effective alternative based on limited training data. Fortunately, ML community has developed a spectrum of techniques for this purpose (relevant review is provided in the next chapter), which, however, have never been used in the context of multiphase mixing.

1.2 Thesis Overview

Accepting the significance and complexity of liquid dispersion presented herein, this thesis aims to bridge the gap in the fundamental understanding of the liquid dispersion process within a mixing system induced by a mechanical agitator. This research encompasses all the stages of the process from the onset of drop breakup through to the attainment of a dynamic steady

state, by applying high-fidelity CFD simulations. Additionally, this thesis explores the applicability of ML-based techniques in the context of multiphase flow mixing. Specifically, it examines whether a data-driven time-series prediction model can produce dispersion performance predictions comparable to those from CFD simulations, especially under the condition where limited simulation cases are available for training. This is to seek a cost-effective alternative to costly high-fidelity simulations.

With these objectives, the rest of this thesis is structured as follows:

Chapter 2 provides a comprehensive review of existing research on multiphase mixing in agitated vessels, focusing on those dedicated to the exploration surrounding fundamental dispersion dynamics, such as drop breakup within mixing systems. In particular, it covers mixing scenarios in the absence and presence of surface active agents (surfactants for short), which are both prevalent in industrial applications. Moreover, existing ML-based techniques relevant to time-series predicting models are reviewed, providing a conceptual background for interdisciplinary research that couples ML with multiphase mixing.

Chapter 3 details the methodologies used in both studies relevant to CFD simulations and ML applications. It includes an in-depth description of the numerical methods employed throughout this thesis, as well as the overall frameworks for developing and deploying ML models pertaining to the aforementioned aspect. Particularly, for the ML application, a brief theoretical background regarding the ML-based techniques used in the ML project is provided prior to the relevant methodology.

Chapters 4 and 5 aim to provide an in-depth analysis of the dispersion process in agitated mixers. Chapter 4 focuses on the effects of impeller speed in a surfactant-free system, while Chapter 5 examines the impact of surfactant physiochemical properties in a surfactant-laden system.

On the other hand, Chapter 6 presents the results of an ML model trained to predict the evolution of dispersion performance when given its initial observations obtained from CFD simulations. The chapter evaluates the performance of different model architectures and quantifies the uncertainty of model predictions, providing an overview of their reliability.

Chapter 2

Literature Review

Contents

2.1 Mechanical Mixing 4

2.1.1 Agitated mixers in process industry 4

2.1.2 Parameters characterising liquid-liquid dispersion 7

2.1.3 Drop breakage in agitated vessels 13

2.1.4 Effect of surfactants 24

2.1.5 Computational fluid mixing 33

2.2 Machine learning in fluid dynamics 37

2.2.1 Machine learning in CFD 37

2.2.2 Sequential predictions with RNNs 38

2.3 Concluding remarks 38

2.1 Mechanical Mixing

2.1.1 Agitated mixers in process industry

Mixing is widely encountered in a high proportion of industrial processes during the preparation towards end products, which could be roughly classified into four types [Paul et al., 2003]: gas-liquid dispersion, solid-liquid dispersion, liquid-liquid (miscible) blending, and liquid-liquid (immiscible) dispersion. One of the examples could be the food processing where an enormous variety of mixers have been designed to cover the broad ranges of mixing duties [Niranjan et al., 1994] including (1) dispersion and dissolution into liquids (e.g., mayonnaise and salad cream), and (2) solid and liquid mixing (e.g., dough and paste). More specifically, the focus of this thesis, liquid-liquid dispersion (or emulsion) is ubiquitous [Schramm, 2006] in the fields of environment (e.g., wastewater treatment), agriculture (e.g., insecticides), manufacturing (e.g., asphalt), medicine (e.g., hormone products) and so forth. Consequently, depending on the scenarios where an agitated mixer is applied, practitioners are required to design the mixing systems for minimizing investment and operating costs when the mass transfer is limiting, and

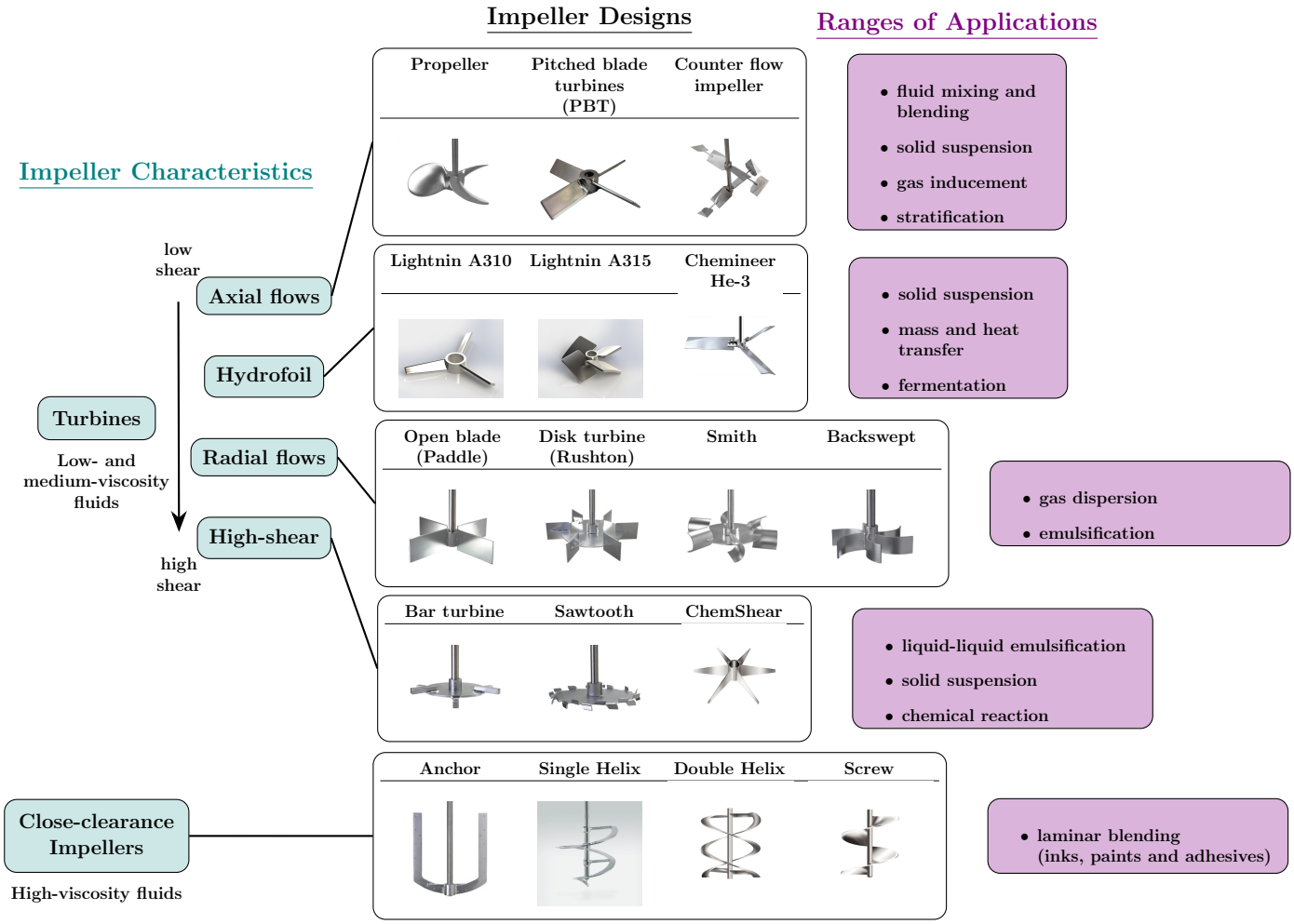


Figure 2.1: An general overview of typical impeller designs in industry.

thus enhancing profitability. For this purpose, hundred types of impellers have been developed and used prominently in industry. Recent development and research progresses relevant to the mechanical mixers can be referred to the review of [Jaszczur and Młynarczykowska, 2020].

Herein, Figure 2.1 provides a general overview of impellers widely used in industry. The selection of impellers can be affected by several factors, such as viscosity of fluids. In this figure, impellers are firstly divided into turbines and close-clearance impellers based on the fluid types they dominantly handle; turbines are employed in systems where low- and medium-viscosity fluids are involved while close-clearance impellers mainly copes with high-viscosity fluids. Furthermore, impellers are classified into different types depending on the flow pattern generated, applications and their geometrical configurations. Particularly, impellers are characterised by differing flow patterns and shear levels based on whether they are axial flows, radial flows, hydrofoils or high-shear configurations. In Figure 2.2, the flow types generated by different impellers are clearly sketched. As shown, in a radial flow motion, the mixing fluid is moved radially in the tank and then either up or down before traveling back to the center, giving rise to two circulating loops in the system, one below and one above the impeller. Alternatively, in the case of axial flow, the liquid is flowing in a vertical direction, solely up and down, introducing a single loop and stronger flow (i.e., higher pumping) compared to radial flow. This attribute

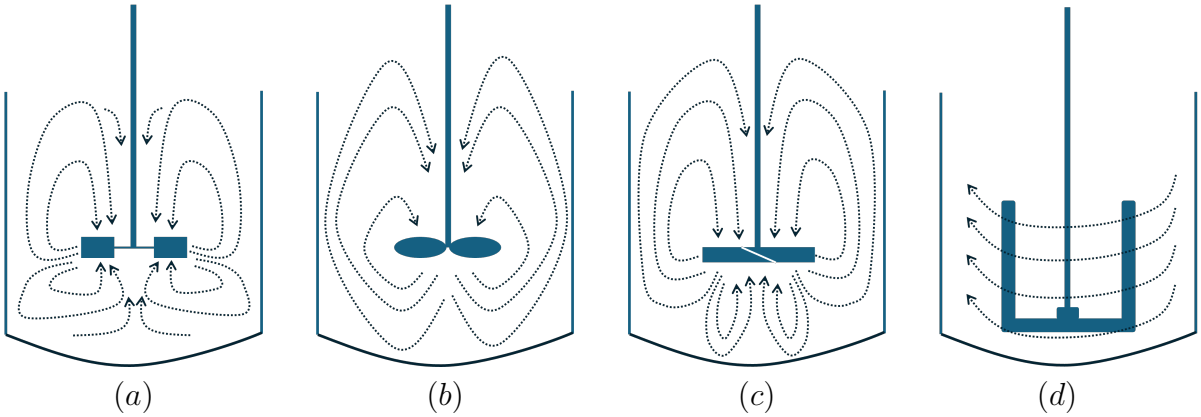


Figure 2.2: Schematic diagrams of flow fields generated by different impeller types: (*a*) radial; (*b*) axial; (*c*) mixed; (*d*) tangential.

also determines the shear level of a impeller and thereby its application ranges for which the impeller is ideally used [Paul et al., 2003, Ghotli et al., 2013]. For example, impeller generating axial flow is most suitable for solid suspension whereas the high shear level of a radial impeller makes it not recommended for processes that are sensitive to shear stress, e.g., bio-processes that involves fragile micro-organisms.

Though being categorised as axial flow impellers, pitched bladed turbines (PBTs) are considered as mixed-flow impellers as the flow discharged from which has both axial and radial components (see Figure 2.2*c*). Unlike radial flow impellers, the blades on PBTs are oriented, typically at a 45°angle. Hence, one of the main features of PBTs is the flexibility of generating varied flow fields with slight change in their configurations, for example, blade inclination and pumping direction. This makes PBTs become one of the most commonly-used impeller types in industrial applications and has led to numerous relevant studies in the literature (see Table 2.1)) [Zhou and Kresta, 1998, Chapple et al., 2002, EL-Hamouz et al., 2009, Furukawa et al., 2012, Major-Godlewska and Karcz, 2018, Mahakal et al., 2023]. This thesis is confined to liquid-liquid dispersion generated through a PBT with four 45°-inclined blades.

Moreover, hydrofoils have been developed to produce more flow and less shear than PBTs while high-shear impellers are designed to provide maximum shear possible. Consequently, hydrofoil impellers are often utilized in processes where axial flow is important and low shear is desired, for example, fermentation and enzyme production in bioreactors [McFarlane and Nienow, 1995]. On the other hand, applications of a high-shear impeller specifically lie in scenarios where high shear rate is preferred [Zhang et al., 2012], for instance, making emulsions at high speeds where a second phase could be added by intense mixing. As for a close-clearance impeller, it generates tangential flow (see Figure 2.2*d*) that moves the fluids horizontally around the vessel and a low level of shear [Paul et al., 2003]. In addition, as its name suggests, close-clearance impeller nearly sweeps along the vessel wall with a comparable size to the tank. These features make close-clearance impellers suitable for handling high-viscosity fluids and are widely used in applications requiring laminar macroscale blending at low speed, such as production of inks and pigment.

As indicated from above, apart from the shear level and flow patterns, there are two more important impeller characteristics for impeller selection, the pumping and the power. The pumping capacity of an impeller can be represented by the volume of fluids discharged from its rotation, while the power consumed by a mixer correlates with the drag and velocity of a specific section of the impeller. Both features depend on the impeller type and the impeller Reynolds number. The latter is defined as:

$$Re = \frac{\rho N D^2}{\mu}, \tag{2.1}$$

where ρ and μ represent the density and the viscosity of the mixing fluid, repectively; N is the impeller rotation speed (in unit of Hz or s^{-1}) and D is the impeller diameter. In stirred vessels, the flow regimes are identified as (a) laminar flow when $Re < 10$, (b) transition in the range of $10 < Re < 10^4$ and (c) turbulent above a value of $Re = 10^4$. Paul et al. [2003] showed that PBT exhibits the highest pumping number under turbulent conditions compared to other type of impellers, which increases with Re when $Re \leq 10^4$ and becomes constant at higher Re. Very few literature is available on the pumping numbers for various types of impellers. In contrast, a spectrum of experimental techniques have been employed to measure the power number of impellers [Ghotli et al., 2013] and numerous studies have provided the values. These studies [EL-Hamouz et al., 2009, Ghotli et al., 2013] revealed that, PBT has a higher power number compared to propeller impellers but lower than radial flow impellers. Similar to the pumping number, the power number remains independent of Re in turbulent regimes. In recent studies wherein researchers aimed to propose novel impeller geometries tailored for specific industrial scenarios, both power consumption and the generated flow characteristics are considered simultaneously [Ameur et al., 2018, Eggl and Schmid, 2022], emphasising the importance of power consumption in impeller selection process.

2.1.2 Parameters characterising liquid-liquid dispersion

Liquid-liquid mixing produces rich phenomena inside stirred vessels, such as mean flow pattern and turbulence, drop suspension, drop breakup and coalescence, interfacial area and drop size distribution (DSD). These phenomena render liquid-liquid dispersion one of the most complicated processes in industries, which are essential for describing liquid-liquid dispersion, leading to numerous studies dedicated to understanding each of them in depth. This part provides an overview of relevant studies that delve into the parameters crucial for describing a liquid-liquid mixing process induced by an agitated mixer. The studies highlighted herein encompass a range of topics including flow characteristics, drop breakage and coalescence, interfacial area and drop size distribution.

2.1.2.1 Flow characteristics: flow patterns, shear, and vortical structures

Flow patterns in stirred vessels are characterised by the relative distribution of mean and turbulent kinetic energy, for instance, Nambiar et al. [1990] reported that 60% of turbulence energy

dissipation occurs in the vicinity of impeller where the volume of this region is only 10% of the vessel volume. This disparity underscores the complexity of the turbulence in agitated vessels, which arises from the coexistence of regions with high turbulence intensities near the impeller and areas of low turbulence intensities further away from the rotating region. Sanjuan-Galindo et al. [2015] noticed that the rotating impeller produces an intermittent radial flow and periodic turbulent eddies, which exerts an influence on drop breakup process. Moreover, flow patterns depend mainly on the impeller design, which is associated with the fact that when the fluids are discharged from the impeller and start to circulate within the vessel, the mean kinetic energy is converted into turbulent kinetic energy, modifying their relative distribution, as described by Kumaresan and Joshi [2006]. Thus, numerous studies have been conducted to understand the relationship between impeller configuration and the corresponding flow characteristics, part of which are listed in Table 2.1. From these studies, flow patterns are characterised by velocity profiles (e.g., average velocity and its components) and turbulence-related parameters (e.g., maximum and mean energy dissipation rate and turbulent normal stress). Details with regard to the relationship between impeller configuration and these characteristics are not presented herein since they extend beyond the scope of this thesis, and the main relevant findings have been summarised in Figure 2.2.

Another flow characteristic that affects the mixing performance is the presence of trailing vortex. This vortical structure is formed behind each impeller blade [Van't Riet and Smith, 1975] and is regarded as the major mechanism governing the mixing and dispersion within a stirred vessel [Schafer et al., 1998]. In addition, high level of turbulence presented in the vortices plays a significant role on phenomena such as drop breakage in the mixer and cell damage in a bioreactor, hence, the identification of trailing vortex (its location, size and strength) has been investigated for different types of impellers, as exemplified in Table 2.1. Furthermore, through relevant studies, researchers have unravelled the intricate nature of mixing in agitated mixers by identifying a spectrum of hydrodynamical structures within the systems, vortex breakdown [Hall, 1972, Spohn et al., 1993, 1998, Piva and Meiburg, 2005], large-scale ring vortex [Desouza and Pike, 1972, Yianneskis et al., 1987] (which is described as flow circulation in Section 4.1.1), tip vortices [Sharp and Adrian, 2001], Moffatt vortices [Biswas and Kalita, 2016] and so forth. These vortical structures introduce a flow field of high complexity where different mechanisms govern the dispersion process depending on the local flow types (details can be found in Section 2.1.3).

Additionally, the rotation of the impeller blade induces velocity differences between adjacent portions of mixing liquids, introducing a high level of shearing forces in the impeller vicinity. These forces, which are represented by shear stress, drive the mixing process and are responsible for fluid circulation, as well as the dispersion and elongation of dispersed phases. The shear stress is a complex function determined by shear rate, which can be influenced by several aspects including the velocity gradients, turbulence level, and viscosity. Nonetheless, the shear rate, along with the macroflow velocity gradient, can be derived by measuring time-averaged

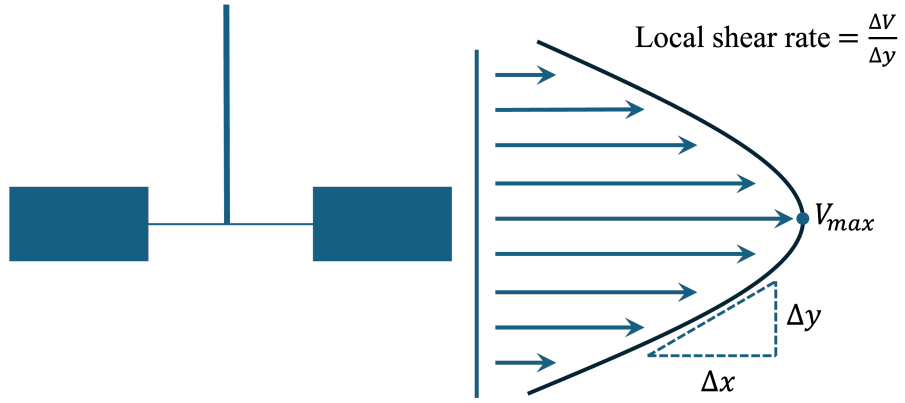
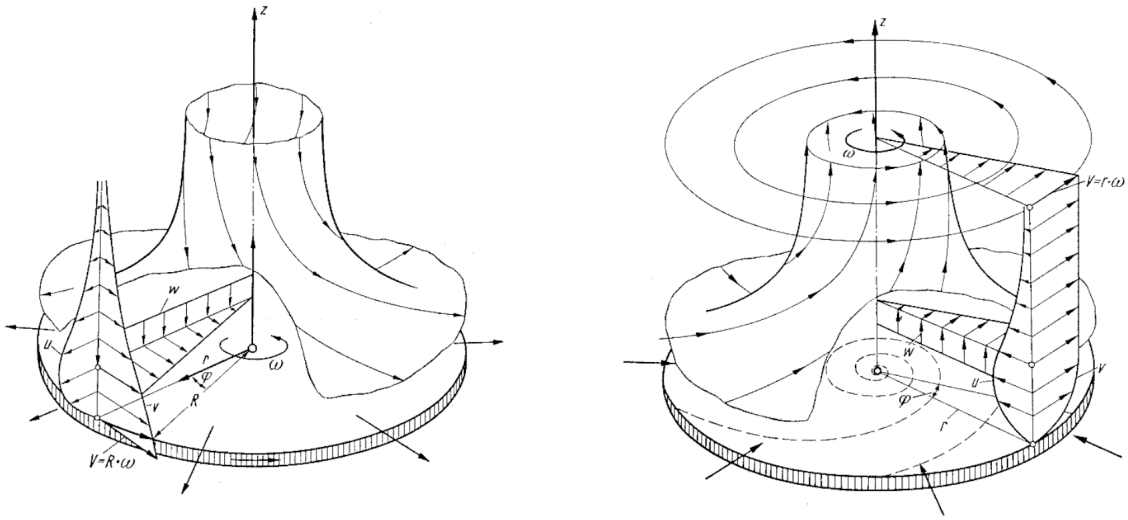


Figure 2.3: Vertical velocity profile adjacent to a impeller blade. Reproduced from Paul et al. [2003].



(a) **(b)**

Figure 2.4: (*a*) Flow at a rotating disk; (*b*) Rotating flow over an infinite ground. Both figures are from Schlichting and Kestin [1961].

velocities in the impeller vicinity (see Figure 2.3) [Paul et al., 2003]. According to Paul et al. [2003], this region yields high shear rates, although it occupies a relatively small volume in the vessel. This leads to the fact that only a minimal proportion amount of the fluids to be mixed experience these shear rates. Likewise, the vortices prevalent in agitated mixers exhibit high shear rates but with a smaller volume. Consequently, the overall mixing process is featured by the combination of shear rates and their corresponding volumes, a level of detail that can only be demonstrated through computational fluid dynamics.

Lastly, it is worth to note that Schlichting and Kestin [1961] describes two general types of boundary layers involving rotation, resembling the flows observed in stirred vessels. In the first case, an infinite disk rotates in a surrounding fluid at rest with a constant angular velocity about an axis perpendicular to its plane. Considering the no-slip condition and the viscosity, the layer of fluid adjacent to the disk moves along with it and is discharged from the disk by the centrifugal force. Subsequently, fresh fluid is dragged down to the disk and driven outwards in a similar way, as displayed in Figure 2.4a. Another case considers a rotating flow over a

Table 2.1: Studies surrounding flow patterns in stirred vessels.

Flow characteristics	Impeller considered	References
Velocity profiles	Rushton turbine	Spencer and Wiley [1951], Aiba [1958], Desouza and Pike [1972], Yianneskis et al. [1987], Costes and Couderc [1988], Mishra et al. [1998], Montante et al. [1999], Yoon et al. [2001], Yoshida et al. [2009]
	PBT	Aubin et al. [2001], Jaworski et al. [2001], Tsui et al. [2006]
	Close-clearance impeller	Tsui and Hu [2011]
Turbulent-flow parameters	Rushton turbine	Nishikawa et al. [1976], Lee and Yianneskis [1998], Derksen et al. [1999]
	PBT	Kresta' and Wood [1993], Gabriele et al. [2009]
Velocity profiles & Turbulence features	Rushton turbine	Wu and Patterson [1989], Schäfer et al. [1997], Sharp and Adrian [2001], Yapici et al. [2008], Basavarajappa et al. [2015]
	PBT	Hockey and Nouri [1996], Patwardhan and Joshi [1999], Khan et al. [2004], Kumaresan and Joshi [2006], Driss et al. [2010]
Trailing vortices	Rushton turbine	Van't Riet and Smith [1975], Yianneskis et al. [1987], Stoots and Calabrese [1995], Escudié et al. [2004]
	PBT	Schafer et al. [1998], Suzukawa et al. [2006], Zhao et al. [2011]

stationary plane, wherein the flows circulate with a constant angular velocity at a distance from the ground. Under this scenario, the fluids near the ground experience a radial pressure gradient directed inwards, in addition to the centrifugal force as in the previous case. However, the centrifugal force in this case is dramatically decreased and thus a radial inward flow is produced, accompanied by a rising axial flow due to continuity (see Figure 2.4b). In both cases, a flow arises such that its direction deviates from that of the outer flow, which is also known as a secondary flow. These fluid behaviours are commonly seen in a vessel equipped with a rotating impeller (see Section 4.1.1).

2.1.2.2 Drop breakage and coalescence

Drop breakage and coalescence are fundamental phenomena inherent in the evolution of turbulent liquid-liquid dispersion. Sathyagal et al. [1996] suggested that quantitative understanding

of the rates of drop breakage and coalescence are crucial for controlling the evolution of drop size distribution and, consequently, optimising the performance of liquid-liquid mixing systems. Studies surrounding the dynamics of breakup and coalescence can be very extensive. A spectrum of experimental techniques are applied to observe these behaviours [Nachtigall et al., 2016, Kamp et al., 2017] and various model equations have been developed for determination of breakage and coalescence under different conditions [Luo and Svendsen, 1996, Maaß et al., 2007, Liao and Lucas, 2009, 2010]. In general, coalescence can be affected by diverse physiochemical properties of the fluids, such as double layer [Paul et al., 2003]. In addition, its visualisation requires a high resolution and careful experimental setups [Kamp et al., 2017]. On the other hand, the breakage process has been widely explored using the framework of population balances [Ramkrishna and Singh, 2014], wherein breakage events arising from each individual drop are considered providing a mathematical formulation for the drop number evolution in a purely breaking dispersion. The main findings relevant to drop breakage visualisation will be discussed in Section 2.1.3.3, and for knowledge regarding breakage and coalescence dynamics this thesis refers the reader to the literature cited above.

When a steady-state dispersion is achieved, breakage and coalescence reach a dynamic equilibrium, where no further change is seen in the average size of drops or their size distribution [Pacek et al., 1999]. In cases where an equilibrium state is not reached, the increase in the amount of dispersed phases will cause the coalescence to become increasingly dominant over the breakage. Several studies investigated the effect of volume fraction in the continuous phase on the breakage-coalescence balance. Wichterle [1995] showed that when a minimal volume fraction is dispersed into the continuous phase, the presence of drops have negligible impact on the continuous phase, with interactions between drops occurring infrequently. Under this condition, the drop size is mainly determined by breakup in the impeller region [Nienow et al., 1997]. In contrast, higher amounts of dispersed phases facilitate the interaction between drops, intensifying the coalescence processes.

2.1.2.3 Drop size distribution

Various methods have been applied to observe drop size distributions in mixing vessels, which are mainly used to measure the final steady-state distribution [Paul et al., 2003, O'Rourke and MacLoughlin, 2005, Bowler et al., 2020]. However, determining the drop size distribution becomes challenging when the dispersed phase volume fraction is high or the drop size is small. Therefore, early studies have introduced an alternative approach, using the mean or Sauter mean diameter (d_{32}) instead of specifying the entire size distribution. Typically, the Sauter mean diameter is defined as [Paul et al., 2003]:

$$d_{32} = \frac{\sum_{i=1}^{i=m} n_i d_i^3}{\sum_{i=1}^{i=m} n_i d_i^2}, \tag{2.2}$$

where m denotes the number of size classes, n_i and d_i represent the number of drops and the nominal diameter of drops in size class i. The subscripts indicates that d_{32} is derived from the

ratio of the third to second moments of the DSD; d_{32} is widely used in experimental work since it is directly related to the dispersed phase volume fraction, ϕ and interfacial area, a_v, through $d_{32} = 6\phi/a_v$. In addition, in turbulent conditions, as a drop diameter decreases, it eventually reaches a point where further deforming stress no longer reduces its size. This stable maximum size of the drop within the impeller region is termed the maximum drop diameter, d_{max}.

As discussed earlier, Hinze [1955] attributed the drop breakage to the balance between disruptive forces and restoring ones, suggesting the correlation with regard to d_{max}, which is valid in those cases where the dispersed phase viscous force can be negligible (for instance, dilute dispersion and non-viscous dispersed phase):

$$\frac{d_{max}}{D} = c_0 We^{-0.6}. \tag{2.3}$$

In addition, d_{max} is related to turbulent dissipation rate ϵ_T through an energy analysis:

$$\frac{d_{max}}{D} = c_1 \epsilon_T^{-0.4}. \tag{2.4}$$

In the above equation, c_0 and c_1 above are constants determined by experiments. However, it is challenging to establish similar correlations for d_{32} through a force or energy analysis. Nonetheless, Sprow [1967] first suggested that d_{32} is proportional to d_{max} ($d_{32} = cd_{max}$ with c as a constant), which was verified using his experimental data. It is accepted that the constant value varies with operating conditions and fluid properties, and a list of literature surrounding this topic is given by Zhou and Kresta [1998]. Though Pacek et al. [1998] doubted the relationship between d_{32} and d_{max}, several studies adopted the assumption and modified Equation 2.3 by considering effects of dispersed phase viscosity and volume fraction [Calabrese et al., 1986, Kraume et al., 2004, Liu et al., 2013]. The review relevant to d_{32} and d_{max} is deferred to Section 2.1.3.2.

Nevertheless, effort has been made to provide an insight into the shape of drop size distribution in agitated mixers. For example, Wang and Calabrese [1986] found that the DSD were fitted well with a Gaussian distribution. Holm et al. [1991] observed a bimodal form of the size distribution that remained unchanged even with further mixing. Zhou and Kresta [1998] reported that four types of DSDs evolve with increasing impeller rotational speed. Moreover, several studies suggested that the log-normal distribution demonstrates the best fit with the experimental DSD [Ruiz et al., 2002, Boxall et al., 2010, Mahakal et al., 2023]. In addition, the effect of physical properties and operating conditions on the DSD were extensively explored. The first general trend revealed by previous studies is that higher impeller speeds leads to a shift towards smaller drops and narrower distributions, indicating a more homogeneous drop size profile [Holm et al., 1991, Pacek et al., 1998, Ruiz et al., 2002, Naeeni and Pakzad, 2019]. Furthermore, Khalil et al. [2010] proposed that power input has an significant impact on the width of DSD, in the sense that impellers with a lower power number tend to produce wider DSD; thus, a propeller generated a narrower DSD compared to that formed by a Rushton turbine. More examples with

regard to this were given by Pacek et al. [1999] and Mahakal et al. [2023] (PBT vs. RT). Apart from this, Shimizu et al. [1999] demonstrated that non-Newtonian properties in the continuous phase resulted in a wide DSD. El-Hamouz [2009] found that at fixed dispersed phase volume fraction, a higher dispersed viscosity gave rise to a wider DSD. They also investigated the effect of drop initial position in the stirred vessel and found that drops injected near the impeller region resulted in a narrower distribution of daughter drops.

2.1.2.4 Interfacial area

Though there are limited studies directly measuring interfacial area in a stirred mixing system [Eckert et al., 1985], it remains a crucial parameter evaluating the dispersion performance. The mixing of immiscible liquids inherently increases interfacial area, which significantly influences the rates of mass and energy transfer in the liquid systems, and affects chemical reactions such as nitration, alkylation and so forth [Ghotli et al., 2013]. From above, interfacial area can be derived from $d_{32} = 6\phi/a_v$, and hence, the determination of the interfacial area is closely linked to that of drop size.

2.1.3 Drop breakage in agitated vessels

Numerous works have been carried out to explore the drop breakage within a stirred mixer, addressing problems such as breakage mechanisms (see Section 2.1.3.1). These studies revealed that the drop breakage has been studied using two approaches [Hasan, 2017]. The first approach, which is common in early studies, involves determining the maximum stable drop diameter (d_{max}) or Sauter mean diameter (d_{32}) for the evolution of drop population, while more recent works attempt to unravel the breakage process by tracking a single drop breakup using high-speed imaging. The literature surrounding these topics is reviewed in Sections 2.1.3.2 and 2.1.3.3, respectively. Topics with regard to surfactant-laden flows and computational fluid mixing will be addressed in Sections 2.1.4 and 2.1.5, respectively.

2.1.3.1 Breakage mechanisms

As mentioned above, the turbulence in stirred vessels is not spatially homogeneous and, therefore, the dispersion process is affected by local flow patterns. Hence, various dispersion mechanisms have been proposed in the literature, which can be mainly classified as follows [Liao and Lucas, 2009, Hasan, 2017]:

Turbulent fluctuation or drop-eddy interaction Turbulence is characterised by the presentation of a highly rotating fluid element called as "eddy", which can be of different sizes, intensities and lifetimes [Kolmogorov, 1949]. The most widely accepted drop breakage mechanism in turbulent conditions comes from Kolmogorov [1949] and Hinze [1955], which postulates that the occurrence of breakup depends on a competition between the restoring forces and the external deforming forces. This mechanism provides predictions of the largest surviving drop size, i.e., d_{max}, experiencing these stresses. Specifically, the cohesive forces encompasses

viscous stress of the dispersed phase τ_μ and interfacial tension stress τ_σ, while the disruptive ones include viscous stress of the continuous phase and turbulent fluctuation at the interface [Zhou and Kresta, 1998]. According to Hinze, the two stabilising stresses are expressed as:

$$\tau_\mu \approx \frac{\mu_d}{D_{\text{drop}}}\sqrt{\frac{\tau_{\text{def}}}{\rho_d}}, \quad \tau_\sigma \approx \frac{\sigma}{D_{\text{drop}}},$$

where τ_{def} denotes the deforming stress due to turbulent velocity fluctuations. According to this theory, the response of the dispersed drop to stress τ_{def} varies depending on the length scale of eddies [Andersson and Andersson, 2006, Paul et al., 2003]. When the drop encounters an eddy that is larger than its diameter, it will be simply transported along in the eddy with little deformation (see Figure 2.5*a*). However, when the drop contacts eddies similar in size, it undergoes deformation, which can lead to two outcomes: being torn apart by co-rotating eddies (Figure 2.5*b*) or stretched by the compression of two counter-rotating eddies (Figure 2.5*c*). Furthermore, interactions with multiple small eddies could occur as shown in Figure 2.5*d*. Hence, the stress τ_{def} can be derived by integrating the energy spectral density function, $E(k)$, for the continuous phase over all eddies of length scale less than D_{drop}; here, $E(k)$ represents the energy per unit volume contained in eddies with wave number ranging from $k = 1/D_{\text{drop}}$ to $k + dk$. As a result, τ_{def} can be written as:

$$\tau_{\text{def}} = \rho_c \int_{1/D_{\text{drop}}}^{\infty} E(k)\, dk = \rho_c \overline{u'^2(D_{\text{drop}})}.$$

Here, $\overline{u'^2(D_{\text{drop}})}$ represents the turbulent mean-square velocity difference across the drop surface, which is obtained from the energy spectral density function. Moreover, the resulting three stresses determine turbulent drop breakup via two dimensionless numbers:

$$We = \frac{\tau_{\text{def}} D_{\text{drop}}}{\sigma}, \quad Oh = \frac{\mu_d}{\sqrt{D_{\text{drop}}\rho_d\sigma}}, \tag{2.5}$$

where We represents the Weber number describing the deforming stress due to velocity fluctuation in comparison to the stabilising effect of the interface tension, while Oh denotes the Ohnesorge number describing relative significance of the stabilising effects arising from the viscosity and the interfacial tension.

The Weber concept requires the Weber number to exceed a critical value for drop breakage. However, despite various proposed expressions for the τ_{def} and $E(k)$ based on the relative drop size to Kolmogorov length (see the summarising table in Rueger and Calabrese [2013]), this theory fails to explain results observed in different mixing applications. Consequently, extensions and modifications of the concept have been suggested in the literature. For example, Risso [2000] criticised this theory and argued that the breakup of drops under turbulent conditions cannot be adequately described by a simple force balance between deforming and stabilising effects. Instead, the author stated that the deformation and relaxation processes prior to the breakage play significant roles. These processes are influenced by stabilising interfacial tension

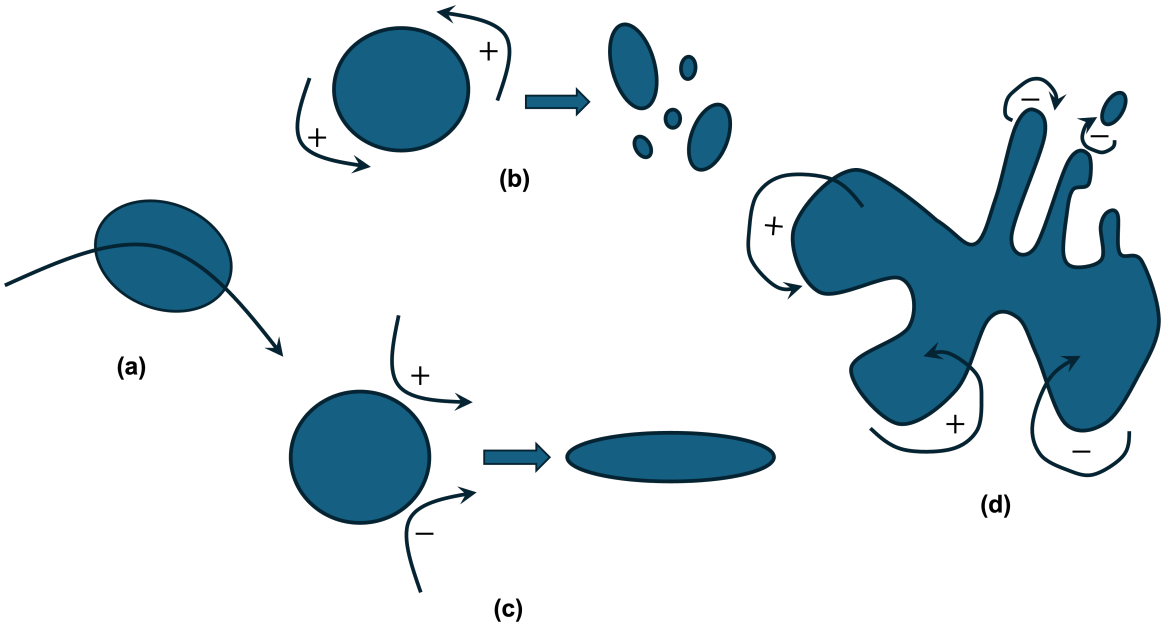


Figure 2.5: Schematic representation of interaction between turbulent structures and drops, adapted from [Paul et al., 2003]. (*a*) Transport with large eddy; (*b*) shear by co-rotating eddies; (*c*) stretching by counter-rotating eddies; (*d*) multiple combined interactions.

and dispersed phase viscosity, in addition to deforming forces from one or more successive interactions with eddies. Furthermore, Kumar et al. [1992] described drop oscillations in stirred vessels using a two-stage model: dispersed drops circulate between the impeller vicinity, where deformations and breakage occur, and the region away from this region where relaxation processes dominate. Consequently, the author demonstrated that drop breakup in stirred vessels can be caused by more successive eddies through resonance effects. Later, Andersson and Andersson [2006] introduced two criteria necessary to describe maro-scale deformations prior to drop breakup. In addition to a stress criterion essential for reaching critical drop deformation, they formulated an energy criterion to elucidate the duration of the deformation process. More criteria for breakup are summarised in [Liao and Lucas, 2009].

Laminar shear stresses Viscous shear forces in the surrounding fluid create a velocity gradient around the interface, which could be another cause to drop deformation and breakage. The drop breakage mechanism in laminar flow is determined by the structure of the flow field and the trajectory that each drop follows [Bigio et al., 1998]. This is practically challenging, and therefore, many studies examined simple and idealised cases of laminar drop breakup (e.g., pure shear or pure extension) as limiting base cases for comparison when analysing sizes of drops formed in complex, real-world flows (e.g., stirred mixing systems.) [Rueger and Calabrese, 2013].

The most representative work with regard to this topic is given by Grace [1982], who studied drop breakup in simple extensional shear flows. For each of their cases, the authors constructed stability curves, relating the maximum drop size to the viscosity ratio, μ_d/μ_c. Similar to the theory in turbulent conditions, the breakup process in this case can be described as a balance

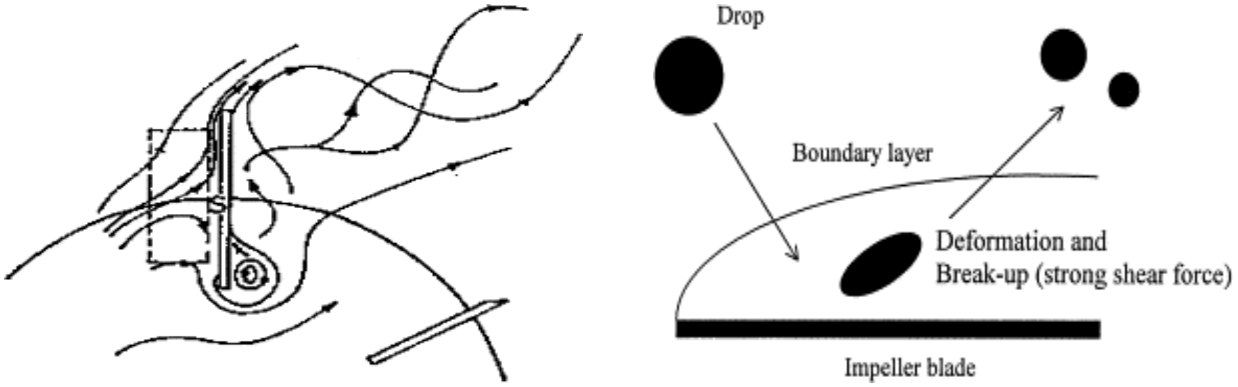


Figure 2.6: (a) Elongational flow in the vicinity of the blade [Kumar et al., 1998];(b) Deformation and breakage of a drop in the boundary layer of the blade [Shimizu et al., 1999].

between external viscous stresses and interfacial tension stress. Grace [1982] expressed this force balance in the form of a dimensionless Capillary number:

$$Ca = \frac{\mu_c \dot{G} R_{drop}}{\sigma}, \tag{2.6}$$

where $\dot{G}$ is the deformation (i.e., shear or extension) rate acting on the drop and R_{drop} is the drop radius. It is reported that the d_{max} occurs when the μ_c/μ_d is close to unity for both studied cases. Another most-cited work is done by Bentley and Leal [1986], where the stability curves was presented correlating the Ca and viscosity ratio for simple shear and extensional flows. More studies have expanded knowledge in this field, for example, Rueger and Calabrese [2013] reported that the drop breakup resulting from simple shear is increased with increasing viscosity of continuous phase, but details are not discussed herein due to the extension of this topic.

Shear of the impeller blade This mechanism expresses that breakage occurs due the shear layer close to the blade surface. Kumar et al. [1991, 1998] suggested that the rotating impeller can produce an elongational flow in its vicinity (see Figure 2.6a). Considering the no-slip condition on the blade, the large gradient between the mother drop and shear layer can break the drop into numbers of daughter drops. Additionally, Shimizu et al. [1999] proposed a mechanism where the drop breakage could occur in the boundary layer of the impeller blade. As demonstrated in Figure 2.6b, the authors suggested that there exists a strong shearing effect in the boundary layer of the blades which leads to a breakage event.

Collision of drops with the blades Finally, the sharp impeller blades can break the drop without previous deformation or within a short deformation time. More information surrounding the roles of impeller mechanics, baffles and vessel wall on the drop breakage can be referred to Sanjuan-Galindo et al. [2015].

2.1.3.2 Studies through d_{max} and d_{32}

Many researchers have tried to construct models to describe the breakage phenomena observed in turbulent dispersion. Generally, there are two types of modelling [Sathyagal et al., 1996]: models for d_{max} and d_{32}, and other models for breakage frequency and daughter drop size distribution. In this section, we focus on the first case as the latter extends outside the main context of this thesis. A comprehensive review of the second type of modelling can refer to Liao and Lucas [2009].

Early studies commonly characterised breakage phenomena by determining d_{32} or d_{max} under different setups. These studies demonstrated that the drop breakage in stirred vessels is influenced by various factors such as physical properties of both continuous and dispersed phases, hydrodynamics in the vessels, geometry of vessel and impeller. The rest of this section reviews the main findings of previous work by the effect of these parameters. A comprehensive table presenting details of relevant works such as experimental setups is provided in Hasan [2017].

Physical properties From the force analysis above, the effects arising from physical properties can be represented by two factors: the interfacial tension of the dispersed phase and the viscosity of two phases. Stamatoudlsr [1985] investigated the effect of continuous phase viscosity on the d_{32}, wherein kerosene and mineral oil were used as dispersed phases. In the former case, the d_{32} increased initially with increasing viscosity of the continuous phase and then reduced after reaching its peak. For mineral oil, the d_{32} grew slightly and then decreased dramatically when the continuous phase viscosity was increased. The authors reasoned this difference to the viscosity ratio between dispersed and continuous phase. On the other hand, Nishikawa et al. [1987] reported that the d_{32} increases linearly with decreasing viscosity of continuous phase. Wang and Calabrese [1986] observed that increasing the viscosity of the dispersed phase (in the range of $\mu_d = 0.001 - 0.1 kg \cdot m^{-1} \cdot s^{-1}$) resulted in an increase in d_{32}, indicating a reduction in breakup events. The authors noted that when the dispersed phase viscosity was low, the drop sizes increased by more than a factor of six, while the drop sizes only varied by a factor of two with high dispersed phase viscosity values due to the diminishing effect of interfacial tension as viscosity rises. Additionally, they also demonstrated that the increase in interfacial tension led to an increase in d_{32} due to the decrease in breakage rate. A similar conclusion was made through the work by Sathyagal et al. [1996] where experiments were performed investigating systems of different dispersed phase viscosity and interfacial tension. They found that the breakage rate decreased considerably as viscosity and interfacial tension were increased, though its dependence on viscosity is weaker compared to that on interfacial tension. However, Kraume et al. [2004] suggested that the viscosity has a larger influence on drop breakup, which is contradictory to the previous finding. Such discrepancy is prevalent in the literature as fluid systems and operating conditions vary across different studies. For other physical properties, Shimizu et al. [1999] studied the effect of non-newtonian properties of continuous phase; Ruiz et al. [2002] provided an insight into the influence of temperature.

Generally, from the findings presented above, increasing the viscosity of the continuous phase enhances the disruptive forces acting on it, which overcome the cohesive forces holding the dispersed drop. Consequently, the breakage rate increases, producing smaller daughter drops. In contrast, higher dispersed phase viscosity and interfacial tension increase the restoring forces that resist deformation, leading to larger daughter drops. However, it is worth noting that the relationship between drop size and these properties is nonlinear and depends on their specific ranges. Meanwhile, as indicated earlier, there is some confusion in the literature regarding the effects of viscosity and interfacial tension on the daughter drop sizes. Some studies suggest that the interfacial has a more pronounced effect, while others state viscosity is more impactful. The general understanding is that both properties affect drop size by influencing the cohesive forces. Typically, higher interfacial tension or viscosity result in larger drops.

Another crucial affecting factor is the phase volume fraction, denoted using ϕ, between the two mixing fluids. Numerous studies have been working on the modification of drop size with varying dispersed phase volume fraction [Weinstein and Treybal, 1973, Zhou and Kresta, 1998, Nishikawa et al., 1987, Boye et al., 1996, Lovick et al., 2005, Galinat et al., 2007, Liu et al., 2013, Ghotli et al., 2019]. Specifically, Boye et al. [1996] demonstrated a change in the breakage mechanism with increasing ϕ, i.e., eddy-drop breakage when $\phi < 0.5$ and boundary layer breakage when $\phi > 0.5$. In addition, Galinat et al. [2007] provided an insight into the effect of ϕ on the flow structures in the stirred vessels. These works consistently showed that increasing ϕ resulted in drop size increment, for example, Ghotli et al. [2019] reported that an increase in ϕ (0.01 to 0.1) led to an increase in d_{32} by approximately $20\% - 40\%$, though Lovick et al. [2005] reported that phase fraction had no obvious effect on the drop size. This discrepancy was attributed to the different fluid properties and experimental setups, as stated by Lovick et al. [2005]. Nonetheless, it seems that the dispersed phase volume fraction has an important role in drop size and coalescence. It is widely accepted that high values of ϕ increase the possibility of dispersed drop collision, and thus the drop coalescence. Hence, studies dedicated to drop breakage process tend to investigate a very diluted system to avoid the effect of coalescence (e.g., $\phi = 0.005$) [Zhou and Kresta, 1998, Shimizu et al., 1999], while those regarding coalescence use highly-concentrated systems with ϕ up to 0.5 [Chatzi and Kiparssides, 1995, Desnoyer et al., 2003, Kraume et al., 2004, EL-Hamouz et al., 2009].

Hydrodynamics As demonstrated previously, turbulence in a stirred vessel is inhomogeneous which makes it challenging to systematically study the relative influence of mean flow, trailing vortices, and turbulence fluctuations on drop breakage [Escudie et al., 2003, Lemenand et al., 2013]. Additionally, the interaction of a drop with the surrounding fluids heavily depends on its trajectory, which is difficult to track with current techniques. As a result, the roles of hydrodynamic behaviours between continuous and dispersed phases remain unclear. Nevertheless, previous studies consistently show that an increase in agitation speed or power input leads to a decrease in drop size [Nishikawa et al., 1987, Ruiz et al., 2002, Shimizu et al., 1999, Naeeni and Pakzad, 2019]. EL-Hamouz et al. [2009] recorded the deformation and consequent daughter

drop size of drops injected from different positions (one near the impeller and another near free liquid surface). Their findings highlighted the importance of drop trajectory, specifically the initial position of drops, a factor often overlooked by many experimentalists.

Geometry Geometry of impeller and vessel affects the drop breakup by influencing the local energy dissipation in the vessel. The parameters considered in previous work include dimension of baffles and impellers, impeller types and its relative position in the vessel. Leng and Quarderer [1982] noticed that the presence of baffles leads to a reduction in drop size. Nishikawa et al. [1987] found that at a fixed energy dissipation rate, d_{32} can be increased by increasing the impeller diameter. Conversely, Patil and Kumar [2010, 2011] reported that larger impeller diameters result in smaller d_{max}. The d_{max} obtained with a 60mm impeller is 2/3 of that attained with a 40mm impeller. This disagreement could be attributed to the sample position in Nishikawa et al. [1987] where coalescence is likely to occur [Laakkonen et al., 2005, Hasan, 2017]. Moreover, Giapos et al. [2005] presented that the increase in number of impeller blades results in an increase in the d_{32}. It is noticed that most of previous works were dedicated to the Rushton turbine, and hence, Table 2.2 provides a list of those studies investigating other impeller types than the Rushton turbine. Specifically, Zhou and Kresta [1998] provided a comprehensive insight into the effect of impeller design on the d_{32} by exploring four types of impellers. They found that the design of the impeller, including its dimension (e.g., diameter) and position, is effective on the breakage rate and thus affects the drop size.

From a practical standpoint, industry incorporates various mixing vessel geometries tailored for different liquid-liquid systems and operating conditions. An optimal design for stirred tanks and selecting the appropriate impeller type and dimensions are crucial for successful mixing processes. From the results stated above, geometrical parameters including vessel size, baffle dimensions and impeller geometry influence significantly the drop size by affecting the breakage processes. However, Hasan [2017] remarked that the extent of influence depends on the physical properties of both mixing fluids and operational conditions (e.g. impeller speed). Generally, increasing the impeller diameter leads to a reduction in daughter drop size by increasing the energy dissipation rate. The geometry of the vessel and impeller affects the trajectory of the mother drop, when it approaches the region of high dissipation rate, the breakage probability increases and smaller daughter drops are produced.

2.1.3.3 Studies through single drop

Determination of d_{32} and d_{max} helps to have an overview of the drop size distribution and its evolution, however, it does not provide knowledge about the interfacial phenomena of the breaking drop. Advancements in high-speed imaging techniques have facilitated the study of these phenomena introduced by liquid-liquid dispersion. By recording the mother drop motion, this type of study provides an unprecedented level of detail regarding the deformation, the breakage locations in the vessel, and the birth of daughter drops. In addition, these studies enable the estimation of sizes and number of daughter drops under highly non-uniform turbu-

Table 2.2: Studies regarding drop size of other impeller types apart from Rushton turbine.

Impeller types	Main objectives	References
A310, HE3, PBT, RT	Correlation between d_{32} and turbulent flow	Zhou and Kresta [1998]
A310, HE3, PBT, RT	Evolution of DSD when different impeller are used	Zhou and Kresta [1998]
RT, 6-blades turbine, HE3S, HE3L, CS2, CS4	Influence of impeller types on DSD	Pacek et al. [1999]
RT, hydrofoil, PBT	Influence of impeller types and agitation condition on DSD	Musgrove and Ruszkowski [2000]
Continuous stirred reactor	Qualifying the effective interfacial area	Quadros and Baptista [2003]
High shear Sawtooth, PBT	Effect of impeller selection	EL-Hamouz et al. [2009]
Hydrofoil impellers(A310, HE3)	-	Podgórska [2009]
RT, flat blade propeller	Test the coupling use of in-situ video probe and automated image analysis	Khalil et al. [2010]
Flat blade impeller	Influence of dispersed phase fraction on DSD	Maaß et al. [2012]
Rotor-stator mixer	Drop breakage in diluted system and effect of phase fraction	Rueger and Calabrese [2013],Rueger and Calabrese [2013]
Rotor-stator homogenizer	Measurement and analysis of bimodal DSD	Liu et al. [2013]
RT,CB,EB,PB,DCB,PBTU, PBTD,HE3	Drop size evaluation with various impeller design	Ghotli et al. [2019]

lence. In this way, relevant studies facilitate a deep understanding of the deformation process prior breakup, the shapes of daughter drop, the trajectory they follow, as well as the deformation and breakage time. These insights are essential for accurately estimating the breakage rate. This part reviews previous single drop experiments and relevant numerical simulations, which contribute to a comprehensive insight with regard to drop breakage in stirred vessels.

Konno et al. [1983] carried out the first single drop experiment across three stirred vessels of varying diameters, wherein the authors tracked the drop breakup trajectory and reported the path length along with the distribution of breakup position. Subsequently, Hančil and Rod [1988] analysed the mother drop lifetime and the average number of daughter drops using a small vessel ($T = 5$cm) with high ratio of impeller to vessel diameter. Later, Maaß et al. [2007] introduced a novel experimental setup, the breakage cell (see Figure 2.7), facilitating the single drop breakup recording. This setup features continuous fluid flow through a fixed single blade in a rectangular channel, simulating a stirred liquid-liquid system's flow field, with single drop injection to replicate breakup phenomena. A number of following works adopted this experimental setup and have reported informative details surrounding drop breakage in

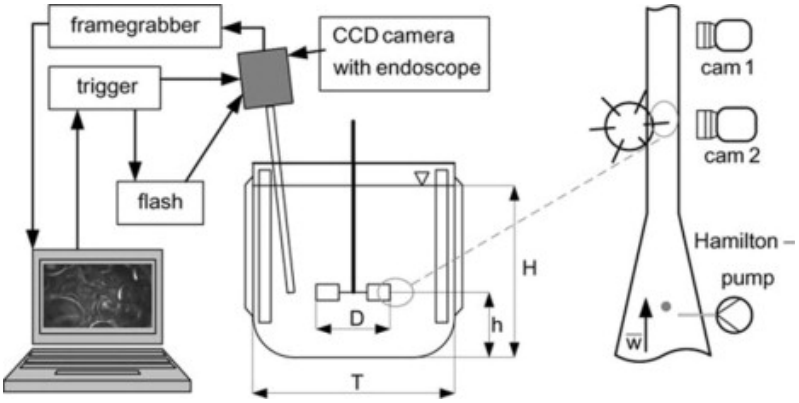
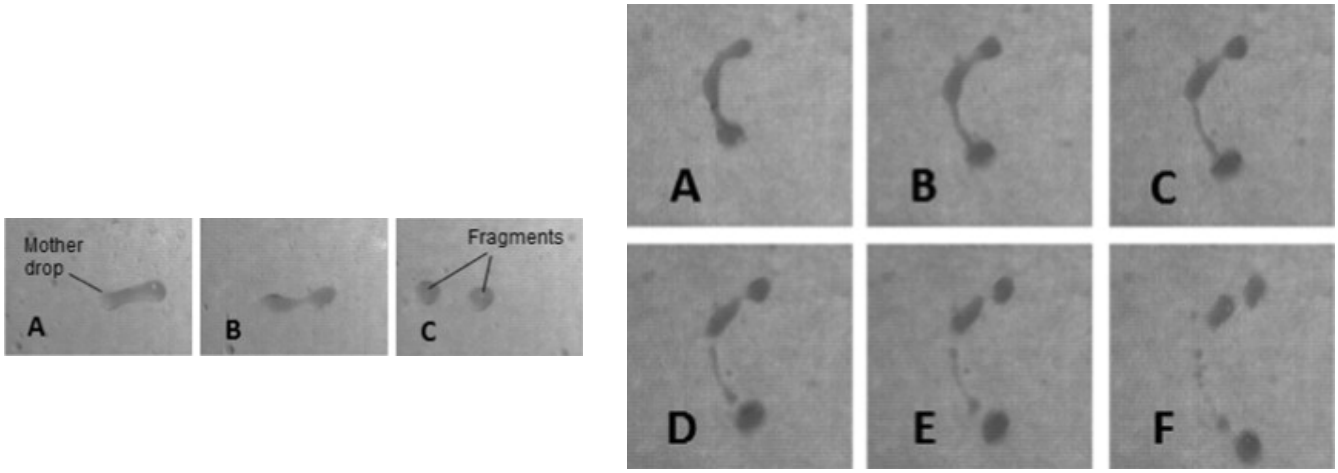


Figure 2.7: The drop breakage cell for simulating breakage phenomena in stirred vessels Maaß et al. [2007]

stirred vessels, for instance, breakage event location [Maaß et al., 2009], breakage rate [Maaß and Kraume, 2012], breakage mechanism [Nachtigall et al., 2012] and deformation mechanism [Nachtigall et al., 2016]. The main findings of Nachtigall et al. [2012] are highlighted here as the authors correlated the drop behaviours with the flow properties of the continuous phase, which illustrated that the extent of deformation is dependent on the stabilising interfacial tension, viscosity, and the disruptive forces exerted by successive turbulent eddies. From these studies, if the mother drop approaches the impeller vicinity, it will experience greater deformation compared to when its trajectory is further away from the impeller. For example, Maaß and Kraume [2012] showed the elongation of a viscous drop in the blade region, where the drop stretches to a long thread prior to its breakup into several daughter drops. Moreover, significant deformation may occur when there is a considerable difference between the speed of flow discharged from the impeller and the mother drop. In this case, the deformation may lead to either breakage or no breakage, which is determined by the interfacial tension of the dispersed phase and the viscosity of both phases. The mother drop either breaks up or becomes highly deformed and subsequently relaxes without breaking. Sanjuan-Galindo et al. [2015] presented that viscous drops elongate, stretch, and break in turbulent flows, which are observed to simply remain stable under non-turbulent conditions. In the case of stirred vessels, both cases are expected due to the non-uniform flow patterns described earlier that exhibit turbulent and non-turbulent conditions simultaneously.

Furthermore, Sanjuan-Galindo et al. [2015] proposed a four-step mechanism for drop breakage in a stirred tank: (1) the approach of the mother drop to the turbulent region; (2) deformation of mother drop; (3) fragmentation and (4) dispersion of daughter drops away from the impeller. From previous work, such processes may lead to various type of breakage events, which are typically characterised by the number of daughter drops produced from the mother drop of a given size. Konno et al. [1983] highlighted that ternary breakup occurs predominantly for the studied range of drop diameter and impeller speed. Hančil and Rod [1988] found that larger volume of the mother drop results in the increase in the average number of produced drops from 2 to 6. Likewise, Sathyagal et al. [1996] reported that increasing the mother drop size leads to an increase in the breakage rate. Furthermore, Kuriyama et al. [1995] found that the number of daughter drop is increased from 5 to 26 by increasing the Reynolds number from 15000 to 42000.



(a) (b)

Figure 2.8: Image sequence of drop breakage events from Solsvik and Jakobsen [2015]. (*a*) Equally-sized binary breakup; (*b*) multiple fragmentation.

A similar conclusion, stating that the number of produced drops increases with the mother drop size and flow velocity, has been made in several studies [Galinat et al., 2005, Maaß et al., 2007, Maaß and Kraume, 2012, Solsvik and Jakobsen, 2015]. Specifically, Solsvik and Jakobsen [2015] provided visualisations of interface behaviours during various breakup events, such as equally sized binary breakage (see Figure 2.8a), ternary drop breakage and multiple fragmentation (see Figure 2.8b). More experimental works are listed in Table 2.3. From the studies above, the number of daughter drops depends heavily on the mother drop size and agitation speed (or, equivalently, the energy dissipation rate). The frequency of multiple breakage increases with increasing mother drop size and energy dissipation rate.

Table 2.3: Experimental studies on single drop breakup. In this table, D is the impeller diameter, T the vessel diameter, d_m the mother drop diameter, P the Power number, V_m the volume of mother drop, N the impeller rotation speed, μ the drop viscosity, $\bar{\epsilon}$ the average energy dissipation rate and u_{flow} stands for the flow velocity of continuous fluid in channel.

Authors	Experimental setup	Dispersed phase	Operating conditions
Konno et al. [1983]	Tank: $T = 12.8, 18.6, 30$cm; RT: $D/T = 1/2, 2/3$	o-xylene $d_m = 0.26 - 1$mm	$P = 5.8$
Hančil and Rod [1988]	Tank: $T = 5$cm; paddle impeller: $D/T = 0.8$	toluene V_m=0.5-39 mm^3	$N = 192$ rpm
Kuriyama et al. [1995]	Loop reactor; propeller	silicone oil $\mu = 0.1, 1.0, 12.6$ Pa$\cdot$s	$Re = 1.5 \times 10^4 - 4.2 \times 10^4$

Continued on next page

Table 2.3 – continued from previous page

Authors	Experimental setup	Dispersed phase	Operating conditions
Maaß et al. [2007]	(1) Tank: $T = 15$cm; RT: $D/T = 1/3$; (2) Single blade fixed in channel	petroleum $d_m = 300\mu$m-2mm	(1) Tank: $N = 400 - 700$ rpm, $\bar{\epsilon} = 0.3 - 1.8 m^2/s^3$; (2) Channel: $u_{\text{flow}} = 0.5 - 1.5$m/s
Zaccone et al. [2007]	Single blade fixed in channel: 30×30mm, $T = 250$mm, $D/T = 0.32$	petroleum $d_m = 1$mm	$N = 550$ rpm
Maaß et al. [2009]	Single blade fixed in channel:30×30mm; RT	toluene $d_m = 0.644, 1$mm	$u_{\text{flow}} = 1.0, 1.5, 2.0$m/s
Hermann et al. [2011]	Single blade fixed in channel:30×30mm; RT	toluene, petroleum, paraffin oil $d_m = 0.7 - 3.1$mm	$u_{\text{flow}} = 1.0, 2.0$ m/s
Maaß and Kraume [2012]	Single blade fixed in channel:30×30mm; RT	petroleum,toluene $d_m = 0.5 - 3.5$mm	$u_{\text{flow}} = 1.0, 1.5, 2.0$m/s
Nachtigall et al. [2012]	Single blade fixed in channel:30×30mm; RT	toluene, petroleum, paraffin oil $d_m = 0.7 - 3.1$mm	$u_{\text{flow}} = 1.5$m/s
Solsvik and Jakobsen [2015]	Tank: $T = 14.3$cm; RT: $D/T = 0.35$	toluene, petroleum, n-dodecane, 1-octanol $d_m = 0.6 - 4$mm	$N = 650$rpm
Sanjuan-Galindo et al. [2015]	Tank: $T = 13.5$cm; Scaba impeller: $D/T = 1/2$	castor oil	$Re = 24000$

Continued on next page

Table 2.3 – continued from previous page

Authors	Experimental setup	Dispersed phase	Operating conditions
Nachtigall et al. [2016]	Single blade fixed in channel:30 × 30mm; RT	petroleum, paraffin oil; addition of surfactants; $d_m = 1$mm; $\mu = 1.7 - 127$mPa · s	$Re = 29000$
Zhou et al. [2021]	Square tank: $100 \times 100 \times 100$mm^3; RT: $D = 44$mm	n-dodecane, silicone oil up to 2mm	$N = 300, 390, 480$rpm

2.1.4 Effect of surfactants

In practice, surface active agents, or surfactants, for short, which are molecules (or particles) inclined to attach to fluids interfaces, are commonly present within liquid-liquid mixing systems. They could be either added by design or as contaminants, affecting both the mixing performance and the final quality of the mixed product. This section attempts to provide contextual understanding of surfactants relevant to this thesis. It starts with a concise overview of surface and interfacial tension concepts, followed by an introduction to the different types of surfactants and their behaviour at equilibrium. Then, it delves into the dynamic behaviour of surfactants within fluids, covering their transport in the bulk and at interfaces. Following this, the dynamics of single surfactant-covered drops is discussed by reviewing studies investigating the effects of surfactant properties on the drop behaviours, such as those arising from the Marangoni stress. Finally, this section closes with a review of relevant studies contributing to the effect of surfactants on drop deformation and breakage in liquid-liquid systems.

2.1.4.1 Interfacial tension

A surface or interface is a region where the properties change across two different phases. Strictly speaking, "surface" refers to an interface between a condensed phase (solid or liquid) [Walstra, 2002] and a gas phase, while "interface" is the generic word. The property transition takes place over finite distances at the molecular scale, implying that all the interfaces have a finite thickness. Nonetheless, at larger scales, for example, within practical mixing systems, this thickness is considered to be negligibly small, and thus the interface is assumed to have area, as opposed to volume [Hiemenz and Rajagopalan, 2016].

The presence of interfacial tension introduces a multitude of interfacial behaviours, such as the rise of liquids through capillaries. From a molecular point of view, interfacial tension originates from the disparity between the energies of molecules located in the bulk and near the interface. According to Manikantan and Squires [2020], a molecule in the bulk is surrounded

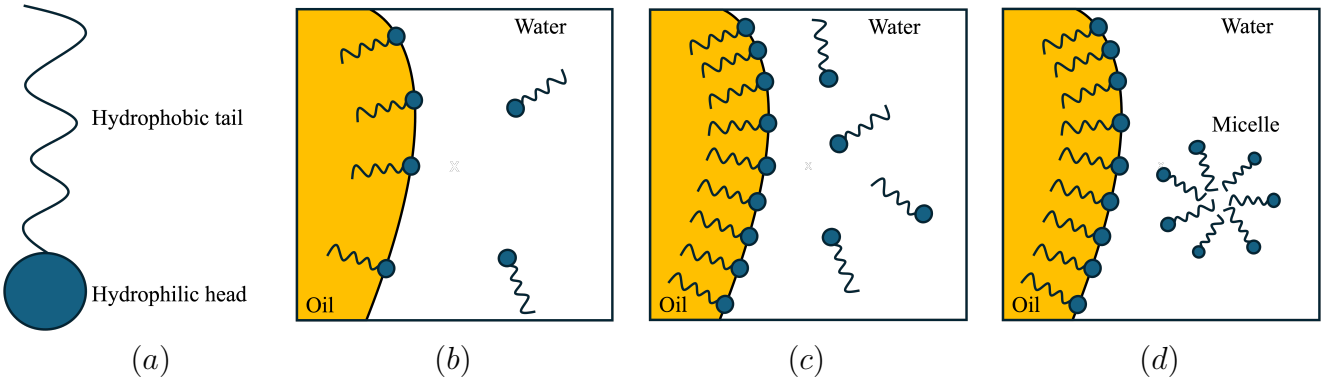


Figure 2.9: (*a*) A schematic structure of generic surfactant molecules. The remaining three diagrams show the surfactant distribution at equilibrium with increasing concentration in the bulk, wherein (*b*) interface is partly covered; (*c*) interface is completely occupied; (*d*) micelles formed in the bulk.

by a symmetric distribution of its neighbours, resulting in no net force acting on it, whereas molecules near the interface experience higher intermolecular attraction toward the bulk and thus are at a higher energy level. Therefore, molecules tend to remain in the bulk phase to minimise their energy, requiring effort (i.e., the work) to move molecules from the bulk to the interface, i.e., generate a new interface. From this perspective, the interfacial tension σ can be defined as the work per unit area required to create a new interface or the force per unit length it acts along:

$$\sigma = \frac{\text{Work}}{\Delta A} = \frac{\text{Force}\,\Delta x}{2L\,\Delta x} = \frac{\text{Force}}{2L}.$$

In this equation, ΔA and Δx are the change in area and length by expanding the interface respectively. The factor of 2 considers that the interface has two sides and L refers to the length of the interface side that the force is acting on. At constant temperature T and pressure p, this work contributes to the Gibbs free energy, G, of the system, which gives alternative thermodynamic expression of σ in the form of:

$$\sigma = \left(\frac{\partial G}{\partial A}\right)_{T,p}. \tag{2.7}$$

More generally, the interfacial tension of a curved interface can be expressed using the pressure difference across the two phases Δp, given by the Young-Laplace equation [Leal, 2007]:

$$\Delta p = \sigma \nabla_S \cdot \mathbf{n},$$

where $\mathbf{n}$ is the unit vector normal to the interface, $\nabla_S = (\mathbf{I} - \mathbf{nn}) \cdot \nabla$ is the surface gradient operator, and $\nabla_S \cdot \mathbf{n}$ represents the mean curvature of the surface.

2.1.4.2 Surfactants at equilibrium

Generally, surfactants are compounds characterised by their "amphiphilic" nature. This means they possess both hydrophilic (aqueous phase-attracting) and hydrophobic (organic phase-attracting) components within their molecular structure (see Figure 2.9*a*). According to Manikantan and Squires [2020], the unique dual chemical nature drives surfactant to adsorb at the

interface between different phases to mitigate unfavourable interactions in fluids. For example, amphiphilic molecules tend to adsorb at the interface, between water and oil, with their hydrophobic part directed away from the water phase (see Figure 2.9*b*). This behaviour of surfactant reduces the energy required to transport molecules to the interface, decreasing the system's interfacial tension according to Equation 2.7. Meanwhile, the adsorption induces an entropy loss within the system, as surfactant molecules, constrained to the interface, exhibit a narrower range of transitional and rotational micro-states, compared to those moving freely in the bulk fluid, resulting in higher entropy in the continuous phase. At equilibrium, the adsorbed surfactants at the interface, with interfacial concentration Γ, establish a state of balance with the dissolved surfactants in the bulk, which are characterised by the bulk concentration C. This equilibrium reflects a balance between the favourable enthalpy change associated with adsorption and the unfavourable entropy loss.

As the bulk concentration increases, the equilibrium shifts in favour of adsorption due to the balance between the energetic cost of keeping hydrophobic groups within the aqueous phase and the entropic decrease incurred by moving to the interface. This shift leads to the formation of a monolayer with an increasing interfacial concentration at the interface (see Figure 2.9*c*). When the bulk concentration increases further, and the interface is fully occupied by surfactants, the surfactant molecules in the bulk start to self-assemble, forming aggregates called "micelles" (see Figure 2.9*d*). Micelles consist of surfactant molecules typically arranged in spherical clusters, where their hydrophobic parts face inward towards the center of the cluster, while their hydrophilic portions face outward towards the surrounding water. The concentration at which this structure occurs is referred to as the Critical Micelle Concentration (CMC). This thesis is focused on systems with dilute surfactant concentrations, and therefore no micellar effects are discussed herein.

There are several mathematical formulations in the literature correlating the interfacial concentration with the bulk concentration, which are known as adsorption isotherms. A comprehensive table listing common isotherms is provided by Manikantan and Squires [2020] and relevant discussion can be found in Pawar and Stebe [1996]. From an adsorption isotherm, the equation of state describing the change in interfacial tension with the surfactant interfacial concentration can be derived. One of the simplest and most popular equations of state associated with the Langmuir adsorption isotherm (often called Langmuir equation of state), is used in this thesis (see Equation 3.25). Alternative equations of state involve the use of more parameters, for example, the Frumkin isotherm [Pawar and Stebe, 1996]. The major drawback of these two equations of state is their tendency to predict unrealistic negative values for the interfacial tension when the interfacial concentration approaches its maximum limit, where surfactant molecules completely cover the entire interface [Bazhlekov et al., 2006]. In contrast, experimental works (for example, Chang and Franses [1995]) showed that the interfacial tension remains constant above a specific value of the interfacial concentration. Herein, modification has been made to avoid the occurrance of negative interfacial tension (see Equation 3.26).

Depending on the nature of the hydrophilic and hydrophobic components of the molecules, surfactants can be classified into various types using different methods. This thesis classifies surfactants into "insoluble" and "soluble" based on their solubility. "Insoluble" surfactant refers to the substances with extremely low solubility in the continuous phase, in other words, the concentration of this type of surfactants in the bulk is negligible, and all the surfactant molecules stay at the interface. On the other hand, "soluble" surfactant exhibits the equilibrium between the interfacial and bulk concentrations, as described above. With higher solubility, surfactants molecules are more likely to depart from the interface and dissolve into the bulk.

2.1.4.3 Dynamics properties

The interfacial tension mentioned above refers to the tension value at the end of the adsorption process, which requires a finite amount of time. Understanding the dynamics of this adsorption process holds paramount importance in applications involving surfactants. For instance, in emulsification processes where a drop undergoes deformation and fragmentation, the resulting size of the daughter drops is significantly affected by the dynamic interfacial tension during deformation. If the surfactant adsorption is not rapid enough to cover the newly created interface during deformation, the dynamic interfacial tension at the moment of breakup will be higher than the equilibrium interfacial tension, leading to the generation of larger drops. This section aims to delve deeper into the dynamic surfactant processes arising from non-equilibrium conditions.

Firstly, departures from a constant equilibrium concentration drives the surfactant transport in the bulk, which is governed by a convection-diffusion equation:

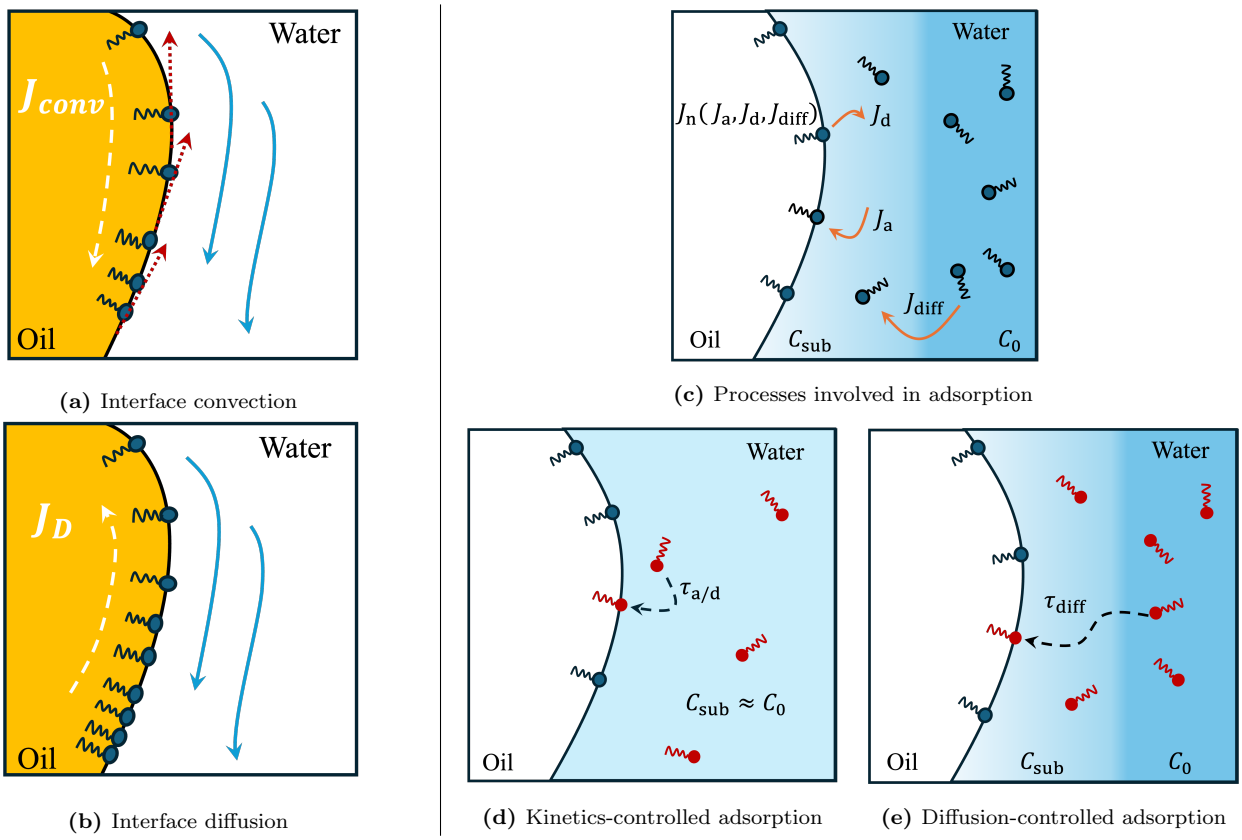
$$\frac{\partial C}{\partial t} = D_b \nabla^2 C - \mathbf{u} \cdot \nabla C, \tag{2.8}$$

where D_b denotes the surfactant diffusivity in the continuous phase. In addition, the surfactant transport at the interface is determined by a conservation equation in terms of its concentration at the interface, Γ [Manikantan and Squires, 2020]:

$$\frac{\partial \Gamma}{\partial t} = -\nabla_S \cdot (\mathbf{J}_D + \mathbf{u}\Gamma) + J_n, \tag{2.9}$$

where $\mathbf{J}_D$ denotes the diffusive flux along the interface, $\mathbf{u}\Gamma$ represents the interface convective flux. The term J_n refers to the net flux resulting from the adsorption and desorption processes occurring between the bulk phase and the interface. These processes are schematically demonstrated in Figure 2.10, and relevant discussions are provided in the following sections.

Interface convection According to Manikantan and Squires [2020], this flux can be decomposed into components along the interface and components normal to the interface, which gives



(a) Interface convection

(b) Interface diffusion

(c) Processes involved in adsorption

(d) Kinetics-controlled adsorption

(e) Diffusion-controlled adsorption

Figure 2.10: Schematic diagrams illustrating the surfactant transport in oil-water system. $(a)-(b)$ display the convection and diffusion of surfactants along the interface, respectively. The red dotted arrows in (a) represent the induced Marangoni stresses; the light blue arrows refer to the fluid motion in the water phase. (c) presents surfactant adsorption and desorption between the interface and sub-phase, along with the surfactant diffusion from the bulk towards the sub-phase. $(d)-(e)$ show the two limiting cases with regard to the surfactant adsorption: kinetics-controlled and diffusion-controlled. Particularly, in figure $(c)-(e)$, the intensity of the background colour corresponds to the concentration of surfactants, where darker blue indicating a higher surfactant concentration.

its interface divergence written as:

$$\nabla_S \cdot (\mathbf{u}\Gamma) = \Gamma(\nabla_S \cdot \mathbf{n})(\mathbf{u} \cdot \mathbf{n}) + \nabla_S \cdot (\mathbf{u}_s\Gamma), \tag{2.10}$$

where $\mathbf{u}_s$ is the interface velocity. In this equation, the first term considers the compression or dilation of surfactant occurring when the curved interface deform (which is not taken into account in this thesis), and the second term captures the compression or dilation of surfactant driven by the fluid motion in the bulk phase (see Figure 2.10a).

Interface diffusion As mentioned above, the fluid motions in the bulk phase leads to non-uniform distribution of surfactant at the interface. The diffusion of surfactant molecules along the interface occurs to mitigate the induced concentration gradient (see Figure 2.10b). Herein, the diffusivity of surfactant is assumed to be a constant D_s, giving the expression of diffusive flux, $\mathbf{J}_D$, as follows:

$$\mathbf{J}_D = -D_s \nabla_S \Gamma. \tag{2.11}$$

Various expressions with regard to this diffusive flux have been developed by considering different forms of diffusivity [Saffman and Delbrück, 1975, Krishna, 1990, Furst and Squires, 2017].

Adsorption/desorption The final term J_n in Equation 2.9 accounts for the exchange of surfactant molecules between the bulk and the interface. Under non-equilibrium conditions, this represents a flux of surfactant entering or exiting, $J_{a/d}$, given by the difference between the adsorption flux J_a and the desorption flux J_d:

$$J_n = J_{a/d} = J_a(\Gamma, C_{\text{sub}}) - J_d(\Gamma, C_{\text{sub}}). \tag{2.12}$$

This expression indicates that the two fluxes are related to the surfactant concentration gradient between the interface and a region of bulk phase adjacent to the interface, called the sub-phase. C_{sub} represents the surfactant concentration in this sub-phase. Meanwhile, the concentration gradient in the bulk could lead to a diffusive flux of surfactant determining the C_{sub} via:

$$J_{\text{diff}} = -D_b \mathbf{n} \cdot \nabla C_{\text{sub}}. \tag{2.13}$$

In addition, this diffusive flux has to balance the kinetic sorptive flux (Equation 2.12) to satisfy the conservation of surfactant, and both mechanisms govern the source term J_n, giving:

$$J_n = J_{\text{a/d}} = J_{\text{diff}}. \tag{2.14}$$

To illustrate the interplay among these processes, consider a newly created interface. Initially, the entire interface is available for adsorption, the surfactant molecules are adsorbed onto the interface from the sub-phase immediately, decreasing the concentration at the sub-phase. This results in a concentration gradient that drives the diffusion of surfactant from the bulk. As the interface becomes more occupied, there is a greater chance that a surfactant molecule encounters an interfacial site already taken, which leads to its longer residence in the sub-phase, effectively increasing the adsorption time. Subsequently, with an adsorption-desorption equilibrium established between the interface and the sub-phase, the concentration in the sub-phase no loner decreases, and thereby diffusion from the sub-phase back to the bulk phase could become significant. Eventually, diffusion ceases when the concentration in the sub-phase equates with that in the bulk, wherein balance is reached between the interface and the bulk.

From above, the surfactant adsorption process consists of two time-dependent processes: the diffusion of surfactant from the bulk and the actual adsorption onto the interface. Consequently, if either diffusion or adsorption/desorption becomes the rate-controlling (slower) step, the J_n could be approximated by that process alone. For example, in the case of *diffusion-limited adsorption*, the time scale $\tau_{\text{a/d}}$ associated with adsorption kinetics is negligible short in relative to the time τ_{diff} required for the diffusion from the bulk, i.e., $\tau_{\text{a/d}} \ll \tau_{\text{diff}}$. Under this scenario, the equilibrium between Γ and C_{sub} is assumed to be established instantly (see Figure 2.10*e*), so that $J_{a/d}$ can be ignored and the adsorption process is solely governed by Equation 2.8 and 2.13. On the other hand, in the case of *kinetics-controlled adsorption*, $\tau_{\text{a/d}} \gg \tau_{\text{diff}}$, wherein the diffusion from the bulk is considered very fast. In this limit, the sub-phase concentration is constant and consistently equal to the bulk concentration, which is assumed equal to the

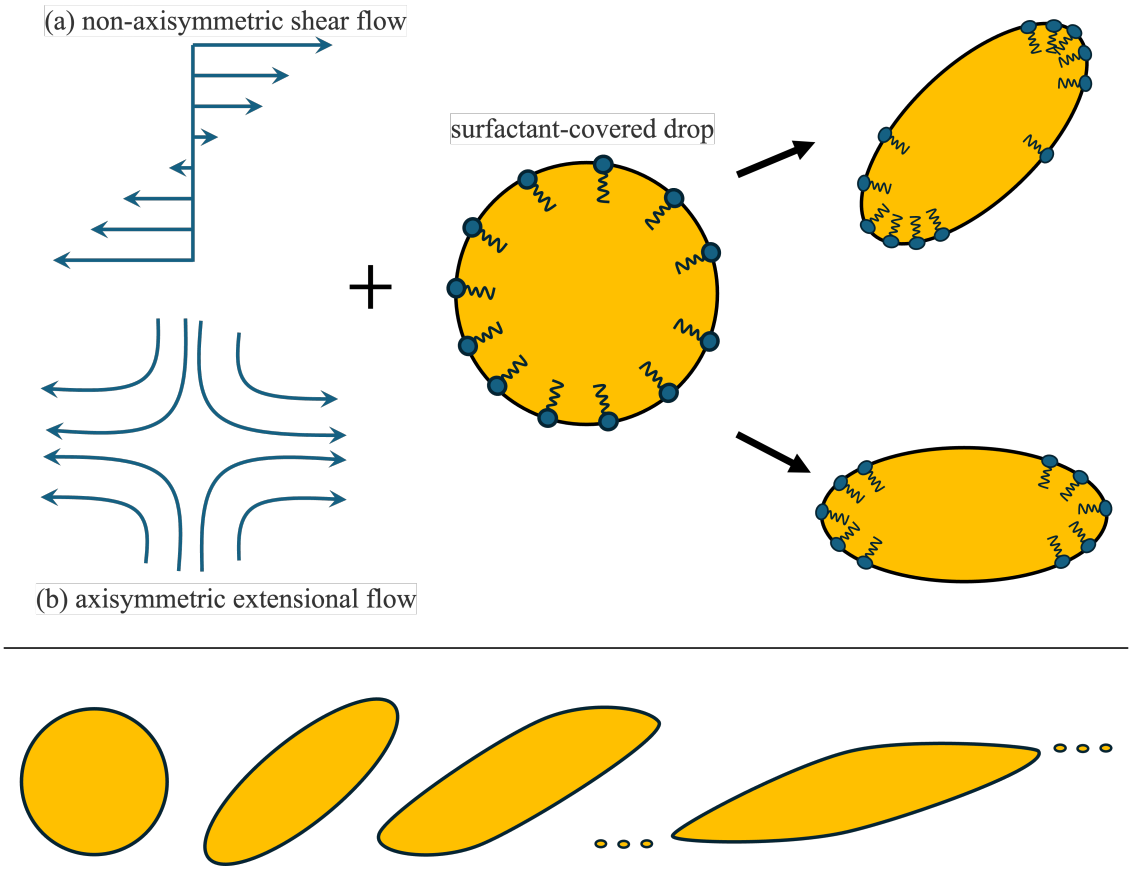


Figure 2.11: (Top panel) Schematic diagram of drop deformation and corresponding surfactant distribution for a surfactant-covered drop subject to (*a*) non-axisymmetric shear flow and (*b*) axisymmetric extensional flow. (Bottom panel) Schematic of tip streaming, adapted from Bruijn [1993].

initial bulk concentration (infinite bulk phase assumption), C_0, giving rise to $C_{\text{sub}} \approx C_0$. In this case, the adsorption process is determined by Equation 2.12 alone. Furthermore, in other cases where neither step is negligible, the adsorption process is described as *mixed-controlled*.

2.1.4.4 Surfactant-laden drop behaviours in liquid-liquid systems

Single drop studies Interfacial dynamics on a surfactant-laden interface have been well studied by investigating drop deformation subjected to a simple flow field, including non-axisymmetric shear flow and axisymmetric extensional flow, which leads to several reviews in this field [Briscoe et al., 1999, Fischer and Erni, 2007]. A list of relevant studies is provided in Table 2.4. In both cases, it is generally found that the effect of surfactant on the drop deformation is related to the two competing physical processes [Leal and Stone, 1990]: (*a*) convection of surfactant, which lowers the interfacial tension and facilitates the deformation at the drop tips; and (*b*) dilution of the surfactant which tends to increase the interfacial tension and suppress drop deformation. The former one is caused by the transport of surfactants along the interface by flow (see Figure 2.11), while the latter one is due to the increase in interfacial area as the drop deforms. Milliken et al. [1993] reported that the influence of surfactant is diminished as the viscosity ratio between dispersed phase and continuous phase increases. Furthermore, whether the surfactant effect is dominated by its dilution or convection depends on several factors. For example, Leal and Stone [1990] investigated the effect of surfactant

elasticity β_s, which measures the sensitivity of interfacial tension to the interfacial surfactant concentration. The authors illustrated that at a fixed surfactant concentration along the interface, larger interfacial tension gradient occurs with increasing β_s, enhancing the surfactant diffusion and thus counteracting the convection of surfactant. In addition, Eggleton et al. [1999] related the surfactant effect to the surfactant saturation Γ_∞ at the interface, which refers to an upper bound to the interfacial concentration that can be adsorbed in a monolayer. In the case of $\Gamma \ll \Gamma_\infty$, when the surfactant diffusion is negligible, a region near the deformed drop equator is observed where Γ can be regarded as zero (see the deformed drops from the top panel in Figure 2.11), while the surfactants are highly accumulated at the drop tips where higher deformation compared to a clean drop interface case takes place. When Γ/Γ_∞ increases, Γ is never zero as the stresses resisting the local accumulation become large, leading to a slight departure of Γ from the uniform distribution and higher mean interfacial tensions. Another work done by Pawar and Stebe [1996] investigated the effect of interface Peclét number Pe_s, which measures the relative significance of surfactant convection to surfactant diffusion along the interface.

It is reported that these parameters alter the surfactant impact through Marangoni stresses [Pawar and Stebe, 1996]. As shown in Figure 2.10*a*, the non-uniform surfactant distribution, leading to a gradient of interfacial tension, generates an additional stress tangential to the interface pointing in the opposite direction to the gradient. This stress is known as Marangoni stress, which, according to Bazhlekov et al. [2006], acts in opposition to the interface velocity, leading to the immobilisation of the interface. This immobilisation can occur either locally or globally, depending on the surfactant concentration at the interface. It is presented by the same author that the Marangoni stress modifies the bulk flows as well by introducing a fluid circulation within the drop.

Another general trend is that the drop deformation in the presence of surfactant at the drop pole is greater than that of a drop with a constant interfacial tension equal to the initial equilibrium value [Leal and Stone, 1990, Li and Pozrikidis, 1997, Feigl et al., 2007]. This surfactant-related drop deformation is termed as "tip stretching" [Pawar and Stebe, 1996, Hu and Lips, 2003]. In addition to drop fragmentation as seen in surfactant-free cases, a new mode of breakup mechanism resulted from this was described by Bruijn [1993] and Eggleton et al. [2001], known as tip streaming (see the bottom panel in Figure 2.11), wherein the ejection of a fluid thread much smaller than the mother drop size is observed at the drop pole. Bruijn [1993] also stated that this observation would disappear when surfactants are moved away from the tip. A more recent work by Kamat et al. [2018] demonstrated that the Marangoni stress acting near the drop pole (as opposed to at the drop pole) contributes to the reduced rate of thread thinning and therefore hinders the formation of multiple daughter drops.

When soluble surfactant is considered, the surfactant convection and diffusion along the interface, as well as the Marangoni effect, can be mitigated by the surfactant transport between the interface and bulk phase [Milliken and Leal, 1994]. For example, the zero-Γ region described

Table 2.4: Relevant studies that explore the deformation of single drop in the presence of surfactants, categorised by the flow types the drops subjected to and the solubility of surfactant under investigation.

Flow types	Solubility	References
Axisymmetric extensional	Insoluble	Leal and Stone [1990], Milliken et al. [1993], Pawar and Stebe [1996], Eggleton et al. [1999, 2001], Kruijt-Stegeman et al. [2004], Herrada et al. [2022]
	Soluble	Milliken and Leal [1994], Eggleton and Stebe [1998], Wang et al. [2014]
Non-axisymmetric shear	Insoluble	Bruijn [1993], Janssen et al. [1994,], Li and Pozrikidis [1997], Hansen et al. [1999], Feigl et al. [2007]
	Soluble	[Eggleton et al., 1999, Mandal et al., 2017]

above could be occupied by the surfactant molecules through adsorption process, smoothing out the constructed concentration gradient. Under this condition, the surfactant effect is normally investigated under two limiting cases as demonstrated earlier: adsorption-desorption controlled [Eggleton et al., 1999, Jin et al., 2006] and diffusion-controlled [Jin and Stebe, 2007, Mandal et al., 2017]. These two scenarios bound the surfactant behaviours as the diffusive flux from the bulk increases in relative to the convective rate at the interface [Chen and Stebe, 1996]. Eggleton and Stebe [1998] showed that in the case of slow sorption kinetics, the surfactant behaviours approach the insoluble limit; as the mass transfer rate between the bulk and the interface increases, the strength of Marangoni stresses is significantly lowered and interface dynamics becomes identical to the clean interface limit. Moreover, the study by Wang et al. [2014] provided a comprehensive examination of soluble surfactant. It delved into the surfactant effect under different assumptions regarding the relative significance of surfactant transport processes. These included considerations of the bulk Peclét number Pe_b considering surfactant convection and diffusion in the bulk, and the Biot number Bi accounting for the relative time scale of bulk flow and surfactant desorption.

More recently, Soligo et al. [2019] carried out direct numerical simulations of surfactant-laden drops dispersed in turbulent flow in which a clear interplay among local flow field (considering shear stress, Maranogoni stress, and the effect of Weber number), surfactant concentration and dispersed phase morphology is displayed. In their subsequent work, Soligo et al. [2020] studied the flow modification introduced by the surfactant-laden drop under the same flow conditions, in terms of velocity profiles, vorticity profiles, and a specifically-defined flow topology parameter [Perry and Chong, 1987].

Emulsification process studies Unlike the studies on single drop, only a few studies have aimed at understanding liquid dispersion in the presence of surfactant inside a stirred vessel. Most of these studies have addressed the problem regarding the surfactant influence on the final drop sizes and their distribution, leaving a gap in the understanding of the underlying physical

mechanisms governing the interfacial behaviours with such system. The earliest system to study the effect of surfactant on drop size was by Lee and Soong [1985] where five liquid-liquid systems and nine types of surfactants were examined. The authors found that the size of drops produced is smaller (compared to the one predicted using correlations based on clean liquid-liquid system) and more uniform (narrower DSD). Later Koshy et al. [1988] developed a drop breakup model to predict the maximum drop size at various surfactant concentrations arguing that the effect of surfactant on stirred-vessel emulsification is not only by the decrease in interfacial tension, but also through the generation of an interfacial tension gradient across the interface (and thus Marangoni stress, which, albeit, was not dealt with sufficient detail in that study). Several subsequent studies expanded knowledge in this field by considering surfactant concentration [Chatzi et al., 1991, El-Hamouz, 2007], rheological properties of surfactant-laden interface [Lucassen-Reynders and Kuijpers, 1992], and types of surfactant head group [Goloub and Pugh, 2003]. Groeneweg et al. [1994] have shown the appearance of a large number of mini-drops (a bi-modal DSD) for the surfactant-laden system, and rationalised that the phenomenon is associated with surfactant-induced tip-streaming [Eggleton et al., 2001]. More related work has been on the surfactant effect on the flow field modification in a stirred vessel [Mishra et al., 1998, Arora et al., 2002, Mavros et al., 2011, Montante et al., 2011].

2.1.5 Computational fluid mixing

The previous sections have provided context of liquid-liquid dispersion in stirred vessels, focusing on the physical phenomena observed within the systems. In contrast, this section aims to review the effort to develop numerical methods to capture detailed information about hydrodynamics and interfacial behaviours in agitated vessels. Key aspects of numerical simulations relevant to this thesis involve a numerical method for turbulence modelling, rotating impeller modelling, and interface localisation. Subsequent sections will outline prevalent approaches to addressing these challenges in the literature.

2.1.5.1 Turbulence modelling

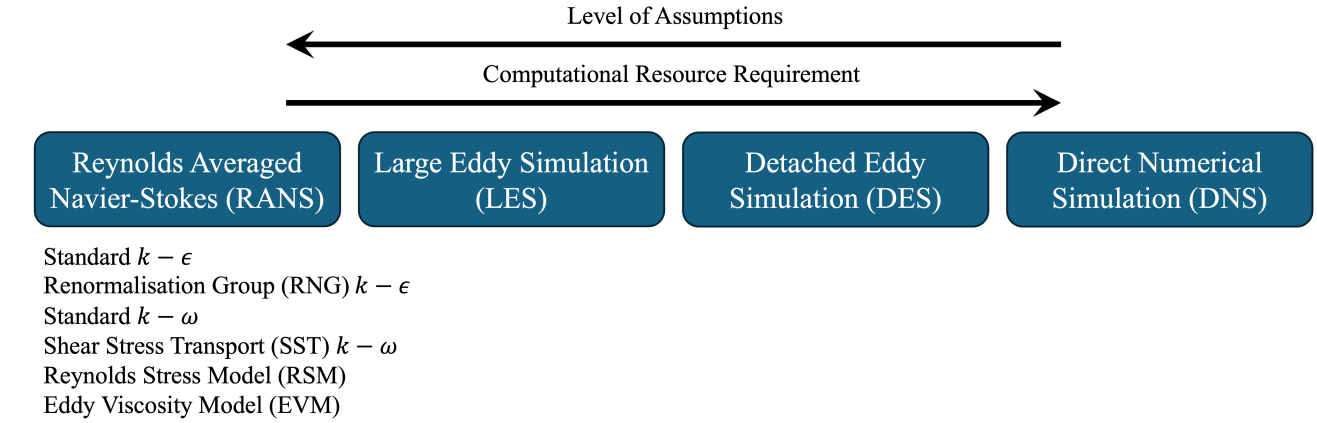
A proper turbulence model could significantly decrease computational requirement and, meanwhile, increase the accuracy of the numerical results [Jaszczur and Młynarczykowska, 2020]. At present, there are three primary approaches that have been employed for modelling turbulent flow motions within an agitated vessel: RANS (Reynolds Averaged Navier-Stokes), the LES (Large Eddy Simulation) and the DNS (Direct Numerical Simulation).

In general, the RANS model is much cheaper computationally compared to LES and much faster than DNS as this method solves the averaged fluid flow equations and the turbulent components are modelled via various turbulence models (see Figure 2.12*a*). There are numerous studies comparing the outcomes of this spectrum of turbulence models used in RANS with the experimental results [Zhu et al., 2021]. Each turbulence model has advantages and disadvantages, and the model selection depends on particular cases and configurations [Singh et al., 2011, Hartmann et al., 2004]. This will not be extended herein since it is beyond the scope of

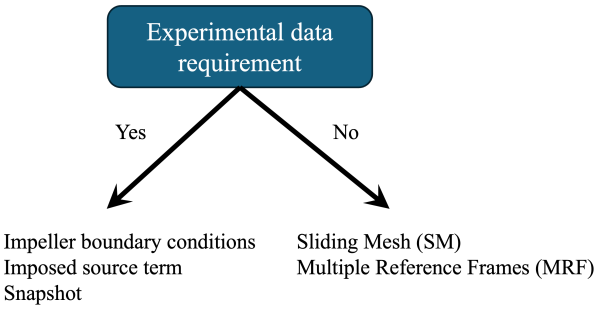
this thesis. Nonetheless, DNS could provide much more accurate results as it directly attains the instantaneous flow variables by solving unsteady three-dimensional Navier-Stokes, requiring no additional models. Similar to DNS, LES fully resolves the large scales, but the sub-grid fluid flow or small eddies have to be modelled using one of the widely available turbulence models. The standard Smagorinsky model [Smagorinsky, 1963] with the constant model parameter C_s is commonly used in the literature, with varied values of C_s in specific applications [Hartmann et al., 2004, Derksen et al., 1999]. More details of implementing LES can be found in Section 3.1.2.3. Another remark to be made here is that LES relies on sub-grid models to account for the effects arising from unsolved turbulence. This becomes significant when dealing with substantial interface deformation. In such cases, the behaviour of interface is heavily influenced by turbulent structures, which can lead to phenomena like turbulent viscosity that LES is unable to resolve. To address this issue, one approach is to enhance computational resolution to better capture the dynamics at the interface and boundary layers. Alternatively, coupling LES with advanced interface-tracking methods can improve the accuracy of simulations involving complex interfacial behaviours. As a consequence, both DNS and LES demand tremendous computational resources, rendering them impractical for engineering applications. Currently, they are primarily limited to simple geometries and low Re, especially DNS. However, in recent years, due to the advancement of computational capacity, the DNS and LES have been increasingly applied in numerical investigation for stirred vessels (DNS: [Gillissen and den Akker, 2012, Tamburini et al., 2018], LES: [Hartmann et al., 2004, Alcamo et al., 2005, Zhang et al., 2008, Shu and Yang, 2018]), producing results that align excellently well with the experimental outcomes. Alternatively, Detached Eddy Simulation (DES) offers a solution to the computational demands encountered by DNS and LES [Gimbun et al., 2012, Devi et al., 2015]. This method integrates the strengths of both RANS and LES methodologies, effectively handling challenges associated with the use of LES in near-wall region. However, it is still rarely used in simulations of stirred vessel, despite requiring less computational resources compared to DNS.

2.1.5.2 Impeller rotation modelling

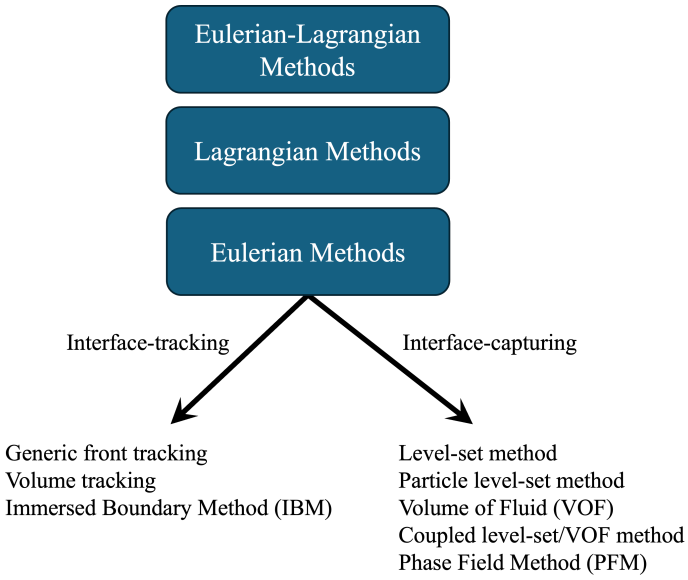
Another crucial element when considering numerical simulations of the stirred vessel is the implementation of modelling rotating impeller. In the past, the impeller rotation was not explicitly simulated, instead, its effect was either modelled by imposing a boundary condition [Harvey et al., 1995, Brucato et al., 1998] to the external flow or was expressed as a source term in the governing equations [Ranade and Dommeti, 1996]. Alternatively, Ranade and den Akker [1994] proposed an approach called snapshot, which essentially involves capturing the flow characteristics of a stirred vessel at a single time instant by solving steady-state equations with boundary conditions specific to that moment in time. These techniques require the specification of boundary conditions regarding velocity and turbulence on the volume or surface swept by the rotating blades, which can only achieved via experimental measurement [Ranade and Dommeti, 1996]. To tackle this issue, more advanced schemes which do not rely on experiments have been developed.



(*a*) Turbulence modelling



(*b*) Impeller rotation modelling



(*c*) Interface localisation methods

Figure 2.12: Classification of modelling methods in the literature.

One of the most popular methods is the Sliding Mesh (SM) technique [Murphy, 1994, Barker et al., 1997]. This method divides the simulated tank into two regions that are treated separately: the impeller region and the tank region consisting of the bulk fluids, tank wall and baffles if applicable. In particular, the impeller region rotates with the same rotating speed as impeller, while the tank region is regarded as stationary. In addition, no-slip boundary conditions are applied at the impeller blades, the impeller shaft, the tank walls and the baffles. This scheme does not require experimental data, however, it is expensive for start-up computation [Jaszczur and Młynarczykowska, 2020]. This comes from the time-dependent nature of SM technique, which allows relative displacement of impeller region to the outer region in discrete time-steps, performing time-dependent calculations with data at successive time-steps. As a result, alternative method called Multiple Reference Frame (MRF) technique was investigated to handle this issue [Naude et al., 1998]. Similarly, the tank simulated through the MRF technique is divided into two or more frames, stationary frames and moving frames. The moving section includes the impeller and the fluid surrounding it, while the stationary frame encompasses the tank, the baffles and the fluids outside the moving frame. In contrast to SM models,

steady-state calculations are conducted with a rotating reference frame in the impeller region and a stationary reference frame in the outer region [Deglon and Meyer, 2006]. In this way, the MRF outperforms previous methods, such as computational snapshot approach, considering interactions between the rotating impeller and the stationary elements such as baffles and tank walls. Furthermore, it is found that MRF provides better computational performance [Deglon and Meyer, 2006] at a fraction of computational time required for the SM scheme [Wechsler et al., 1999].

2.1.5.3 Methods for interface localisation

As presented in Figure 2.12(c), various methods have been applied to implement the simulation of multiphase flows involving an interface. According to Smolianski [2005], three levels of modelling could be distinguished when handling this problem:

- **flow modelling**: Eulerian, Lagrangian and mixed Eulerian-Lagrangian methods;
- **interface motion modelling**: interface-tracking and interface-capturing;
- **flow-interface coupling**: integrated and segregated

Herein, we will briefly outline the characteristics of these methods and provide typical examples of techniques for interface localisation.

Firstly, the three classes of numerical algorithms for flow modelling are Eulerian, Lagrangian and mixed Eulerian-Lagrangian methods. The Lagrangian schemes consider particles as discrete entities, tracking the trajectory of each individual particle [Xu et al., 2020]. In these methods, the object carrying discretised quantities is moving with the continuous fluid. From a computational point of view, each computational cell in Lagrangian methods always contains the same fluid element, and the entire grid moves with the fluid flow. The early works done by Hirt et al. [1970] and Okamoto and Kawahara [1990] strictly applied Lagrangian algorithm together with finite-volume and finite-element method, respectively. In contrast, Eulerian methods are characterised by a fixed computational mesh, wherein the fluid and other objects flow across different computational cells. Alternatively, the mixed Eulerian-Lagrangian methods are based on both Eulerian and Lagrangian concepts. One of the most cited work using the Eulerian-Lagrangian framework was done by Hirt et al. [1974], where the widely-used algorithm called arbitrary-Lagrangian-Eulerian (ALE) was proposed [Hughes et al., 1981, Maury and Pironneau, 1996]. This classification distinguishes different ways of describing flow systems involving two or more fluid, and the selection among these methods highly depends on specific problems and their objective.

However, this level of modelling does not provide any information regarding the approaches to modelling the motion of the interface [Smolianski, 2005]. In this regard, another commonly-used classification categorise all methods into either interface-tracking or interface-capturing. For the interface-tracking approaches, the interface is determined by a series of Lagrangian markers,

whose location is explicitly tracked along the paths of fluid particles. This often leads to the integration of interface-tracking with either Lagrangian methods or mixed Eulerian-Lagrangian methods. Generic front tracking [Tryggvason et al., 2001, 2011], volume tracking [Harlow et al., 1965, Nakayama and Mori, 1996] and immersed boundary method [Peskin, 1977, 2002, Li et al., 2013] are typical examples of this type of methods. On the other hand, the interface in the interface-capturing methods is reconstructed from an Eulerian scalar field characterising the flow properties, such as fluid fraction or density. These techniques can be exemplified by the level-set method [Tryggvason et al., 2011, Balcázar et al., 2014], volume of fluid [Hirt and Nichols, 1981, Tryggvason et al., 2011], phase field method [Jacqmin, 1999, Tryggvason et al., 2011, Kim, 2012] and so forth.

Finally, the coupling of the flow and the freely moving interface can be achieved through either a "segregated" or "integrated" approach. In the segregated scheme, the flow is initially computed with a "frozen" interface, and subsequently, a new position for the interface is determined using the previously-computed flow variables. On the contrary, in the integrated approach, the flow variables and interface location are solved simultaneously. Herein, how each method is implemented would not discussed given its comprehensive extension in the literature, nonetheless, details of methods used in this thesis is presented in the Methodology (chapter 3).

2.2 Machine learning in fluid dynamics

As mentioned in the Introduction (chapter 1), this thesis concerns the feasibility of ML models to duplicate the prediction of dispersion performance comparable to those from CFD simulations. Therefore, this part aims to provide context relevant to these two areas: main effort that has been done to combine ML and multiphase mixing as seen in Section 2.2.1 and sequential prediction using ML models presented in Section 2.2.2.

2.2.1 Machine learning in CFD

As indicated by the CPU time of high-fidelity CFD simulations given earlier, combining CFD and ML is an emerging and rapidly developed research area. A large amount of studies have explored various ways to integrate these fields to improve simulation reliability, speed and predictive capabilities. One of rapidly-developing direction in this domain is to construct data-drive turbulence modelling, which leads to a review done by Durbin [2018] covering notable related studies. Recent work such as Jiang et al. [2021] and Novati et al. [2021] respectively demonstrate how deep neural networks and reinforcement learning can aid construct turbulence modelling in LES. Another popular area is applying surrogate model to accelerate CFD simulations. One of the most cited work in this field is done by Kochkov et al. [2021] wherein the authors used deep learning to produce comparable modelling of two-dimensional turbulent flow to those simulated via DNS and LES in fraction of computational time, most importantly, without comprise of accuracy. In addition, ML-based techniques have been applied to multiphase systems, a comprehensive review is given by Zhu et al. [2022] and a series of latest researches

in this domain are showcased in Basha et al. [2024]. Furthermore, ML has also been integrated with data assimilation to improve CFD predictions [Cheng et al., 2023,] and optimise CFD simulation for control purpose [Li et al., 2022].

2.2.2 Sequential predictions with RNNs

As demonstrated previously, CFD simulations offers time-dependent insights into hydrodynamics and interfacial behaviours in agitated mixers. Consequently, the ML-based models aiming to produce comparable outcomes must be capable of predicting time-series (or sequential) data. This task is distinct from the other types of learning problems, as it requires preserving temporal order of observations during both model training and deployment. ML-based models that are capable for such a task are often referred to time-series forecasting or sequence modelling. The key types of models used for this purposes include but not limited to Recurrent Neural Networks (RNNs), Temporal Convolutional Networks (TCNs), transformers, and autoregressive models. Recall that the purpose is to test the applicability of ML-based technique in the context of multiphase mixing. An RNN is used herein as it has been well developed since its initial conceptual introduction by Jordan [1990].

The defining characteristic of the RNN architecture is its cyclic connections, which allow the RNN to update its current state based on both previous states and the current input data. However, when the sequence length grows, it becomes unable to learn the summary that connects the current state with the state further back in time [Hochreiter, 1998]. To tackle this problem, long short-term memory (LSTM) networks and gated recurrent unit (GRU) are introduced. Other variants of RNN have been tailored for specific applications, thus making them less applicable for chemical engineering processes, such as Hopfield networks and NARX-type RNNs for identification and control of nonlinear dynamic systems. In contrast, LSTM and GRU have been commonly used in a wide range of applications. For instance, LSTM networks have been trained using simulation data for prediction tasks including material leakage position [Kim et al., 2019, Selvaggio et al., 2022] and bio-oil yield of a fluidized bed [Zhong et al., 2023]. Furthermore, the LSTM unit has been integrated with reduced order modelling to effectively capture the fundamental characteristics underlying turbulent flows [Mohan and Gaitonde, 2018]. Likewise, a coupling of these two frameworks has been applied to perform transonic aeroelastic analysis [Li et al., 2021]. More recently, novel models based on LSTM have been developed to forecast the hydrodynamics of submarine prototypes [Hou et al., 2022] and the behaviour of ocean waves [Zhao et al., 2023]. Similarly, GRU has gained attention for its comparable performance at a seemingly lower model complexity, as discussed in detail in the Methodology chapter 3.

2.3 Concluding remarks

From the literature review above, immiscible liquid mixing is heavily involved in our daily life (e.g., food and cosmetics) and in high-end industrial applications (e.g., drug delivery),

which drives the development of diverse mechanical agitators for specific applications in the real world. The essential aspect of controlling these mixing systems is the understanding of the interfacial flows under highly dynamic conditions. In addition, the presence of surfactant, which is a prevalent scenario in industry, provides an additional level of complexity of understanding liquid-liquid mixing mechanisms underlying practical operational units. Although the fundamentals of single drop dynamics in the absence and the presence of surfactant have been well established through numerous experimental investigation, information regarding interfacial behaviours, especially those subjected to complex flow conditions is rarely accessible. In this respect, numerical analysis using CFD methods were conducted, wherein the mixing efficiency within practical agitated vessels under real conditions can be evaluated. Particularly, the number of parameters that CFD simulations can deliver is significantly large and detailed, typically including power consumption and flow field pattern. However, the simulations of fluid flows involving a freely moving interface is still challenging due to limited computational capacity, despite the fact that there exists a spectrum of numerical schemes proposed for handling this type of systems. This results in the relative scarcity of information available on interfacial dynamics and its coupling with corresponding flow structure in practical mixing units, and more specifically, in the presence of surfactant.

In the context of applying ML-based techniques to multiphase mixing, the ML community provides a range of tools to address time-series prediction. These tools provide potential solutions for chemical engineers to mitigate the high computational cost of high-fidelity CFD simulations by training time-series prediction models. On the other hand, numerous studies combining ML and CFD simulations highlight the transformative power brought by ML communities and challenges encounter in fluid dynamics simulations.

Chapter 3

Methodology

Contents

3.1 CFD Simulations 40

3.1.1 Simulation Configuration 40

3.1.2 Governing Equations 42

3.1.3 Numerical technique for interface localisation 51

3.1.4 Solutions procedures 55

3.1.5 Validation 63

3.2 ML applications 67

3.2.1 RNNs: LSTM and GRU 67

3.2.2 Procedure for time-series prediction 70

3.1 CFD Simulations

3.1.1 Simulation Configuration

Two mixing systems have been studied in this thesis:

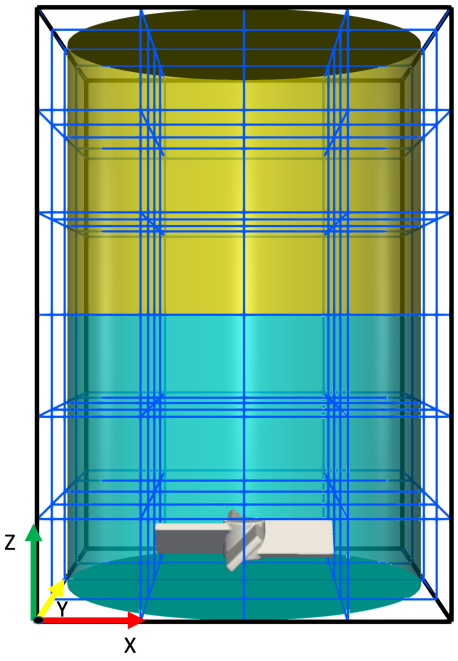
- **surfactant-free** oil-water emulsion formation,
  where the rotating speed of impeller was altered to investigate the effect of changing operational conditions to the mixing system;

- **surfactant-laden** oil-water emulsion formation,
  wherein the effects arising from surfactant types have been examined.

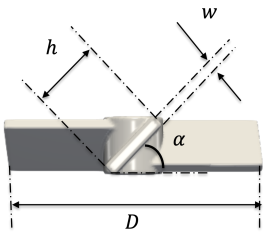
Specifically, as shown in Figure 3.1*b*, the simulated cylindrical vessel is in a size of diameter $T = 8.5$ cm and height $H = 12.75$ cm, equipped with a 4-pitched-blade-turbine (PBT). The vessel is filled with water in the lower half (coloured in blue) and an overlaying oil phase above (coloured in gold), giving a high volume fraction $\phi = 0.5$. Such vessel is simulated using a Cartesian domain $\mathbf{x} = (x, y, z) \in [0, 8.6]^2 \times [0, 12.5]$ cm^3, which consists of $4 \times 4 \times 6$ sub-domains; these sub-domains contain 64^3 Cartesian structured grids each, giving a total grid number of

Impeller geometry [cm]	
diameter, D	4.25
width, h	1
thickness, w	0.2
length, l	2.5
clearance, C	1
inclined angle, α [°]	45
Physical properties	
surfactant-free interfacial tension, σ_s [Pa·m]	0.035
oil viscosity, μ_o [Pa ·s]	5.4×10^{-3}
water viscosity, μ_a	1.0×10^{-3}
oil density, ρ_o [kg/m^3]	824
water density, ρ_a	998

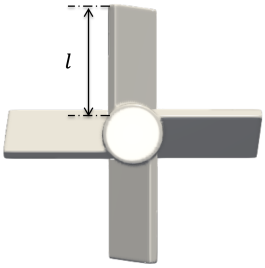
(a)



(b)



(c)



(d)

Figure 3.1: (a) Details of impeller geometry and physical properties of the two liquid phases. (b) Schematic illustration of the computational domain for the oil-water mixing system: a stirred vessel, filled with oil in the upper-half (coloured in gold) and water below (coloured in blue) is equipped with a 4-pitched-blade-turbine; the impeller blades have length l, width h, and thickness w, and are inclined at an angle α to the horizontal. The computational domain is divided into $4 \times 4 \times 6$ subdomains. The number of the Cartesian structured grids per subdomain is 64^3, which gives a total grid number of $256 \times 256 \times 384$; $(c) - (d)$ display side- and top-views of the turbine, respectively. Figures are reproduced from Liang et al. [2022].

$256 \times 256 \times 384$. The associated mesh stability test can be referred to Section 3.1.5.1. For the PBT, it has a diameter of $D = 4.25$ cm which corresponds to an impeller-to-vessel diameter ratio of $D/T = 0.5$, and rotate with frequency N [rps]. More details of the PBT geometry and the physical properties of liquids are listed in Figure 3.1a.

The employed PBT is built using a combination of primitive geometric objects (planes, cylinders and rectangular blocks) where each objct is defined by a static distance function $\psi(x, y, z)$, positive in the fluid and negative in the solid. The resulting shape of the impeller shown in Figure 3.1c, d corresponds to the iso-value $\psi(x, y, z = 0)$. Details on how to construct similar complex objects are described in Kahouadji et al. [2018]. The implementation of the complex geometry of the impeller and its rotation in the simulations is achieved via the so-called Direct-Forcing Method, which will be presented in Section 3.1.4.7.

To give an insight into the computational requirement, simulations presented in this thesis are implemented based on the High Performance Computing service of Imperial College London, using 2 nodes of 48 CPUs for each case. All of the studied cases were computed in parallel, and each case took roughly 6-8 weeks (depending on the impeller rotational speed) to finish given the computational wall time as either 48 or 72 hours.

3.1.2 Governing Equations

This section presents the governing equations used to describe the complex flow systems in the simulated vessel. It starts with outlining several principles or assumptions for the modelling, followed by the derivation of equations responsible for conservation (mass and momentum), as well as surfactant transport.

3.1.2.1 Assumptions for derivation

Five assumptions are made in this thesis serving as the basis of the derivation of governing equations presented in the pursuing section:

- **Incompressible, Newtonian, and isotropic flow:** Liquid phases are considered as incompressible and to display Newtonian rheological characteristics. This assumption implies a density field that remains constant over time and a shear-invariant viscosity field. Moreover, it is assumed that the fluid properties exhibit uniformity in all directions.
- **Continuum hypothesis** The fluids are regarded as a continuum whose macroscopic behaviour is the same as if they were perfectly continuous in structure [Batchelor, 1999]. This assumption originates from the fact that the analysis of fluid flows is based on large scale length where the molecular structure of matter and molecular motion could be ignored [Versteeg and Malalasekera, 2007]. This allows for physical quantities such as mass and density to be smoothed out to a single value.
- **Sharp interface** The boundary or interface between immiscible liquid phases is regarded to be extremely thin with a vanishing thickness, aligning with the previous continuum hypothesis. As a result, the transition of physical properties of fluid occurs abruptly across the interface.
- **Neglect of intermolecular forces** The forces acting on the fluid particles are reduced to body and interfacial forces, neglecting intermolecular forces such as electromagnetic forces in charged fluids. Intermolecular forces that are significant in interface physics, for example, van der Waals forces, are expressed in models by focusing on their primary impact: capillarity [Tryggvason et al., 2011].
- **Isothermal system:** All the flow systems presented in this thesis are regarded as isothermal, wherein no energy transfer takes place. Hence, only principles of mass and momentum conservation are considered.

3.1.2.2 Mass and momentum conservation

There are two main approaches to formulating equations that governs the conservation of mass and momentum in a flow system: one can either derive their integral form, which considers the overall fluxes and accumulations within a control volume V [Tryggvason et al., 2011], or derive their differential form, which characterises the behaviour of mass and momentum at each point within a fluid element $\mathrm{d}v$ [Versteeg and Malalasekera, 2007]. In general, the principle of mass

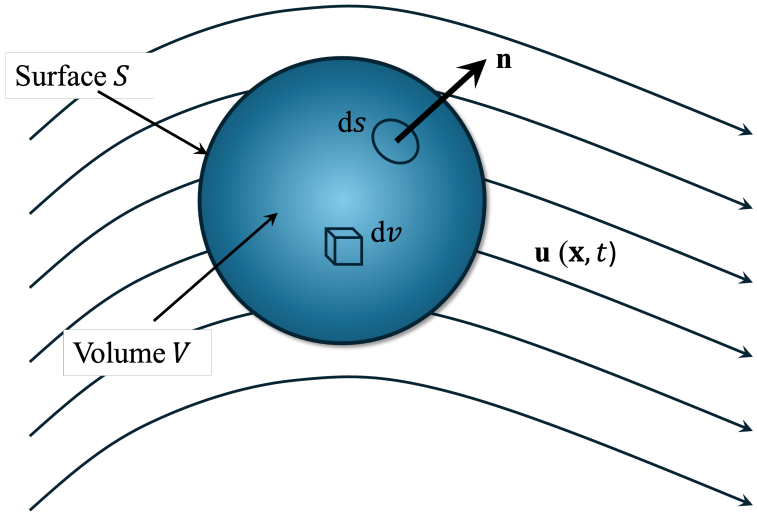


Figure 3.2: Schematic representation of a stationary control volume V subjected to a velocity field $\mathbf{u}(\mathbf{x}, t)$, which is enclosed by a surface S. $\mathrm{d}v$ and $\mathrm{d}s$ denote the infinitesimal volume and surface, respectively; $\mathbf{n}$ represents the normal vector to the interface. This figure is reproduced based on [Tryggvason et al., 2011].

conservation states that mass cannot be created or destroyed. When consider a fixed volume V enclosed by boundary S (see Figure 3.2), this can be interpreted as that the change of the mass within this volume over any time interval equates the mass that crosses the interface during that period. Hence, the mass balance can be written in a mathematical formulation as:

$$\frac{\mathrm{d}}{\mathrm{d}t}\int_V \rho \,\mathrm{d}v = -\oint_S \rho \mathbf{u}\cdot\mathbf{n}\,\mathrm{d}s, \tag{3.1}$$

where $\mathbf{n}$ and $\mathbf{u}$ represent the outward normal vector and velocity vector, respectively; ρ is the density and t refers to the time. Aligning with the above interpretation, the left-hand side accounts for the rate of change of mass in the volume V and the right-hand side corresponds to the net flux through the interface S. By applying the divergence theorem to the latter term, and moving the former term inside the integral, Equation 3.1 can be transformed into one single volume integral. Therefore, the differential form of mass conservation can be obtained:

$$\frac{\partial \rho}{\partial t} + \nabla\cdot(\rho\mathbf{u}) = 0. \tag{3.2}$$

The validity of this equation is supported by two assertions [Tryggvason et al., 2011]: (a) the volume is fixed in space and (b) the single volume integral evaluates to zero for any arbitrary volume only when the integrand (i.e. Equation 3.2) is zero. Furthermore, since incompressible fluid is considered in this thesis, this differential form can be reduced to:

$$\nabla\cdot\mathbf{u} = 0. \tag{3.3}$$

A similar procedure is followed for the derivation for equations of momentum conservation, using the momentum-conservation principle.

The equation of motion states that the overall rate of change of fluid momentum in the volume V must balance out the difference in momentum flux across the interface S plus the net forces

acting on the volume. Following the assumption of neglecting intermolecular forces, the forces considered herein are reduced to body and interface forces [Batchelor, 1967, Tryggvason et al., 2011], giving the formulation as follows:

$$\frac{\mathrm{d}}{\mathrm{d}t}\int_V \rho\mathbf{u}\,\mathrm{d}v = -\oint_S \rho\mathbf{u}(\mathbf{u}\cdot\mathbf{n})\,\mathrm{d}s + \int_V \mathbf{f}\,\mathrm{d}v + \oint_S \mathbf{n}\cdot\mathbf{T}\,\mathrm{d}s. \tag{3.4}$$

By applying the same argument as in the mass conservation, this equation can be rewritten in its differential form:

$$\frac{\partial\rho\mathbf{u}}{\partial t} = -\nabla\cdot(\rho\mathbf{u}\mathbf{u}) + \mathbf{f} + \nabla\cdot\mathbf{T}, \tag{3.5}$$

Here, $\mathbf{f}$ is the force per unit volume, which is solely associated to the gravitational force $\rho\mathbf{g}$ (though in our single-fluid formulation below, Equation 3.21, an ineterfacial force will be appended to this equation). The last term on the right-hand side accounts for the total interface force, where the tensor $\mathbf{T}$ denotes a symmetric tensor which is used to describe the stress acting on an interface element. Again, considering incompressible fluids ($\nabla\cdot\mathbf{u} = 0$), $\mathbf{T}$ can be written as:

$$\mathbf{T} = (-p)\mathbf{I} + 2\mu\boldsymbol{\mathcal{S}}, \tag{3.6}$$

where $p, \mathbf{I}, \mu$ respectively represent the pressure, the unit tensor, and the viscosity; $\boldsymbol{\mathcal{S}}$ is the rate-of-strain, or rate-of-deformation tensor, which can be expressed as:

$$\boldsymbol{\mathcal{S}} = \frac{\nabla\mathbf{u} + \nabla\mathbf{u}^T}{2}, \text{with its components as } S_{ij} = \frac{1}{2}\left(\frac{\partial u_i}{\partial x_j} + \frac{\partial u_j}{\partial x_i}\right). \tag{3.7}$$

From the above, the equations of mass (Equation 3.3) and momentum (Equation 3.5) conservation constitute the Navier-Stokes equations.

3.1.2.3 Large eddy simulation (LES)

In this work, large eddy simulation (LES) is employed to compute the turbulent flow. As briefly described in Section 2.1.5, LES applies a spatial filtering operation on the Navier-Stokes equations prior to the computations. Through this filtering, any eddy larger than a cutoff scale Δ is resolved, while the information related to the smaller eddies is captured through appropriate modelling. Consequently, the filtered equations of mass and momentum conservation become:

$$\nabla\cdot\bar{\mathbf{u}} = 0, \tag{3.8}$$

$$\frac{\partial\rho\bar{\mathbf{u}}}{\partial t} = -\nabla\cdot(\rho\overline{\mathbf{u}\mathbf{u}}) + \mathbf{f} + \nabla\cdot\bar{\mathbf{T}} \tag{3.9}$$

where $\bar{\mathbf{T}} = (-\bar{p})\mathbf{I} + 2\mu\overline{\boldsymbol{\mathcal{S}}}$ and $\overline{\boldsymbol{\mathcal{S}}} = (\nabla\bar{\mathbf{u}} + \nabla\bar{\mathbf{u}}^T)/2$. Here, the bar in these equations and those following designates filtered flow variables. According to Versteeg and Malalasekera [2007], in order to resolve the first term on the right-hand side of Equation 3.9, this term can be decomposed into:

$$\nabla\cdot(\rho\overline{\mathbf{u}\mathbf{u}}) = \nabla\cdot(\rho\bar{\mathbf{u}}\bar{\mathbf{u}}) + \nabla\cdot\boldsymbol{\tau}.$$

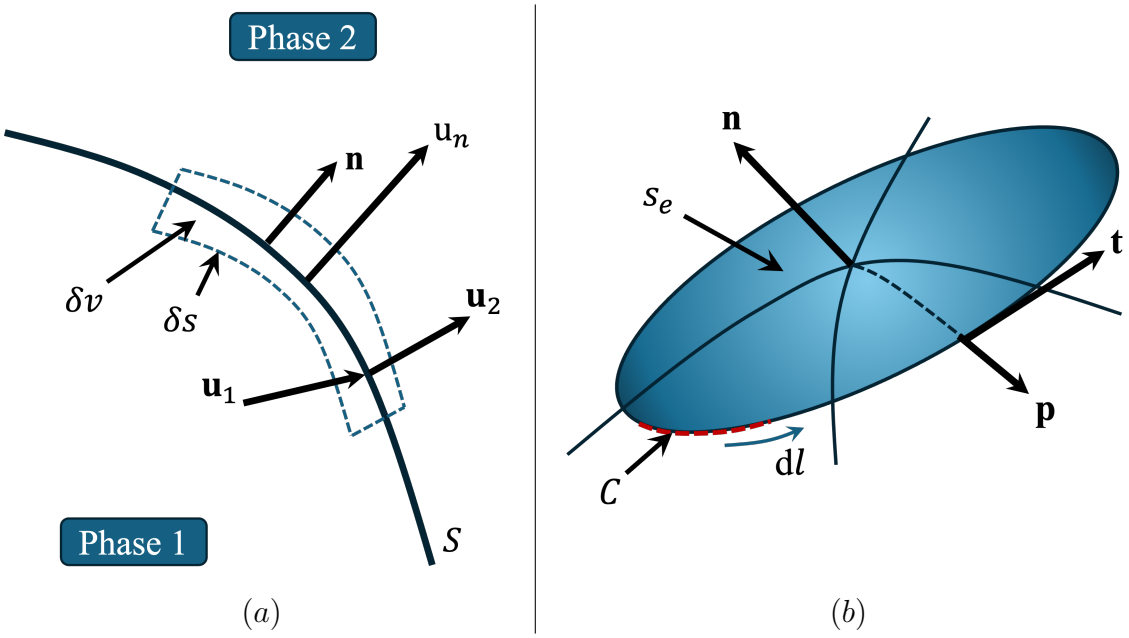


Figure 3.3: Schematic representations of (a) a thin control volume δv enclosed by interface δs consisting of a portion of both phases and their interface S, wherein the label $u_n, \mathbf{u}_i$ denote the normal velocity of the interface and velocities for phase i; (b) a small element of the interface, s_e, with its boundary annotated as a contour C, and $\mathbf{n}, \mathbf{t}$ and $\mathbf{p}$ represent the vector at the interface to the direction of normal, tangential and perpendicular, respective;y. Both figures are reproduced based on [Tryggvason et al., 2011].

where $\nabla \cdot \boldsymbol{\tau}$ incorporates the lost information of the smaller eddies, together with their interaction with the larger, resolved eddies. The components of $\boldsymbol{\tau}$ are $\tau_{ij} = \rho\overline{u_i u_j} - \rho\bar{u}_i\bar{u}_j$, which constitute what are known as sub-grid-scale (SGS) stresses. In LES, SGS stresses are included by means of a sub-grid scale model. In this thesis, the most widely-used model in the literature, Smagorinsky-Lilly SGS model, is employed, where the τ_{ij} are approximated as being proportional to the local rate of strain of the resolved flow [Versteeg and Malalasekera, 2007, Andersson et al., 2011]:

$$\tau_{ij} = -2\mu_s \overline{S}_{ij}, \tag{3.10}$$

Here, μ_s is the SGS viscosity, which is evaluated based on Prandtl's mixing length model [Bradshaw, 1974]:

$$\mu_s = \rho(C_s\Delta)^2 \left|\bar{S}\right| = \rho(C_s\Delta)^2\sqrt{2\overline{S}_{ij}\overline{S}_{ij}}, \tag{3.11}$$

where C_s is the Smagorinsky-Lilly coefficient, which is fixed to 0.2 herein (as its values varies between 0.1-0.3 in the literature [Lilly, 1966, 1967, Deardorff, 1970, McMillan and Ferziger, 1979, Pope, 2004]); Δ is set to $V^{1/3}$, with V representing the volume of a grid cell, written as $V = \Delta x \Delta y \Delta z$. By substituting the above equations into Equation 3.9, the filtered momentum conservation equation can be rewritten as:

$$\rho\left(\frac{\partial \bar{\mathbf{u}}}{\partial t} + \bar{\mathbf{u}} \cdot \nabla\bar{\mathbf{u}}\right) = -\nabla\bar{p} + \nabla \cdot \left[\left(\mu + \rho C_s^2\Delta^2\left|\bar{S}\right|\right)\left(\nabla\bar{\mathbf{u}} + \nabla\bar{\mathbf{u}}^T\right)\right] + \rho\mathbf{g}, \tag{3.12}$$

which is solved in this thesis (as opposed to Equation 3.9).

3.1.2.4 Interfacial boundary conditions

Considering an interface separating two immiscible fluids, a set of jump conditions at the interface are required for the velocity field to satisfy the Navier-Stokes equations. These conditions can be derived by applying mass and momentum conservation at a thin control volume (see Figure 3.3*a*), and the corresponding normal, tangential, and perpendicular vectors at the interface that would be used during the derivation are explicitly sketched in Figure 3.3*b*. Firstly, following the sharp interface assumption, no accumulation is expected inside the interface with vanishing thickness, which gives rise to the fact that inward mass flux is equal to the outward mass flux. This statement can be expressed mathematically as:

$$\rho_1(\mathbf{u_1} \cdot \mathbf{n} - u_n) = \rho_2(\mathbf{u_2} \cdot \mathbf{n} - u_n),$$

where the terms in brackets represent the flow in phase i with $\mathbf{u}_i$ as the velocity vectors in the corresponding phase, as shown in Figure 3.3*a*; $u_n = \mathbf{u} \cdot \mathbf{n}$ stands for the normal velocity at the interface. In the case of incompressible fluids without the presence of phase change, this equation holds for any arbitrary density ratios, giving rise to the so-called "no-penetration" condition [Deen, 1998]:

$$\mathbf{u_1} \cdot \mathbf{n} = \mathbf{u_2} \cdot \mathbf{n}. \tag{3.13}$$

In addition, no restriction on the tangential velocity components are imposed by the mass conservation, which is supported by the experimental observation that there is no relative motion between viscous liquids at the interface [Tryggvason et al., 2011]. This leads to the known "no-slip" condition which can be described by:

$$\mathbf{u_1} \cdot \mathbf{t} = \mathbf{u_2} \cdot \mathbf{t}. \tag{3.14}$$

Hence, both Equation 3.13 and Equation 3.14 serve as interfacial boundary conditions for the velocity field, imposing continuity of the velocity across the interface.

Similarly, the application of momentum conservation at the interface element gives rise to additional jump conditions. However, in this case, extra forces present at the interface must be considered, i.e., the interfacial tension. As stated in Section 2.1.4, the interfacial tension can be regarded as a force per unit length acting perpendicularly to the interface. Accordingly, consider an interfacial tension tensor $\mathbf{T}_S^\sigma = \sigma \mathbf{I}_S$, where $\mathbf{I}_S$ is the interface identity tensor and σ refers to the interfacial tension, the force applied on the edge of a small interface element to expand the interface can be written as $\mathbf{T}_S^\sigma \cdot \mathbf{p}$, where $\mathbf{p}$ denotes a vector normal to the edge of the element and in the tangent plane to the interface. Therefore, the overall force $\delta\mathbf{F}_\sigma$ acting on an interface element bounded by a curve C can be obtained by integrating this term over its edges:

$$\delta\mathbf{F}_\sigma = \oint_C \mathbf{T}_S^\sigma \cdot \mathbf{p}\, \mathrm{d}l = \int_S \nabla_S \cdot \mathbf{T}_S^\sigma \, \mathrm{d}s_e, \tag{3.15}$$

where $\mathrm{d}l$ is the edge length, and $\mathrm{d}s_e$ refers to interface area of the infinitesimal interface el-

ement s_e. The subscript e of the latter term is dropped henceforth for consistency denoting infinitesimal interface in general. The integrand of the rightmost term can be interpreted as the interfacial force per unit area $\mathbf{f}_\sigma$ and therefore it can be written as:

$$\mathbf{f}_\sigma = \nabla_S \cdot \mathbf{T}_S^\sigma = \nabla_S \cdot \sigma \mathbf{I}_S = \sigma \nabla_S \cdot \mathbf{I}_S + \mathbf{I}_S \cdot \nabla_S \sigma, \tag{3.16}$$

which can be be represented as:

$$\mathbf{f}_\sigma = \sigma \kappa \mathbf{n} + \nabla_S \sigma, \tag{3.17}$$

with $\nabla_S \cdot \mathbf{I}_S = \kappa \mathbf{n}$, the detailed derivation of which is shown in Tryggvason et al. [2011]. Here, κ, the interface curvature, can be obtained via $\kappa = -\nabla_S \cdot \mathbf{n}$. This equation describes that the local interfacial force can be decomposed into its normal component, $\sigma\kappa\mathbf{n}$, associated with the mean interfacial tension, and its tangential component, $\nabla_S\sigma$, the Marangoni stress induced by the interfacial tension gradient.

With the velocity continuity at the interface, and the formulation of interfacial tension derived above, the momentum balance on the control volume is in the form of:

$$0 = -\oint_{\delta s} \rho \mathbf{u}(\mathbf{u} \cdot \mathbf{n} - u_n)\, \mathrm{d}s + \oint_{\delta s} \mathbf{n} \cdot \mathbf{T}\, \mathrm{d}s + \int_S \mathbf{f}_\sigma\, \mathrm{d}s. \tag{3.18}$$

It is worth highlighting that the integration for the first two terms on the right-hand side is around the bounding curve of the control volume, δs, while the last term is integrated directly along the interface S. Recalling the definition of u_n from above and considering the incompressible fluids in the absence of phase change, the first term is cancelled out. Meanwhile, with the sharp interface assumption, the boundary of the volume and the interface is forced to coincide, which yields an additional jump condition at the interface:

$$\mathbf{n} \cdot (\mathbf{T}_1 - \mathbf{T}_2) = \sigma \kappa \mathbf{n} + \nabla_S \sigma. \tag{3.19}$$

3.1.2.5 One-fluid formulation for multiphase flows in complex configurations

To describe a whole fluid flow domain involving a sharp interface, one could construct the flow equations for each phase and apply the above-derived jump conditions to couple the solutions across the interface [Tryggvason et al., 2011]. Alternatively, a single set of conservation equations can be formulated for the entire system, circumventing the specification of jump conditions. This approach is known as the "one-fluid" formulation where both phases are regarded as one fluid with their physical properties, such as density and viscosity, changing abruptly at the interface. To incorporate the jump conditions at the interface, one must add singular terms to the governing equations [Tryggvason et al., 2011]. Specifically, the interfacial tension is added as a body force to the equation of momentum conservation, Equation 3.12. In addition, in the context of agitated vessels, fluid-solid interaction force, $\mathbf{F}_{\text{fsi}}$, which accounts for the interaction effect between rotating impeller blades and mixing fluids, is considered as an additional body force.

Similar to the previous derivations, the interfacial tension force $\mathbf{f}_\sigma$ integrated over the interface area s_e, the part of the entire interface S which encloses the control volume, can be transformed into integration over the volume using the Divergence Theorem. Here, a function δ_S is defined, which has the property of changing volume (or surface) integrals into interface (or line) integrals [Tryggvason et al., 2011]. For an arbitrary function f:

$$\int_V \delta_S(\mathbf{x}) f(\mathbf{x})\,\mathrm{d}v = \int_S f(\mathbf{x})\,\mathrm{d}s,$$

where δ is the ordinary Dirac delta distribution and δ_S is concentrated on the interface as a δ function is concentrated on one point. Therefore, the interfacial tension force can be rewritten as:

$$\int_S \mathbf{f}_\sigma \mathrm{d}s = \int_V \mathbf{f}_\sigma \delta_S(\mathbf{x}-\mathbf{x}_S)\mathrm{d}v. \tag{3.20}$$

Here, $\delta_S(\mathbf{x}-\mathbf{x}_S)$ indicates that the delta distribution is non-zero only when $\mathbf{x}=\mathbf{x}_S$, i.e., at the interface. By adding this term, along with the $\mathbf{F}_{\text{fsi}}$, to Equation 3.12, this equation becomes:

$$\rho\left(\frac{\partial \bar{\mathbf{u}}}{\partial t}+\bar{\mathbf{u}}\cdot\nabla\bar{\mathbf{u}}\right) = -\nabla\bar{p}+\nabla\cdot\left[\left(\mu+\rho C_s^2\Delta^2\left|\bar{S}\right|\right)\left(\nabla\bar{\mathbf{u}}+\nabla\bar{\mathbf{u}}^T\right)\right]+\rho\mathbf{g} \\ +\mathbf{F}_{\text{fsi}}+\mathbf{f}_\sigma\delta_S.$$

A definition of $\mathbf{F}_{\text{fsi}}$ will be provided in Section 3.1.4.7. With the definition of the δ function provided above, and by substituting $\mathbf{f}_\sigma$ using Equation 3.17, the last term in the above equation can be equivalently expressed as an area integral over an interface element:

$$\rho\left(\frac{\partial \bar{\mathbf{u}}}{\partial t}+\bar{\mathbf{u}}\cdot\nabla\bar{\mathbf{u}}\right) = -\nabla\bar{p}+\nabla\cdot\left[\left(\mu+\rho C_s^2\Delta^2\left|\bar{S}\right|\right)\left(\nabla\bar{\mathbf{u}}+\nabla\bar{\mathbf{u}}^T\right)\right]+\rho\mathbf{g} \\ +\mathbf{F}_{\text{fsi}}+\int_S\left[\sigma\kappa\mathbf{n}+\nabla_S\sigma\right]\delta(\mathbf{x}-\mathbf{x}_S)\,\mathrm{d}s, \tag{3.21}$$

where $\delta(\mathbf{x}-\mathbf{x}_S)=\delta(x-x_S)\delta(y-y_S)\delta(z-z_S)$. This equation, together with Equation 3.3, serve as the governing equations for mass and momentum conservation in this work.

For completeness, the density ρ and viscosity μ are given in terms of a numerical indicator Heaviside function, $\mathcal{H}(\mathbf{x},t)$:

$$\begin{aligned}\rho(\mathbf{x},t) &= \rho_o+(\rho_a-\rho_o)\,\mathcal{H}(\mathbf{x},t),\\ \mu(\mathbf{x},t) &= \mu_o+(\mu_a-\mu_o)\,\mathcal{H}(\mathbf{x},t),\end{aligned} \tag{3.22}$$

where the function is defined as zero in phase "o" and unity in phase "a". The Heaviside function could be generated in different ways using the geometrical information on the tracked interface [Shin and Juric, 2002, Shin et al., 2009, 2017]. Further details are presented in Section 3.1.3.3.

3.1.2.6 Surfactant transport

In the case of a surfactant-laden system, additional equations are solved considering surfactant transport. In this thesis, surfactant is soluble in the continuous phase (i.e., bulk), hence, surfactant transport is resolved both in the bulk and on the interface. These surfactant behaviours have been comprehensively demonstrated in Section 2.1.4, wherein sets of describing equations are presented. By substituting with Equation 2.11 and 2.10, Equation 2.9 becomes:

$$\frac{\partial \Gamma}{\partial t} + \nabla_S \cdot (\Gamma \mathbf{u}_t) = D_s \nabla_S^2 \Gamma + J_n, \tag{3.23}$$

where $\mathbf{u}_t$ is the tangential velocity vector on the interface, which is computed from the interface velocity, $\mathbf{u}_s$, via $\mathbf{u}_t = (\mathbf{u}_s \cdot \mathbf{t})\,\mathbf{t}$, with $\mathbf{t}$ being the unit vector tangential to the interface. Furthermore, the sorption flux can be rewritten as:

$$J_{\mathrm{a/d}} = k_a C_{\mathrm{sub}}(\Gamma_\infty - \Gamma) - k_d \Gamma, \tag{3.24}$$

where k_a and k_d are the kinetic coefficients for adsorption and desorption, respectively, and Γ_∞ is the saturation concentration on the interface. As mentioned in Section 2.1.4, the Langmuir equation of state is used to describe the change in interfacial tension with surfactant concentration at the interface:

$$\sigma = \sigma_s + \mathcal{R}T\Gamma_\infty \ln\left(1 - \frac{\Gamma}{\Gamma_\infty}\right) = \sigma_s \left[1 + \beta_s \ln\left(1 - \frac{\Gamma}{\Gamma_\infty}\right)\right]. \tag{3.25}$$

In this equation, $\mathcal{R}$ denotes the ideal gas constant, T the temperature, and β_s is a dimensionless parameter defined as surfactant elasticity, which measures the sensitivity of the interfacial tension to change in the surfactant concentration. The Langmuir equation expresses that the interfacial tension drops steeply as the surfactant concentration approaches unity from below [Chang and Franses, 1995]. However, this relation could predict unrealistic behaviours, i.e., the interfacial tension becomes negative for finite values of Γ. To avoid this, the relation is modified as follows [Shin et al., 2018]:

$$\sigma/\sigma_s = \max\left[0.05, 1 + \beta_s \ln\left(1 - \frac{\Gamma}{\Gamma_\infty}\right)\right]. \tag{3.26}$$

The equations governing the surfatcant concentration and diffusion in the bulk remain unchanged from Equation 2.8 and 2.13, respectively, and are not presented in this section for the sake of brevity.

3.1.2.7 Dimensionless parameters

Following the derivation presented above, the governing equations are rewritten in dimensionless form according to the scaling below:

$$\tilde{\mathbf{x}} = \frac{\mathbf{x}}{D}, \quad \tilde{t} = \frac{t}{1/N}, \quad \tilde{\mathbf{u}} = \frac{\bar{\mathbf{u}}}{ND}, \quad \tilde{\mathbf{g}} = \frac{\mathbf{g}}{g},$$
$$\tilde{p} = \frac{\bar{p}}{\rho_a(ND)^2}, \quad \tilde{\mu} = \frac{\mu}{\mu_a}, \quad \tilde{\rho} = \frac{\rho}{\rho_a}, \tag{3.27}$$

where the tildes indicate the dimensionless quantities. As presented, space $\mathbf{x}$ and time t are scaled by the impeller diameter, D and the duration for one impeller revolution, $1/N$, respectively. Accordingly, the velocity is made non-dimensional based on the impeller velocity, ND, and the pressure by the term, $\rho_a(ND)^2$. Hence, the governing equations become:

$$\nabla \cdot \tilde{\mathbf{u}} = 0, \tag{3.28}$$

$$\tilde{\rho}\left(\frac{\partial \tilde{\mathbf{u}}}{\partial \tilde{t}} + \tilde{\mathbf{u}} \cdot \nabla \tilde{\mathbf{u}}\right) + \nabla \tilde{p} = \frac{1}{Re}\nabla \cdot \tilde{\mu}\left(\nabla \tilde{\mathbf{u}} + \nabla \tilde{\mathbf{u}}^T\right) - \nabla \cdot \left(\tilde{\rho} C_s^2 \tilde{\Delta}^2 \left|\tilde{S}\right|\right)\left(\nabla \tilde{\mathbf{u}} + \nabla \tilde{\mathbf{u}}^T\right) + \frac{1}{Fr}\tilde{\rho}\tilde{\mathbf{g}}$$
$$+ \tilde{\mathbf{F}}_{\text{fsi}} + \frac{1}{We}\,\tilde{\mathbf{f}}_\sigma \delta_S, \tag{3.29}$$

where the dimensionless parameters are defined as followed:

$$Re = \frac{\rho_a N D^2}{\mu_a}, \quad We = \frac{\rho_a N^2 D^3}{\sigma_s}, \quad Fr = \frac{N^2 D}{g}. \tag{3.30}$$

Here, Re, We and Fr stand for the Reynolds, Weber, and Froude numbers respectively, providing a measure of the relative significance of inertial to viscous, interfacial tension, and gravitational forces, respectively.

Similarly, the governing equations describing surfactant transport (Equation 2.8, 3.23, 3.24, 2.13, 3.26) can be written in their dimensionless form:

$$\frac{\partial \tilde{C}}{\partial \tilde{t}} + \tilde{\mathbf{u}} \cdot \nabla \tilde{C} = \frac{1}{Pe_b}\nabla^2 \tilde{C}, \tag{3.31}$$
$$\frac{\partial \tilde{\Gamma}}{\partial \tilde{t}} + \nabla_S \cdot \left(\tilde{\Gamma}\tilde{\mathbf{u}}_t\right) = \frac{1}{Pe_s}\nabla_S^2 \tilde{\Gamma} + \tilde{J}, \tag{3.32}$$
$$\tilde{J}_{a/d} = Bi\left[k\tilde{C}_{\text{sub}}(1-\tilde{\Gamma}) - \tilde{\Gamma}\right], \tag{3.33}$$
$$\tilde{J}_{\text{diff}} = -\frac{1}{Pe_b h}\mathbf{n} \cdot \nabla \tilde{C}|_{\text{sub}}, \tag{3.34}$$
$$\tilde{\sigma} = \max\left[0.05,\ 1 + \beta_s \ln\left(1-\tilde{\Gamma}\right)\right], \tag{3.35}$$

given the scaling:

$$\tilde{\sigma} = \frac{\sigma}{\sigma_s}, \quad \tilde{\Gamma} = \frac{\Gamma}{\Gamma_\infty}, \quad \tilde{C} = \frac{C}{C_0}, \quad \tilde{C}_{\text{sub}} = \frac{C_{\text{sub}}}{C_0}, \tag{3.36}$$

where C_0 denotes the initial surfactant concentration in the bulk. Additional dimensionless parameters are defined:

$$\begin{aligned} Pe_b &= \frac{ND^2}{D_b}, \quad Pe_s = \frac{ND^2}{D_s}, \quad Bi = \frac{k_d}{N}, \\ h &= \frac{\Gamma_\infty}{DC_0}, \quad k = \frac{k_a C_0}{k_d}, \quad \beta_s = \frac{\mathcal{R}T\Gamma_\infty}{\sigma_s}. \end{aligned} \tag{3.37}$$

Pe_b and Pe_s are the bulk and interfacial Peclét numbers, separately providing the relative significance of convection and diffusion in the bulk and on the interface. The Biot number, Bi, expresses the ratio of the characteristic desorptive to convective speed on the interface; h stands for the adsorption depth that characterises the diluted region beneath the interface caused by adsorption; k is the adsorption parameter, representing the ratio k_a/k_d.

As demonstrated previously, an important effect induced by the presence of surfactant arises from the Marangoni stress, due to surfactant concentration gradients and hence can be computed via $\tilde{\Gamma}$:

$$\tilde{\tau} \equiv \nabla_S \tilde{\sigma} \cdot \mathbf{t} = -\frac{\beta_s}{1-\tilde{\Gamma}} \left(\mathbf{t} \cdot \nabla_S \tilde{\Gamma} \right). \tag{3.38}$$

For simplicity, the tildes that designate dimensionless quantities are dropped henceforth. Finally, the dimensionless timescale used in chapter 4 and 5, in the form of $t = n \times Rev.$, refers to the instant when n impeller revolutions are completed.

3.1.3 Numerical technique for interface localisation

In Section 2.1.5, various methods for interface localisation have been presented and summarised. In this work, a hybrid front-tracking/level-set framework, known as the Level Contour Reconstruct Method (LCRM), is adopted to track interface in simulations. The first version of this scheme was introduced and detailed by Shin and Juric [2002], which has been refined in subsequent works to include an enhanced interface reconstruction strategy for more robust local mass conservation [Shin and Juric, 2007] and more accurate interface edge computation [Shin et al., 2009], the introduction of a solver for interfacial tension forces [Shin et al., 2005], and the adaptation of the surfactant transport formulation within the framework [Shin et al., 2018]. More recent advancements and detailed implementations with regard to this method can be found in Shin et al. [2011, 2017]. This section aims to provide a conceptual understanding of LCRM, starting with a brief introduction to the two conventional methods from which LCRM originates: the generic front tracking method and level-set interface capturing method.

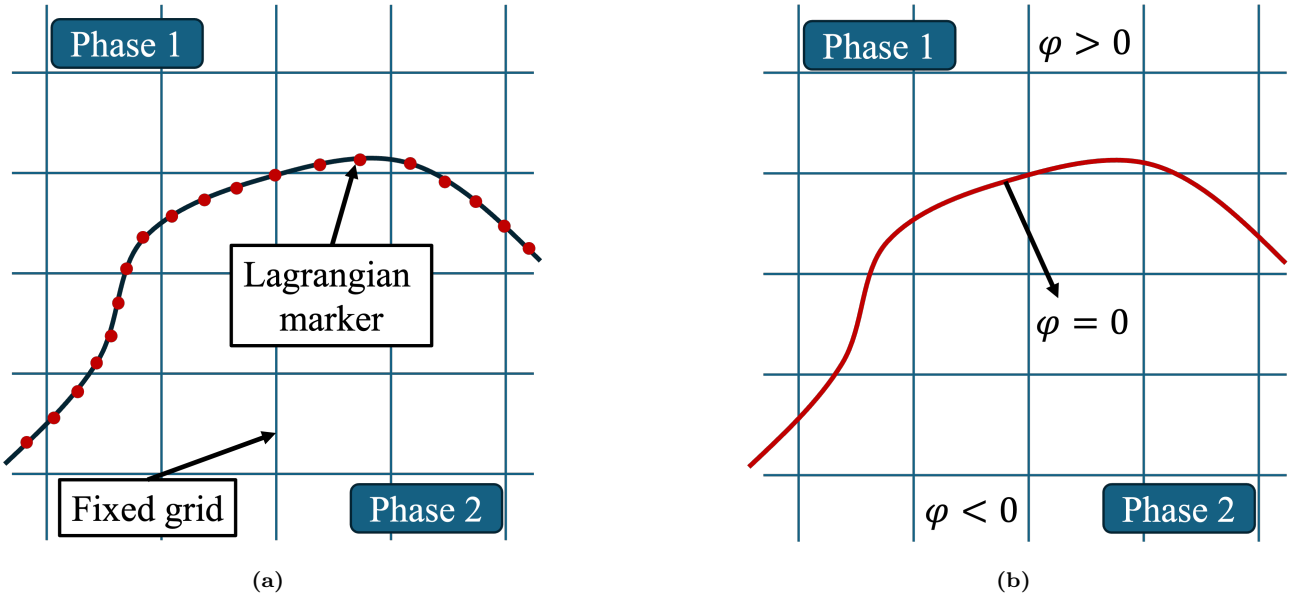


Figure 3.4: Schematic representations of interface in (a) front tracking method, wherein Lagrangian markers are advected with velocity from fixed grids; (b) level-set method, wherein the interface is computed as contour level of a distance function. say φ.

3.1.3.1 Front tracking

In the original front tracking method [Unverdi and Tryggvason, 1992, Tryggvason et al., 2001], two types of grids are used. One is a stationary Eulerian grid on which the governing equations for flow variables are solved; the other is a moving Lagrangian grid used to explicitly track the motion of the interface. In this method, the Lagrangian marker particles, which localise either on the exact position of the interface or in the volume around the interface (see Figure 3.4a), offer a triangulation (3D) or a piecewise linear (2D) description of the interface. The primary advantage of the front tracking method is that it yields accurate prediction of interface physics at a subgrid level [Tryggvason et al., 2011]. This provides a highly reliable depiction of interface's location and geometry, allowing for precise computation of interfacial tension forces directly on the interface. However, the main drawback of the front tracking method also comes from its explicit tracking strategy, which brings algorithmic complexity when it comes to 3D simulations. Furthermore, the explicit tracking requires the procedure for bookkeeping the connectivity among the marker points, which makes the calculation of interface geometry, especially during topology change processes, more challenging in 3D systems.

3.1.3.2 Level-set

In contrast to the front-tracking method, the level-set method falls into the category of interface capturing methods, in which the interface is defined on the fixed grid (see comprehensive review by Sethian [2001], Osher and Fedkiw [2002]). Specifically, a smooth marker function, $\varphi(\mathbf{x}, t)$, which denotes the minimum distance to the interface front, is used to identify the different phases in the level-set method. By definition, this function is positive in one fluid and takes negative values in the other; the interface or boundary separating the fluids is therefore defined by the level contour where $\varphi = 0$ (see Figure 3.4b). The propagation of the interface front in the system relies on the evolution of the function φ moving with the Eulerian fluid, which is

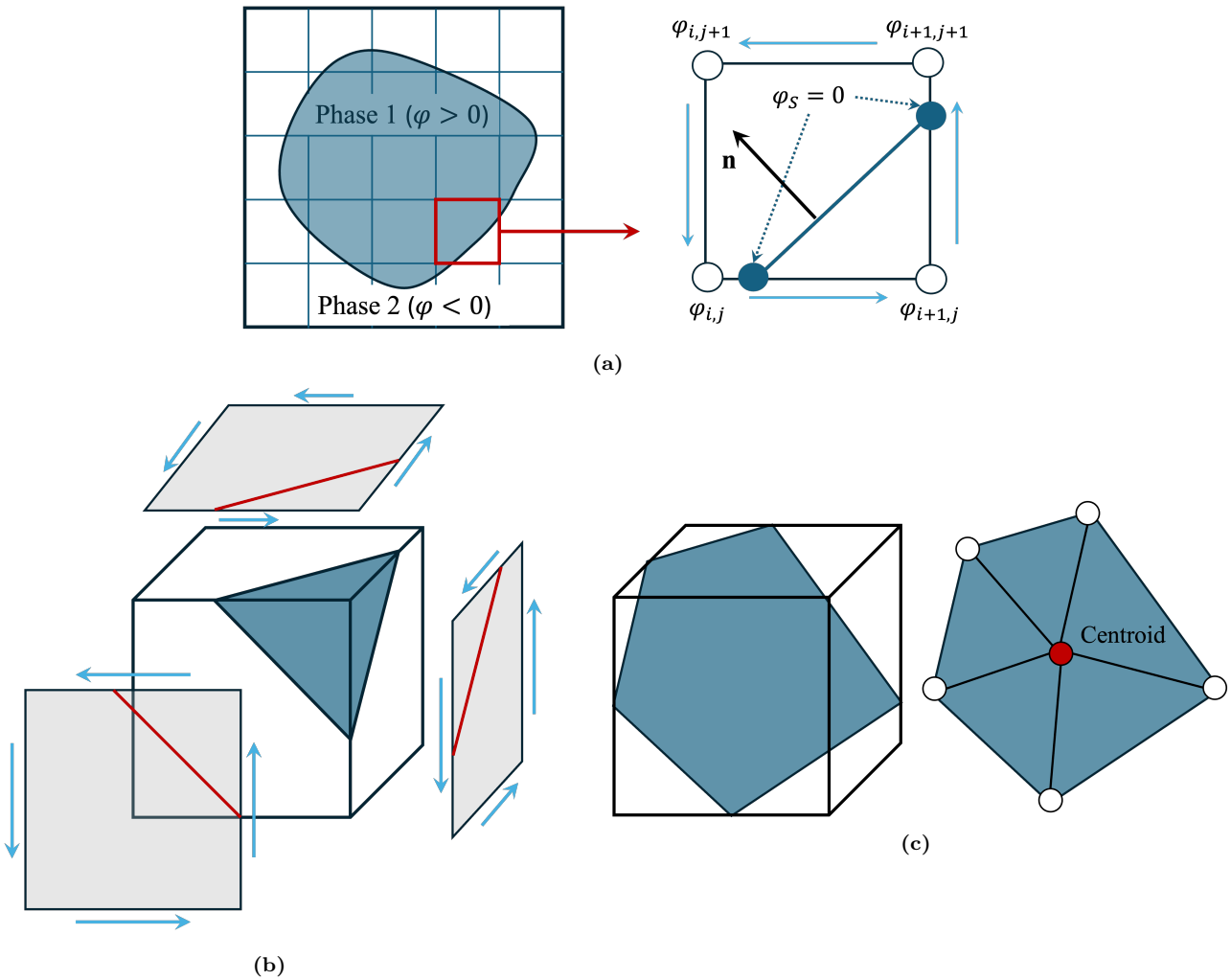


Figure 3.5: Schematic diagram of the interface reconstruction process in LCRM, (a) for two-dimensional simulation; $(b), (c)$ for three-dimensional simulations.

described as:

$$\frac{\partial \varphi}{\partial t} + \mathbf{u} \cdot \nabla \varphi = 0.$$

Since the level-set marker function is smooth, its advection along with the fluid can be obtained via any numerical solution that follows hyperbolic conservation laws [Sethian, 2001, Tryggvason et al., 2011]. Additionally, the equation presented above is the sole additional component in the level-set method, avoiding the need for further complex steps like adding new computational objects in the front tracking scheme. However, this method's simplicity is offset by its significant issues with mass conservation, which results in mass losses due to the artificial shift of the interface front [Tryggvason et al., 2011, Ferziger et al., 2019]. Although various modifications have been implemented to handle these problems [Sussman et al., 1994, 1998, Sussman and Puckett, 2000], they introduce additional layers of complexity to the refined versions, making their implementation difficulty comparable to other techniques.

3.1.3.3 Level contour reconstruct method (LCRM)

The main contribution of LCRM stems from the fact that it provides an alternative interface tracking framework, which eliminates the procedure for bookkeeping interface connectivity in

the original front-tracking method [Unverdi and Tryggvason, 1992], and simultaneously retains the advantage of explicit Lagrangian interface tracking providing accurate interface geometry and information regarding topology change.

Recall that the Heaviside function $\mathcal{H}(\mathbf{x}, t)$ is used to describe the material properties (Equation 3.22) in the one-fluid formulation. Hence, this provides additional representation of interface in LCRM, namely a certain contour level of the Heaviside function. This indicator serves as a smoothed characteristic function for the interface [Shin et al., 2009]. In LCRM, the interface elements are periodically discarded and updated with new ones which are reconstructed on $\mathcal{H}$. According to the collection of papers surrounding the LCRM, this indicator function can be calculated by either (1) solving the Poisson equation [Shin and Juric, 2002, Shin et al., 2005]:

$$\nabla^2 \mathcal{H} = \nabla \cdot \int_S \mathbf{n} \delta(\mathbf{x} - \mathbf{x}_S) \, \mathrm{d}s, \tag{3.39}$$

or (2) using Eulerian field variables such as a vector-valued distance function, say denoted as φ, as in the level-set method [Shin et al., 2009].

Likewise, the construction of interface element can be achieved by interpolating the given indicator function either (1) in a linear manner [Shin and Juric, 2002, Shin et al., 2005] or (2) by using a high-order spline kernel [Shin and Juric, 2007, Shin et al., 2009]. Schematic diagrams in Figure 3.5 exemplify the interface reconstruction using linear interpolation of the distance function φ in 2D and 3D simulations. As demonstrated, in the case of 2D simulations, a local field of φ can be computed directly at the vertices of one Eulerian grid based on the given locations of the Lagrangian interface [Shin et al., 2009]. Once the φ field is constructed, by using linear interpolation, a contour line at $\varphi = 0$ can be drawn which intersects the boundary edges of the Eulerian grid cell, giving rise to the new interface element (the dark blue line segment shown in Figure 3.5*a*). In this way, the reconstructed interface elements share common end points at the edge of grid cell, which are therefore implicitly connected in this framework. Furthermore, the orientation of the elements are determined (detailed procedure refers to Shin and Juric [2002]) such that the normal vectors of all elements point toward the inside of the volume enclosed by the interface (see Figure 3.5*a*). Consequently, LCRM affords to handle interface deformation, merging and breakup automatically and robustly [Shin and Juric, 2002] as in the level-set method. Similarly, in 3D simulations, the line segments obtained from each faces of the grid cell connect and form an interface element (refers to the triangular component coloured in blue in Figure 3.5*b*). In the case where more than three line segments are attained in one grid cell, the formed polygon is divided into triangular elements from its centroid (see Figure 3.5*c*) and the element orientations can be found following the same procedure as in 2D cases. The selection of element shape as triangular effectively solves the problem of directional ambiguity encountered in both 2D and 3D system, more details can be found in Shin et al. [2011].

From above, LCRM retains the Lagrangian interface tracking of arbitrarily moving interface from the conventional front tracking method, ensuring precise treatment of interface tension forces, and meanwhile, takes the advantages of level-set distance function approach for periodic interface construction, obviating the algorithmic complexity encountered in the former scheme. In addition, according to Shin et al. [2017], LCRM inherently addresses the mass conservation problem when the level-set method is used, since the distance function field, φ, herein is not involved in the advection of the interface. Alternatively, the interface elements are advected in a Lagrangian manner by integrating:

$$\frac{\mathrm{d}\mathbf{x}_S}{\mathrm{d}t} = \mathbf{V}, \tag{3.40}$$

where $\mathbf{V}$ is the interface velocity which is interpolated from the Eulerian velocity with a second-order Runge-Kutta method [Shin et al., 2017].

3.1.4 Solutions procedures

From previous sections, the governing equations for all the simulations presented in this thesis are the Navier-Stokes equations for incompressible, Newtonian flows, along with sets of those considering surfactant transport in the continuous phase and at the interface. Furthermore, one-fluid formulation of the Navier-Stokes equation (Section 3.1.2) is used herein where a single set of equations are solved to depict the motion of all the fluids present. In addition, hybrid Lagrangian-Eulerian grids are employed for interface propagation. This section provides an overview of the techniques for numerical implementation under these settings.

The CFD code consists of two main components [Shin et al., 2017]:

1. a module for **solving variables on the Eulerian grids** such as those involved in the Navier-Stoke equations (3.3, 3.21) and surfactant concentration in the continuous fluids (2.8);

2. a module for **solving variables at the Lagrangian interface grids** covering Lagrangian interface advection (3.40), surfactant concentration at the interface (3.23), as well as interface tracking and reconstruction procedure in LCRM.

This code is written in computing language Fortran 2008 and adopts an algebraic domain decomposition scheme for parallelisation, where the information transfer between subdomains are managed via the Message Passing Interface (MPI) protocol [Shin et al., 2017].

3.1.4.1 Time integration

Firstly, the primary variables of velocity $\mathbf{u}$ and pressure p on the fixed Eulerian grids are computed via Chorin's projection method [Chorin, 1968]. The code herein provides a choice of explicit or implicit time integration to either first or second order. In this work, the temporal scheme is based on a second-order Gear method [Tucker, 2013] with implicit solution of the viscous terms of the velocity components. In this method, adaptive time steps Δt are applied,

which the value is carefully chosen at each temporal iteration in order to satisfy a robust numerical stability via a criterion based on:

$$\Delta t \leq \min\left\{\Delta t_{\text{cap}},\ \Delta t_{\text{vis}},\ \Delta t_{\text{CFL}},\ \Delta t_{\text{int}},\ \Delta t_{\text{surf}}\right\}, \tag{3.41}$$

where Δt_{cap}, Δt_{vis}, Δt_{CFL}, Δt_{int}, and Δt_{surf} represent the capillary, viscous, Courant-Friedrichs-Lewy (CFL), interfacial CFL, and surfactant time-steps, respectively, defined by:

$$\begin{aligned}
\Delta t_{\text{cap}} &\equiv \frac{1}{2}\left(\frac{(\rho_o+\rho_a)\,\Delta x_{\text{min}}^3}{\pi\sigma}\right)^{1/2},\\
\Delta t_{\text{vis}} &\equiv \min\left(\frac{\rho_a}{\mu_a},\frac{\rho_o}{\mu_o}\right)\frac{\Delta x_{\text{min}}^2}{6},\\
\Delta t_{\text{CFL}} &\equiv \min_j\left(\min_{\text{domain}}\left(\frac{\Delta x_j}{\|u_j\|}\right)\right),\\
\Delta t_{\text{int}} &\equiv \min_j\left(\min_{s_e(t)}\left(\frac{\Delta x_j}{\|\mathbf{V}\|}\right)\right),\\
\Delta t_{\text{surf}} &\equiv \frac{\Delta x_{\text{min}}^2}{6D_b},
\end{aligned}$$

where $\Delta x_{\text{min}} = \min_j(\Delta x_j)$ refers to the minimum size x at a given cell j; u_j, and $\mathbf{V}$ are the maximum fluid and interface velocities, respectively; $s_e(t)$ denotes the interface element whose location is time-variant. The term of surfactant time-steps, Δt_{surf}, is unique for the surfactant-laden systems while the others are considered in both simulation cases regardless of the presence of surfactant.

To demonstrate the time integration scheme used in this work, a first-order method is described and the second-order approach can then be easily extended. With a first-order, explicit, forward-in-time discretization of the time derivative, the discrete form of momentum equation (3.21) can be written as:

$$\frac{\mathbf{u}^{n+1}-\mathbf{u}^n}{\Delta t} = \frac{1}{\rho^{n+1}}(\mathbf{A}_h^n+\mathbf{F}_h^n) - \frac{1}{\rho^{n+1}}\nabla_h p. \tag{3.42}$$

In this equation, $\mathbf{A}_h^n$ is introduced to denote numerical approximations of the convective ($\rho\bar{\mathbf{u}}\cdot\nabla\bar{\mathbf{u}}$), diffusion (second term on the right in Equation 3.21) and gravitational ($\rho\mathbf{g}$) terms; $\mathbf{F}_h^n$ incorporates the interfacial tension forces and solid-fluid interaction force. ∇_h is a spatially discrete operator and $n, n+1$ are used to denote the time-steps. In incompressible flows, the role of pressure is to ensure that the divergence of the velocity field remains zero [Tryggvason et al., 2011, Shin et al., 2005], giving rise to the property of the velocity at the later time-step as $\nabla_h\cdot\mathbf{u}^{n+1}=0$. Hence, to solve Equation 3.42, a new velocity field $\mathbf{u}^*$ is introduced where the effect of pressure is ignored, by splitting the equation into:

$$\frac{\mathbf{u}^*-\mathbf{u}^n}{\Delta t} = \frac{1}{\rho^{n+1}}(\mathbf{A}_h^n+\mathbf{F}_h^n) \tag{3.43}$$

and

$$\frac{\mathbf{u}^{n+1}-\mathbf{u}^{*}}{\Delta t}=-\frac{1}{\rho^{n+1}}\nabla_h p. \tag{3.44}$$

This velocity can be found using Equation 3.43:

$$\mathbf{u}^{*}=\mathbf{u}^{n}+\frac{\Delta t}{\rho^{n+1}}(\mathbf{A}_h^n+\mathbf{F}_h^n). \tag{3.45}$$

As for the pressure, it can be found by taking the divergence of Equation 3.44. Applying the divergence-free property of the $\mathbf{u}^{n+1}$, 3.44 becomes the elliptic Poissson equation:

$$\nabla_h\cdot\left(\frac{1}{\rho^{n+1}}\nabla_h p\right)=\frac{\nabla\cdot\mathbf{u}^{*}}{\Delta t}, \tag{3.46}$$

which is non-separable in parallel computing due to the density discontinuity present in two-phase flows ($\rho_o \neq \rho_a$). A parallel 3D V-cycle multigrid solver is used herein for this equation, which is a modified scheme based on the work by Kwak and Lee [2004]. More description of this framework can be found in Shin et al. [2017]. Since the pressure is found, the updated velocity can be obtained using Equation 3.44:

$$\mathbf{u}^{n+1}=\mathbf{u}^{*}-\frac{\Delta t}{\rho^{n+1}}\nabla_h p. \tag{3.47}$$

For a second-order method for the integration in time, from a programming point of view, two first-order steps could be implemented and then average $\mathbf{u}^n$ and $\mathbf{u}^{n+2}$ [Tryggvason et al., 2011]. This process is therefore equivalent to what is shown above.

3.1.4.2 Spatial discretization

Spatial discretization of the governing equations in this work is implemented using the well-known staggered mesh, Marker-and-Cell (MAC) method [Harlow et al., 1965]. In this method, the material properties are stored on a separate grid, as opposed to the so-called collocated grids where the variables are located on the same grid node. Specifically, the pressure, surfactant concentration, and vector valued distance function are located at the cell centers while the components of velocity are stored in the cell faces. These quantities are transferred between grids via linear interpolation if required, for example, velocity components needed at the cell centers are linearly interpolated from cell faces. Furthermore, the convective term on the left-hand side of 3.21 is approximated using a discretization scheme coupled with a second-order Essentially Non-Oscillatory (ENO) method [Shu and Oshers, 1989, Sussman et al., 1998], while the rest of spatial derivatives are approximated using standard second-order centered differences. The corresponding discrete expressions can be found in Shin and Juric [2002], Shin et al. [2005].

3.1.4.3 Communication between Lagrangian and Eulerian grids

As described previously, both Lagrangian and Eulerian grids are used in LCRM framework, indicating that the information transfer is required when solving variables (or material properties) stored on these separate grids. Herein, the immersed boundary method (IBM) developed by Peskin [1977, 2002] is applied to connect Eulerian and Lagrangian variables via a smoothed approximation of the Dirac delta function [Shin and Juric, 2002]. This function is used to distribute Lagrangian variables over several Eulerian grids near the interface, and similarly interpolate Eulerian variables from the fixed grid to the Lagrangian interface.

To briefly illustrate this, consider the integral of an interface source term, m, (similar to the last term in Equation 3.21) can be generally written as:

$$M = \int_S m\delta(\mathbf{x} - \mathbf{x}_S)\,\mathrm{d}s. \tag{3.48}$$

Take a 2D domain as an example, consider an interface discrete source term m_p stored at a Lagrangian grid point positioned at $\mathbf{x}_p = (x_p, y_p)$, while a discrete field variable R_{ij} is located at $\mathbf{x}_{ij} = (x_{ij}, y_{ij})$ on the Eulerian grid, where each cell has dimensions $(\Delta x, \Delta y)$. Accordingly, m_p can be distributed on the Eulerian grid, denoted as m_{ij}, by using:

$$m_{ij} = \sum_s m_p D_{ij}(\mathbf{x}_p)\Delta s, \tag{3.49}$$

where $D_{ij}(\mathbf{x}_p)$ is the IBM distribution function at the point p, and Δs represents the interface element length (or element area in 3D domains). Similarly, R_{ij} can be interpolated to the Lagrangian front as R_p via discrete summation written as:

$$R_p = \sum_{i,j} R_{ij} D_{ij}(\mathbf{x}_p)\Delta x \Delta y. \tag{3.50}$$

The distribution function $D_{ij}(\mathbf{x}_p)$ employed herein is adapted from the work done by Peskin and McQueen [1995], which is defined as:

$$D_{ij}(\mathbf{x}_p) = \frac{h(d_x)h(d_y)}{\Delta x \Delta y}, \tag{3.51}$$

where d_x, d_y represent the scaled distances between the interface and the grid line. These terms are explicitly defined as $d_x = \frac{x_p}{\Delta x} - x_{ij}$ and similarly for d_y. Furthermore, the function h is formulated as follows with d representing either d_x or d_y:

$$h(d) = \begin{cases} h_1(d) & |d| \le 1, \\ 1/2 - h_1(2 - |d|) & 1 < |d| < 2 \\ 0 & |d| \ge 2 \end{cases}$$

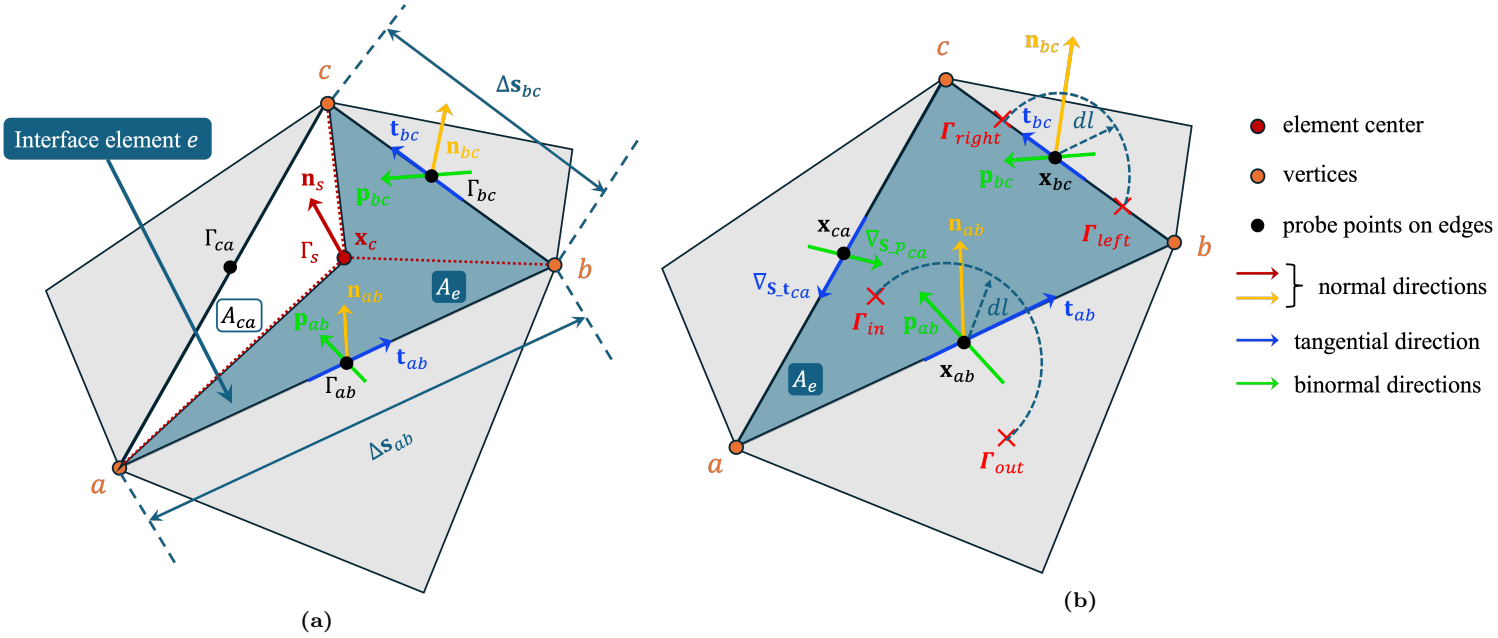


Figure 3.6: Schematic diagrams for an individual interface element with element area of A_e. The element is composed of three edge line ab, bc, and ca. (a) Geometrical information on the element: surfactant interface concentration Γ_s is stored at the element center $\mathbf{x}_c$, and Γ_{ab}, Γ_{bc}, and Γ_{ca} are the interpolated values at the mid point of the three edges, respectively; relevant vectors for this element are annotated, including the normal vector at the center of element, and vectors at the element edges including normal (yellow), tangent (blue), binormal (green). (b) Exemplified implementation of probing technique in the directions of $\mathbf{p}$ (edge ab) and $\mathbf{t}$ (edge bc).

where

$$h_1(d) = \frac{3 - 2|d| + \sqrt{1 + 4|d| - 4d^2}}{8}.$$

3.1.4.4 Surfactant interface concentration

For the solution with regard to the surfactant concentration at the interface (3.23), the CFD code follows the derivation of Muradoglu and Tryggvason [2014] except for the diffusion term $(D_s \nabla_S^2 \Gamma)$ to retain the LCRM's ease of parallelization. Accordingly, the integral of the transient and convective terms (left-hand side's terms) can be discretized using Leibniz formula:

$$\int_{A_e} \left[\frac{\partial \Gamma}{\partial t} + \nabla_S \cdot (\Gamma \mathbf{u_t}) \right] \mathrm{d}A_e \approx \frac{(\Gamma A_e)^{n+1} - (\Gamma A_e)^n}{\Delta t}, \tag{3.52}$$

where A_e represents the area of the triangular interface element as shown in Figure 3.6 and $n, n+1$ refer to the time-levels. In a similar manner, the right-hand side of Equation 3.23 can be rewritten into its discrete form:

$$\int_{A_e} \left(D_s \nabla_S^2 \Gamma + J_n \right) \mathrm{d}A_e = D_s \int \int_{A_e} \nabla_S^2 \Gamma \, \mathrm{d}A + (J_n A_e)^n. \tag{3.53}$$

Here, the first term on the right represents the surfactant diffusion along the interface, which is the sole obstacle when implementing time integration for surfactant conservation equation at the interface. From the formulation of Muradoglu and Tryggvason [2014], this term can be evaluated as a line integral along the edges of the element C, which has been depicted in

Figure 3.3:

$$D_s \int \int_{A_e} \nabla_S^2 \Gamma \, \mathrm{d}A_e = D_s \int_C \nabla_S \Gamma \cdot \mathbf{p} \, \mathrm{d}s. \tag{3.54}$$

In this equation, $\mathbf{p}$ refers to the binormal vector presented in Figure 3.6, which is orthogonal to both normal and tangential vectors at the element edges. This line integral can be computed as a discrete summation of the interface gradients ($\nabla_S \Gamma$) along the element edges, leading to:

$$D_s \int_C \nabla_S \Gamma \cdot \mathbf{p} \, \mathrm{d}s = D_s \sum_{k=1}^{3} (\nabla_S \Gamma)_k \cdot \mathbf{p}_k \Delta s_k \tag{3.55}$$

$$= D_s \left[(\nabla_S \Gamma)_{p_{ab}} \Delta s_{ab} + (\nabla_S \Gamma)_{p_{bc}} \Delta s_{bc} + (\nabla_S \Gamma)_{p_{ca}} \Delta s_{ca} \right], \tag{3.56}$$

where Δs_k refers to the length of edge k as exemplified in Figure 3.6*a*. In addition, it is shown that the interfacial surfactant concentration Γ_s is stored at the element center $\mathbf{x}_c$. With this information, the interpolated Γ_s at each edge can be obtained, which refer to Γ_{ab}, Γ_{bc}, and Γ_{ca} presented in the figure. Using these values, $(\nabla_S \Gamma)_k \cdot \mathbf{p}_k$, which denotes the interface gradient in the $\mathbf{p}$ direction, can be computed via a probing technique which was originally introduced by Udaykumar et al. [1999]. As showcased in Figure 3.6*b*, following the construction of the probe point $\mathbf{x}_{ab}$ at the interface element edge (using the contour level of distance function $\varphi = 0$), surfactant concentrations Γ_{in} and Γ_{out} are interpolated at the either side of the interface from $\mathbf{x}_{ab}$. The interface gradient can then be gained as:

$$\nabla_{S_p_{ab}} \Gamma = \frac{\Gamma_{out} - \Gamma_{in}}{2\mathrm{d}l}, \tag{3.57}$$

where $\mathrm{d}l$ is taken as the grid size herein. The corresponding gradients at edges bc and ca can be obtained using the same procedure and the resulting direction is exemplified at edge ca as shown in Figure 3.6*b*. From above, the updated surfactant concentration at the interface can be obtained via:

$$\Gamma^{n+1} = \Gamma^n \left(\frac{A_e^n}{A_e^{n+1}} \right) + \Delta t \left[\frac{\delta \Gamma_{D_e}^n}{A_e^{n+1}} + J_n^n \right], \tag{3.58}$$

where $\delta \Gamma_{D_e}^n$ is equivalent to the right hand side of Equation 3.55. Details of procedure for updating Γ is demostrated in Shin et al. [2018].

The derivation above shows the computation for interface gradient in the $\mathbf{p}$ direction. Moreover, for further computation regarding the interfaceial forces, interface gradient in the $\mathbf{t}$ direction is required, which can be obtained via the same procedure except for Γ_{left} and Γ_{right} are interpolated in this case on either side of the probe point along the element edge (refer to Figure 3.6*b*). Hence, the gradient can be formulated as:

$$\nabla_{S_t_{ab}} \Gamma = \frac{\Gamma_{right} - \Gamma_{left}}{2\mathrm{d}l}. \tag{3.59}$$

From above, each Lagrangian element stores the values of $\Gamma_{left}, \Gamma_{right}, \Gamma_{in}, \Gamma_{out}$ and Γ_s, which could be transferred to the Eulerian grid for the implementation of LCRM. This can be simply achieved through the IBM methodology described in the previous section, replacing the interface

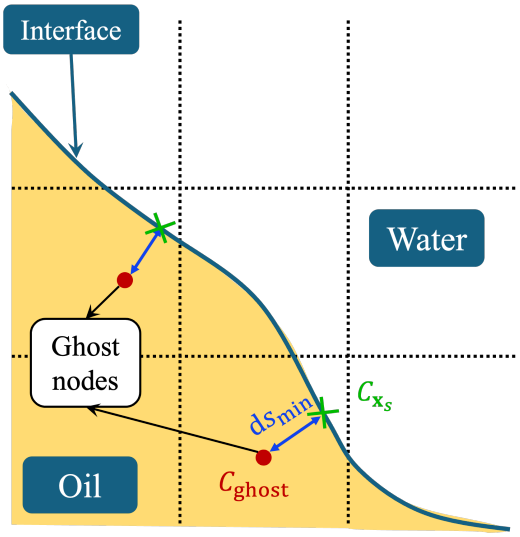


Figure 3.7: Schematic representation of the ghost points near the interface. The two red dots are the defined ghost nodes in the dispersed phase, storing the extrapolated values of bulk concentrations. Diagram is adapted from Shin and Choi [2016], Shin et al. [2018].

term m with Γ. The implementation of changing interface tension is referred to Section 3.1.4.6.

3.1.4.5 Sharp boundary condition for surfactant bulk concentration

The governing equation for surfactant bulk concentration is a straightforward convection-diffusion equation (2.8). The main challenge in solving this equation lies in addressing the source term at the interface, $\mathbf{n} \cdot \nabla C_{\text{sub}}$, which appears in Equation 2.13. Recall that C_{sub} represents the surfactant concentration in a region of bulk phase adjacent to the interface, this source term connects the surfactant concentrations in the bulk and at the interface via [Shin et al., 2018]:

$$\mathbf{n} \cdot \nabla C_{\text{sub}} = \frac{\partial C}{\partial \mathbf{n}}\Big|_{\text{sub}} = -\frac{J_{a/d}}{D_b}. \tag{3.60}$$

In conventional front tracking method, this interfacial source term is embedded in the governing equation using a Dirac distribution, which requires an iterative fitting to the prescribed boundary values at the interface. In contrast, current methodology applies a ghost-type method [Fedkiw et al., 1999, Sussman et al., 2007] modified by Shin and Choi [2016] to enforce the above condition for the surfactant bulk concentration. Key features of this method is briefly described here and more details can be found in the listed studies. As mentioned earlier, the surfactant in this study is exclusively soluble in the continuous (or aqueous) phase, and consequently, bulk concentration is only allowed in that phase. Accordingly, the ghost method defines "ghost nodes" in the dispersed phase which store the extrapolated concentration values (C_{ghost}) from the continuous phase (refer to Figure 3.7). The concentration gradients at the interface can then be approximated using first-order gradient formulation written as:

$$\frac{\partial C}{\partial \mathbf{n}}\Big|_{\text{sub}} = \frac{C_{\text{ghost}} - C_{\mathbf{x}_S}}{\mathrm{d}s_{\text{min}}}, \tag{3.61}$$

where $C_{\mathbf{x}_S}$ represents the surfactant concentration on the interface element, and $\mathrm{d}s_{\text{min}}$ is the minimum distance between the interface and the given ghost node, as shown in Figure 3.7.

The ghost nodes are found using the distance function [Shin et al., 2018] (see Section 3.1.3). With Equation 3.60 and 3.61, the concentration at the interface boundary C_{ghost} can then be computed using the updated surfactant concentration field obtained through the procedure described in the previous section.

3.1.4.6 Implementation of interface tension varying with Γ

From the derivation of the momentum equation (3.21), the interface tension force is divided into its normal and tangential components, denoted as $\mathbf{F}_n$ and $\mathbf{F}_s$, respectively:

$$\mathbf{F}_\sigma = \int_S (\sigma\kappa\mathbf{n} + \nabla_S\sigma)\,\mathrm{d}s = \int_S \sigma\kappa\mathbf{n}\,\mathrm{d}s + \int_S \nabla_S\sigma\,\mathrm{d}s = \mathbf{F}_n + \mathbf{F}_s.$$

According to Shin et al. [2005], $\mathbf{F}_n$ can be expressed by a hybrid of the Langrangian representation $\mathbf{F}_L$ and the Eulerian representation $\mathbf{F}_E$. In the classic front tracking approach, $\mathbf{F}_L$ is computed directly on the Lagrangian interface grid and then distributed onto the Eulerian grid using the IBM:

$$\mathbf{F}_L = \int_S \sigma\kappa_L\mathbf{n}\delta(\mathbf{x} - \mathbf{x}_S)\,\mathrm{d}s = \sigma\kappa_H\mathbf{G}, \tag{3.62}$$

where κ_L is twice the mean interface curvature obtained directed from the tracked interface, while κ_H refers to the Eulerian expression for the curvature [Shin et al., 2005]. Here, the term $\mathbf{G}$ is then defined and calculated using the IBM distribution function, which takes the form of Equation 3.48 and 3.49:

$$\mathbf{G} = \int_S \mathbf{n}\delta(\mathbf{x} - \mathbf{x}_S)\,\mathrm{d}s, \quad \text{and} \quad \mathbf{G}_{ij} = \sum_s \mathbf{n}_p D_{ij}(\mathbf{x}_p)\Delta s. \tag{3.63}$$

It can be easily observed that $\mathbf{G}$ can be computed by solving the Poisson equation (3.39) as $\mathbf{G} \equiv \nabla\mathcal{H}$. Furthermore, by applying the scalar product on both sides of Equation 3.62 with $\mathbf{G}$, the term $\sigma\kappa_H$ can be expressed on the Eulerian grid using the quantities that solely computed on the tracked interface:

$$\sigma\kappa_H = \frac{\mathbf{F}_L \cdot \mathbf{G}}{\mathbf{G} \cdot \mathbf{G}}. \tag{3.64}$$

which gives the final expression of $\mathbf{F}_n$ as:

$$\mathbf{F}_n = \frac{\mathbf{F}_L \cdot \mathbf{G}}{\mathbf{G} \cdot \mathbf{G}}\nabla\mathcal{H}. \tag{3.65}$$

Similarly, the tangential component $\mathbf{F}_s$ can be expressed in the form of $\delta-$function:

$$\mathbf{F}_s = \int_S \nabla_S\sigma\delta(\mathbf{x} - \mathbf{x}_S)\,\mathrm{d}s \tag{3.66}$$

Regarding the approximation of this component, it involves the interface gradient of the interfacial tension $\nabla_S\sigma$, which is intrinsically related to the surfactant concentration $\nabla_S\Gamma$ through the Langmuir equation of state (3.25). Hence, the evaluation of $\nabla_S\sigma$ is implemented following the same probing approach as illustrated in Figure 3.6*b*, along with the equations 3.57 and 3.59.

$\nabla_S \sigma$ can be further decomposed into components in the $\mathbf{p}$ and $\mathbf{t}$ directions:

$$\nabla_S \sigma = (\nabla_S \sigma)_p \mathbf{p} + (\nabla_S \sigma)_t \mathbf{t} \tag{3.67}$$

Thus, in the similar fashion of Equation 3.55, $\mathbf{F}_s$ can be obtained through this equation:

$$\mathbf{F}_s = \sum_{k=ab,bc,ca} \left[(\nabla)_{pk} \mathbf{p})_k + (\nabla)_{tk} \mathbf{t})_k \right] \delta(\mathbf{x} - \mathbf{x}_k) A_k, \tag{3.68}$$

where A_k denotes the one-third of the element area, which is bounded by two vertices and the element center, as depicted in Figure 3.6*b* exemplified by A_{ca}.

3.1.4.7 Implementation of fluid-solid interaction force

The last crucial element in solving the governing equations is to incorporate the complex geometry of the impeller and its rotation. This is achieved herein via the implementation of the so-called direct forcing method [Fadlun et al., 2000], embedding additional body force source term, the fluid-solid interaction force $\mathbf{F}_{\text{fsi}}$, in the momentum equation (3.21). This force is numerically defined using the latest step of the time integration of 3.21:

$$\rho \frac{\mathbf{u}^{n+1} - \mathbf{u}^n}{\Delta t} = \text{local}^n + \mathbf{F}^n_{\text{fsi}}, \tag{3.69}$$

where the term "local" stands for the right-hand side of Equation 3.21 consisting of the pressure gradient, viscous, gravitational and interface tension force terms. In the solid domain corresponding to the impeller, the rotational motion is enforced via $\mathbf{V}^{n+1}$:

$$\mathbf{u}^{n+1} = \mathbf{V}^{n+1} = 2\pi N \begin{pmatrix} y - y_0 \\ -(x - x_0) \\ 0 \end{pmatrix} \tag{3.70}$$

where $(x_0, y_0) = (4.25, 4.25)$ represents the position of the impeller axis. Hence, $\mathbf{F}^n_{\text{fsi}}$ can be calculated as:

$$\mathbf{F}^n_{\text{fsi}} = \rho \frac{\mathbf{V}^{n+1} - \mathbf{u}^n}{\Delta t} - \text{local}^n \tag{3.71}$$

Finally, the no-slip condition is imposed on the velocity and the interface at the edge of the impeller parts.

3.1.5 Validation

The CFD framework detailed above has been extensively validated against series of numerical simulations involving complex interfacial phenomena, including capillary breakup in a turbulent jet [Constante-Amores et al., 2021], the bursting of bubbles interfaces [Constante-Amores et al., 2021], and the coalescence of drops with interfaces [Constante-Amores et al., 2021]. Specially, exceptional agreement with diverse scaling arguments has been shown in these works. In addition, this code has been examined with experimental data and empirical correlation for

studies involving falling film [Batchvarov et al., 2020] and drop impacts [Constante-Amores et al., 2023]. Furthermore, the feasibility of the model has been proved through industrially relevant scenarios such as capillary tubes for microfluidic applications [Batchvarov et al., 2020] and industrial mixing processes [Kahouadji et al., 2020]. In the case where surfactant is present, a systematic validation against several analytical solutions regarding the surfactant module is provided in [Shin et al., 2018].

Although the aforementioned studies have demonstrated the capability of the CFD code reliably predicting fundamental interfacial phenomena, such as ligament stretching and retraction [Constante-Amores et al., 2020], and fragmentation through capillary instability [Constante-Amores et al., 2021], which are the core physical mechanisms investigated in Chapter 4 and 5, this section provides additional test to cover interfacial dynamics observed in more specific and applied configuration relevant to this thesis, namely agitated mixers. Section 3.1.5.1 provides a validation against drop breakup in the absence of surfatcant, along with a mesh sensitivity test, whereas Section 3.1.5.2 focuses on a system with surfactant present.

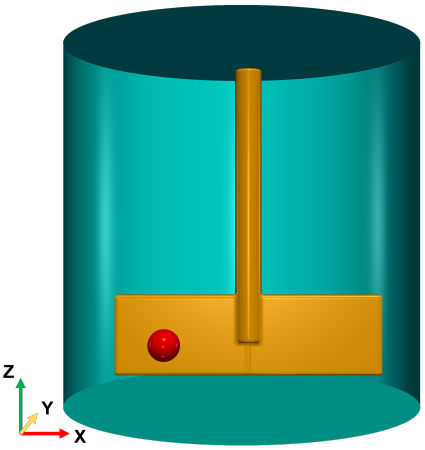
3.1.5.1 Clean single drop breakage in stirred vessel

All the predictions via the described simulation configuration have been validated against the experimental work of Hančil and Rod [1988], who carried out a single drop breakup experiment in a stirred vessel. To verify the reliability of the predictions via above-described simulation setup, we duplicated the experimental setup of the work (see Figure 3.8a, b) as my simulation configuration and predicted the breakup of a single drop of volume 39 mm^3 inside such a mixer ($Re = 5110$). The goal was to confirm that the simulation can correctly predict the number of daughter drops which was reported as 6 in the experiment. Since the authors provided no information for the initial position of the drop, its clearance from vessel bottom and its radial position relative to the vessel center were fixed as 10mm and 20mm, respectively. Meanwhile, different initial positions were tested by changing the azimuthal displacement (θ) of the impeller before it touches the drop (via clockwise rotation). Herein, the initial position of $\theta = 120^{\circ}$and the corresponding predicted daughter drops n_{dd} are presented in Figure 3.8c, d. As shown the prediction of n_{dd} is 5; this is reasonably close to the value reported by Hančil and Rod particularly considering the uncertainty related to the initial condition highlighted above.

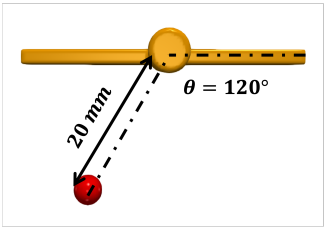
Subsequently, a mesh stability test was implemented by repeating the prediction with low, medium, and high computational resolutions, which give the values of smallest mesh size (in unit of volume [cm^3]) from coarse to fine as $6.71 \times 10^{-5}, 1.99 \times 10^{-5}, 2.48 \times 10^{-6}$, respectively. As shown in the Figure 3.9, the prediction of n_{dd} for three tested resolutions stay unchanged. Additionally, the drop sizes for the produced drops from the three resolutions are recorded in Table 3.1. It can be noted that the drop sizes converge well, particularly the fact that the deviation from reference case (of highest computational resolution) decreases with higher resolutions. Through the validation and the mesh stability test, it is verified that the mesh size used in Chapter 4 for the emulsion process (3.75×10^{-5}cm^3, comparable to 1.99×10^{-5})

Vessel Geometry [cm]	
vessel diameter, T	5
vessel height, H	5
Impeller Geometry [cm]	
clearance, C	0.8
impeller diameter, D	4
shaft radius, r_s	0.2
blade length, l	2
blade height, h	1.2
blade thickness, w	0.2
Computational Domain	
domain size	5.2^3 [cm^3]
total grid number	192^3

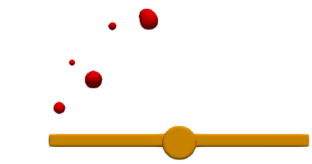
(a)



(b)



(c)



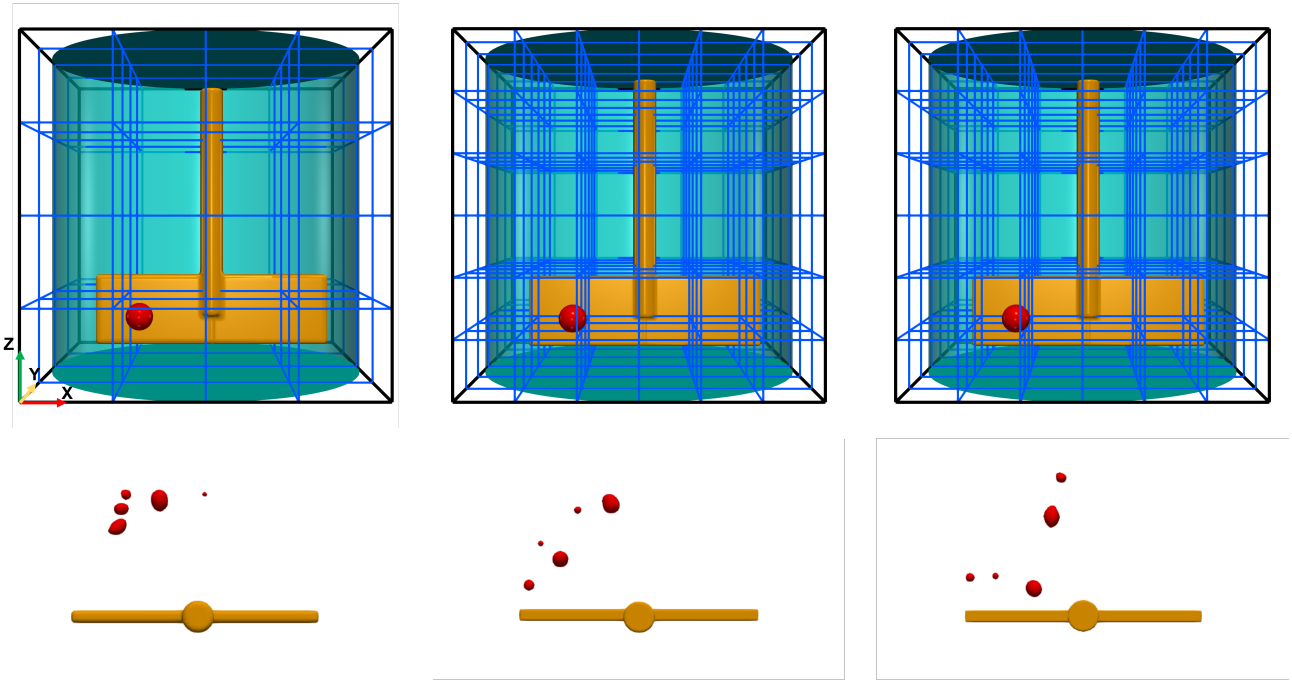
(d)

Figure 3.8: (a) Details of mixer geometry and (b) schematic configuration for the single-drop breakup validation against experimental data [Hančil and Rod, 1988]; (c) initial drop position and (d) the predicted emergent number of daughter drops n_{dd} following breakup.

is sufficient to provide reliable prediction of real liquid-liquid mixing, especially in this case where the main concern is the macroscopic interfacial dynamic in such system. Nevertheless, the mechanisms regarding drop coalescence will not be discussed in this thesis given that finer resolution is required to uncover the coalescence process which involves more sophisticated mechanisms such as film rupture and drainage. In this respect, simulations presented herein are focused on illustrating drop breakup mechanisms, and the statistic analysis related to drop size distribution along the mixing are mainly affected by breakup process. In other words, the simulations are terminated at a statistical steady-state which occurs instantly after the dynamics developing in the vessel stagnates, reducing to sporadic breakup and subsequent coalescence chains. More details will be seen in the following result chapters.

	Coarse resolution		**Current resolution**		**Fine resolution**
	Volume	*Abs. Dev.*	Volume	*Abs. Dev.*	Volume (*Ref.*)
Drop 1	2.386×10^{-10}	4.33%	7.686×10^{-10}	1.17%	5.771×10^{-10}
Drop 2	1.949×10^{-9}	1.13%	1.162×10^{-9}	3.74%	2.438×10^{-9}
Drop 3	5.430×10^{-9}	2.16%	1.999×10^{-9}	2.98%	3.570×10^{-9}
Drop 4	1.022×10^{-8}	2.24%	1.191×10^{-8}	1.39%	1.529×10^{-8}
Drop 5	1.344×10^{-8}	1.02%	1.982×10^{-8}	1.15%	1.613×10^{-8}
Average *Dev.*		2.17%		2.09%	-

Table 3.1: Size (in volume [m^3]) of daughter drops in the tested computational resolutions from smallest (Drop 1) to largest (Drop 5). *Abs. Dev.* is the absolute deviation of drop size calculated using the log-scale volumes based on the fine resolution as reference (*Ref.*).



Coarse resolution
subdomains: 4^3
grids per subdomain: 32^3
total grid number: 128^3
(a)

Current resolution
subdomains: 6^3
grids per subdomain: 32^3
total grid number: 192^3
(b)

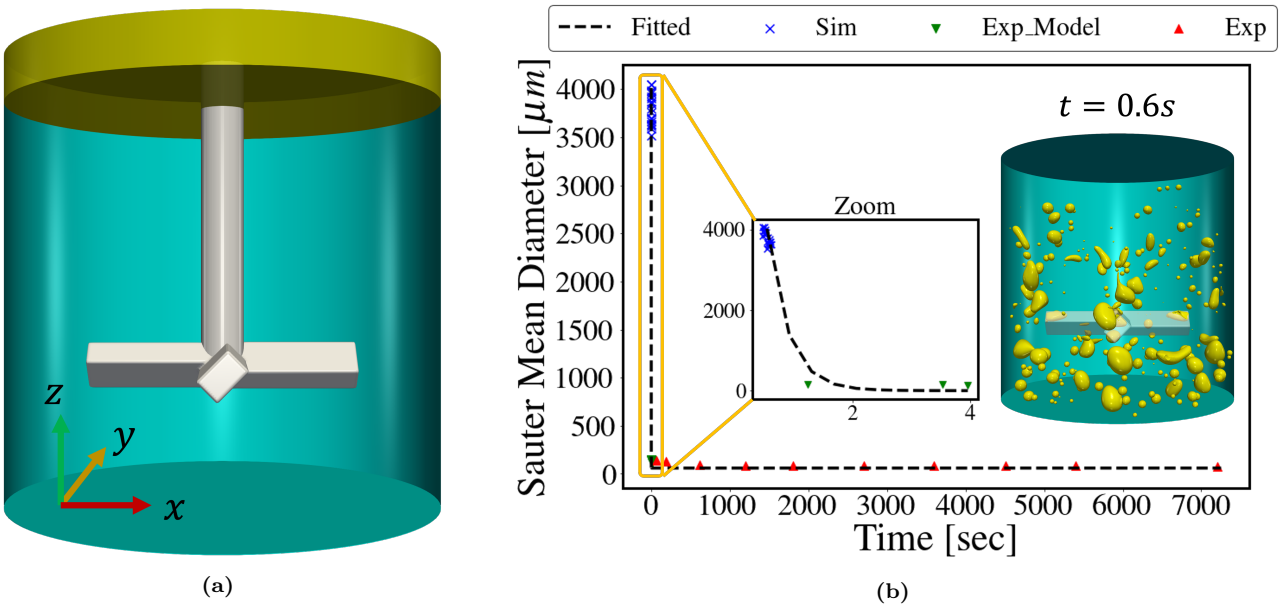
Fine resolution
subdomains: 6^3
grids per subdomain: 64^3
total grid number: 384^3
(c)

Figure 3.9: Mesh stability test with three resolutions and the corresponding predicted n_{dd}.

3.1.5.2 Drop size in surfactant-laden stirred beaker

Simulations for surfactant-laden system have been validated against a recent experimental investigation on drop size in oil-water dispersion done by Liu et al. [2017]. In their work, the temporal evolution of the drop size in terms of Sauter mean diameter (d_{32}) is reported for a mixing time ranging from $60s$ to $7000s$. However, from the perspective of high-fidelity simulations, it is extremely time-consuming to simulate identical mixing system for such long period of time. Fortunately, the intermediate d_{32} change from the initial instance to $60s$ is fitted to a prediction model using the experimental data. Hence, the goal of this validation is to verify that the simulation presented in Chapter 5 can capture d_{32} as described by the prediction model and the experimental data.

Similar to what have been done for the clean case, we replicated the experimental setup as my simulation configuration (Figure 3.10a). To achieve the above-mentioned goal, we simulated the mixing process up to $t = 0.6s$ and tracked the d_{32} evolution. The corresponding state of the system is shown in the inset of Figure 3.10b. Subsequently, we performed a curve fitting using the simulation data and the experimental data, which is presented in Figure 3.10b. As seen in the zoom panel, the prediction data point coloured in green (reproduced from the prediction model of Liu et al. [2017]) lie close to the fitted curve, which can be interpreted as the latter being capable of correctly predicting the rapid variation in d_{32} at early to intermediate times expressed by the prediction model. Taken together, these facts serve to illustrate that the



(a) (b)

Figure 3.10: (*a*) The simulation configuration reproduced from the experimental work of [Liu et al., 2017]; (*b*) the curve-fitting (black dotted line) using our simulation data (coloured in blue) and the experimental data (coloured in red) from [Liu et al., 2017]. The green triangles in the zoom panel represents the sample data reproduced from the prediction model, which is represented in Fig.10 in [Liu et al., 2017], and the inset image shows the state of simulated system at $t = 0.6s$.

numerical model used in this thesis can provide an accurate representation of the experimental data, albeit for the computationally-accessible early times. This, therefore, indicates that the results of the numerical simulations presented herein are physically reliable.

3.2 ML applications

One additional project has been performed in this thesis to explore the applicability of AI-related techniques in the context of multiphase mixing with CFD simulation data, which is presented in:

- **Chapter 6**, wherein an inexpensive time-series model has been developed using RNNs for liquid dispersion performance forecast based on its initial observation

Here, a brief theoretical background regarding the machine learning (ML)-based techniques utilised in the above-listed chapter is provided in Section 3.2.1. Following this, workflow developed is detailed in 3.2.2.

3.2.1 RNNs: LSTM and GRU

RNNs exhibit structure of loops which allow the information from one time-step to be passed to the next. As displayed in Figure 3.11a, when an RNN is trained to predict a dynamical quantity in the future from the past, the network incorporates the information from the input observations $\mathbf{x}$ into the hidden state $\mathbf{h}$, which is passed forward through time. The diagram illustrates a dynamic loop where the current state is fed back into the network influencing its future state. The presence of black square indicates that such an interaction occurs with a

delay of one time-step. Once the entire historical sequence, $\mathbf{x}_t$, is scanned, the RNN learns a summary, $\mathbf{h}_t$, of the relevant features in the past up to time t. Following this, an architecture layer, known as *output layer*, is added to read information out of the $\mathbf{h}_t$ to make predictions.

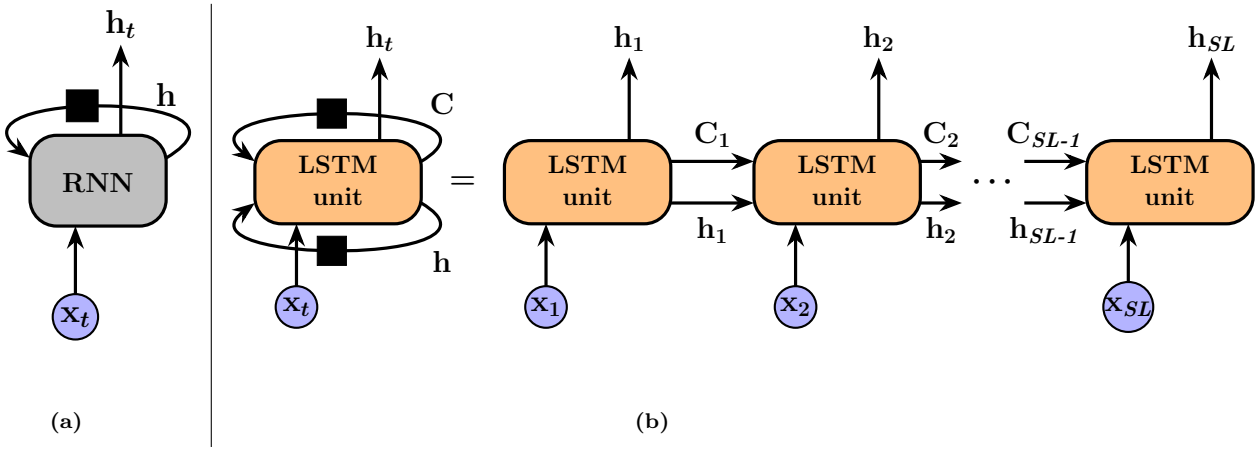


Figure 3.11: (*a*) Circuit diagram of a RNN with no output layers; (*b*) circuit diagram (left) and its unrolled version (right) until a final time-step labelled as sequence length (*SL*) of a LSTM network. This figure is reproduced from Liang et al. [2024].

A traditional RNN has only one hidden state, $\mathbf{h}_t$, which is sensitive to short-term inputs. In contrast, LSTM networks harness a cell state $\mathbf{C}_t$ to store the long-term information, as presented in Figure 3.11b. As with RNNs, the information flows through time in LSTM networks, but both short-term and long-term memory are carefully carried via hidden state and cell state, respectively. Several variants of the LSTM unit have been developed [Gers et al., 2000, Yu et al., 2019] since the LSTM unit was first proposed [Hochreiter and Schmidhuber, 1997]. The *standard* LSTM [Gers et al., 2000] is used in Chapter 6 as it has been verified to outperform other variants [Greff et al., 2017] and has been used extensively over a broad range of applications [Cheng et al., 2022, 2023].

The core advantage of LSTM is its capability to control information deletion from or addition to the cell state. As depicted in Figure 3.12a, the cell state runs through the LSTM unit at the top of the diagram with some minor interactions, which implies that the information stored in the cell state could propagate with slight or no changes. These interactions are carefully regulated by different gates [Hochreiter and Schmidhuber, 1997]. The role of the first one, the *Forget Gate*, is to decide how much information from $\mathbf{C}_{t-1}$ should be discarded. This decision is made by a Sigmoidal activation function $\sigma(x) = 1/(1+e^{-x})$ looking at the previous hidden state, $\mathbf{h}_{t-1}$, and the current input, $\mathbf{x}_t$:

$$f_t = \sigma(\mathbf{W}_f \mathbf{h}_{t-1} + \mathbf{W}_f \mathbf{x}_t + b_f). \tag{3.72}$$

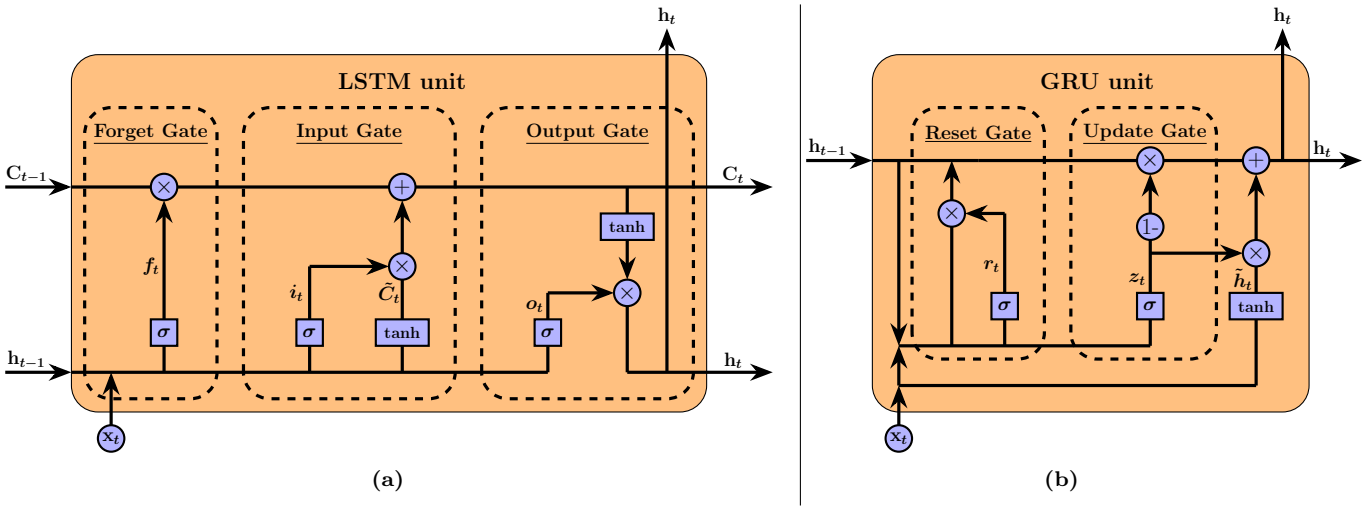


Figure 3.12: Diagram of different gates in (a) *standard* LSTM unit and (b) GRU unit. This figure is reproduced from Liang et al. [2024].

The subsequent *Input Gate* determines the new information to be memorised in $\mathbf{C}_t$:

$$\begin{aligned} i_t &= \sigma(\mathbf{W}_i \mathbf{h}_{t-1} + \mathbf{W}_i \mathbf{x}_t + b_i), \\ \tilde{C}_t &= \tanh(\mathbf{W}_C \mathbf{h}_{t-1} + \mathbf{W}_C \mathbf{x}_t + b_C). \end{aligned} \tag{3.73}$$

Herein, the candidate cell state, $\tilde{C}_t$, is introduced to describe the current input. Later, the cell state is updated by:

$$\mathbf{C}_t = f_t \odot \mathbf{C}_{t-1} + i_t \odot \tilde{C}_t, \tag{3.74}$$

where $\odot$ denotes the Hadamard product, i.e., element-wise multiplication ($A \odot B$ gives a matrix of the same dimension with A and B, where elements are given by $(A \odot B)_{ij} = (A)_{ij}(B)_{ij}$) of vectors and matrices. Lastly, the *Output Gate* is applied to settle the final output of the LSTM cell:

$$\begin{aligned} o_t &= \sigma(\mathbf{W}_o \mathbf{h}_{t-1} + \mathbf{W}_o \mathbf{x}_t + b_o), \\ \mathbf{h}_t &= o_t \odot \tanh(\mathbf{C}_t), \end{aligned} \tag{3.75}$$

which contains the $\mathbf{h}_t$, a cache of the recent information from $\mathbf{h}_{t-1}$, and long-term aspects from $\mathbf{C}_t$. In the equations above, $\mathbf{W}$ and b are trainable parameters of LSTM unit, which represent the weight vectors and the offset term for different gates, respectively. These equations are computed for each time-step and hence with a subscript t denoting the time-step. As described above, LSTM is capable of learning aspects in long-time sequences and thus has been used in modelling dynamical systems [Kim et al., 2019, Selvaggio et al., 2022, Zhong et al., 2023]. A detailed architecture of the model employed in this work will be presented in the pursuing Section 3.2.2.

GRU is proposed more recently by Cho et al. [2014], which reduces the number of manipulating gates to two. This type of recurrent unit exhibits comparable performance to the LSTM. As presented in Figure 3.12b, the two gates consist of a *Reset Gate*, r_t, and an *Update Gate*, z_t,

which could be written in the form similar to those in the LSTM unit:

$$r_t = \sigma(\mathbf{W}_r \mathbf{h}_{t-1} + \mathbf{W}_r \mathbf{x}_t + b_r),$$
$$z_t = \sigma(\mathbf{W}_z \mathbf{h}_{t-1} + \mathbf{W}_z \mathbf{x}_t + b_z). \tag{3.76}$$

In addition, GRU-RNN has only one hidden state as the traditional RNN presented as:

$$\tilde{h}_t = \tanh(\mathbf{W}_h (r_t \odot \mathbf{h}_{t-1}) + \mathbf{W}_h \mathbf{x}_t + b_h),$$
$$\mathbf{h}_t = (1 - z_t) \odot \mathbf{h}_{t-1} + z_t \odot \tilde{h}_t. \tag{3.77}$$

With these equations, GRU saves the one gate and one internal memory state and thus the associated parameters to be computed. As a result, its training time is expected to be shorter than that for LSTM. In Chapter 6 the performance of both architectures are compared briefly, in addition to the computation time and memory occupation during the training.

3.2.2 Procedure for time-series prediction

The computational framework employed in Chapter 6 follows a three-stage workflow consisting data acquisition (Section 3.2.2.1), data reconditioning (Section 3.2.2.2), and model training, deployment and explainability (Section 3.2.2.3), as illustrated in Figure 3.13 and detailed throughout this section. Essentially, a multivariate RNN is developed capable of predicting the temporal evolution of various dispersion performance metrics across multiple time-steps, without requiring detailed knowledge of the mixing process itself.

3.2.2.1 Data acquisition

Problem statement: CFD simulation of mixing systems This work utilises high-fidelity CFD data from the previous chapters, obtained through the simulations of the widely employed stirred mixer in the industry handling two-phase liquid-liquid flows. The extracted data sets comprise multidimensional time-series data containing three crucial metrics for evaluating dispersion performance: interfacial area growth (IA), drop count (ND), and DSD. The selection of these parameters leverages the explicit and robust interface-tracking scheme, LCRM, integrated into the CFD code used (see Section 3.1.3.3).

A comprehensive set of 14 simulations was considered, exploring various rotational speeds (N) and surfactant profiles. These 14 cases are divided between clean (varying N) and surfactant-laden systems. The specific parameters, combinations and value ranges explored for each set of cases are detailed in Table 3.2. The split between training, validation, and test cases was set as (9, 2, 3) achieving a rough 75-25% split between training and testing sets. The case selection for each set was done manually to guarantee a sufficiently diverse split to capture all features considered (i.e., surfactant activity and operational conditions). For instance, all three data sets contain cases with either surfactant activity or different impeller rotating speed (as seen in the legends for Figure 6.1 and 6.2 presented in Chapter 6). In addition, validation and test

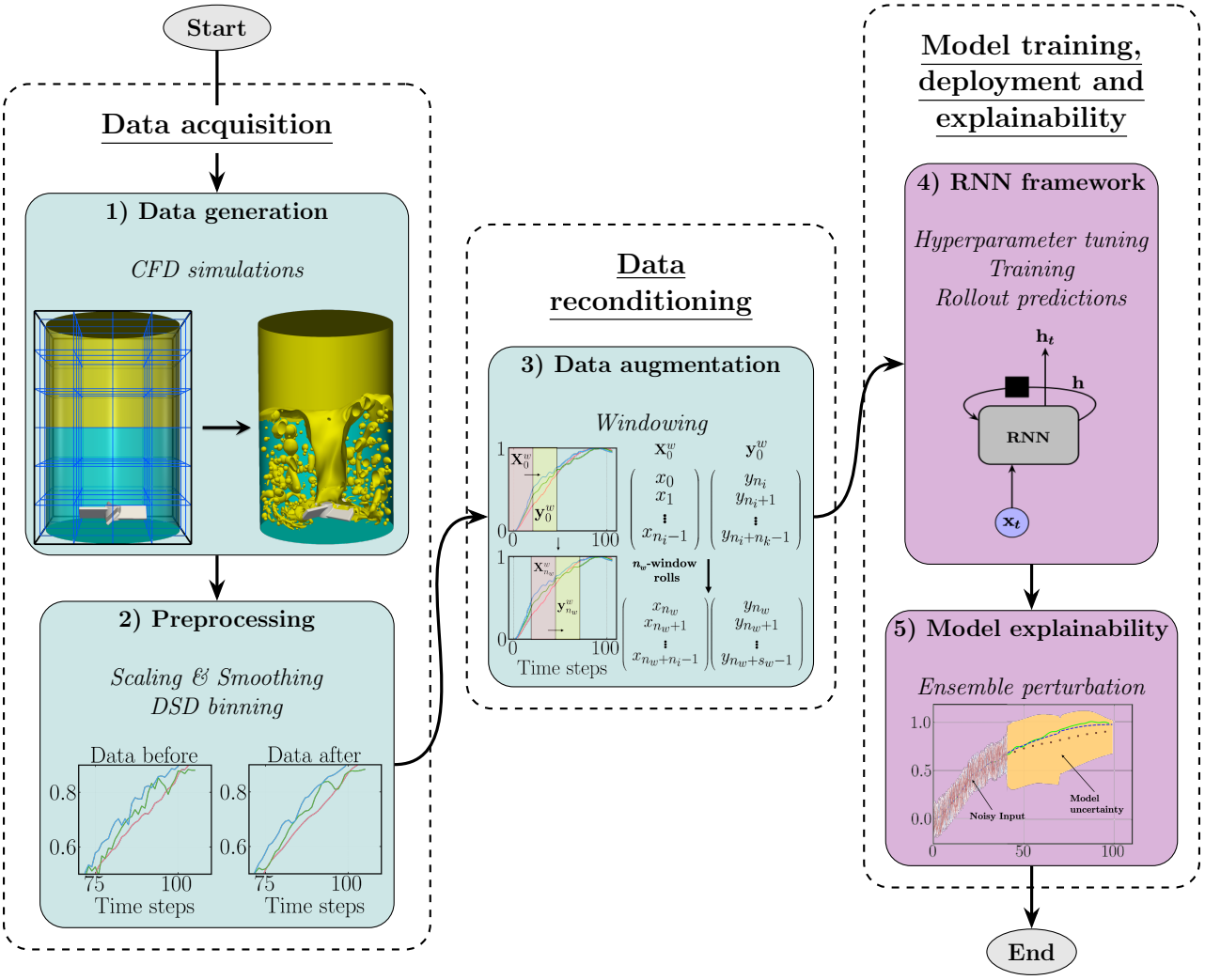


Figure 3.13: Flowchart that illustrates the architecture of the overall framework designed for training and deploying a multivariate multi-step RNN model with two-phase mixing performance data from high-fidelity CFD simulations. Colour-coded blocks denote general data pre-processing (teal) and model operations and exploration (violet).

cases attempt to cover a broad spectrum of features by including both high- and low-solubility surfactants, as well as clean cases with different impeller speeds. Specifics on the problem formulation, numerical consideration and validation of each system have been detailed in the previous Section 3.1.

Data pre-processing: Scaling, smoothing and DSD binning The initial set of features considered in this study consists of two scalar quantities, namely, IA and ND, and a variable-sized list of scalars (i.e., drop volumes) representing the DSD. To ensure dimensional consistency in the first two features across all cases, a post-sequence truncation is applied up to a final time-step τ_f (see table illustration in Figure 3.14), which corresponds to the length of the shortest sequence within the pool of cases. However, the length of the DSD feature remains dependent on the number of drops at each time-step t (ND_t), which is inherently linked to the governing physics of each case. This disparity results in a three-feature input sequence with a case-specific, uneven feature size of (1, 1, ND_t) for each time-step t.

Table 3.2: Simulation cases considered in this study, categorised into two groups according to the focus of each study: varying surfactant properties and modification of impeller speeds.

Case	Parameters and value ranges	# Cases
Surfactant profiles	$Bi = [0.001, 1]$	5
	$\beta_s = [0.5, 0.9]$	3
Operational configuration	$N(\text{Hz}) = [5, 10]$	6

Managing input sequences with varying feature lengths poses a difficulty for the network architectures implemented here, as RNN, especially standard LSTM networks are designed to have a predetermined fixed structure (i.e., consistent parameter size) [Staudemeyer and Morris, 2019], hence necessicating fixed-sized input sequences with identical feature lengths [Gers et al., 2002, Dwarampudi and Reddy, 2019]. This requirement of uniform size aims to prevent potential concerns such as information loss and limitations on model's capability to capture meaningful long-term dependencies. Previous works have employed methods to address this issue, such as padding, truncation, or "attention" mechanisms. The former two are frequently used in text recognition [Khotijah et al., 2020] and image processing [Dwarampudi and Reddy, 2019]. In these methods, the length of the longest (padding) or shortest (truncation) sequence is considered as the reference, and each sequence is either padded with zeros or shortened accordingly by removing data. Despite the advantages offered by longer padded sequences (as demonstrated by Khotijah et al. who consistently achieved higher model accuracy with longer sequences) and the easiness of truncating data sets, alternative methods have been proposed, for example, nearest neighbour interpolation, arguing that padding could be computationally demanding and naive truncation methods can lead to critical information loss [Wang et al., 2020]. More sophisticated methods such as attention layers [Chen and Ge, 2019] have presented remarkable potential in adequately filtering relevant input subsets. Nonetheless, they have been seen to fail when handling long-time-step predictions [Xiao et al., 2021].

From above, we tailored an approach specific to the current context to handle the fluctuating DSD feature size without compromising the integrity of the data sets or substantially increasing the model's complexity and resource demands. The proposed method, depicted in Figure 3.14, consists of transforming drop volume data into discrete drop counts for different size ranges. These counts can be then partitioned into a fixed number of M bins ($[B_0, B_{M-1}]$), each representing individual features which track the quantity of drops entering or leaving a particular size range over time. These features are subsequently scaled to a range of [0,1] through a normalised probability density estimation procedure, using the count of each bin as density estimate. This process is showcased in Equation 3.78 and 3.79 for a bin $B_l \in [B_0, B_{M-1}]$ at a time t,

$$\hat{p}_{l,t} = \hat{p}(C_{l,t}) = \frac{C_{l,t}}{ND_t \times w_l}, \tag{3.78}$$

$$\hat{n}_{l,t} = \hat{n}(C_{l,t}) = \frac{\hat{p}_l(C_{l,t})}{\sum_{j=0}^{M-1} \hat{p}_l(C_{j,t})}, \tag{3.79}$$

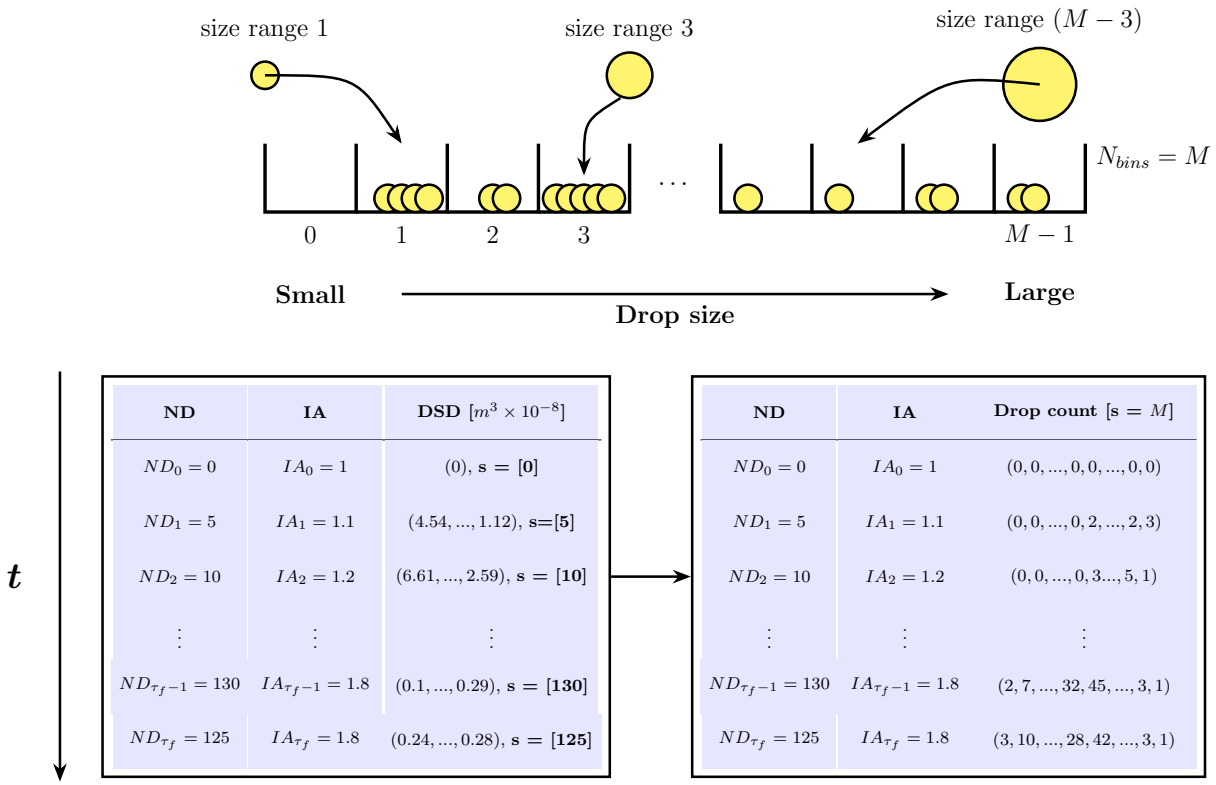


Figure 3.14: Schematic detailing DSD binning transformation. Top diagram showcases the drop size sorting and counting process in each size range, while the bottom tables show the transition from variable-sized volume lists (s = ND_t) to discrete drop counts in a fixed number of bins (s = M). This figure is reproduced from Liang et al. [2024]

where $\hat{p}_{l,t}$ and $\hat{n}_{l,t}$ denote the probability and normalised density estimators, respectively, for a drop count value $C_{l,t}$ corresponding to B_l at time t. ND_t refers to total drop count at time t, and w_l stands for the width of B_l. This approach introduces M additional features to the RNN, thus increasing the computational resources required for training. However, the resolution of the DSD (M) can be modified based on the systems under investigation, serving as a parameter for fine-tuning that balances accuracy and computational cost. In this work, M was initially set to 20, aiming to provide sufficient resolution for the DSD data based on statistical analyses conducted in Chapter 5. To eliminate outliers and uninformative features (i.e., bins predominately remaining as 0 across the time frame), M was ultimately cut to 10 bins ($B_0 - B_9$). This involved proportionally removing the boundary bins at each end of the size range, yielding a total of 12 features for the RNN to handle.

Finally, the ND and IA features were scaled and smoothed individually to mitigate potential biases arising from their significantly different scales ($\sim O(10^2)$ vs. $\sim O(1)$) and the sharply fluctuating trend observed for the ND data. The scaling procedure was applied separately to each feature on a per-case basis, using a linear sklearn MinMaxScaler method, which confines values to a range of [0,1]. Subsequently, three smoothing schemes were tested, namely, moving average, Savitzky-Golay filter and Locally Weighted Scatterplot Smoothing, or "Lowess". Following an initial visual examination, the Lowess method with a fraction of $\delta = 0.06$ yielded the best behaviour for the data. This selection was based on the filter's ability to effectively reduce noise in the ND feature while preserving other critical characteristics of ND and IA, for

example, inflection points. This method conducts a weighted linear regression at each point using a cubic weight function $W(x) = (1 - |x|)^3$, based on the nearest $N \times \delta$ data points. The normalised density estimation from the binned DSD data were not subjected to smoothing due to their extremely noisy behaviour (see Figure 6.3 in Chapter 6). The methods explored herein were found to be inadequate in retaining the most relevant temporal trends, particularly for the boundary bins (i.e., the largest and smallest sizes).

3.2.2.2 Data reconditioning: Augmentation through windowing

Data augmentation involves generating synthetic data by incorporating existing knowledge of invariant properties from the original data against specific transformations. This process lowers the risk of model over-fitting and enhances its accuracy and generalisation capabilities by providing a diverse yet realistic dataset [Rashid and Louis, 2019]. While data augmentation has been extensively explored for classification models in the domain of computer vision (e.g., flipping, rotating, scaling images, adding Gaussian noise/distortion), it has been less explored in time-series scenarios due to their vulnerability to transformation procedures [Rashid and Louis, 2019, Oh et al., 2020]. The augmentation methods used for image data are not well generalised with time-series data, as some of their intrinsic properties, such as temporal dependency, are not fully utilised by such methods. Hence, there is no guarantee that the meaning of the raw data will remain unchanged [Oh et al., 2020, Wen et al., 2020].

Though applying a frequency domain transformation to time-series data may enable the use of certain methods, additional complications arise when dealing with complex or inherently intertwined multivariate time-series data [Wen et al., 2020], which is the case for the features studied in this part. In such situations, it is suggested to develop a customised augmentation methodology that conserves the original data semantics [Oh et al., 2020]. Considering the above, and given the limited number of simulation runs available for model training, we devised a basic time domain sequence-to-sequence (S2S) rolling window augmentation scheme. This scheme aims to expand the available training data while preserving their original characteristics. In the following, the features of the data and the training procedure without augmentation is examined.

Let $\mathbf{X}$ be the original time-series array of a case with dimensions $D = (\tau_f + 1, M + 2)$, where $\tau_f + 1$ and $M + 2$ correspond to the total number of time-steps and features, respectively. This time-series array can be represented as:

$$\mathbf{X} = \begin{bmatrix} x_0 \\ x_1 \\ \vdots \\ x_{\tau_f} \end{bmatrix} = \begin{bmatrix} \mathrm{ND}_0 & \mathrm{IA}_0 & \hat{n}_{0,_0} & \cdots & \hat{n}_{M-1,_0} \\ \mathrm{ND}_1 & \mathrm{IA}_1 & \hat{n}_{0,_1} & \cdots & \hat{n}_{M-1,_1} \\ \vdots & \vdots & \vdots & & \vdots \\ \mathrm{ND}_{\tau_f} & \mathrm{IA}_{\tau_f} & \hat{n}_{0,_{\tau_f}} & \cdots & \hat{n}_{M-1,_{\tau_f}} \end{bmatrix}, \tag{3.80}$$

where $x_t \in \mathbb{R}^{M+2}$. The RNN training requires the original time series, $\mathbf{X}$, to be divided into

input (denoted as $\mathbf{x}$) and target (denoted as $\mathbf{y}$) arrays. The latter serve as the ground truth for the model to evaluate its predictions. Accordingly, n_i is defined as the number of input steps to be fed into the RNN and n_k as the target steps to predict into the future. Assuming $\tau_f = n_i + n_k - 1$, we then define subsets $\mathbf{x}^{(n_i)}$, $\mathbf{y}^{(n_k)} \in \mathbf{X}$, which refer to the input and target sequences from the original time-series, with dimensions $D_{\mathbf{x}} = (n_i, M+2)$ and $D_{\mathbf{y}} = (n_k, M+2)$, respectively, as given by Equation 3.81.

$$\mathbf{x}^{(n_i)} = \begin{bmatrix} x_0 \\ x_1 \\ \vdots \\ x_{n_i-1} \end{bmatrix}, \quad \mathbf{y}^{(n_k)} = \begin{bmatrix} x_{n_i} \\ x_{n_i+1} \\ \vdots \\ x_{n_i+n_k-1} \end{bmatrix}. \tag{3.81}$$

This method would lead to an insufficient training data sets (1 set per case). Therefore, the case-wise windowing is implemented here to augment the number of input-target sequence pairs $\{\mathbf{x}^{(n_i)}, \mathbf{y}^{(n_k)}\}$ from a single data set. This process is explained below and presented schematically in Figure 3.15:

1. **Window creation:** This step is to split the original data set, $\mathbf{X}$, into a set of $n_w + 1$ input and target sequences, denoted as $\left\{\mathbf{X}_j^w, \mathbf{y}_j^w\right\}_{j=0}^{n_w}$, with arbitrarily reduced dimensions $D_{\mathbf{X}^w}$ and $D_{\mathbf{y}^w}$. These denotations follow the same definitions introduced earlier for n_i and n_k, but considering $n_i + n_k << \tau_f$. The input/target pair is referred to as "window", and its size along the temporal axis is defined as $s_w = n_i + n_k$. The procedure starts by building the first window, Window 0, from t_0 to t_{s_w-1}, as seen in Figure 3.15. This can be expressed as:

$$\mathbf{X}_0^w = \mathbf{X}[0 : n_i - 1, :], \quad \mathbf{y}_0^w = \mathbf{X}[n_i : s_w - 1, :].$$

2. **Window rolling:** Window 0 is then rolled forward to generate Window 1:

$$\mathbf{X}_1^w = \mathbf{X}[1 : n_i, :], \quad \mathbf{y}_1^w = \mathbf{X}[n_i + 1 : s_w, :].$$

   This rolling operation follows a stride s defined by the user, which in this study was set to $s = 1$ (see Figure 3.15). In general, the window for the next iteration $j + 1$ with $s = 1$ is:

$$\mathbf{X}_{j+1}^w = \mathbf{X}[j + 1 : j + n_i, :], \quad \mathbf{y}_{j+1}^w = \mathbf{X}[j + n_i + 1 : j + s_w, :].$$

3. **Data stacking:** The rolling procedure in step 2 is repeated n_w times, where n_w is determined by the expression $n_w = \tau_f + 1 - s_w$, taking $s = 1$. After each roll, the generated input/target sequences $\{\mathbf{X}_j^w, \mathbf{y}_j^w\}$ in each window are stacked separately into

new tensors $\mathbf{W_X}$, $\mathbf{W_y}$, respectively, as shown in Equation 3.82:

$$\mathbf{W_X} = \{\mathbf{X}_0^w, \cdots, \mathbf{X}_j^w, \cdots, \mathbf{X}_{n_w}^w\}^T = \begin{bmatrix} x_0 & x_1 & \cdots & x_{n_i-1} \\ x_1 & x_2 & \cdots & x_{n_i} \\ \vdots & \vdots & \cdots & \vdots \\ x_{\tau_f+1-s_w} & x_{\tau_f+2-s_w} & \cdots & x_{\tau_f-n_k} \end{bmatrix},$$
$$\mathbf{W_y} = \{\mathbf{y}_0^w, \cdots, \mathbf{y}_j^w, \cdots, \mathbf{y}_{n_w}^w\}^T = \begin{bmatrix} x_{n_i} & x_{n_i+1} & \cdots & x_{n_i+n_k-1} \\ x_{n_i+1} & x_{n_i+2} & \cdots & x_{n_i+n_k} \\ \vdots & \vdots & \cdots & \vdots \\ x_{\tau_f-n_k+1} & x_{\tau_f-n_k+2} & \cdots & x_{\tau_f} \end{bmatrix}, \tag{3.82}$$

where $x_t = (\mathrm{ND}_t,\ \mathrm{IA}_t,\ \{\hat{n}_{l,t}\}_{l=0}^{M-1}) \in \mathbb{R}^{M+2}$, $\mathbf{W_X} \in \mathbb{R}^{n_w \times n_i \times (M+2)}$ and $\mathbf{W_y} \in \mathbb{R}^{n_w \times n_k \times (M+2)}$. The augmentation process outlined above avoids data leakage issues given the specific data loading and training procedure used in this study, which will be discussed in the upcoming section.

In this work, n_i and n_k are user-defined parameters in the RNN architecture. These parameters serve a dual purpose: specifying the number of input and output steps for the network and limiting the number of windows generated. On the other hand, τ_f is an inherent characteristic of the original time-series dataset. It is worth noting that n_i, n_k, and thus n_w, can influence the outcome of RNN training and rollout procedure. They determine how many times the model iterates over its output and, consequently, the extent of error propagation the results undergo (as discussed later). However, this aspect of the model was not treated as a tunable hyperparameter as it would require reprocessing the entire raw dataset for each variation tested during model training. This would lead to a significant increase in computational costs. The values for (n_i,n_k) were set to (50,50), yielding $n_w = 286$ windows per case considering the mixer's τ_f. Consequently, 2574 windows were allocated for the training set, whereas 572 windows were generated for the validation set (more discussion can be found Section 3.2.2.3).

3.2.2.3 Model training, deployment and explainability

RNN model architectures & training procedure Recall that this work aims to construct a multivariate RNN network to perform multi-step time-series predictions. The framework was built using Python package PyTorch, which inherently supports multi-step input/target sequences with a consistent number of features. The first architecture examined is a simple network composed of a single RNN layer (with either LSTM or GRU units) and one fully connected layer (RNN-FC). The latter reads and reshapes the hidden state, $\mathbf{h}_t$, from the former to generate a predicted sequence. As shown in Figure 3.16, the RNN layer processes a complete input sequence of n_i elements sequentially. Each element, $x_t \in \mathbb{R}^{M+2}$, contains all $M+2$ features per time-step, as explained earlier. Then, the hidden state from the last time-step, $\mathbf{h}_{n_i-1}$, is fed into the FC layer to produce the predicted output sequence. This output sequence consists of n_k elements, each holding the same dimensions as those assigned to the elements in the input sequence. Continuing from the previous discussion, Figure 3.16 showcases the

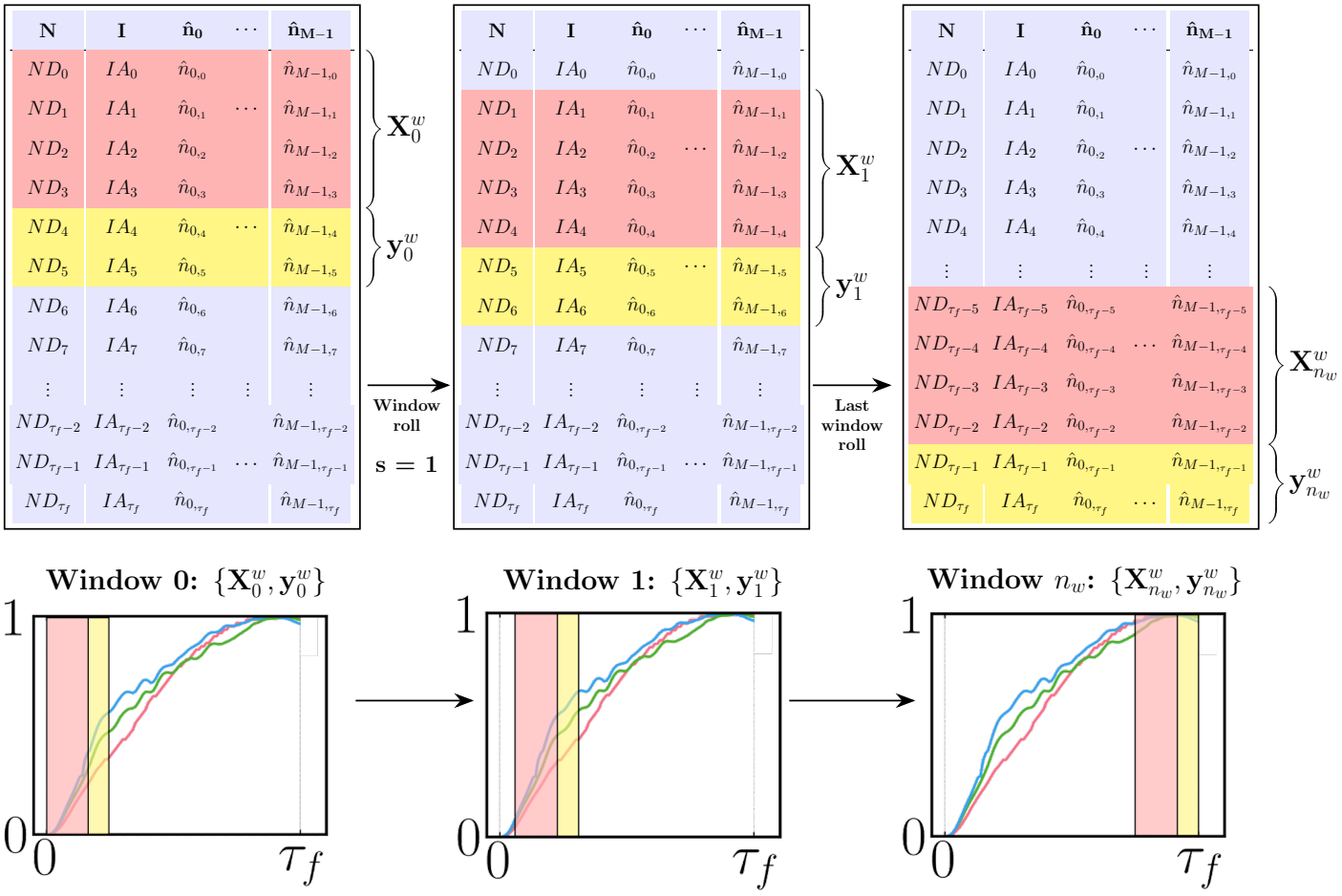


Figure 3.15: Schematic representation of the time-domain S2S windowing procedure implemented in Chapter 6. Top part provides a tabular representation of the windowed datasets, while bottom figures illustrate the rolling window procedure on top of a generic feature. Here, the window size is set to $s_w = 6$, where the number of input and target steps is $n_i = 4$ and $n_k = 2$, respectively. The window is shown to be rolled with a stride of $s = 1$. This figure is reproduced from Liang et al. [2024].

RNN-FC network handling Window 0, wherein it reads the first element $\mathbf{W}_{\mathbf{X}}^{\mathbf{0}} = \{\mathbf{X}_0^w\}$ as an input sequence and predicts $\widehat{\mathbf{y}}_0^w$, corresponding to the target sequence $\mathbf{W}_{\mathbf{y}}^{\mathbf{0}} = \{\mathbf{y}_0^w\}$.

Despite the simplicity of the previous neural network, architecture tailored for multi-step forecasting have been developed with more specialised features. A common example is the RNN encoder-decoder architecture (RNN-ED) as coined by Cho et al.. This is also referred to as a multi-step RNN, which comprises two RNN sub-layers. The input layer, known as the *Encoder*, derives a compressed representation of the input sequence, which is termed the encoded state. The second sub-layer, referred as the *Decoder*, interprets this encoded representation and use it to generate the predicted target sequence. Unlike the previous model, predictions in this method are computed sequentially from the hidden states of the RNN units themselves, rather than being derived from a single reshaping layer at the end of the network. As illustrated in Figure 3.17, the last element of the input sequence, x_{n_i-1}, along with the encoded state of the last RNN unit in the encoder layer (comprising its hidden and cell state $\mathbf{h}_{n_i-1}$, $\mathbf{C}_{n_i-1}$, respectively) are sent to the decoder layer, which is the one responsible for generating a time-step prediction for each RNN unit.

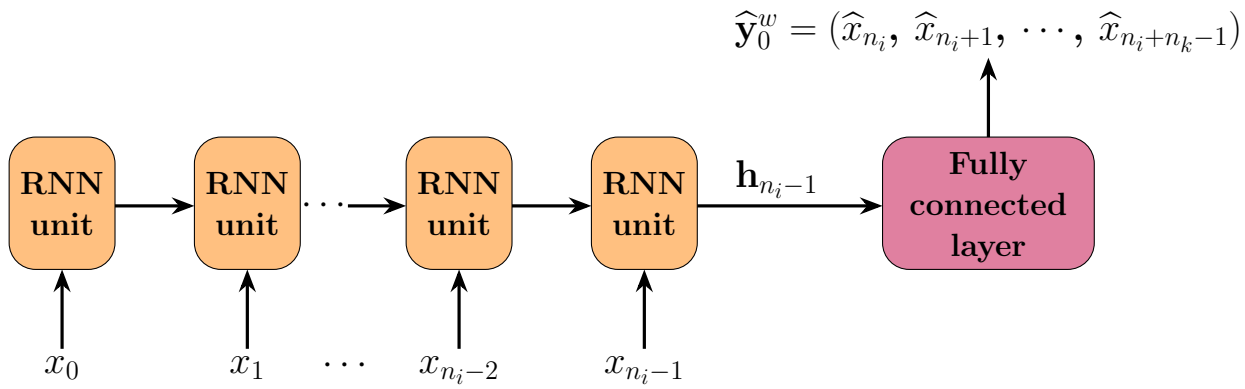


Figure 3.16: Diagram of an RNN-FC neural network architecture, where each unit can be either an LSTM or GRU. This figure is reproduced from Liang et al. [2024].

An important advantage of this more complex architecture over the RNN-FC lies in its adaptability to various training methodologies. Firstly, the predicted output of each RNN unit in the decoder layer can be recursively fed back into the subsequent unit until an output of the desired length is generated. This process is commonly known as *recursive* prediction. Alternatively, true or target data can be exclusively provided to the decoder units for computation, a method termed *teacher forcing*. Lastly, both predicted outputs and target data can be alternatively fed throughout the decoder layer; in this case, the model is said to use *mixed teacher forcing*. For both *teacher forcing* and *mixed* methods, a *teacher forcing ratio* parameter or *t.f.* ratio is defined. Its role is closely related to the batch-wise nature of the training approach implemented in this study, as discussed in more detail shortly. The *t.f.* ratio in mixed predictions determines the proportion of true data versus predicted outputs used in the decoder layer of the model per batch. On the other hand, the *t.f.* ratio for teacher forcing predictions dictates whether batches exclusively receive ground truth or predicted outputs. In a nutshell, in the *mixed* method, batches are fed with a combination of ground truth and predicted outputs, while in the *teacher forcing* approach, batches are exclusively provided with either true or predicted data. In addition, a Boolean *dynamic teacher forcing (d.t.f.)* parameter is introduced. When set to "True", this parameter gradually reduces the teacher forcing ratio at each epoch (i.e., one complete pass of the training dataset during model training). In this way, the model initially

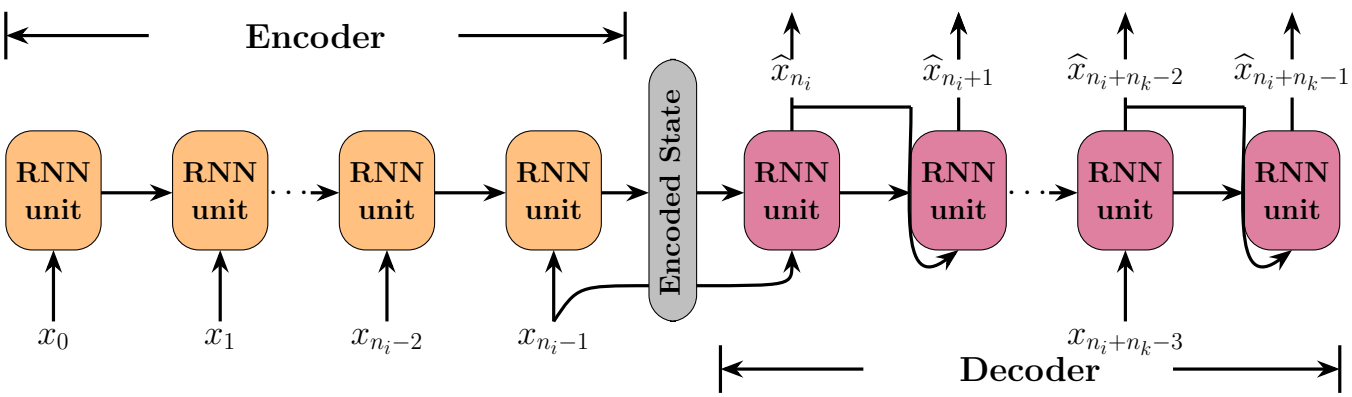


Figure 3.17: Diagram of an RNN Encoder-decoder (ED) architecture, implementing mixed teacher forcing training. As with Figure 3.16, the RNN units can either be LSTM or GRU. This figure is reproduced from Liang et al. [2024].

learns patterns from the target data but gradually relies more on its own output to generate future predictions.

In this work, a shuffled batch-wise training methodology was adopted for both RNN architectures. This method involves dividing the windowed tensors, $\mathbf{W}_{\mathbf{X},\mathbf{y}}$, into smaller subsets or "batches", which limits the number of samples presented to the network during training before each weight updates, thereby enhancing computational efficiency. In this scheme, a collection of input/target sequence pairs or windows, grouped into a batch $\mathbf{W}_{batch} = \{\mathbf{X}_j^w, \mathbf{y}_j^w\}_j^{\text{batch size}}$, are indexed and randomly shuffled before being fed into the network. By batching and randomising sequences, the model's capacity to generalise effectively across different datasets is enhanced, in addition, its ability to identify common patterns is improved and it is prevented from learning biases associated with the data order. Furthermore, in this context, window shuffling effectively mitigates the risk of data leakage by preventing the model from unintentionally learning dependencies between consecutive windows. This ensures that the model treats each window as a unique and independent instance.

In addition, a custom loss function was incorporated during the training procedure, consisting of a standard Mean Square Error (MSE) loss function with an added penalty term written as $w_p * \frac{1}{N}\sum_{i=1}^{N}(\text{ReLU}(-\hat{\mathbf{y}}_j^w))$, where w_p is a user-defined penalty weight; $\text{ReLU}(x)$ denotes the Rectified Linear Unit activation function, defined as $\max(0, x)$, and $\hat{\mathbf{y}}_j^w$ refers to a predicted sequence. This penalty term aims to prevent negative predictions, which in this context, could lead to non-physical results, such as negative drop count. This is achieved by identifying and averaging all initially predicted negative values by the network, and then adding a fraction of this average as penalty. In this way, loss decreases as negative predictions are minimised. Moreover, two regularisation terms Lasso and Ridge regression, denoted as L_1 and L_2, were added to the loss function to help manage over-fitting. L_1 introduces a penalty term based on the absolute value of the coefficient magnitudes, expressed as $l_1 \sum |\beta|$, while L_2 adds a penalty based on the square magnitude of the coefficients, given by $l_2 \sum \beta^2$. Both penalty terms are regulated by coefficients l_1, l_2, respectively.

In the final phase of model training, we implemented two key strategies: an early-stopping procedure and a "*ReduceLROnPlateau*" scheduler. The early-stopping mechanism continuously monitors improvements in the validation loss score and saves the best-performing model before any degradation occurs, which effectively prevent over-fitting. Meanwhile, the scheduler enhances model convergence by dynamically reducing the learning rate once the model performance stagnates (i.e., when the validation loss stops improving). It is worth noting that the scheduler applied here uses the well-known adaptive moment estimation (Adam) optimiser [Kingma and Ba, 2014], which is also employed for the backpropagation process throughout the training.

Hyperparameter tuning Prior to initiating the training procedure to estimate the network's learnable parameters (i.e., *weight* and *biases*), we conducted a comprehensive parametric sweep to optimise the framework's user-defined parameters, also known as "hyperparameters". As explained earlier, the input and target sequence size (n_i, n_k) were not considered in this tuning step due to computational constraints. The remaining hyperparameters adjusted in this study include the hidden size (hidden state dimension), learning rate (step size for adjusting model weights during training), batch size (number of windows fed during training before weights update), and the custom penalty weight w_p. These hyperparameters are tuned for both network architectures and cell types. The coefficients l_1 and l_2 controlling the corresponding regression penalty terms described prior were only varied for RNN-FC models, while the values were fixed to zero for RNN-ED to prioritise other more influential hyperparameters. Additionally, the latter model consider three extra hyperparamters related to the training method adopted in the decoder layer, as described previously, the "prediction type", the "*t.f.* ratio" and Boolean feature "*d.t.f.*".

The exploration surrounding the above-listed hyperparameters were carried out using AI scaler package Ray Tune. The hyperparamter sample space investigated is detailed in Table 3.3, along with each network best-performing model configuration. It is worth mentioning that 85% of the sample space were investigated in search for optimal configuration, representing a total of 2478 and 3060 parameter combinations for the FC and ED architectures. The parameter candidate values were selected based on early sensitivity trials and their relevance in the context of this work. For instance, a finer batch sample space was explored given the relatively limited dataset available for training and validation. This decision was made because noise effects resulting from varying batch size could have more significant impact on the generalisation performance of the model. This is reflected in the widely different sizes obtained across the studied scenarios. Other settings yielded expected results, such as nearly constant penalty weights, w_p, given the similar nature of all features. Similarly, from the search for FC architecture, the L_1 and L_2 penalty terms were essentially deemed unnecessary for the models, as over-fitting has already been mitigated in various other ways, as previously described (e.g., batch randomisation). This also supports the decision made prior that to fix these terms as zero for RNN-ED. On the other hand, the LSTM-ED architecture preferred a *recursive* training method, implying that the model does not rely on the ground truth to perform predictions throughout the decoder layer but runs exclusively on its output from the onset. This is not the case when dealing with GRU unit for ED network, which relies heavily on the ground truth given the preference for a *mixed* approach with a high *t.f.* ratio (0.4). In addition, this model tends to activate the dynamic teaching forcing mode (i.e., *d.t.f* set as "True"), indicating its need for access to the ground truth at the early stage to improve its performance.

Prediction via sequence generation (rollout) When trained, the model is expected to predict the evolution of dispersion features, e.g., dispersed drop count, up to a desired future time-step. Specifically, instead of performing time-consuming high-fidelity simulations for the

Table 3.3: Hyperparameter search space and best-performing network configuration for each correpsonding architecture and RNN unit type.
* *batch size range lies between 8 and 40, with a step of 4 for RNN-FC and 8 for RNN-ED, rendering 9 and 5 parameter values for each case, respectively.*

Hyperparameters	**Network architecture**			
	FC (LSTM/GRU)		**ED (LSTM/GRU)**	
	Value ranges	**Best**	**Value ranges**	**Best**
Hidden size	64, 128, 256	(256/64)	64, 128, 256	(64/128)
Learning rate	0.002, 0.005, 0.01	(0.005/0.01)	0.002, 0.005, 0.008, 0.01	0.002
Batch size	(8∼40, 4)*	(8/32)	(8∼40, 8)*	16
w_p	0.01, 0.1, 1, 10	0.1	0.01, 0.1	(0.01/0.1)
l_1	0, 0.00001, 0.0001	0	N/A	0
l_2	0, 0.00001, 0.0001	0.00001	N/A	0
Prediction type	N/A	-	recursive, *t.f.*, mixed	(recursive/mixed)
t.f. ratio	N/A	-	0.02, 0.05, 0.1, 0.2, 0.4	(-/0.4)
d.t.f.	N/A	-	True, False	(-/True)

entire mixing process, users of the model carry out the CFD simulation solely for early mixing stage. The early observations of mixing performance metrics are subsequently fed into the trained model which extracts information from the input and iteratively predicts the corresponding evolution profile.
As explained earlier with the introduction of the windowing process and the model architectures, the RNN network is designed to map an input sequence of length n_i to an output sequence of fixed length n_k, where $n_k + n_i << \tau_f$. Recall that the objective of this work is to predict the entire temporal evolution of the dispersion features up to the final time-step, τ_f, where simulations are terminated. To achieve this, a "rollout" procedure is implemented, wherein the trained model is iteratively reused until the desired time-step is reached. During each iteration, the previous output sequence is fed back into the trained model to predict the next n_k sequence. The number of iterations or "rollouts" is therefore determined by the length of the output sequence, following the expression $r = (\tau_f - n_i)/n_k$.

The selection of n_i and n_k is not a trivial task since these two values determine the size and number of data samples available for the model to be trained with (refer to Section 3.2.2.2), which naturally has a direct effect on model performance and uncertainty. Considering the differing lengths of the time-series data sets for each simulation case, acknowledging that they were truncated to $\tau_f = 385$ and the values for n_i and n_k were fixed to (50, 50). Accordingly, the number of rollouts, r, is computed as 7.

Uncertainty quantification from a ensemble of perturbed inputs After adequately training the model, the next logical step is to estimate its prediction uncertainty. Regarding this, many researchers have contributed to understanding and quantifying the uncertainty in

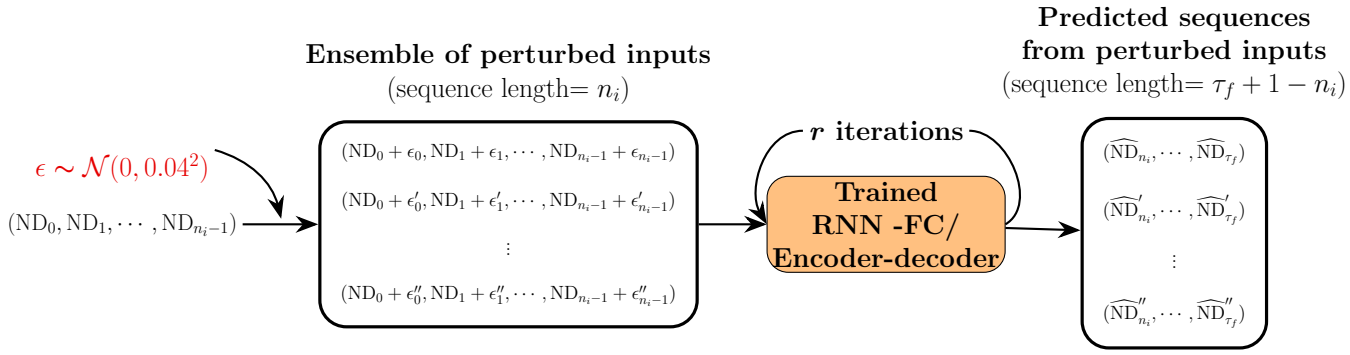


Figure 3.18: Diagram showcasing the procedure of ensemble-based uncertainty quantification. Take ND as an example, perturbations are introduced to the input sequence by adding noises, ϵ, drawn from a Gaussian distribution, $\mathcal{N}(0, 0.04^2)$, at each time-step, giving rise to the ensemble of perturbed inputs. All of the ensemble members are fed into the trained model which progressively produces the ensemble of predicted sequences (with a sequence length of $\tau_f + 1 - n_i$). r is the number of iterations determined by the target sequence length, $r = (\tau - n_i)/n_k$. This figure is reproduced from Liang et al. [2024].

a neural network's prediction (see the comprehensive review by Gawlikowski et al.). Yet, an approach to uncertainty quantification in current work is required to cope with the fact that the trained model iterates over its output numerous times, as described above through the rollout procedure. In other words, a method required herein is capable of tracking the evolving model uncertainty and granting access to the model performance through the propagation. To achieve this, an ensemble-based procedure, adapted from the ensemble forecasting technique that has been extensively used in numerical weather prediction [Zhu, 2005, Leutbecher and Palmer, 2008, Parker, 2013], is proposed.

As showcased in Figure 3.18, we started by introducing perturbations represented by ϵ to the input sequence. This involves adding noise, drawn from a distribution, to the feature values at each time-step (Figure 3.18 takes ND as an example). Herein, a Gaussian distribution with mean $\mu = 0$ and standard deviation (referred to as *std. dev.* henceforth) $\sigma_{s.d.} = 0.04$ is used, namely $\epsilon \sim \mathcal{N}(0, 0.04^2)$, such that the feature values in the perturbed input sequence represent a probable uncertainty arising from observed feature values at early dispersion. For instance, the measured dispersed drop count at early times could be a few drops off if measurement errors are considered. It is worth noting here that the added noise could lead to negative feature values in the perturbed input sequence, which would be physically unrealistic; nonetheless, the purpose of their inclusion is to examine the capability of the trained model to handle any type of disturbance in the input data. In this way, an arbitrary perturbed input ensemble containing 200 members is generated, which subsequently enters the trained model to produce an ensemble of corresponding predicted sequences. With these sequences, the *std. dev.* was computed across the 200 ensemble members at each time-step using the empirical *std. dev.* expression per sample:

$$\sigma_{s.d.} = \sqrt{\frac{\sum (b_i - \bar{b})^2}{N_e - 1}},$$

where b_i, $\bar{b}$, and N_e denote the i^{th} member in the ensemble, the ensemble average, and the ensemble size ($N_e = 200$), respectively. Then, a prediction interval was calculated to give an

overview of the range wherein the model prediction is likely to occur (with a 95% confidence) given the unperturbed input sequence, which could be written as:

$$[\mu - z\sigma_{s.d.}, \mu + z\sigma_{s.d.}], \quad z = 1.96.$$

Finally, the prediction interval is used to suggest a fair indicator of the model performance, namely the absolute residual between the targeted perturbed evolution and its predicted counterpart from the trained model using the unperturbed input sequence. Corresponding results and relevant discussion are presented in Chapter 6.

Chapter 4

Oil-water emulsion formation in stirred vessels: the effect of impeller speed

Contents

4.1 Results and Discussion 84

4.1.1 Flow evolution 85

4.1.2 Interfacial behaviours 88

4.1.3 Drop count and their size distribution 92

4.2 Concluding Remarks 96

Overview

This chapter bridges the gap in the understanding of all the stages of the oil-water emulsification process, from the onset of drop breakup through to the attainment of a statistical steady-state (which refers to a state that occurs instantaneously after the dynamics developing in the vessel stagnates, reducing to sporadic breakup and subsequent coalescence chains as described later). In particular, it constructs a transparent connection between the interfacial deformation, the prevailing flow conditions (parameterised by the impeller rotational speed) and their associated vortical structures. The validation associated with the simulation results presented in this chapter has been presented in Section 3.1.5.1. This chapter provides a comprehensive discussion of the vortical structures and interfacial dynamics inside the stirred vessel as a function of the impeller speed ($N = 1 - 10$ RPS with corresponding $Re = 1802 - 18026$ and $We = 2.19 - 219$), followed by an analysis of the drop size distribution.

4.1 Results and Discussion

In this section, the spatio-temporal evolution of oil-water emulsion formation in a stirred vessel equipped with a PBT is demonstrated. More specifically, the effect of impeller speed on the mixing process is comprehensively studied by exploring a wide range of frequencies, $N = 1 - 10$ RPS (i.e., Revolution per Second) with corresponding $Re = 1802 - 18026$ and $We = 2.19 - 219$.

First, a discussion surrounding the generated vortical flow structures and associated interfacial dynamics is provided as a function of the impeller speed. Then, the results correspond to an examination of the drop size distribution evolution and its dependence on Re and We are presented.

4.1.1 Flow evolution

At the onset of impeller rotation, the impeller pumps the flow radially towards the vessel wall, analogous to the von Kármán flow over a infinite rotating disc [Schlichting and Kestin, 1961]. The no-slip fixed vessel wall modifies this flow, along which the flow develops upward to the interface, and then is dragged to the vessel center by a centrifugal force at the interface. After this, a strong elongational flow presented at the vessel center drives the fluid to travel down back to the impeller, giving rise to the flow circulation shown in Figure 4.1. The close-up view in this figure, where gold and cyan are respectively used to designate the oil and aqueous phases, the red solid line for their interface, depicts the flow field prior to the interface deformation for $N = 5$ RPS, $(Re, We) = (9013, 55)$. The flow field is represented by streamlines drawn on a $x-z$ plane at $y = 4.25$ cm; such a format is followed by the flow field diagrams henceforth. As can be seen from Figure 4.1, there exists a rich dynamics and a flow field of high complexity. Figure 4.2 demonstrates the evolution of flow by the example for the lowest impeller rotational speed studied, $N = 1$ RPS corresponding to $(Re, We) = (1802, 2.19)$.

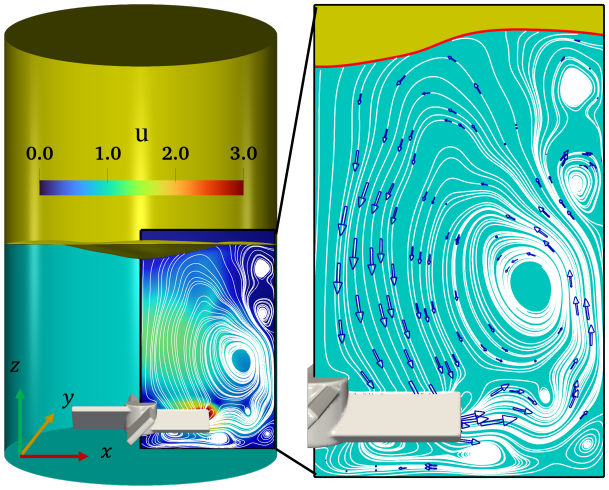


Figure 4.1: Flow field prior to the interface deformation ($t = 8 \times Rev.$) for $N = 5$ RPS, $(Re, We) = (9013, 55)$, represented by streamlines drawn on a $x - z$ plane at $y = 4.25$ cm. The inset of the three-dimensional vessel is coloured by the velocity magnitude; the blue arrows displayed in the close-up view are scaled by the velocity magnitude, indicating the velocity orientation. This figure is reproduced from Liang et al. [2022].

In addition to the above-described primary vortex (i.e., the flow circulation) generated at early times ($t = 0.5 \times Rev.$), a secondary vortex is created near the bottom of impeller (see Figure 4.2b). This vortex rotates radially in the opposite direction compared with the primary vortex. Furthermore, a suite of vortical structures accompany the development of the primary vortex, corresponding to Moffatt, blade-tip, and wall-end vortices (see Figure 4.2$c - e$). Since the velocity is continuous across the interface, a large vortex is also created in the oil phase but with the opposite circulation to that in the aqueous phase as the overlying flow is dragged radially inward. At $t = 6 \times Rev.$, a swirling flow is observed near the interface in the aqueous phase, which centrifuges the upper oil adjacent to it radially outward producing a small vortex of opposite circulation to the large one (Figure 4.2f). Later, a vortex breakdown appears at the interface in the oil (Figure 4.2g), which grows, squeezing the large meridional flow to the

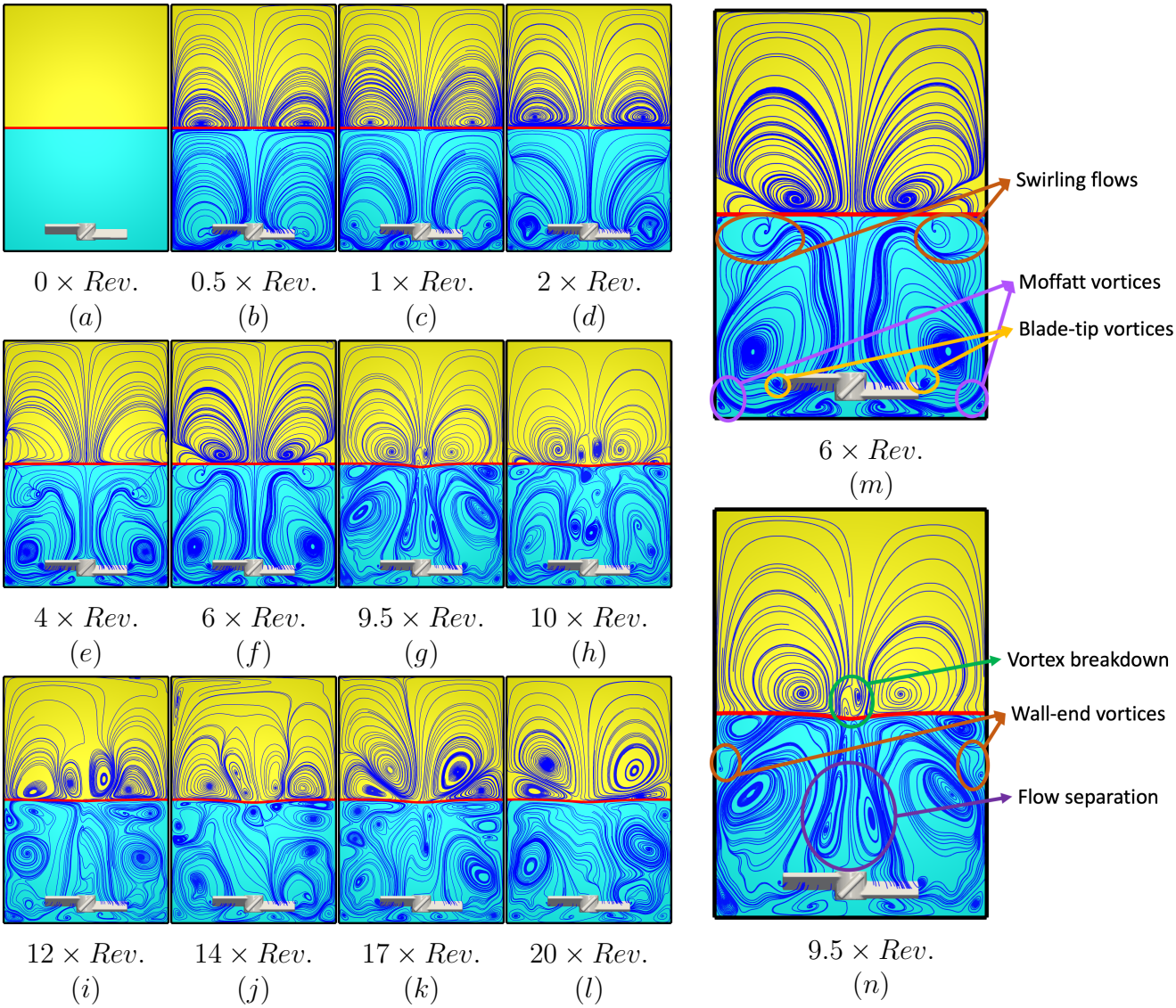


Figure 4.2: Spatio-temporal evolution of the vortical structures for $N = 1$ RPS, $(Re, We) = (1802, 2.19)$ from an initial static state (a) until $t = 20 \times Rev.$ (l). In this and subsequent figures, the results are displayed in the $x - z$ plane at $y = 4.25$ cm, and cyan and gold are used to designate the aqueous and oil phases, respectively, while the red solid line represents the interface location. Enlarged snapshots of the vortical structures with corresponding annotations are shown for $t = 6 \times Rev.$ and $t = 9.5 \times Rev.$ in (m) and (n), respectively. This figure is reproduced from Liang et al. [2022].

sidewall until it gives way to two large circulation cells with a radially outward direction (Figure 4.2$h - k$). More discussion surrounding vortex breakdown at higher impeller speed will be given later. The oil flow then remains in a configuration where the original meridional flow is confined to a thin layer in the vicinity of the interface while the counter one dominates in the oil phase (Figure 4.2l). On the other hand, in the aqueous phase, the counterpart of vortex breakdown, the so-called flow separation, occurs close to the edge of the rotating impeller (Figure 4.2g). Moreover, the aqueous flow is characterised by a high level of turbulence involving the development of a multitude of vortices of varying scales.

Recall the occurrence of vortex breakdown in the oil phase, this phenomenon is also observed when impeller speed increases up to $N = 5$ RPS, which corresponds to a range of $Re = 1802 - 9013$ and $We = 2.19 - 55$. As seen, Figure 4.3 pictures the vortical structures when the

flow has reached a statistical steady-state where the vortex breakdown has developed into the dominant circulation cells along with the counter-rotating ones confined to a thin layer near the interface. Though not presented herein, with higher Re and We, the vortex breakdown appears earlier, for example, at $t \approx 7 \times Rev.$ for $N = 5$ RPS, $(Re, We) = (9013, 55)$ in comparison to $t \approx 9.5 \times Rev.$ for $N = 1$ RPS, $(Re, We) = (1802, 2.19)$.

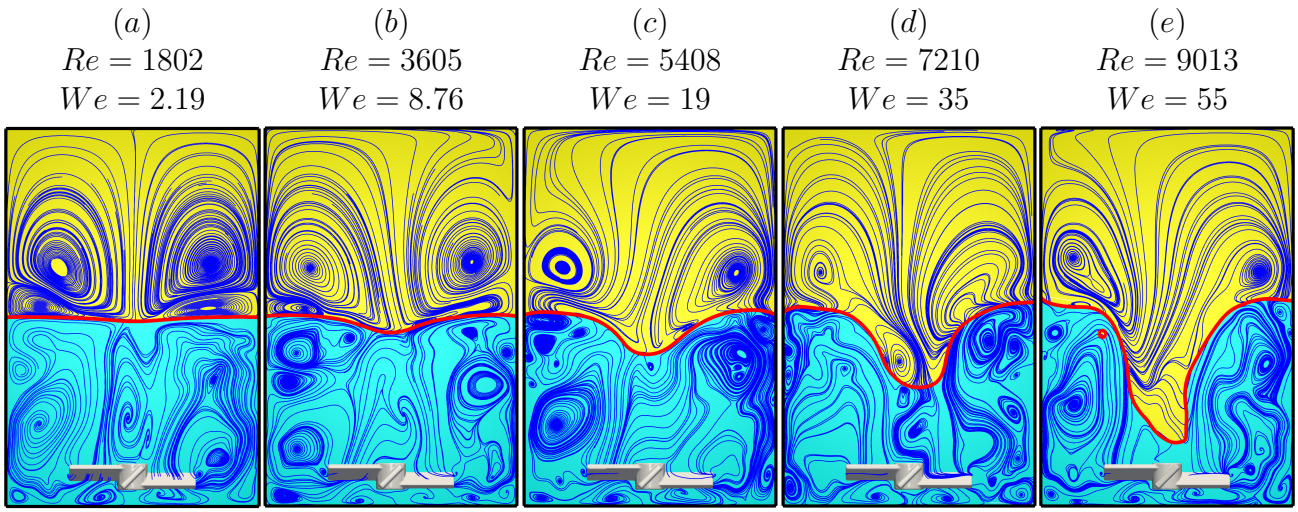


Figure 4.3: Vortical flow structures for $N = 1-5$ RPS corresponding to (Re, We) combinations of (1802,2.19), (3605,8.76), (5408,19), (7210,35), and (9013,55) are shown in $(a) - (e)$, respectively, at $t = 25 \times Rev.$ when the flow has reached a statistical steady-state. This figure is reproduced from Liang et al. [2022].

When higher impeller speed is considered, i.e., $N > 5$ RPS, the generated flow field is modified accordingly. In Figure 4.4, the spatio-temporal evolution of the vortical structures for higher impeller cases is presented, exemplified by $N = 7$ RPS and 10 RPS, corresponding to $(Re, We) = (12618, 107)$ and $(Re, We) = (18026, 219)$, from an early-time state (at $t = 2 \times Rev.$, see Figure 4.4a) to a stage of the flow at which the deforming interface has reached the impeller (at $t = 9 \times Rev.$, see Figure 4.4f). During the early stages of the flow, the vortical structures observed are similar to those seen for lower impeller speed in that the primary and secondary vortices are generated accompanying the occurrence of rich vortical structures including Kelvin-Helmholtz vortices (Figure 4.4b). However, instead of the subsequent vortex breakdown, the streamline configuration for higher Re and We indicates a strong tendency of the interface to be dragged towards the impeller (Figure 4.4e). Although the aqueous phase is dominated by the primary vortex, there are a number of secondary vortices close to the vessel sidewall adjacent to the interface, pumping the fluid upward along the wall (Figure 4.4$c - f$). This could be the cause of the slight fluctuation of interface height (represented as red solid line). When impeller speed increase further ($N = 10$ RPS), the vortical structures in the oil and aqueous phases during the early and intermediate stages of the dynamics resemble those discussed above, as presented in the bottom panels of Figure 4.4. Nonetheless, the strength of these vortices is higher as indicated by the earlier interface deformation (stretching) shown in Figure 4.4k.

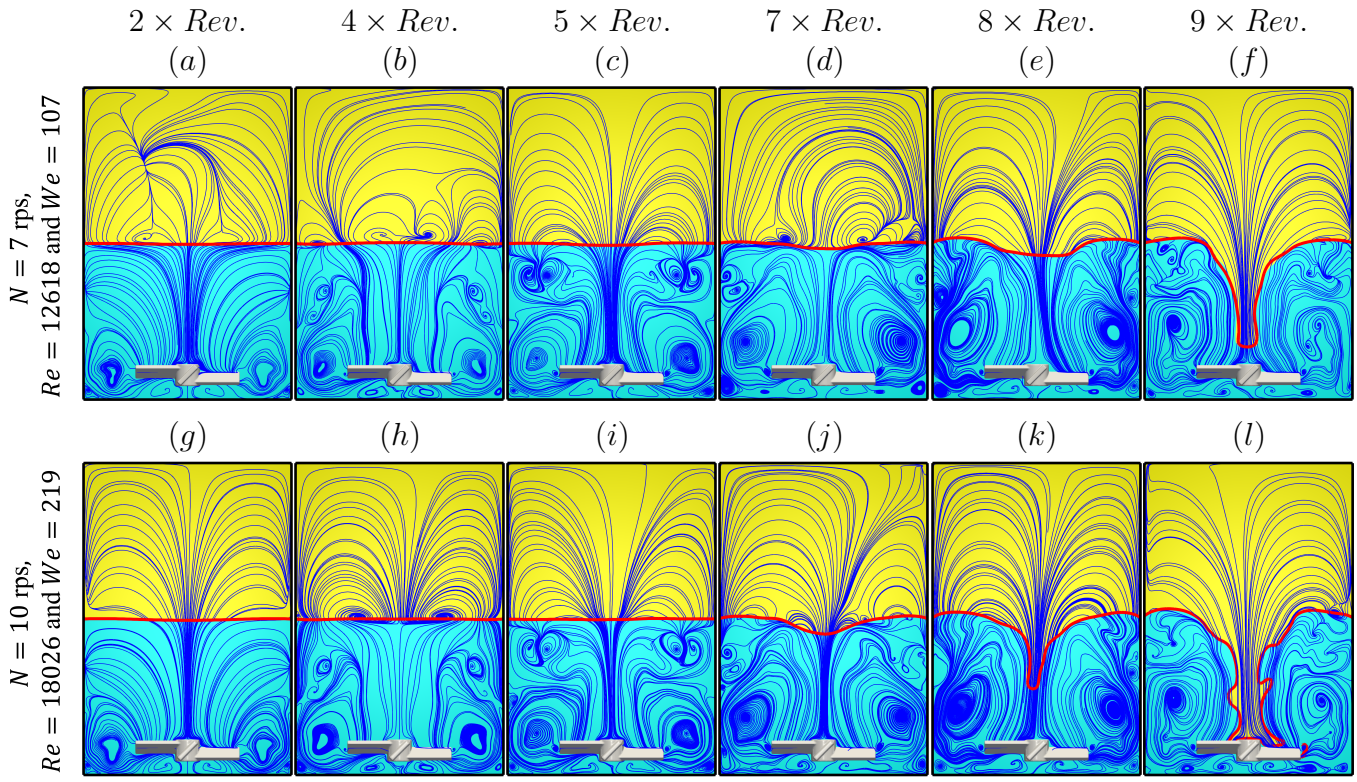


Figure 4.4: Spatio-temporal evolution of the vortical structures for $N = 7$ and 10 RPS, corresponding to $(Re, We) = (12618, 107)$ and $(Re, We) = 18026, 219$ at $t = 2 - 9 \times Rev.$ shown in $(a) - (f)$, respectively. This figure is reproduced from Liang et al. [2022].

4.1.2 Interfacial behaviours

Following the flow field pictured above, the spatio-temporal evolution of interface shape is now presented. Firstly, in the case of low and moderate impeller speeds, it is observed that the deforming interface remains in a statistical steady-state assuming a shape of so-called Newton's Bucket [Laymon, 1978, Jansson et al., 2006, Kahouadji and Witkowski, 2014] (see Figure 4.5). In addition, the depth of Newton's Bucket increases, getting closer to the impeller, with higher Re and We. More specifically, for $N = 1 - 3$ RPS, the impeller speed is not sufficient to generate single dispersed drop in the system, whereas liquid dispersion begins to occur in the case of $N \geq 4$ RPS.

For a system of low Re and We, the liquid dispersion in the studied configuration is achieved, generally by following several steps: (1) interface deformation, (2) ligament formation, and finally (3) drop breakup. This process is presented by exemplifying the mixing system with $N = 4$ RPS, $(Re, We) = (7210, 35)$, as displayed in Figure 4.6. As the impeller rotates, the azimuthal velocity generated by the impeller exerts a torque on the interface, deforming it and then dragging it toward the impeller (Figure 4.6$a - b$). For this particular impeller speed, the impeller rotation is not sufficiently rapid so as to cause the interface to reach the impeller; instead, the interface deforms into a helical shape as seen in Figure 4.6c. Later, a long ligament detaches from the deforming interface, which subsequently breaks into a group of daughter drops (Figure 4.6d, e). After that, a large dispersed drop spirally stretches to become

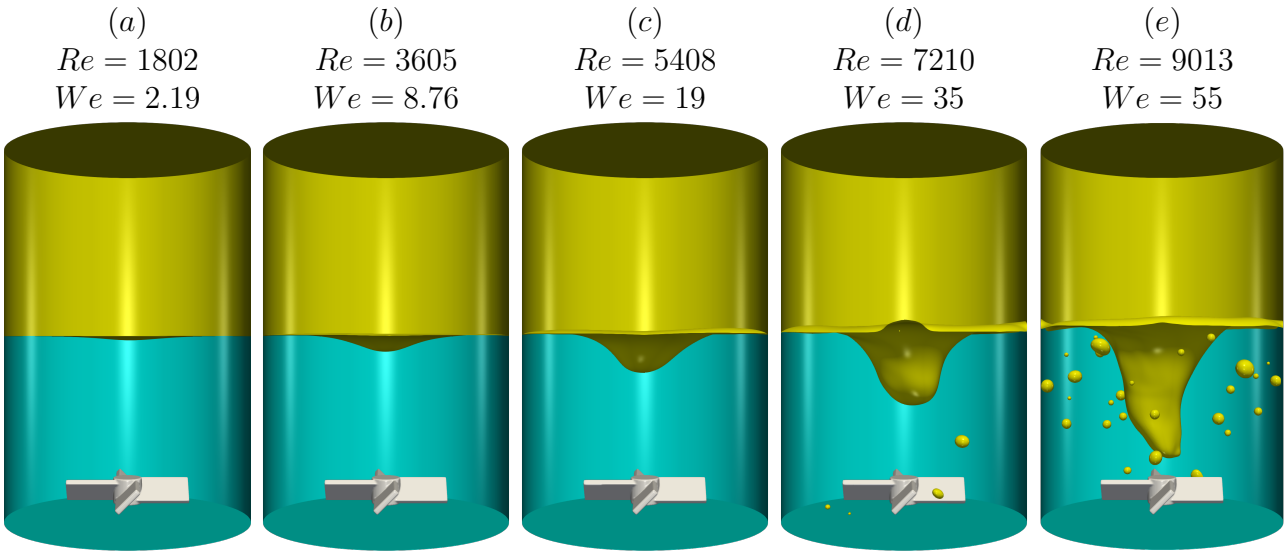


Figure 4.5: Interface shape at a statistical steady-state for $N = 1 - 5$ RPS corresponding to (Re, We) combinations of (1802,2.19), (3605,8.76), (5408,19), (7210,35), and (9013,55) shown in $(a) - (e)$, respectively, at $t = 25 \times Rev$. This figure is reproduced from Liang et al. [2022].

longer and thinner before it reaches the impeller and meanwhile reattaches the deforming interface (Figure 4.6$f - i$). This cycle of ligament detachment, breakup and re-attachment is repeated until the system reaches a statistical steady-state where small drops remain dispersed in the aqueous phase together with the deforming interface in the shape of a Newton's Bucket (Figure 4.6$j - l$). The existence of both ligament re-attachment, due to the action of interfacial tension, and elongation, due to the interaction with the turbulent flow, highlights the presence of the delicate interplay amongst the various competing forces which results in the complexity associated with the mixing process. Furthermore, particularly for $N = 5$ RPS, the deforming interface initially attaches to the impeller (instead of what is described for $N = 4$ RPS), producing dispersed drops, and subsequently retracts due to the interfacial tension competing against the elongational flow. This leads to the cessation of interface-impeller contact and no further ligaments being produced; meanwhile, the dispersed drops are likely to travel up to the overlying oil phase given the underlying flow field, and in addition, due to buoyancy.

A close-up view of the drop breakup process is provided in Figure 4.7, which presents the concurrence of multiple drops pinch-offs along one single ligament. This figure presents the possibility of the employed CFD simulation to serve as data source for constructing population balance models, especially drop breakage models, which requires the knowledge of daughter drops produced via breakup. Close inspection reveals that the ligament initially takes time to elongate, giving rise to thread-like regions between nodules, which continue to thin until they break up into individual droplets via a capillary instability (described in details in [Janssen and Meijer, 1993] as "transient dispersion" and "capillary breakup"). This mechanism is also analogous to the "end-pinching" phenomenon depicted in [Janssen et al., 1994], which refers to the breakup of an elongated drop after a sudden halt of the flow rate, where the flow rate interruption corresponds to the inherently periodic velocity field [Wu and Patterson, 1989,

Li et al., 2017, Fan et al., 2021] introduced by the impeller rotation herein. To explain the phenomenon observed within the mixing system, we examined closely the vorticity profiles around the ligament. Figure 4.8 presents four horizontal planes that depict the flow, coloured by the vorticity magnitude. As shown, these diagrams illustrate the relative position of the ligament to the vorticity distribution in the flow plane, that the ligament (represented as white solid lines) lies in the high vorticity region (coloured in red) generated by the impeller rotation. This interaction of the strong vorticity with the interface leads to the instability of the ligament; such an effect is particularly pronounced in the near-impeller regions where the vorticity magnitude is dramatically larger than those close to the vessel walls.

When the impeller speed is increased ($N > 5$ RPS), no retraction of the deforming interface from the impeller is observed. In Figure 4.9$a - f$, the evolution of interface shape for $N = 7$ RPS, $(Re, We) = (12618, 107)$ is shown for $t = 9 - 25 \times Rev$. After the interface reaches the impeller (Figure 4.9a), it is further stretched radially and long oil ligaments are created when the impeller blades cut through the rotating curtains (Figure 4.9b). The long ligaments subsequently stretch to become thinner until pinch-off occurs, giving rise to multitudes of smaller drops (Figure 4.9c). After that, the formation of new ligaments remains in place as seen in Figure 4.9d. The small drops created from ligament breakup either travel upwards under the

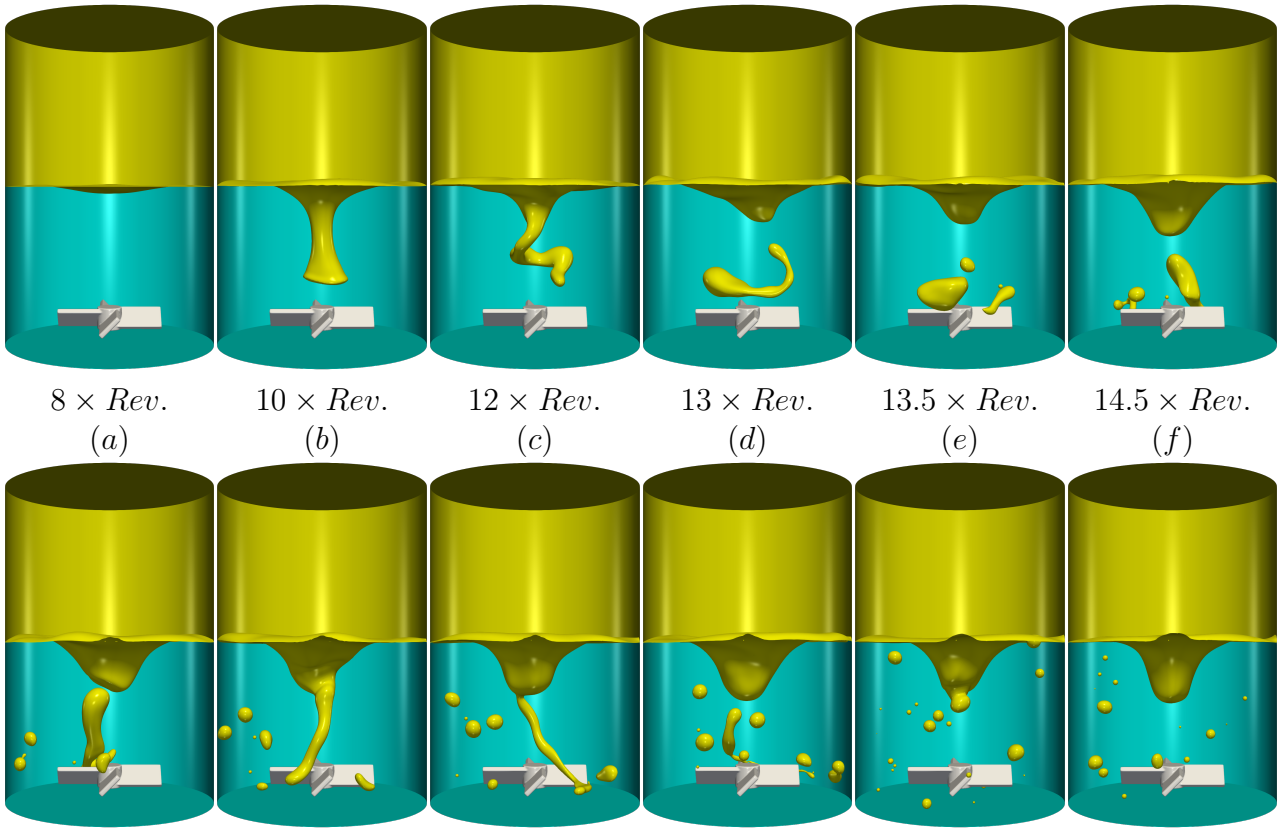


Figure 4.6: Spatio-temporal evolution of interface for $N = 4$ RPS, $(Re, We) = (7210, 35)$ from a state where the interface starts to deform (a) until $t = 20 \times Rev.$ (l). This figure is reproduced from Liang et al. [2022].

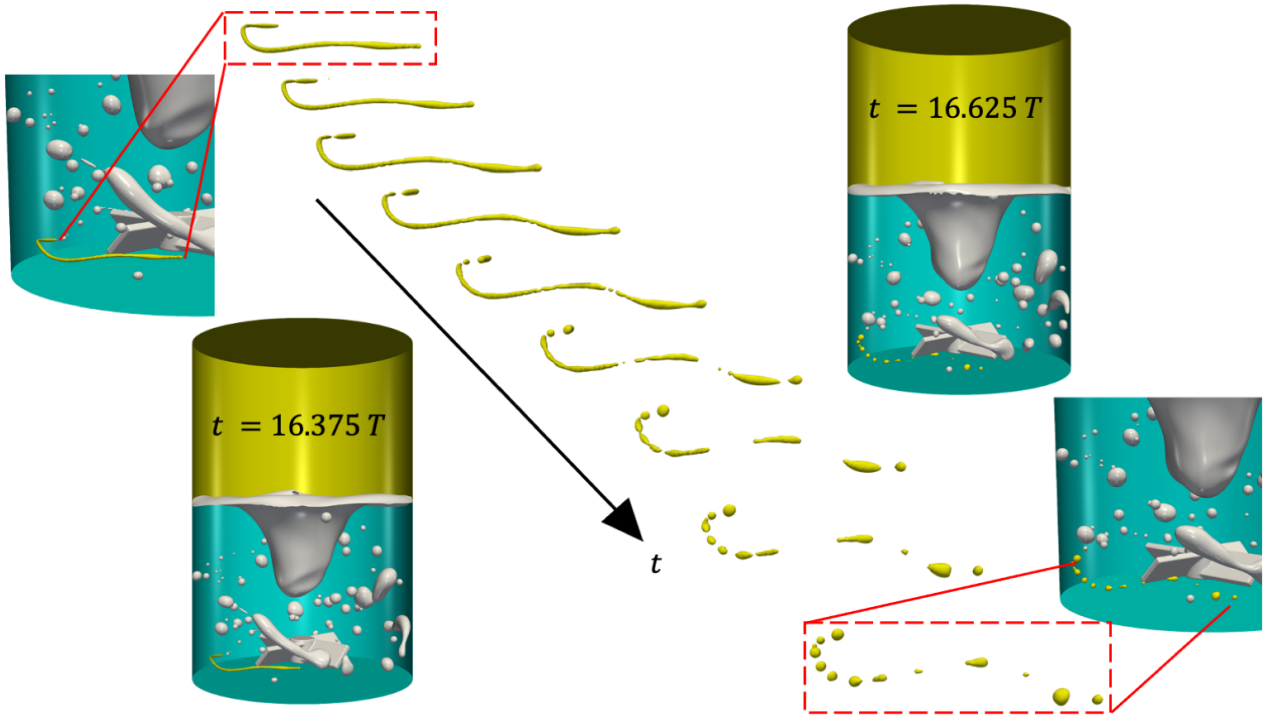


Figure 4.7: Close-up view of single ligament breakup into drops for $N = 5$ RPS, $(Re, We) = (9013, 55)$ during time frame $t = 16.375 - 16.625 \times Rev$. This figure is reproduced from Liang et al. [2022].

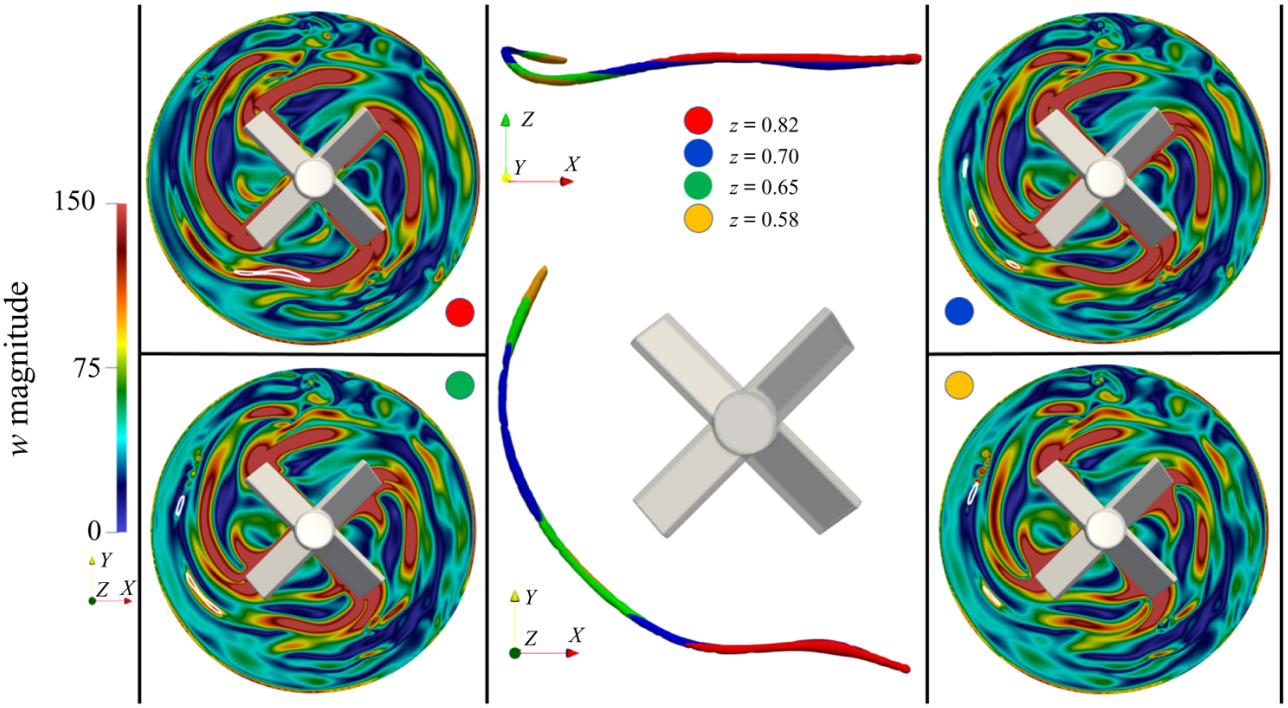


Figure 4.8: Vorticity in the ligament surroundings for $N = 5$ RPS, $(Re, We) = (9013, 55)$. Four horizontal planes generated at z[cm] $= 0.82, 0.70, 0.65, 0.58$, corresponding to the red-, blue-, green-, and yellow-labelled planes, are coloured according to the vorticity magnitude. The side- and top-view of the ligament are presented in the middle, and parts of the ligament are highlighted by white solid lines in the vorticity panels. This figure is reproduced from Liang et al. [2022].

action of buoyancy, eventually merging with the oil phase (Figure 4.9*e*), or remain dispersed in the aqueous phase until they coalesce with other drops.

At larger impeller speeds, drop coalescence starts to dominate over breakup, as revealed by the inspection of Figure 4.9$g-l$. In contrast to the lower Re and We cases discussed above, a larger torque is generated in the present case which results in a deforming interface of a helical shape with four rotating curtains (Figure 4.9*g*). Later, long ligaments are rapidly and continually created from the impeller tips; consequently, they merge to form a relatively large mass of oil that collects around the vessel bottom before breaking up into smaller drops (Figure 4.9*h*). Likewise, as can be seen in Figure 4.9*i*, the dispersed phase in this high Re case is composed mainly of stretched oil ligaments rather than the individual drops observed to accompany the process at lower Re. An additional remark to be made is that, with increasing time, an increasing amount of oil is entrained into the aqueous phase; as a result, the latter is displaced upwards along the vessel sidewall lifting the interface as seen in Figure 4.9j,k. Finally at $t = 25 \times Rev.$, the dynamics is characterised by complex interfacial topology; it is notable that the number of small droplets has decreased due to coalescence giving way to large dispersed-phase structures resulting from the merging of ligaments and drops (Figure 4.9*l*). More discussion surrounding the number of dispersed drops and their size distribution as a function of the impeller speed is provided in the following section.

From the above discussion, we recall again the occurrence of vortex breakdown in the oil phase; we noticed that this phenomenon aligns with the statistical steady-state where the interface remains in the shape of a Newton's Bucket. With this, it may be possible to use the onset of vortex breakdown as an indicator of, and a surrogate for, the fact that the interface will eventually remain sufficiently far from the impeller and therefore unattached to it, at steady state. A methodology that focuses on the detection of vortex breakdown (whether it occurs or not) for a given set of parameters, and then tracks the dependence of the breakdown over a range of such parameters, can lead to a map in (Re, We) space in which the region of limited mixing is demarcated. Such an approach would obviate the need for lengthy computations to resolve the intricate and rapidly evolving interfacial dynamics.

4.1.3 Drop count and their size distribution

From an industrial point of view, it is often important to track the evolution of the dispersed-phase statistics and metrics in terms of number of drops, their size distribution, the interfacial area, and hold up. Based on previous discussion, this section are focused on those cases with liquid dispersion observed. Figure 4.10 presents the temporal evolution of the number of dispersed drops ($t = 5 - 25 \times Rev.$) for $N = 5 - 10$ RPS ($Re = 9013 - 18026$ and $We = 55 - 219$), along with the corrsponding interface shapes at $t = 25 \times Rev.$ For all presented frequencies, no dispersed drops appear until there is a steep increase from a zero drop count at $t \approx 8 \times Rev.$, caused by the above-mentioned capillary breakup from long ligaments (i.e., multiple drops being produced simultaneously). Furthermore, Figure 4.9b,h provide clear evidence that, when

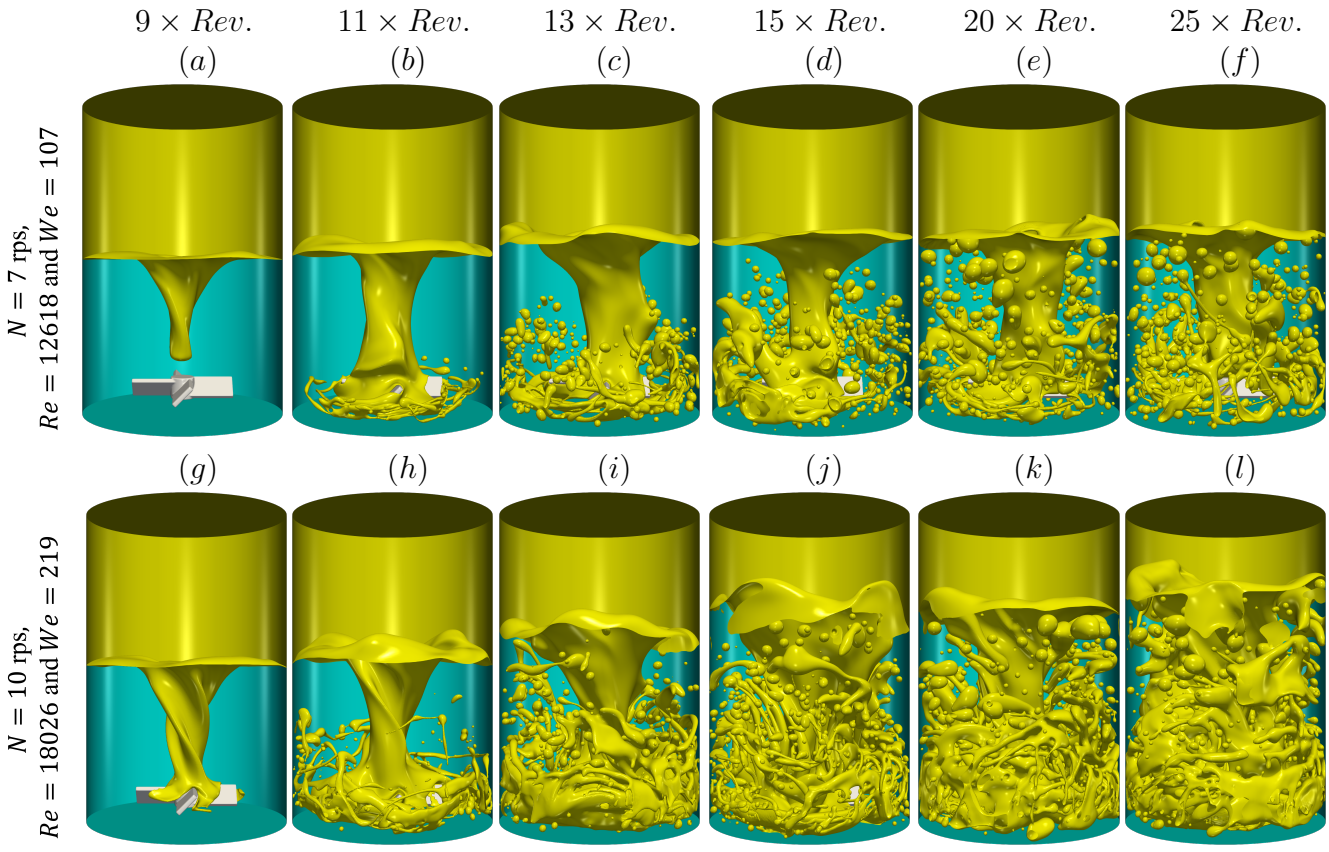


Figure 4.9: Spatio-temporal evolution of the interface toward the development of an oil-in-water emulsion for $(Re, We) = (12618, 107)$ and $(18026, 219)$ shown in the top and bottom panels, respectively, for $t = 8-25 \times Rev.$ in $(a) - (f)$, respectively. This figure is reproduced from Liang et al. [2022].

the rotation frequency is increased, a larger part of the deforming interface attaches to the impeller and therefore more ligaments are produced, which corresponds to the steeper increase in drop counts. After that, the number of dispersed oil drops for $N = 5$ RPS falls off gently since the deforming interface no longer makes contact with the impeller while dispersed drops tend to coalesce with the oil overlaying the aqueous phase. This is not the case at higher impeller speeds as the drops "lost" due to coalescence are replenished via continual ligament formation and subsequent breakup; hence, the dispersed oil drop count continues to increase for $N > 5$ RPS. In addition, for cases with $N \geq 8$ RPS, an overshooting peak is observed prior to the number decreasing towards a statistical steady-state. This phenomenon could be attributed to the fact that the large amount of ligaments and drops produced simultaneously increases the coalescence probability in the system, which thereby leads to a stage where the coalescence rate is larger than the breakup rate, giving rise to the reduction in drop counts. For all cases, the drop count eventually reaches a steady number which corresponds to the balance between coalescence and breakup rates.

Though the over-shooting peak of drop count increases with higher rotation frequencies, it is evident from Figure 4.10 that the number of dispersed drops (at the last simulated time-step) has a non-monotonic dependence on the impeller speed, for example, $N = 7$ RPS has higher drop count (≈ 550) than that for $N = 10$ RPS (≈ 350). On the other hand, the interfacial

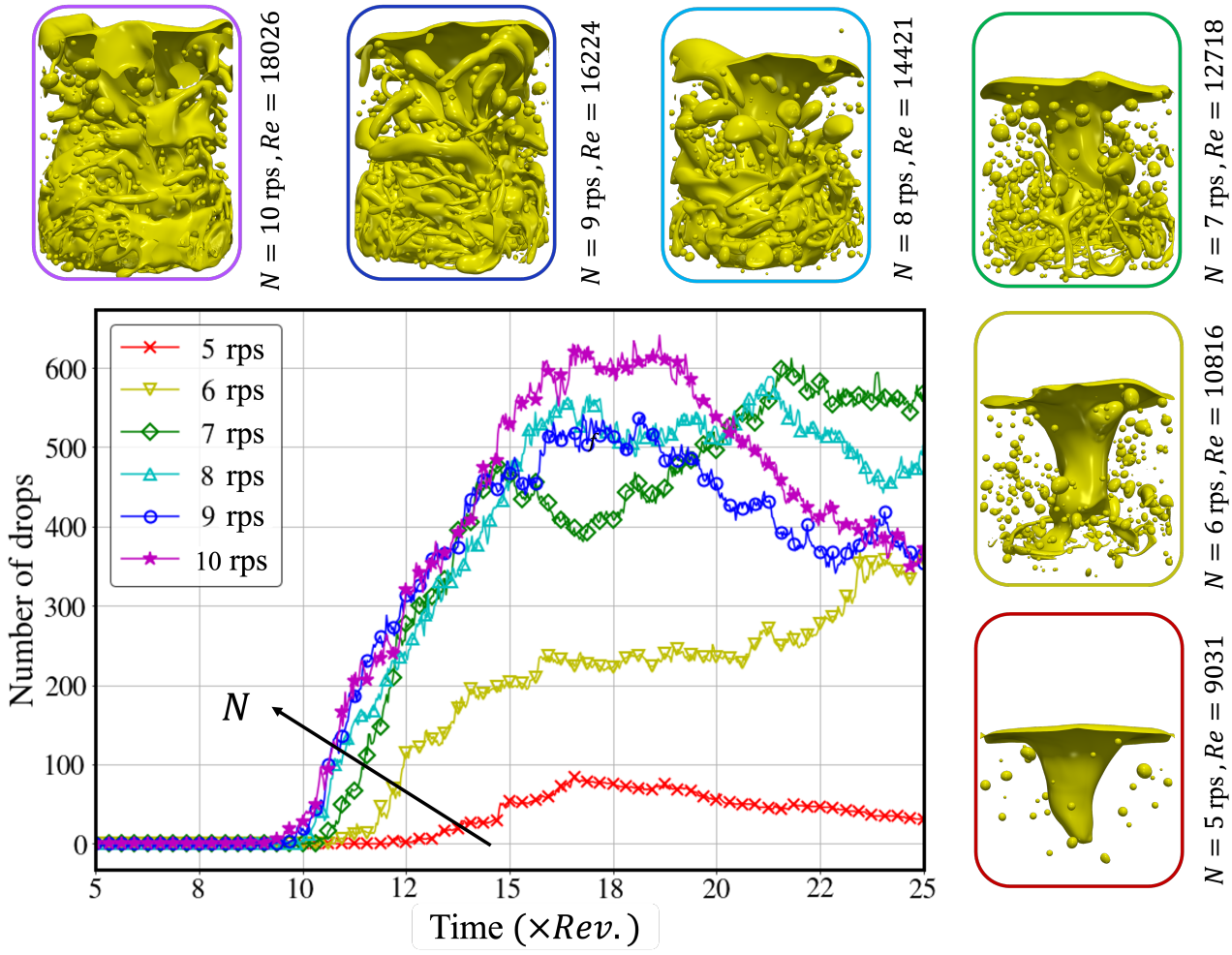


Figure 4.10: Temporal evolution of the number of dispersed drops for frequencies $N = 5, 6, 7, 8, 9, 10$ RPS, which correspond to $Re = 9013 - 18026$ and $We = 55 - 219$. Snapshots of the interface shapes at $t = 25 \times Rev.$ are also presented for each frequency. The black arrow indicates the earlier drop occurrence and the steeper increase from a zero drop count when the impeller speed is increased. This figure is reproduced from Liang et al. [2022].

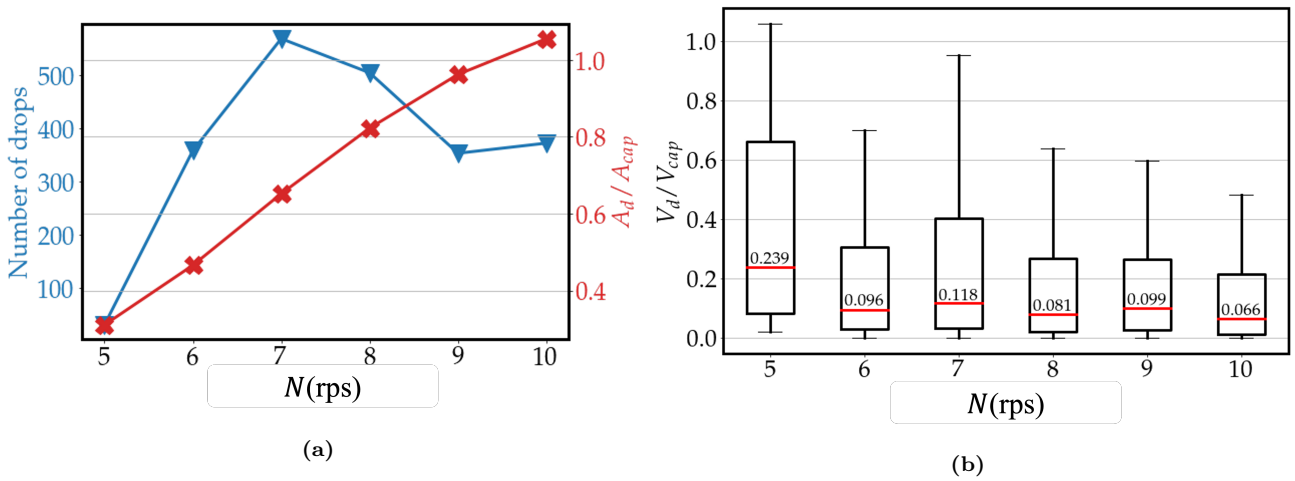


Figure 4.11: (a) Number of drops (blue line, inverted triangle markers) and interfacial area (red line, cross-shaped markers) of dispersed oil phase. (b) Box plot distribution of the drop size (outliers are not shown here), at $t = 25 \times Rev.$ for frequencies $N = 5, 6, 7, 8, 9, 10$ RPS, which correspond to $Re = 9013 - 18026$ and $We = 55 - 219$. Here, the median value of V_d/V_{cap} is indicated by the horiztonal red lines. This figure is reproduced from Liang et al. [2022].

area of dispersed phase at steady state ($t = 25 \times Rev.$) shows no such trend as presented in Figure 4.11a. This interfacial area is calculated as A_d/A_{cap}, where A_d refers to the interfacial area of all dispersed drops and A_{cap} is the surface area of a sphere whose diameter corresponds to the capillary length scale, $\lambda_c = \sqrt{\sigma_s/\Delta\rho g}$; here, $\Delta\rho$ is the difference in density between the oil and aqueous phases. The interfacial area appears to be proportional to the increased impeller speed (up to $N = 10$ RPS) even though the number of dispersed drops reaches its peak at an intermediate frequency ($N = 7$ RPS). The reason for this could be that at larger impeller speeds, long ligaments, with larger interfacial areas, dominate the dispersed-phase morphology (see Figure 4.9). From Figure 4.11a, the optimal impeller speed can be selected depending on the relative importance of the interfacial area and dispersed drop number to the particular application in question.

Moreover, We examined the drop size distribution for all frequencies ($N \geq 5$ RPS) at $t = 25 \times Rev.$ Herein, a dimensionless "drop" size is defined as V_d/V_{cap}, where V_d represents the volume of a dispersed phase entity (which can be a deformed drop or a ligament) and V_{cap} is the sphere volume with the capillary length (provided above) as its diameter. A box plot distribution of V_d/V_{cap} at $t = 25 \times Rev.$ is presented in Figure 4.11b, indicating that the overall trend is that an increase in impeller speed leads to a narrower distribution and smaller median drop size; this is consistent with the conclusion reported in previous studies [Pacek et al., 1998, Zhou and Kresta, 1998]. This trend is also demonstrated in Figure 4.12 where the fitted drop size distribution is plotted against logarithmic V_d/V_{cap}. For $N = 5$ RPS, the drop size is best fitted to a normal distribution, while for higher impeller speeds, the drop size follows a generalised logistic distribution. The narrow distribution for $N = 5$ RPS indicates that relatively large (median value to the left Figure 4.12) drops of well-distributed size are produced; on the other hand, with increasing impeller speed, the median drop size moves to smaller sizes, while a skewed shape towards the more frequently produced small drops is observed. Additionally, a

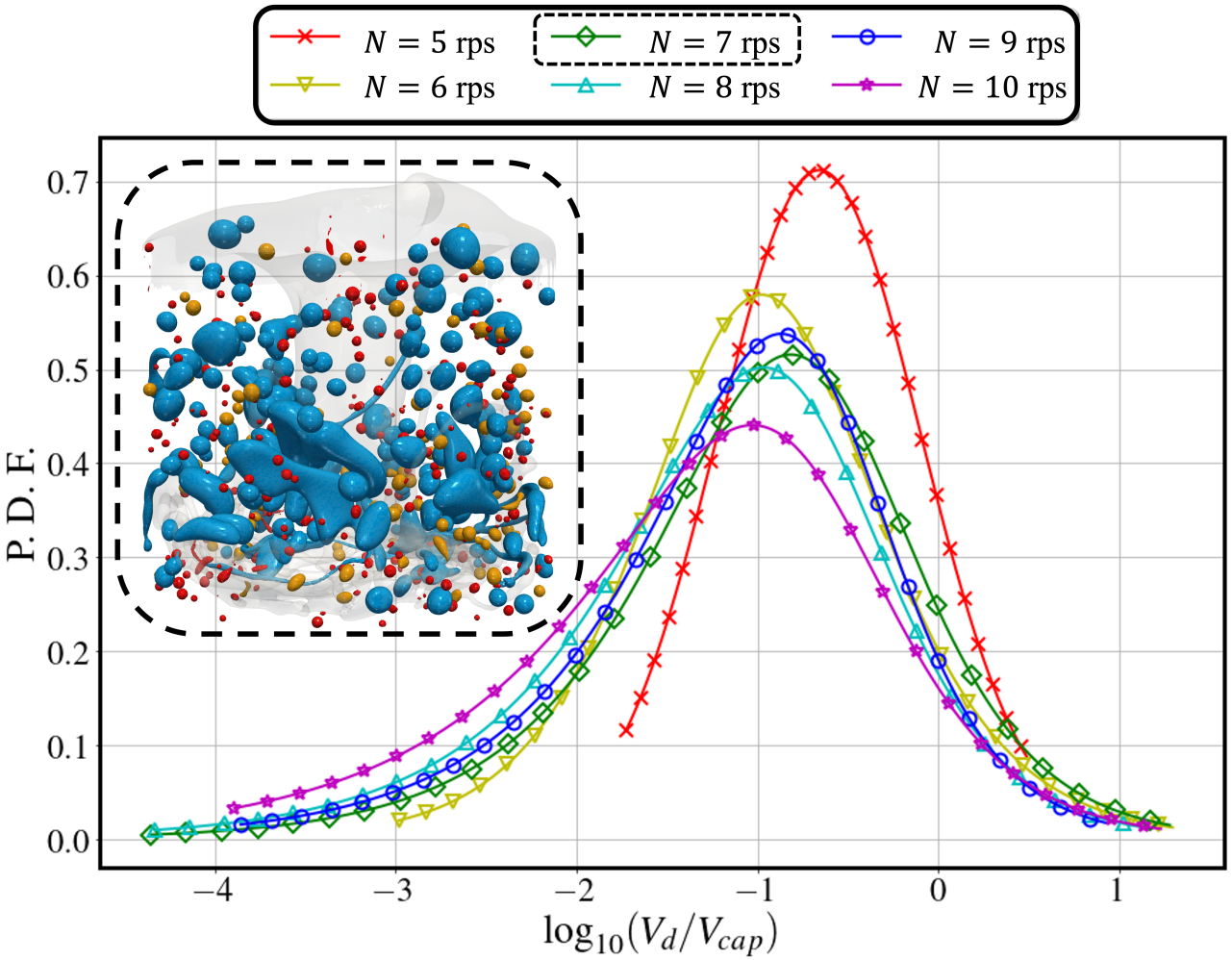


Figure 4.12: Drop size distribution of the dispersed oil phase at $t = 25 \times Rev.$ for $N = 5, 6, 7, 8, 9, 10$ RPS ($Re = 9013 - 18026$ and $We = 55 - 219$). The attached image shows a drop size map for $N = 7$ RPS at $t = 25 \times Rev.$ where all the dispersed phases are coloured by red, yellow and blue according to their size as small, moderate and large, respectively. This figure is reproduced from Liang et al. [2022].

drop size map for $N = 7$ RPS is also shown in Figure 4.12, wherein all the dispersed-phase entities are classified into three size categories and coloured accordingly. This gives a clear indication that "large-sized" drops contain the long ligaments that have not broken up entirely, whereas the "small-" and "moderate-sized" drops are composed of individual droplets of various sizes.

4.2 Concluding Remarks

In this chapter, the effect of impeller rotational speed on the complex interfacial dynamics during oil-water mixing in a stirred vessel with a 4-pitch-blade turbine has been studied, using high-fidelity three-dimensional simulations. The rotational speeds in the range of $N = 1 - 10$ RPS were explored, which correspond to Reynolds and Weber number ranges of $Re = 1802 - 18026$ and $We = 2.19 - 219$, respectively. We have shown that the interface shape and vortical structures within such a system are strongly dependent on the impeller speed. In particular, we have demonstrated the possibility of using vortex breakdown as an indicator that the interface undergoes little breakup due to very little interaction with the impeller.

In addition, we have also conducted a comprehensive analysis of drop size across the entire frequency range investigated, examining the temporal evolution of dispersed drop number and its size distribution at steady state. The results show that it is effective to select impeller speed given the specific requirements of the application at hand.

Chapter 5

Oil-water emulsion formation in stirred vessels: the effect of surfactant

Contents

5.1 Adopted Values of Dimensionless Parameters 98

5.2 Results and Discussion 100

5.2.1 Surfactant effect on interface evolution 100

5.2.2 Comparative statistics 108

5.2.3 Effect of surfactant elasticity, β_s 111

5.2.4 Effect of surfactant solubility, Bi 114

5.3 Concluding Remarks 117

Overview

This chapter presents a discussion of the simulation results surrounding surfactant-laden mixing systems, starting with a comparison of the current predictions against the previous chapter where we studied the flow profiles and interfacial dynamics inside a surfactant-free agitated vessel. Relevant validation has been presented in Section 3.1.5.2. Using qualitative visualisation and quantitative statistics (i.e., time evolution of dispersed entity number and drop size distribution at the instant where the simulation is terminated), the comparison provides an insight into how the presence of surfactant modifies the liquid dispersion process in the studied system. We then demonstrate the effect of surfactant elasticity (β_s) and Biot number (Bi) via two sets of parametric studies.

5.1 Adopted Values of Dimensionless Parameters

In the previous chapter, the interface evolution is investigated under a range of impeller speeds, $N = 1 - 10$ RPS. In this chapter, the impeller speed is fixed to $N = 5$ RPS, since the current focus is on the effect of surfactant. This gives values of $Re = 9013$, $We = 55$, and $Fr = 0.1$.

The large Weber number indicates the heavy dominance of inertial forces in the system; in addition, as presented in the section 4.1.1, complex interacting structures (or vortices) are generated. Hence, the studied system, especially the region near the impeller, is treated as turbulent, where the physics we extract is therefore generic to turbulent oil-water emulsification in stirred vessels.

To investigate the surfactant effect, we first set up a "base" surfactant-laden case with surfactant-related parameters fixed to $C_0 = 4 \times 10^{-4}$mol m^{-3}, $k_a = 6.68 \times 10^4$ m^3 mol$^{-1}s^{-1}$, $k_d = 3.14s^{-1}$, and $\Gamma_\infty = 1 \times 10^{-5}$mol m^{-2}. In particular, C_0 is calculated via $C_0 = \Gamma_\infty / R$, where R is the radius of the impeller, as a reference bulk concentration, which is also chosen as its initial value. Typical values for the surfactant adsorption and desorption coefficients, k_a and k_d, are quoted from relevant reviews provided in [Pan et al., 1998, Dong et al., 2000, He et al., 2015], where k_d is claimed to be within the range of $O(10^{-4}) < k_d\,[s^{-1}] < O(10^2)$ depending on the chemical structure of the surfactant molecules, while k_a is in the range $O(10^{-1}) < k_a \left[\text{ m}^3 \text{ mol}^{-1}s^{-1}\right] < O(10^6)$. In the base case, k_a and k_d are selected as the listed values exploring the scenario where the surfactant is inclined to adsorb onto the interface, with a ratio of adsorption to desorption $k = k_a C_0 / k_d \approx 10$. In this limit, combined with the value of Bi via k_d/N ($= O(10^{-1})$ indicating a fast convection driven by ambient flow in comparison to surfactant desorption), the adsorbed surfactant can approximately perform as an insoluble layer. In addition, the maximum packing concentration at the interface is set to $\Gamma_\infty \approx O(10^{-5})$ mol m^{-2}, as the same order of magnitude reported in experimental results for the surfactant such as Sodium Dodecyl Sulphate (SDS) [Chang and Franses, 1995]. This gives the values of $\beta_s \approx 0.7$ computed using the room temperature, $T = 298.15K$, and $h \approx 0.5$.

Table 5.1: Parameter values used in the two parametric studies surrounding β_s and Bi.

Case	β_s	Bi	
1	0.5		
2	0.7	$O(10^{-1})$	0.1
3	0.9		
4			0.001
5		$O(10^{-3})$	0.002
6	0.7		0.004
7		$O(10^{-2})$	0.01
8		$O(10^0)$	1

In this chapter, the values of β_s and Bi are varied to investigate the effects of surfactant arising from its sensitivity and solubility. Specifically, an upper and lower limit of β_s, in addition to the base case, are explored in the former case (i.e., $\beta_s = 0.5, 0.7, 0.9$), whereas five additional cases with regard to the Bi are considered by changing the k_d. The latter parametric study covers a range of Bi, from $O(10^{-3})$ to $O(10^0)$. From Equation 3.37, with a smaller Bi, the k_d decreases, resulting in slower surfactant desorption from the interface. Consequently, the surfactant solubility is lowered, indicating that more surfactant species tend to remain on the interface. Meanwhile, the upper limit for Bi in this context is set to unity. This is determined by the numerical solver used herein, where the source term, $\tilde{J}$, in Equation 3.32 governing the surfactant transport at the interface, is expressed as $\tilde{J} = \text{Bi}\left[k\tilde{C}_{\text{sub}}(1-\tilde{\Gamma}) - \tilde{\Gamma}\right]$ [Shin et al., 2018]. This equation corresponds to a kinetic-controlled system [Jin et al., 2006], as opposed to a diffusion-controlled system [Jin and Stebe, 2007]. Hence, the relative significance of surfactant transport in the system requires that

the adsorption-desorption process to be inherently slow compared to the interface convective flux [Eggleton and Stebe, 1998], i.e., $Bi < 1$. The values of relevant parameters in the two sets of studies are detailed in Table 5.1.

We also fix both Peclèt numbers in the bulk and on the interface as $Pe_b = Pe_s = 4.6 \times 10^2$. This comes from the recent remarks from [Kamat et al., 2018, Constante-Amores et al., 2021,] stating that negligible effect arises from Pe_s when it is increased further above 10^2; on the other hand, a Pe_b is kept equal to Pe_s as suggested in [Constante-Amores et al., 2021], which also follows the guideline given by Ratulowski and Chang [1990] to achieve a balance between adsorption and interfacial convection, assuring both convective and diffusive transport are resolved in the simulated system. It is also worth noting that the values of both Peclèt numbers are not comparable in the order of magnitude to those reported in experimental works.

5.2 Results and Discussion

Recall that the liquid dispersion in the studied configuration, with an impeller speed $N = 5$ RPS, consists of steps: (1) interface deformation, (2) ligament formation, (3) drop breakup, and (4) cessation of interface-impeller contact. This part compares three cases regarding these interface evolution steps including (1) surfactant-free system from previous chapter, (2) surfactant-laden I($|\tau| > 0$), and (3) surfactant-laden II with Marangoni stress turned off ($|\tau| = 0$). The last case is set up by eliminating the term $\nabla_S \sigma$ from Equation 3.21, which allows us to unequivocally elucidate the mechanisms by which the interfacial tension reduction and surfactant concentration gradient act in tandem to modify the surfactant-free interface dynamics.

5.2.1 Surfactant effect on interface evolution

5.2.1.1 Step 1: Interface deformation

Figure 5.1 presents the interfacial shapes at early times ($t = 8.5 - 12 \times Rev.$) for the three cases, where the interface begins to deviate from its flat position, and a few dispersed entities are formed. The first observation from the figure is that the deformation of the surfactant-laden interface (I) is accelerated compared to its surfactant-free counterpart (see Figure 5.1a, b and f, g). This is expected since the presence of surfactant reduces the average interfacial tension, and therefore, promotes the interface deformation under the same flow condition.

However, Figure 5.1c, and h show that the deforming interface for the two cases subsequently reach similar positions (relative height in the vessel). To better delineate this observation, Figure 5.2a depicts the deformation by plotting the temporal evolution, in terms of minimum position of the interface and the corresponding axial component of interfacial velocity at that position (as schematically shown in Figure 5.1a). The position refers to the relative height in the cylindrical vessel which is scaled using the vessel height, $\tilde{z} = (2z - H)/H$, and only the magnitude of velocity is plotted as $|u_z|$, since it always points downward during this step. As presented, while the interface approaches the impeller (reflected as decreasing $\tilde{z}$), $|u_z|$ increases

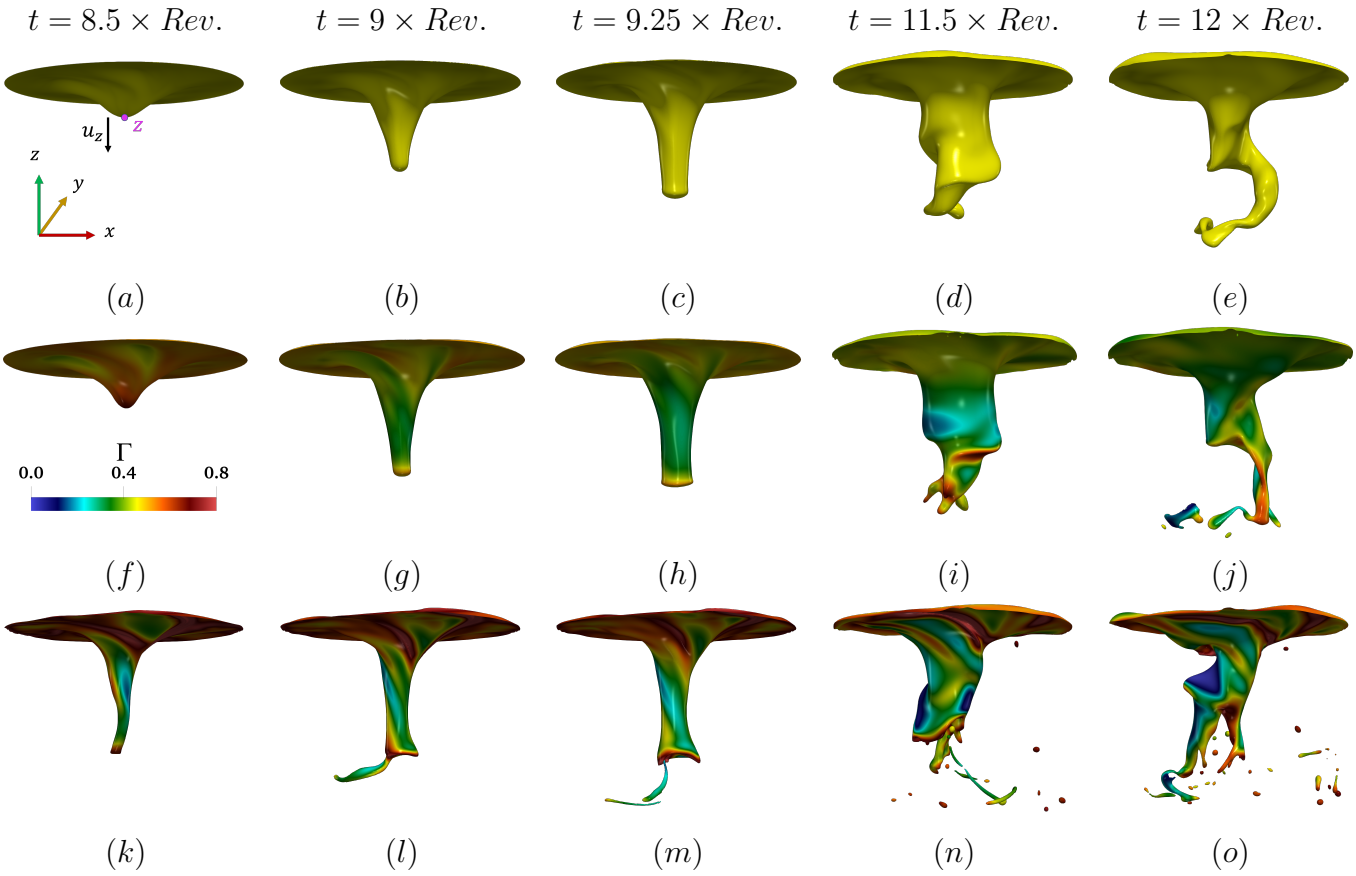


Figure 5.1: Comparative evolution of interfacial shapes for the surfactant-free (top), surfactant-laden I ($|\tau| > 0$, middle) and surfactant-laden II ($|\tau| = 0$, bottom) systems for $t = 8.5 - 12 \times Rev$. The interface is coloured by the magnitude of Γ. The values of surfactant-related parameters correspond to the "base" case (see Section 5.1). This figure is reproduced from Liang et al. [2023].

to a peak value and then a reduction occurs. A similar conclusion as above, that the accelerated deformation is associated with the surfactant-laden interface (I), can be made prior to the velocity peak. It is also evident that the subsequent decrease in $|u_z|$ is more significant for the surfactant case I. This can be explained by the fact that surfactant on the deforming interface is accumulated at its minimum position, namely the descending leading edge of the interface, which introduces an opposing Marangoni stress pointing upward. Figure 5.2 exemplifies the surfactant distribution on the interface at $t = 9 \times Rev$. As shown, the induced Marangoni stress, which opposes the downward flow at the vessel center, acts to decelerate the interface deformation. A possible explanation to the overall acceleration prior to the velocity peak can be the dominance of the inertia, namely the strong downward flow where the retraction driven by the Marangoni stress is negligible. After that, the interface reaches the vicinity of the impeller, at which the flow field begins to develop radially, and therefore the vertical deformation of interface slows down. Thus the retarding effect of the Marangoni stress [Eggleton et al., 2001, Kamat et al., 2018] commences to function, causing the further decrease in $|u_z|$ seen for the surfactant-laden case I. This process of deformation is clearly depicted via $\tilde{z}$ in Figure 5.2*a* that, at $t = 10 \times Rev.$, the surfactant-laden interface (I) reaches the same height in the vessel as the surfactant-free interface after the acceleration and the subsequent deceleration.

Furthermore, the effect of Marangoni stress demonstrated above can be better appreciated via

the surfactant-laden system II. The visualisation of the Marangoni-free interface indicates that Marangoni stress plays a role in retaining the plump and thick shape of the deforming interface as well as the relatively uniform surfactant concentration over the interface. The evidence can be seen in Figure 5.1*k*, which indicates that the Marangoni-free interface is in a slender shape with varying interfacial surfactant concentration, as opposed to what is shown for the surfactant-laden system in the presence of Marangoni stress. Additionally, from Figure 5.2*a*, decelerating deformation occurs for the Maranogi-free system while the interface is near the impeller. However, the "braking" (i.e., $|u_z| \to 0$ and negligible change in $\tilde{z}$) observed for the other two cases no longer takes place, which provides additional support to the previous statement that Marangoni stress leads to further deceleration of interface deformation in addition to that which arises due to the radially-developing flow field.

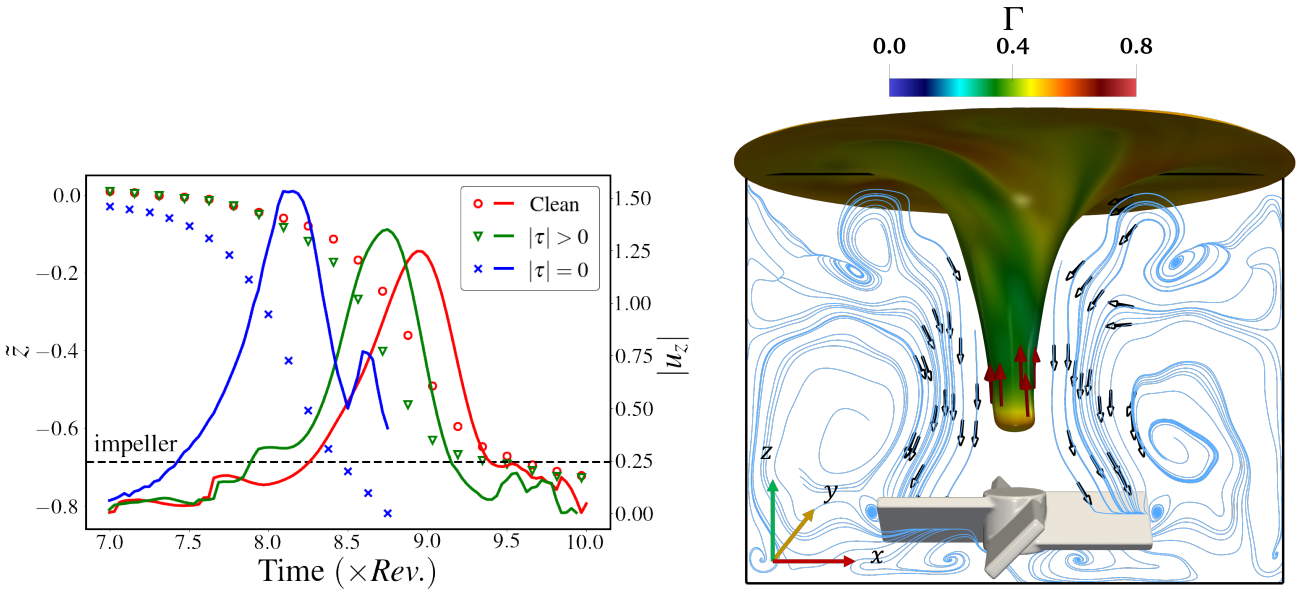
Another interesting phenomenon is the formation of the "branches" at the surfactant-laden interface (I) (see Figure 5.1*i*). Such an observation can be related to the fact that given the underlying flow described previously, which develops towards the vessel wall, ligaments are prone to be formed elongating radially behind the impeller hub. Furthermore, this can be better demonstrated using the flow topology parameter, $\mathcal{Q}$, which was first used in [Perry and Chong, 1987] and recently became popular in the field of multiphase flows [Soligo et al., 2020]. This parameter helps distinguish among the three types of flow topology locally, and is computed using the rate-of-deformation, $\boldsymbol{\mathcal{S}}$, and rate-of-rotation tensors, $\boldsymbol{\Omega}$:

$$\mathcal{Q} = \frac{\boldsymbol{\mathcal{S}}^2 - \boldsymbol{\Omega}^2}{\boldsymbol{\mathcal{S}}^2 + \boldsymbol{\Omega}^2} \begin{cases} = -1, & \text{for rotational flow} \\ = 0, & \text{for shear flow} \\ = +1, & \text{for elongational flow,} \end{cases} \tag{5.1}$$

where $\boldsymbol{\mathcal{S}}^2 = \boldsymbol{\mathcal{S}} : \boldsymbol{\mathcal{S}}$ and $\boldsymbol{\Omega}^2 = \boldsymbol{\Omega} : \boldsymbol{\Omega}$; $\boldsymbol{\mathcal{S}}$ and $\boldsymbol{\Omega}$ can be calculated from the velocity gradient tensor $\nabla \mathbf{u}$:

$$\boldsymbol{\mathcal{S}} = \frac{\nabla \mathbf{u} + \nabla \mathbf{u}^T}{2},$$
$$\boldsymbol{\Omega} = \frac{\nabla \mathbf{u} - \nabla \mathbf{u}^T}{2}.$$

Figure 5.3 compares the probability density function (P.D.F.) of parameter $\mathcal{Q}$ at the surfactant-free and surfactant-laden interfaces (I) at $t = 11.5 \times Rev.$, corresponding to Figure 5.1*d* and *i*, respectively. In this case, the statistics are only computed at the interface, which exclude the effect of internal and external flow enabling us to isolate the flow modification induced by the interfacial tension reduction. Nevertheless, albeit not presented herein, negligible difference is observed in terms of the internal and external flow types for both systems (dominated by the pure shear flows), which indicates that the different flow type experienced by the interface comes from the different interface location between the two cases. As seen from Figure 5.3, from a surfactant-covered interface (I), there is a decreasing possibility of seeing elongation-dominated flow, while a large probability to experience shear-like flow is observed.



(a) (b)

Figure 5.2: (*a*) Temporal evolution of the interfacial deformation for the three studied cases for $t = 7{-}10 \times Rev.$ regarding the minimum position of the deforming interface ($\tilde{z}$ shown by symbols) and the magnitude of the velocity of the vertical interface deformation ($|u_z|$ shown by lines); (*b*) the interplay between the flow field (streamlines in blue along with black arrows representing their directions) at the vessel center and the induced Marangoni stresses (red arrows) at the deforming interface for $t = 9 \times Rev$. The interface is coloured by the magnitude of Γ. The surfactant-related parameter values remain unchanged from Figure 5.1. This figure is reproduced from Liang et al. [2023].

This could be a possible explanation for "branch" formation as the deforming interface is more likely to be torn apart, rather than being stretched, under the modified flow topology. Consequently, these "branches" give way to ligament development accompanied by dispersed drop production via a surfactant-induced tip-streaming mechanism (more discussion in the following section 5.2.1.2). In contrast, as shown in Figure 5.1*e*, the surfactant-free interface keeps elongating and thinning, following a helical trajectory due to the impeller rotation, until the first ligament is formed ($\approx 12.375 \times Rev.$, which is not presented in the figure).

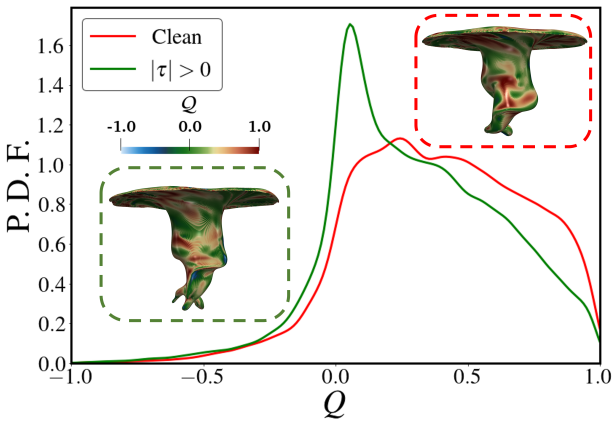


Figure 5.3: Probability density function of parameter $\mathcal{Q}$ for surfactant-free and surfactant-laden I interfaces at $t = 11.5 \times Rev$. The interfaces are coloured by $\mathcal{Q}$. The surfactant-related parameters are the same as in Figure 5.1. This figure is reproduced from Liang et al. [2023].

For the Marangoni-free system, a sequence of thin ligaments are produced at the minimum position of the interface (Figure 5.1*n*, *o*), all of which is a consequence of the plummeting interfacial tension that takes place in regions with surfactant surplus. These observations, once again, reflect the fact that Marangoni stress is activated to avoid surfactant from accumulating

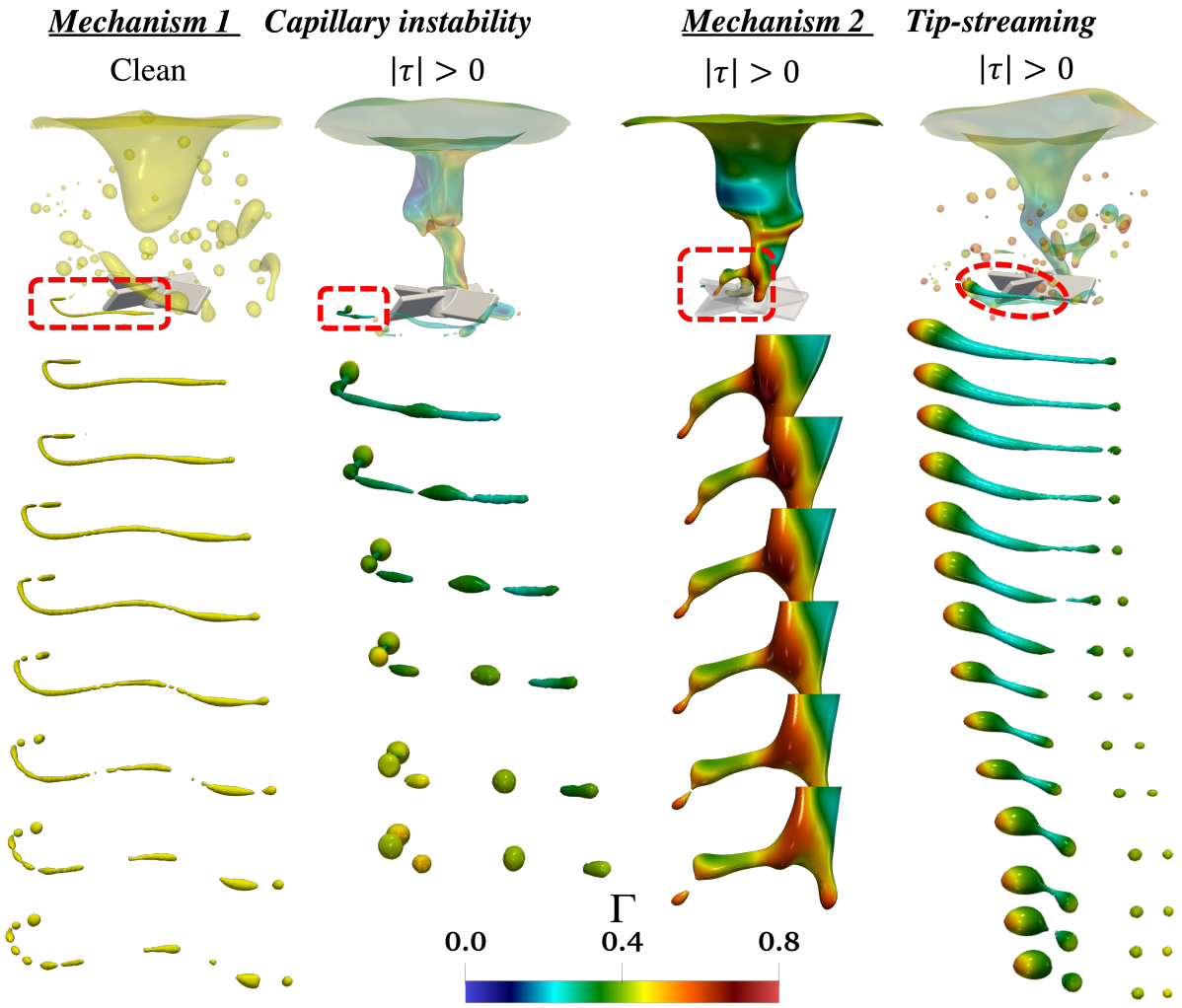


Figure 5.4: Close-up visualisations of drop breakup mechanisms observed in surfactant-free system (left) at $t = 16.375 \times Rev.$, and surfactant-laden I system, at $t = 11.625, 12.375, 15.4 \times Rev.$ (from second left to right, respectively). The presented breakup events are via the capillary instability (left two columns), and surfactant-enhanced tip-streaming (right two columns). Two scenarios for tip-streaming are given, one initiated from the deforming interface and another from an elongated ligament. The surfactant-related parameters remain unchanged from Figure 5.1. This figure is reproduced from Liang et al. [2023].

in excess at the minimum position of the interface. The absence of this phenomenon is directly responsible for the "free" escape and detachment of ligaments from the deforming interface, as seen in Figure 5.1m, n.

5.2.1.2 Step 2 & 3: Ligament and drop formation

As indicated earlier, during steps 2 and 3, a large amount of dispersed entities is produced via distinct mechanisms. In the previous chapter, it was demonstrated that following the ligament generation, dispersed drops in the surfactant-free system are formed via a capillary instability (see Figure 5.4), where one elongated ligament gives birth to multiple individual drops. For the surfactant-laden system I, an additional drop breakup mechanism is promoted, namely tip-streaming/dropping [Groeneweg et al., 1994, Eggleton et al., 2001]. Figure 5.4 displays the close-up visualisations of various drop breakup events observed in the surfactant-free and surfactant-laden I systems (during $t = 12 - 18 \times Rev.$), exemplifying those via capillary in-

stability and tip-streaming. For the former mechanism, two examples from different systems are presented, whereas two scenarios for surfactant-induced tip-streaming are extracted from the surfactant-laden system I. The first tip streaming is initiated from the deforming interface, which leads to an individual drop formation prior to long ligament formation, in contrast to what is observed from the surfactant-free system. This can be an influencing factor on the transient dispersed entities number profile (more details are deferred to section 5.2.2.1). Likewise, in the second case, where the breakup is from an elongated ligament, tip-streaming generates drop intermittently, leaving a large and relatively clean (i.e., covered by less surfactant) drop after emission of several drops.

An interesting feature for the Marangoni-free case is that drop breakup via capillary instability is suppressed, and dispersed drops are formed via either binary breakup from larger drops or tip-streaming from stretching ligaments. Figure 5.5*a* illustrates the effect of Marangoni stresses on the stretching ligament prior to its breakup via capillary instability (using the example shown in Figure 5.4). As presented, Marangoni stresses play different roles on each end of the ligament depending on the local surfactant distribution. First, for the ligament pole labelled as A, surfactant is accumulated at the bulbous end, which introduces a Marangoni stress towards the ligament body, impeding the formation of an individual drop. On the other hand, surfactant concentration at the pole B is lower relative to the nodule region, giving rise to a Marangoni stress pointing outward and thus enhancing the ligament elongation. From this perspective, Marangoni stress encourages the commencement of breakup events driven by capillary instability by facilitating the ligament's stretching motion and inhibiting drops from bursting at the poles. This effect, combined with the promotion of tip-streaming, leads to the observation that both breakup mechanisms exist in the surfactant-laden system I.

Nevertheless, in the case of drop deformation, it is common to see the same surfactant distribution profile as in the pole A, since the surfactant tends to be swept towards the poles. As stated in the discussion related to Step 1, Marangoni stress acts as a stabilising factor against drop formation, either delaying or even avoiding the new drop production in this step. Figure 5.5*b* provides evidence of this by comparing the behaviour of one drop located in the vicinity of the impeller at $t = 15.5 \times Rev.$ for both surfactant-laden systems (case of $|\tau| = 0$ and $|\tau| > 0$ shown at the top and bottom of the figure, respectively). The critical Weber number for drop breakup has been reported for various types of flows, which consistently lies in the range of $O(10^1)$; for instance, $\mathrm{We}_{\mathrm{crit}} \approx 1$ for turbulent emulsification [Hinze, 1955, Håkansson et al., 2022], $\mathrm{We}_{\mathrm{crit}} \approx 3 - 7$ in the cases of uni-axial shear and elongation flow [Grace, 1982] and nonuniform shear [Chin and Han, 2000]. Based on this, both drops are likely to breakup given their sizes ($D_{d,|\tau|>0} = 0.53$ cm and $D_{d,|\tau|=0} = 0.40$ cm, obtained as the corresponding sphere diameter of its interfacial area) and their local Weber numbers ($\mathrm{We}_{|\tau|>0} = 103.6$ and $\mathrm{We}_{|\tau|=0} = 93.2$, calculated with the impeller tip velocity and average interfacial tension at the interface). However, it is evident that the drop with Marangoni stress turned on retracts to its spherical shape rather than the predicted drop fragmentation according to $\mathrm{We}_{\mathrm{crit}}$. This is

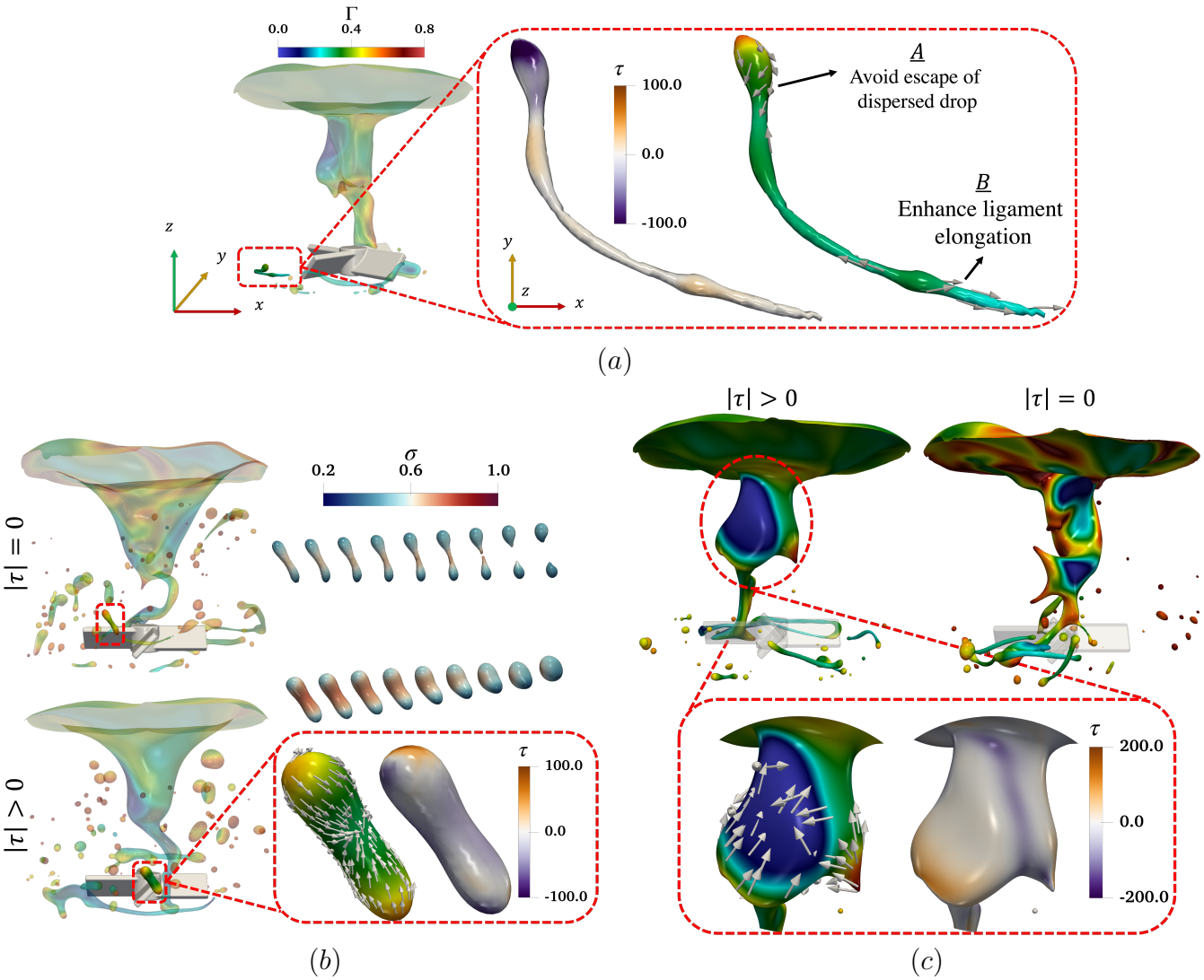


Figure 5.5: Visualisations of Marangoni stresses under different scenarios: (a) ligament elongation prior to its fragmentation towards multiple drops; (b) drop deformation where the evolving drops are coloured using σ; and (c) evolution of the deforming interface shape. The insets consist of two identical interfacial states coloured in Γ and τ, respectively; the negative sign of τ represents its direction, and the grey arrows refers to the direction of Marangoni stresses. The surfactant-related parameters remain unchanged from Figure 5.1. This figure is reproduced from Liang et al. [2023].

attributed to, as shown in the figure inset, the existence of Marangoni stress pointing from the drop poles to its equator. This comparison strengthens what has been demonstrated previously that Marangoni stress hinders elongation and induces the retraction of the drop back to its spherical shape. Furthermore, the presence of Marangoni stress reduces the deformability of the deforming interface making it more rigid as shown in Figure 5.5*c*. From the figure, surfactant is accumulated at the stretching tip of the deforming interface and is less concentrated at the belly, which establishes a surfactant concentration gradient. Consequently, the induced Marangoni stress immobilises the interface preventing it from deforming into multiple branches (as shown for the Marnagoni-free case), which is inclined to generate dispersed drops freely.

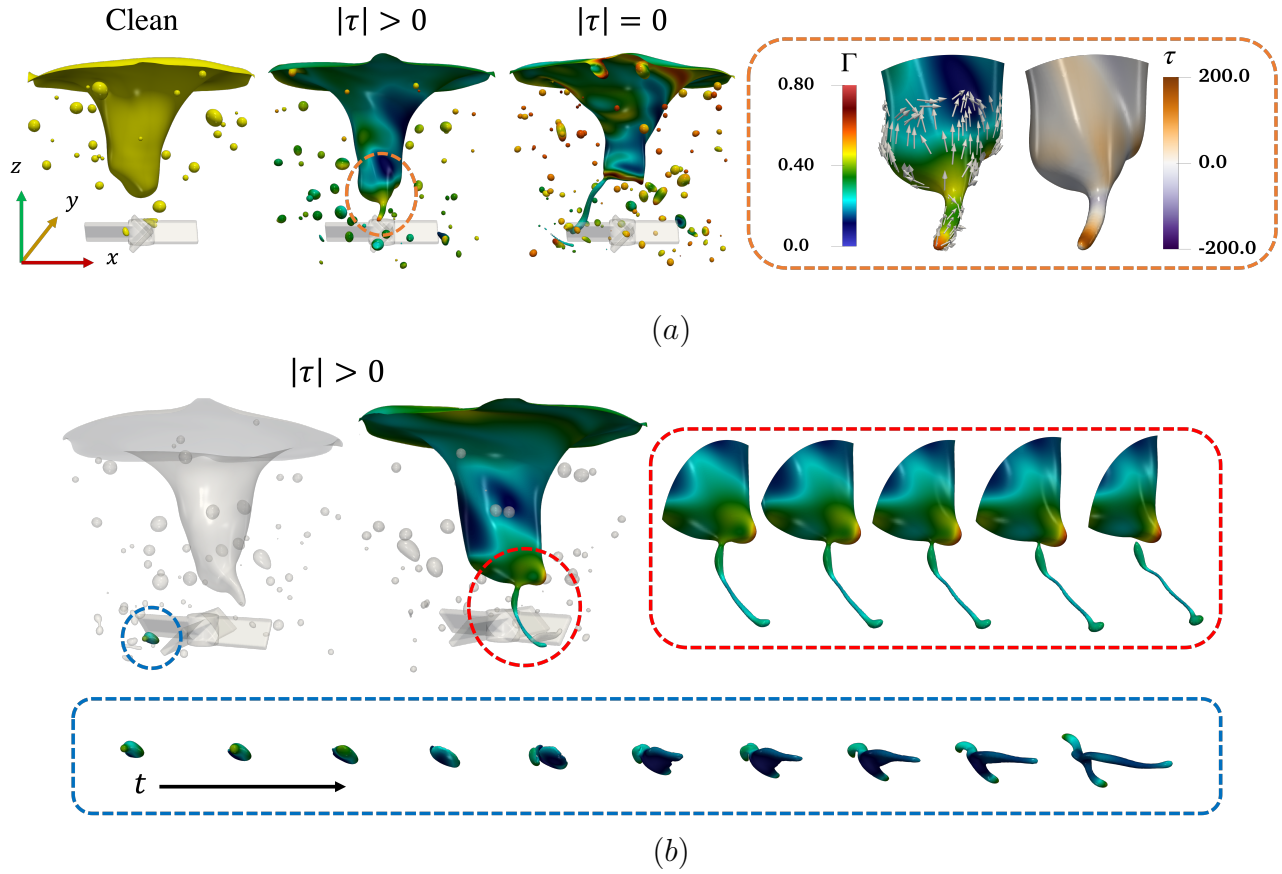


Figure 5.6: (a) Interfacial shapes for the three studied systems at $t = 25 \times Rev.$, along with a similar inset showing the direction and magnitude of Marangoni stress as in Figure 5.5; (b) exemplified interfacial evolution in the surfactant-laden I system presenting the different outcomes depending on dispersed drop behaviours: (i) coalescence: ligament formation from consequent larger drop (circled in blue) elongation; (ii) merging back with the deforming interface: recurring ligament formation (circled in red) from the deforming interface. The surfactant-related parameters remain unchanged from Figure 5.1. This figure is reproduced from Liang et al. [2023].

5.2.1.3 Step 4: Cessation of interface-impeller contact

As mentioned previously, the deforming interface retracts upward at $t = 20 \times Rev.$, leading to the cessation of interface-impeller contact thereafter. Figure 5.6*a* exemplifies the interfacial behaviours for the three cases at $t = 25 \times Rev$. As shown, the interface remains in a generally concave shape, which shows some resemblance to the Newton's Bucket flow generated in a rotating cylinder, or the air-water surface deflection in the shape of an inverted bell observed in rotating flows [Vatistas, 1990]. Herein, given the current impeller speed, the surfactant-free interface rotates following the impeller motion and no further ligaments are generated. In contrast, intermittent ligament formation is seen for the two surfactant-laden systems despite the cessation of interface-impeller contact. This is presumably caused by the surfactant accumulation at the minimum position of the interface which decreases the interfacial tension that would otherwise have counteracted ligament formation. In addition, the visualisation of interface in the presence of Marangoni stress highlights its increased rigidity (circled in orange in Figure 5.6*a*) relative to its Marangoni-free counterpart, which indicates again the immobilisin effect of the Marangoni stress aginst interfacial deformation.

It is also worth noting that the dispersed drop tends to either coalesce with one another or merge back with the "inverted bell". Each case leads to different outcomes, as exemplified by the interfacial evolution in the case of surfactant-laden system I, as displayed in Figure 5.6*b*. In the first scenario, an emergent interfacial structure (circled in blue) formed from a coalescence event is elongated by the local flow and broken up again into several smaller drops. For the latter case, ligament production from the deforming interface (circled in red) eventually recurs given that adequate dispersed drops are merged back with the deforming interface.

5.2.2 Comparative statistics

5.2.2.1 Temporal evolution of dispersed entity number

In order to quantify the qualitative interfacial behaviours described above, the transient count of dispersed entities, which could be either stretching ligament or an individual drop, is tracked. The four steps of liquid dispersion can be related to three stages of the transient number profile of dispersed entities. Figure 5.7*a* presents the number profile along with the interfacial shape at the corresponding instants. Initially, no dispersed drop (Stage A, shown by dashed lines) formation is observed during the interface deformation (Step 1) since the interface is approaching the impeller. Then, the onset of ligament formation and subsequent breakup events (Step 2 and 3) lead to a dramatic increase (Stage B, shown by solid lines) in the dispersed entity count. Finally, the cessation of interface-impeller contact (Step 4) gives rise to a gentle fall-off (Stage C, shown by dotted lines) as the dispersed drops tend to coalesce, or merge back with the overlying oil-phase (exemplified by close-up views in Figure 5.7*a*), while less or no new dispersed drops are formed.

The first distinction among the three cases is the compression of Stage A associated with a shortened duration of interface deformation. This can be explained with the accelerated interface deformation as demonstrated previously. Furthermore, it is noticeable that there exists distinguished increasing patterns at early Stage B for the three cases, as highlighted in the orange rectangle in Figure 5.7*a*. The abrupt jump seen for the surfactant-free system comes naturally from the breakup events via capillary instability. In contrast, a mild increase appears prior to the steep rise for the surfactant-laden system I, which is associated with the early drop breakup events via tip-streaming from the deforming interface. Again, the early and pronounced increase for the Marangoni-free system reflects the inhibiting effect of Marangoni stress on the drop deformation and therefore the breakup events.

During Stage B in Figure 5.7*a*, an abrupt jump in the number of dispersed entities with a larger amplitude compared to the surfactant-free system is observed in the case of the surfactant-laden system I. This is due to the onset of drop breakup events via both mechanisms (capillary instability, and concurrently, tip-streaming). However, there exits a plateau following the dramatic increase ($t \approx 15 \times Rev.$), which indicates a deceleration of the dispersed phase formation. This can be related to the fact that tip-streaming, which generates drop intermittently, is promoted in surfactant-laden system I, and consequently, some ligaments generating drops via tip-streaming

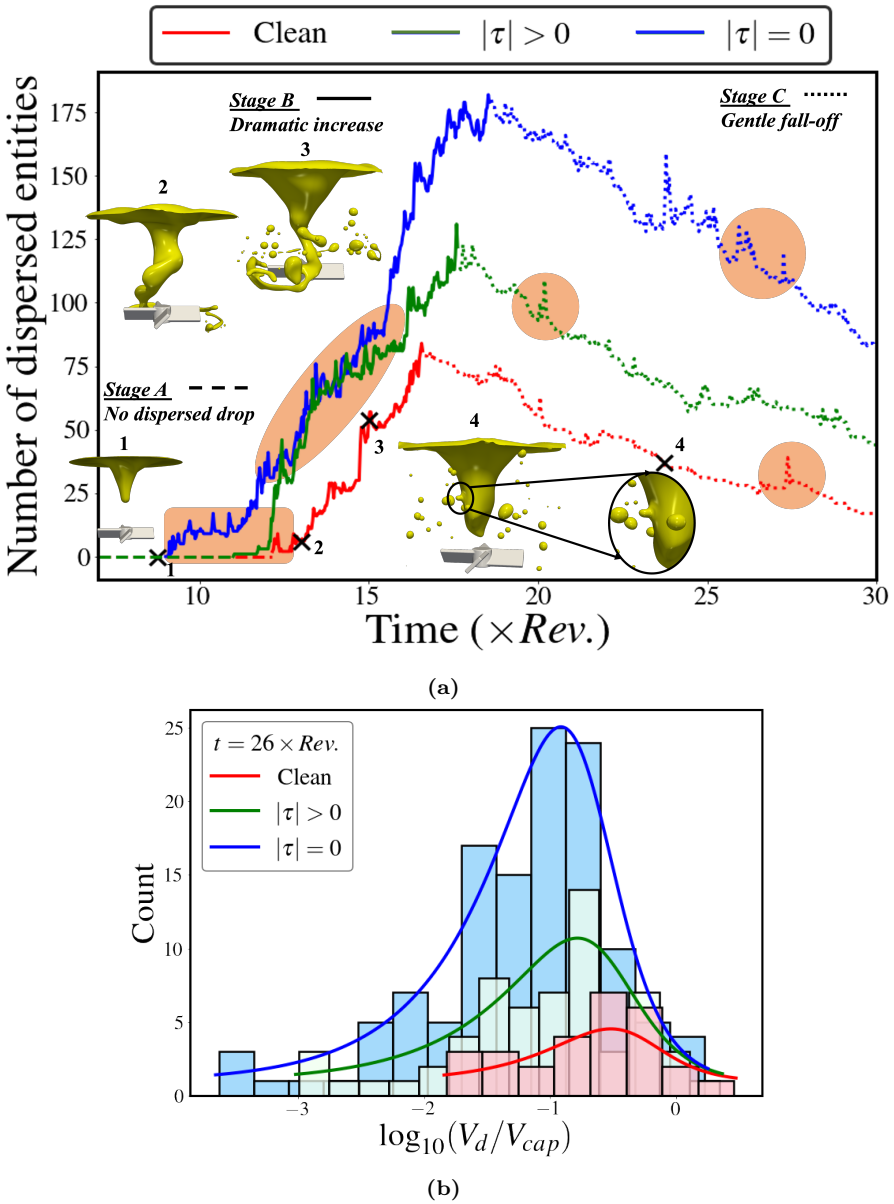


Figure 5.7: (a) Temporal evolution of dispersed entities number for surfactant-free, surfactant-laden I, and surfactant-laden II systems for a time frame of $t = 7-30 \times Rev.$, along with the representative interfacial shapes corresponding to the four steps of liquid dispersion (at $t = 9, 13, 15, 23.5 \times Rev.$, exemplified by the surfactant-free case). This profile is divided into three stages: (A) no dispersed drop, (B) dramatic increase and (C) gentle fall-off, which are respectively shown by dashed, solid, and dotted lines; (b) fitted drop size distribution (Probability Density Function with respect to log-scale of normalised drop volume) at $t = 26 \times Rev.$ for the three cases. The surfactant-related parameters remain unchanged from Figure 5.1. This figure is reproduced from Liang et al. [2023].

in that system break up into drops through capillary instability in surfactant-free system. Another interesting trend is the overlap between the two surfactant-laden cases, as highlighted in orange oval in Figure 5.7a. As demonstrated earlier, this reflects the fact that Marangoni stress aids the commencement of breakup events via capillary instability in the system with Marangoni stress turned on. Consequently, dispersed drops are generated rapidly enough to reach comparable amount to that in the Marangoni-free system, though a delayed appearance of the first dispersed drop is observed for the former system. Following the overlap, the drop count for the Marangoni-free system rises sharply until its peak. This is due to the fact that a large amount of thin ligaments are formed simultaneously from the deforming interface, along

with the drop production, which give rise to similarly increasing rate as in the case of a single breakup event via capillary instability. This provides additional evidence for the effect of the Marangoni stress on the interfacial dynamics and associated phenomena as reported in section 5.2.1.2 and Figure 5.5.

Another key aspect to highlight from Figure 5.7*a* is the appearance of humps in Stage C for all three cases (circled in orange), which can be indicative of the occurrence of dispersed interfacial structure formation, either from recurring ligament production or large coalesced drop fragmentation, as discussed in section 5.2.1.3. Eventually, the rate of drop formation and coalescence seems to stabilise somewhat, with a steady decline in the number of drops and smaller rates for the clean and Marangoni-free cases after $t = 28 \times Rev.$ compared to the onset of Stage C. From this point onward, the dynamics developing in the vessel stagnate, reducing to sporadic coalescence and subsequent breakup chains as described in section 5.2.1.3. For this reaseon, the simulations were terminated after this point.

Finally, the dispersed entities number at the instant where the simulations were terminated takes the following order: surfactant-free (17) < surfactant-laden I (43) < surfactant-laden II (82) systems. This provides further indication of the surfactant effect on the liquid dispersion in the studied configuration as summarised below:

- The reduced interfacial tension promotes tip-streaming (or tip-dropping), which contributes to the formation of more dispersed drops in the surfactant-laden system I;
- The Marangoni stress, in general, acts to counteract and retard interfacial deformation and drop deformation, which explains the larger dispersed phases number in its absence;
- The Marangoni stress encourages the breakup events via capillary instability, which commonly occurs under general emulsion scenarios [Janssen and Meijer, 1993], and, to some extent, suppresses tip-streaming.

5.2.2.2 Drop size distribution

The dispersed entities number alone is not a representative metric of the effect of surfactant in the stirred mixer. Additionally, a drop size distribution analysis at $t = 26 \times Rev.$ is carried out for the three studied cases herein, as presented in Figure 5.7*b*. The drop size definition in this part remains consistent with that in the previous chapter, i.e., the volume of a dispersed entity, V_d, normalised by the volume of a spherical drop, V_{cap}, whose diameter corresponds to the capillary length scale, $\lambda_c = \sqrt{\sigma_s/\Delta\rho g}$.

The data structure has been evaluated using quantile-quantile (Q-Q) test and box plots, and the outliers, namely non-physical tiny drops and elongating large ligaments are removed from the analysis. In the field of statistics, one commonly applies the Kolmogorov-Smirnov (K-S) test [Massey Jr, 1951] and the Anderson-Darling (A-D) test [Anderson and Darling, 1954] to examine the goodness of one population of data to fit one specific distribution; a non-parametric

analysis of variance, for example, Kruskal-Wallis (K-W) test [Kruskal and Wallis, 1952] is then used to contrast the distributions and the following Dunn's test [Dunn, 1961, 1964] specifies the distinct sets of data. Following such procedure, the filtered data sets are fitted to a logistic distributions, satisfying both the K-S test and the A-D test with a significance level of 0.05. Furthermore, K-W test is conducted to contrast the distributions, where statistical significance is implied among the three data sets. More specifically, subsequent Dunn's test determines that the Marangoni-free system is distinct from (lower than) the other two systems, as far as their medians are concerned. This finding is consistent with the prior work [Aldana and Calabrese, 2005] pointing out the manifold effect of surfactant on the average drop size, especially in mixing scenarios, as opposed to the assertion that the addition of surfactant simply reduces the interfacial tension, and therefore, the dispersed drop size. The deviation for the Marangoni-free data strengthens this statement indicating that the effect of surfactant on the drop size is not limited to lowering interfacial tension but also arises from the Marangoni stress, which plays a role in drop breakup mechanisms as demonstrated in previous sections.

Moreover, skewness and kurtosis are computed to examine the asymmetry (i.e., tail) of the distributions. First, negative skewness for all three cases signifies the left-tailed shape, which can be translated as all three cases exhibit an inclination to produce small drops. In regard to the magnitude (absolute value) of skewness, incremental skewness is obtained for the three cases following the order: surfactant-free (-0.23) < surfactant-laden I (-0.76) < surfactant-laden II (-1.01). In addition, the kurtosis indicates "heavier" tails for the same ordering, in other words, the surfacatnt-laden system II produces the largest amount of small drops, followed by the surfactant-laden I, and finally surfactant-free system. This comparison leads to a similar conclusion as above: interfacial tension reduction promotes the production of smaller drops while the Marangoni stress acts to mitigate this effect.

5.2.3 Effect of surfactant elasticity, β_s

Figure 5.8*a* and *b* provide a quantitative insight into the mixing process in systems of varying elasticity numbers by the evolution of the interfacial area (made dimensionless via the initial interface area, A_0) and dispersed phases count; *a* corresponds to the three cases with Marangoni stress turned on and *b* presents the Marangoni-free systems. It can be seen that prior to dispersed entity formation (i.e., Stage *A* defined in Section 5.2.2.1), a slight change in interfacial area is seen for both Marangoni-free system and its counterpart in the presence of Marangoni stress. This is consistent with what we demonstrated in Section 5.2.1.1 that the elongational flow experienced by the deforming interface is so strong that the effect of increasing β_s (and therefore the modified interfacial tension and Marangoni stress) is negligible during this step. After that, increasing β_s, which augments the sensitivity of interfacial tension to the surfactant concentration, generally promotes interface deformation and formation of dispersed entities (presented as incremental A/A_0 and entities count, respectively, in Figure 5.8*b*). However, these effects are only prominent prior to the fall-off (Stage *C* defined in Section 5.2.2.1). Following the onset of the fall-off, no distinguishable trend regarding either the interfacial area

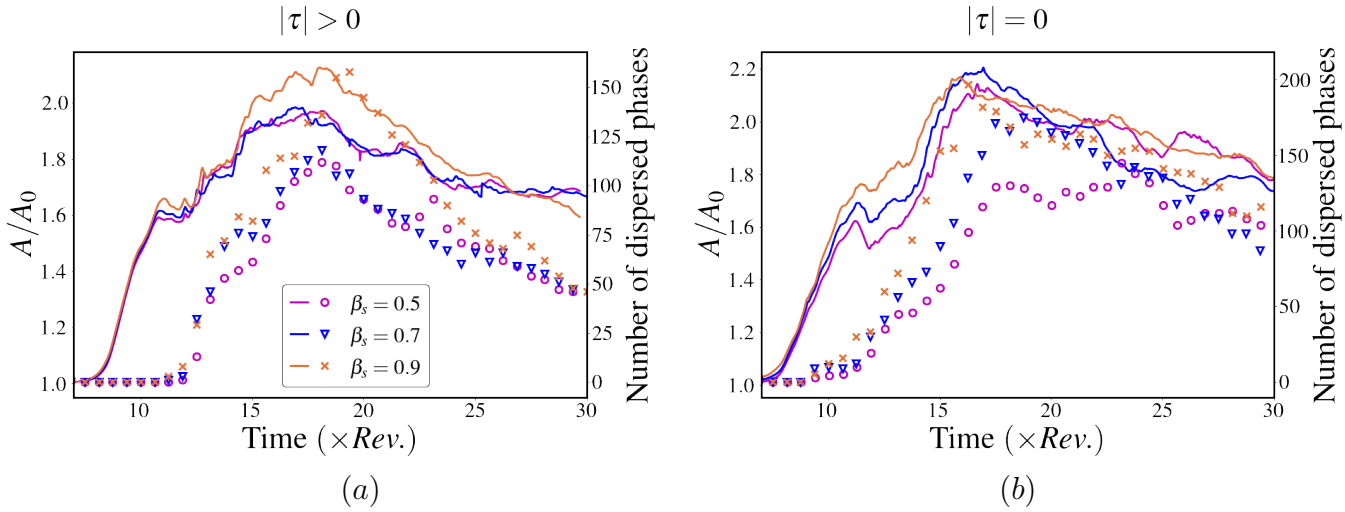


Figure 5.8: A general quantitative insight into the mixing process for the systems with Marangoni stress turned on (a) and off (b), with regard to the evolution of interfacial area (lines) and dispersed entities count (symbols). Profiles of both metrics are displayed for varying surfactant elasticity numbers $\beta_s = 0.5, 0.7, 0.9$ during $t = 7 - 30 \times Rev$. Except for the variations in β_s, the rest of the surfactant-related parameters remain unchanged from Figure 5.1. This figure is reproduced from Liang et al. [2023].

or dispersed entities count is observed for increasing β_s. Furthermore, in comparison with Figure 5.8a, the presence of Marangoni stress mitigates the effects described above. In other words, under realistic scenarios, increasing β_s from 0.5 to 0.7 leads to insignificant change in interfacial area and dispersed phases count. Instead, an obvious increase is seen in both metrics at $t = 15 - 25 \times Rev$. for $\beta_s = 0.9$, the largest β_s studied herein.

To elucidate the observations highlighted above, Figure 5.9 provides a comparison at $t = 9 \times Rev$. among the three cases with Marangoni stress turned on, in terms of surfactant-related properties on the interface. First, to gain a comprehensive insight into the surfactant property profile on the deforming interface, a quantity (for instance, the surfactant concentration, Γ), is averaged over a horizontal slice of the interface. The averaged Γ, $\bar{\Gamma}$, on a sequence of horizontal slices located at different heights of the interface, is then tracked. This leads to Figure 5.9a where the markers refer to the $\bar{\Gamma}$ over the horizontal slice at the corresponding height, as demonstrated in the schematic inset. Likewise, Figure 5.9b plots the averaged interfacial tension and the strength of Marangoni stresses along the interface (vertically). From these figures, larger β_s results in lower interfacial tension, as expected, more uniform surfactant concentration (narrower range of $\bar{\Gamma}$), and larger Marangoni stress induced along the interface. As shown in the figure, the Marangoni stress on the "waist" of the interface (labelled as a, $\tilde{z} \approx 0.6$) is larger in magnitude augmenting deformation (negative, pointing downward); likewise, that induced in the lower part of the interface (labelled as b, $\tilde{z} \approx 0.1$) is stronger retarding deformation (positive, pointing upward). Meanwhile, the retarding force exceeds the augmenting one (take $\beta_s = 0.9$ as an example, $|\tau|_b \approx 32 > |\tau|_a \approx 9$). Hence, the sum of these effects is reflected as a trivial change in interfacial area, shown as overlapping lines in Figure 5.8.

The ensuing Figure 5.9c provides a comparison of the interfacial shapes for the three cases in the presence of Marangoni stress, illustrating the cause of the significant increase in interfacial

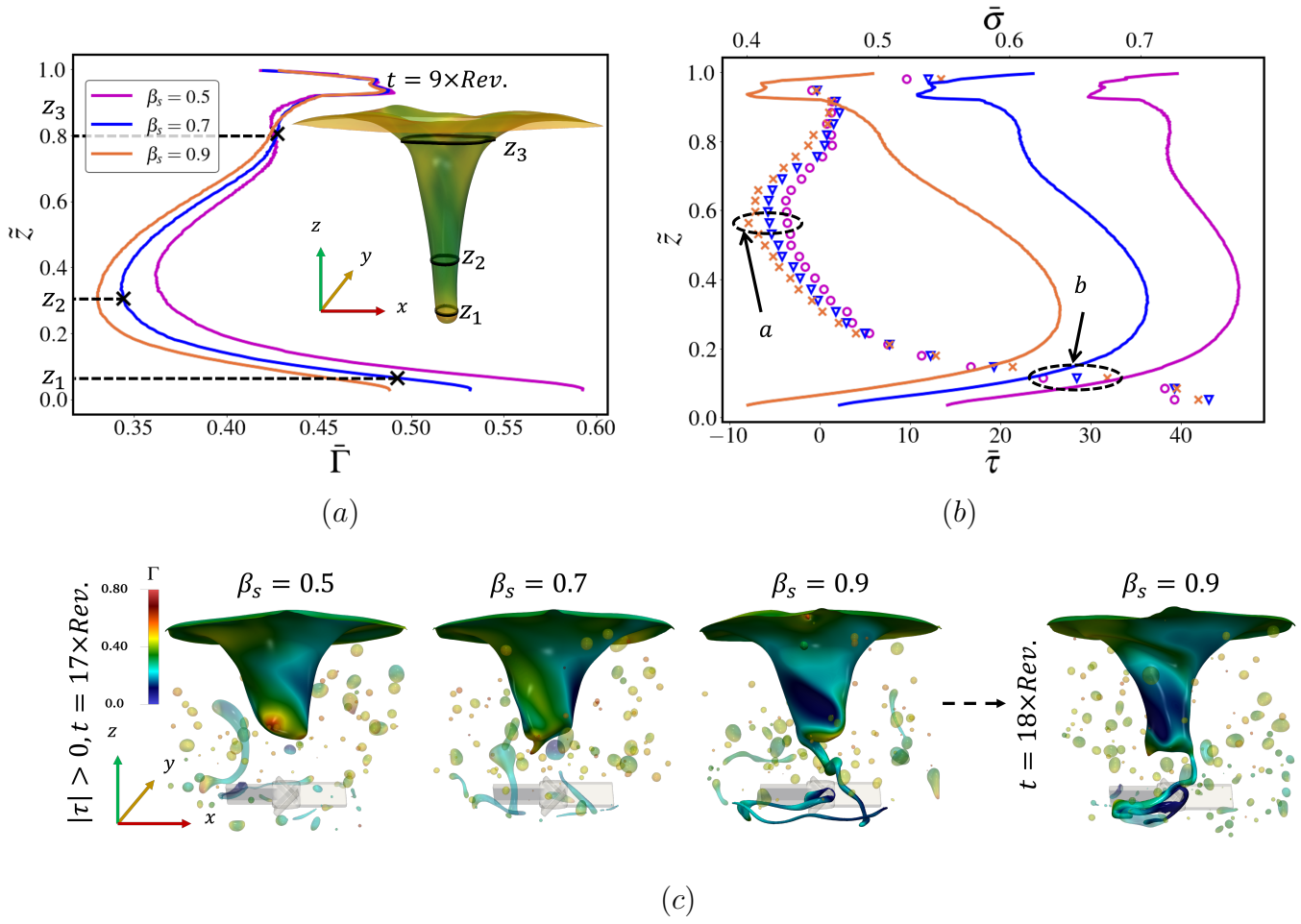


Figure 5.9: The averaged surfactant properties along the interface at $t = 9 \times Rev.$, (a) the averaged surfactant concentration, $\bar{\Gamma}$; (b) the averaged interfacial tension ($\bar{\sigma}$, lines) and the averaged magnitude of Marangoni stresses ($\bar{\tau}$, symbols). Here, $\tilde{z}$ refers to the dimensionless height on the interface, scaled using the minimum position of the deforming interface as in Figure 5.2; here, negative τ represents its direction pointing downward; (c) a comparison of the interfacial shapes for the three systems in the presence of Marangoni stress at $t = 17 \times Rev.$ Except for the β_s variations, the rest of the surfactant-related parameters remain unchanged from Figure 5.1. This figure is reproduced from Liang et al. [2023].

area and dispersed entities count for $\beta_s = 0.9$. As presented, while the deforming interfaces in the other two cases start to retract and detach the impeller hub ($t = 17 \times Rev.$), the $\beta_s = 0.9$ case exhibits an interface in the shape of a tail extending to the vessel bottom. Several long stretching ligaments are also generated, which subsequently produce multiple dispersed drops leading to a sharp increase in dispersed drop count. Such a phenomenon lasts until $t = 18 \times Rev.$ On the other hand, this feature is missing for the Marangoni-free system. This provides further indication that one of the effects exerted by Marangoni stress is to encourage drop breakup via long ligament fragmentation driven by the capillary instability (see Section 5.2.1.2).

From above, the effect of β_s is best appreciated during the intermediate period of the mixing process, which corresponds to Steps 2 and 3 of the interfacial behaviours defined in Section 5.2.1. After the cessation of the impeller-interface contact, the effect of changing surfactant elasticity diminishes as displayed in the plots at the instant where simulations were terminated; the cases associated with the three studied β_s produce similar interfacial area and dispersed entity count, for both the scenarios with Marangoni stress turned on and off. This implies

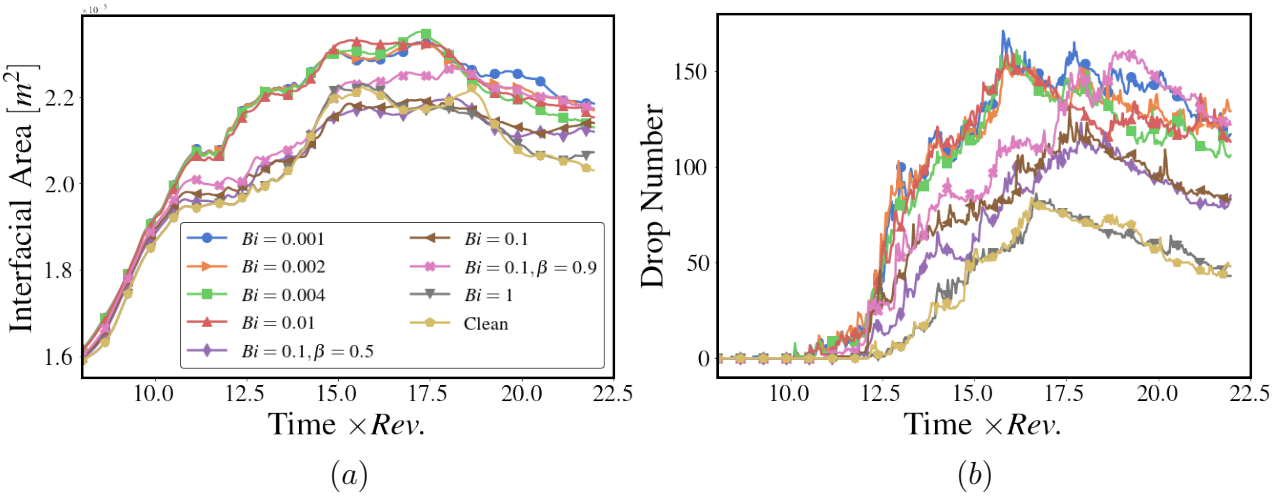


Figure 5.10: Temporal evolution of interfacial area (a) and dispersed drop number (b) for the cases with varying Bi and β_s during $t = 7 - 22 \times Rev$.

that the effect of changing β_s is more pronounced on drop dispersion compared to coalescence. It should be noted, however, that due to the complex nature of the flow considered in this part, larger computational resolution is required to recover the potential (and subtle) effect of surfactant on drop coalescence, which is beyond the discussion presented herein.

5.2.4 Effect of surfactant solubility, Bi

Similar to what have been done on β_s, Figure 5.10a and b present the evolution of interfacial area and dispersed phases count for the cases of varying Bi, respecively. In this part, the cases with changing β_s and the surfactact-free case are incorporated to provide a more comprehensive insight into the modified mixing process influenced by the two surfactant parameters. As shown in Figure 5.10a, prior to Stage A, no clear distinction among all the cases studied is observed. This is attributed to the same fact as demonstrated previously that the strong elongational flow prevailing at this stage mitigates or even offset the effects arising from modified surfactant profiles. However, a notable increase in interfacial area occurs subsequently for the cases where $Bi \leq 0.01$, in relative to the other cases. This trend persists for the remainder of the displayed time frame. It is worth noting that the case of $Bi = 0.1, \beta_s = 0.9$ exhibits comparable interfacial area with the low Bi cases from $t = 17.5 \times Rev$. This is due to the presence of "stretching tail" in this specific case, as illustrated earlier, which is caused by the enhanced Marangoni stress encouraging the formation of long ligaments. Moreover, with further increase in Bi ($Bi = 1$), the associated change in interfacial area aligns closely with the case where the surfactant is absent. This outcome is expected since a high Bi value gives rise to a system where surfactants are prone to rapidly leave the interface, resulting in an interface with minimal or no surfactant presence. Similar patterns to the change in interfacial area are seen for the evolution of drop counts, as displayed in Figure 5.10b. However, when focusing on the number of dispersed drops generated at Stage C, which is regarded as stagnant phase of the mixing process, it becomes evident that this number is divided into three levels depending on the values of Bi. The largest number of drops are produced when $Bi \leq 0.01$, followed by $Bi = 0.1$ and the fewest drops observed for $Bi = 1$ and the case without surfactant. Likewise, the drop count corresponding

to the case $Bi = 0.1, \beta_s = 0.9$ is comparable to those produced in the cases with $Bi \leq 0.01$.

Figure 5.11 provides visualisations depicting the interfacial shapes evolution in a time frame of $t = 8.5 - 25 \times Rev.$ for $Bi = 0.001$, complementing the temporal profiles of the two mixing metrics described above. Compared to the observations in Figure 5.1$f - j$, the first remark made from Figure 5.11 is that larger amount of surfactant species remains at the interface, reflected as higher interfacial concentration in Figure 5.11$a - c$. This outcome aligns with the expectation given the small Bi for this system, which corresponds to the lower end of the studied range, resulting in a significantly slower desorption rate of surfactant from the interface. Consequently, the associated interfacial tension reduces further relative to the case shown in Figure 5.1. This leads to similar interfacial behaviours for both $Bi = 0.001$ and $Bi = 0.1$, for example, the early appearance of dispersed phase compared to that observed in the surfactant-free case, along with the formation of "branches" at the deforming interface (see Section 5.2.1.1). However, the former case exhibits a larger amount of dispersed entities (Figure 5.11d) and more elongated filaments or branches (Figure 5.11e). This phenomenon can be explained by the accumulation of surfactant at the trailing edge of the deforming interface, which is driven by the ambient flow field, promoting drop formation via tip-streaming; subsequently, as certain amount of surfactant departs from the deforming interface with dispersed drops, the consequent surfactant concentration gradient on the deforming interface starts to suppress the drop production and instead encourage elongation of ligaments. When $t \geq 13 \times Rev.$, as shown in Figure 5.11$f - g$, the presence of long ligaments persists, accompanied by the production of numerous dispersed drops. The interfaical shapes in the surfactant-free case at these time steps can be seen in Figure 5.7a.

It can be seen from Figure 5.11h that the contact between impeller and interface ceases (Step 4) from $t = 17 \times Rev$. An evident feature in this case is the presence of branches extending from the deforming interface, which is absent in the case $Bi = 0.1$ as presented in Figure 5.9c. Similarly, this arises from the accumulation of surfactant at the stretching tip of the deforming interface, as demonstrated earlier, which thereby decreases the interfacial tension rendering it prone to deformation. This phenomenon continues for the entire Step 4 of the interface evolution, until $t = 25 \times Rev.$, and the counterpart interfacial shapes for the case $Bi = 0.1$ can be seen in Figure 5.6b.

Furthermore, Figure 5.12 provides an insight into the effect of changing Bi on the interfacial surfactant concentration. In this figure, the ratio of the concentration to its initial value is tracked during early dispersion ($t = 0 - 10 \times Rev.$) when Bi is increased from $O(10^{-3})$ to $O(10^{1})$. In addition, the profiles of interfacial surfactant concentration are exemplified by the case of $Bi = 0.001$ and $Bi = 0.1$, as displayed in the insets. As seen, when Bi equals to 0.001 and 0.01, there is minimal departure of surfactant species from the interface initially until $t \approx 7 \times Rev.$, when the interface starts to deform from its flat position. The subsequent increasing rate of reduction in surfactant concentration can thus be attributed to the expanding

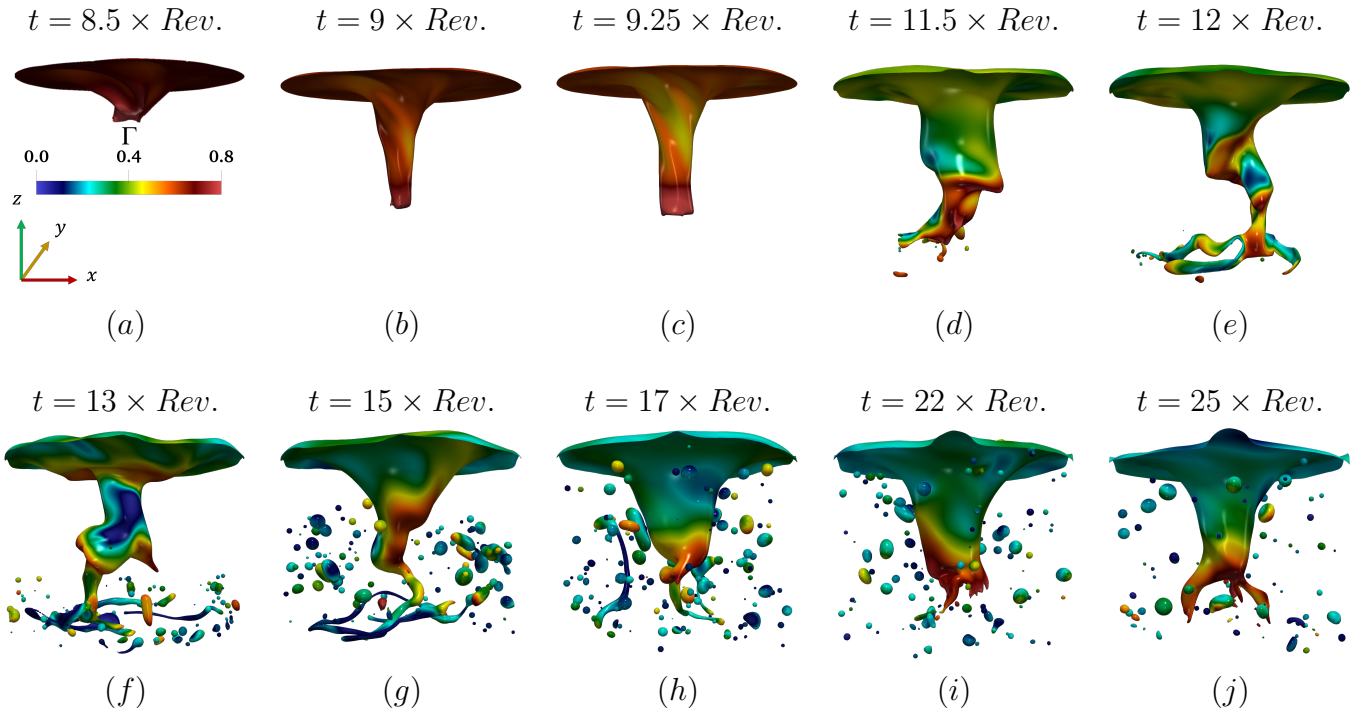


Figure 5.11: Evolution of interfacial shapes for the case $Bi = 0.001$ for $t = 8.5 - 25 \times Rev$. The interface is coloured using the same colour map as in Figure 5.1. Except for the Bi variation (and therefore k_d), the rest of the surfactant-related parameters remain unchanged from Figure 5.1.

interfacial area due to the interface deformation. Nonetheless, the interfacial surfactant concentration remains notably high, accounting for up to 75% of its initial value for these systems. The similar behaviours observed in these two cases explain the overlapping trends seen in the temporal profiles of interfacial area and dispersed drop count, indicating that the increase in Bi values from $O(10^{-3})$ to $O(10^{-2})$ exerts a negligible effect on the concerned mixing system. On the other hand, with an increase in Bi to 0.1, approximately 20% of the species departs from the interface at the onset of the impeller rotation. Later, the interfacial surfactant concentration gradually decreases to a comparable level to that of the low Bi cases. The described difference in initial departure of surfactant species among these cases can be observed in the surfactant concentration profiles on the interface (see insets for $t = 1 \times Rev.$). Meanwhile, an interesting observation is that the remaining surfactant on the interface is displaced radially inward, leading to an accumulation of surfactant at the vessel center and a less concentrated region near the wall. This is induced by the centrifugal flow generated by the impeller rotation at early times, as illustrated in the previous chapter (see Section 4.1.1). Subsequently, this flow gives rise to a periodic surfactant concentraion profile, as depicted in the insets for $t = 3 \times Rev.$, characterised by the alternating high and low concentration radially near the wall and a highest concentration at the center. As Bi is increased to 1, representing a scenario where the surfactant is highly soluble, almost all surfactant species leave the interface before $t = 4 \times Rev$. After that, the interface behaves similarly to its surfactant-free counterpart, which is consistent with the observation drawn from Figure 5.10.

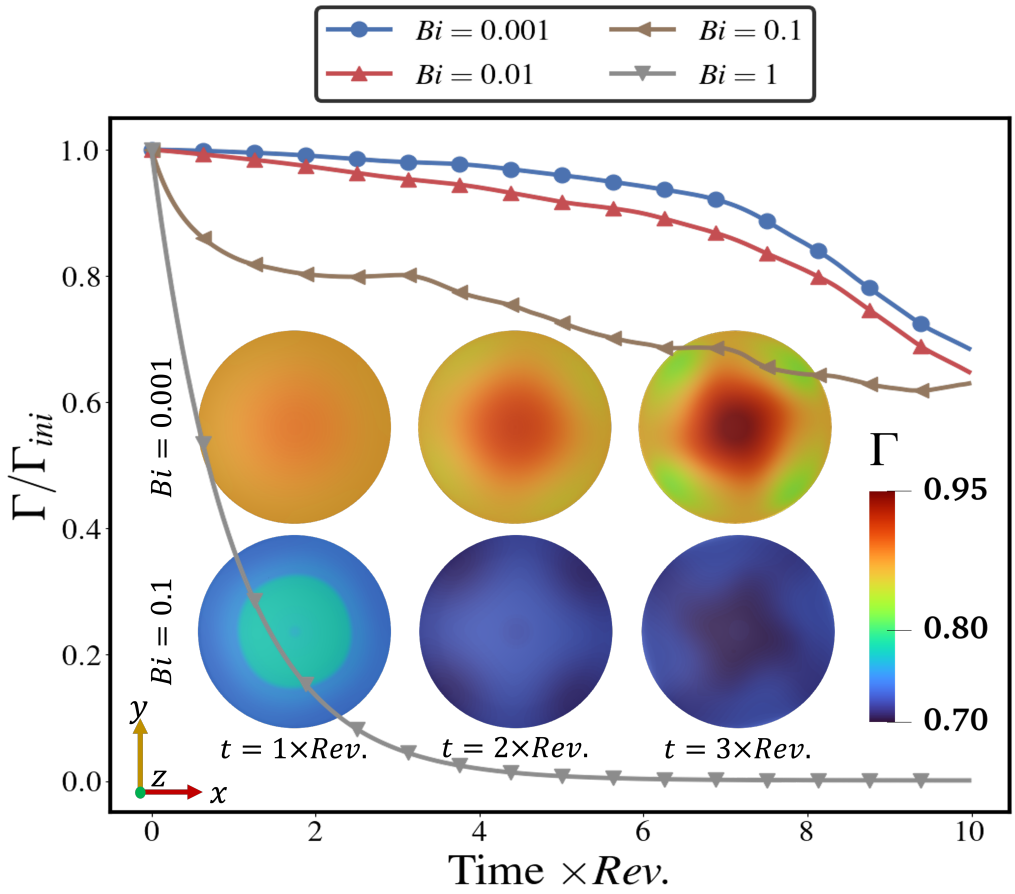


Figure 5.12: Evolution of surfatcant concentration on the interface, in terms of the ratio between the concentration and its initial value, for $t = 0 - 10 \times Rev$. Several insets are displayed to exemplify the interfacial surfactant concentration profiles by the cases of $Bi = 0.001$ and $Bi = 0.1$ at $t = 1, 2$ and $3 \times Rev$. These insets present the top view of interface and are coloured by Γ.

5.3 Concluding Remarks

This chapter has extended my previous work on numerical analysis surrounding oil-water emulsification inside an un-baffled stirred vessel by accounting for the presence of soluble surfactant. We have compared systems with surfatcant presence and absence, analysing interfacial dynamics during mixing, transient number of dispersed phases, and drop size distributions at the instant where the simulations are terminated. Additionally, the numerical methods used herein enables the deactivation of the Marangoni stress, an impractical feat in experimental setups. In this way, we have isolated the effects that arise from interfacial tension reduction and the Marangoni stress induced by surfactant concentration gradient. In general, the decrease in interfacial tension facilitates interface deformation and drop formation in the studied system, particularly promoting a second drop breakup mechanism, the tip-streaming/dropping, which is absent in surfactant-free system. On the other hand, the role of Marangoni stress varies depending on local surfactant concentration distributions. It could either encourage breakup events via capillary instability or retard interfacial elongation and thereby drop production, especially via tip streaming. Regarding drop size, the presence of surfactant manifests distinct effects: reduced interfacial tension aids the production of smaller drops, while the Marangoni stress mitigates this influence.

Furthermore, we have performed two parametric studies to address the effect of surfactant elasticity β_s and the Biot number Bi. In the first case, we have demonstrated that increasing β_s eases interface deformation and thus drop formation by reducing the average interfacial tension. However, the presence of Marangoni stress counteracts these effects, leading to a notable increase in both interfacial area and dispersed phases count for the largest β_s ($\beta_s = 0.9$) during $t = 15 - 20 \times Rev$. This phenomenon arises from the promotion of long ligament formation (and subsequent drop production) by the Marangoni stress. However, as the simulations terminate, this deviation vanishes, with similar drop numbers and interfacial areas observed. For the effect of the Biot number, temporal profiles with regard to interfacial area and drop counts have consistently shown that low values of Bi ($Bi \leq 0.01$) encourage the drop production during mixing. In addition, exclusive interfacial phenomena have been highlighted for low Bi cases, for example, the extending tails from the deforming interface presented throughout the entire interface evolution. In contrast, high Bi systems exhibit similar trends, in terms of generated area, dispersed drop count, as well as interfacial behaviours, as those observed for surfactant-free system. These observations are attributed to the modified desorption rate of surfactant species, which have clearly illustrated by the temporal profile of surfactant concentration at the interface.

Throughout this work, we have provided a detailed insight into surfactant-laden interfacial dynamics within a practical operation unit, i.e., the stirred vessel. Though all the results are from a specific configuration, the physics that have been discussed is generic to stirred mixers.

Chapter 6

Dispersion performance prediction and uncertainty quantification using RNNs

Contents

6.1 Results and discussion 120
6.1.1 Comparative RNN unit performances: LSTM vs. GRU 120
6.1.2 Model generalisation: performance on training and validation data . . 123
6.1.3 Model performance: prediction via rollout 124
6.1.4 Uncertainty quantification 129
6.2 Concluding remarks 130

Overview

This chapter presents the results of time-series prediction based on the CFD simulation data from Chapter 4 and 5, using the multivariate RNN-models constructed through the framework that has been detailed in Methodology chapter (Section 3.2). In particular, two model architectures (namely RNN layer with one fully connected layer, RNN-FC, and encoder-decoder architecture, RNN-ED) with two types of RNN units (namely LSTM and GRU) are examined. These models are capable of predicting temporal evolution of distinct dispersion performance metrics across multiple time-steps into the future, without requiring detailed knowledge of the mixing process itself. Hence, this model potentially serves as a cheap alternative to the high-fidelity CFD simulation which demands tremendous computational resources.

This chapter is organised as follows: first, a brief comparative evaluation of model performance is provided, examining accuracy and resource consumption metrics between both network architecture when using either LSTM or GRU cells (Section 6.1.1). From this, the best-performing RNN unit is selected as the primary focus for the remainder of this chapter. Subsequently, a discussion is presented surrounding the chosen model's generalisation (Section 6.1.2) based on its performance on both training and validation datasets. Following this, we continue with an in-depth exploration of the chosen framework's performance on the testing datasets (Section

Table 6.1: Volumes of the dispersed entities corresponding to the size ranges presented in Figure 6.3.

Bin	**Stirred mixer** $\lambda_c = 0.0045[m]$	
	Bin edge $\log_{10}(V_d/V_{\text{cap}})$	**Actual size** $[m^3 \times 10^{-8}]$
B_3	[-3.50, -3.00]	$[1.54 \times 10^{-3}\ ,\ 4.86 \times 10^{-3}]$
B_5	[-2.50, -2.00]	[0.02, 0.05]
B_6	[-2.00 -1.50]	[0.05, 0.15]
B_8	[-1.00, -0.50]	[0.49, 1.54]

6.1.3). This involves a thorough analysis of the predicted temporal evolution for all features, namely, ND, IA, and DSD, across the network architectures. In particular, the DSD predictions are interpreted through selected bins, i.e., B_3, B_5, B_6, and B_8, containing the normalised density estimators, $\hat{n}_{l,t}$, introduced for the binning procedure in the Section 3.2.2.

The drop size is defined in the same manner as in the previous chapters. In this part, the drop size is recovered from the density estimators as a log-scale normalised drop volume, $\log_{10}(V_d/V_{\text{cap}})$, where V_d is the volume of the dispersed drop and V_{cap} denotes the volume of a spherical drop whose diameter corresponds to the capillary length scale, $\lambda_c = \sqrt{\sigma_s/\Delta\rho g}$. Accordingly, the drop sizes covered in this work lie in a range of $\log_{10}(V_d/V_{\text{cap}}) = [-4.5, 0.0]$. Following the binning procedure described in Section 3.2.2.1, the actual volumes corresponding to each of the bins treated in this chapter are listed in Table 6.1. Lastly, the ensemble-based approach implemented to quantify the model's uncertainty (Section 6.1.4) is showcased using features ND and IA from one testing case.

6.1 Results and discussion

6.1.1 Comparative RNN unit performances: LSTM vs. GRU

As mentioned at the onset of this chapter, two highly relevant and frequently employed RNN units, LSTM and GRU, were deployed to comparatively assess their performance and accuracy in an industrially relevant case study. The primary distinction between these units is the absence of a cell state or long-term memory in the GRU structure, as opposed to LSTM. This aims to reduce computational requirements, such as training time, while still maintaining performance and model's capability to capture long-term dependencies to a significant extent.

Table 6.2 provides a comprehensive evaluation of all possible combinations between RNN architectures and units, wherein R^2 and RMSE associated with training, validation and testing sets are presented. The following discussion is focused on the testing sets. First, when concerning the overall RMSE, LSTMs exhibit slightly lower values for the two network architectures compared to their GRU counterparts, suggesting a generally better predictive capability. Likewise,

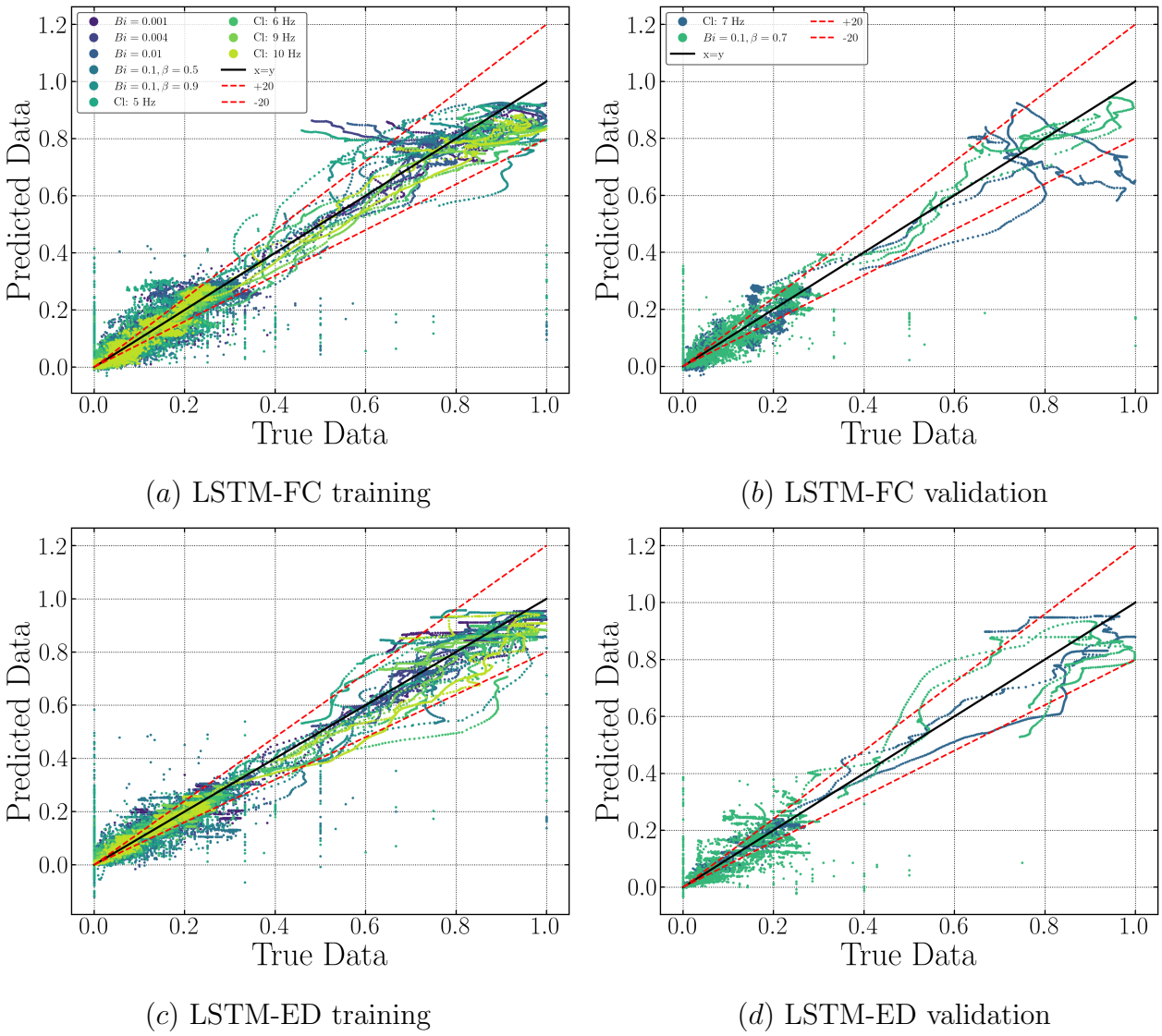
for the overall R^2 coefficient, the LSTM models consistently achieve higher values, albeit with the difference being marginal in certain instances (e.g., <1% for the testing sets). As expected, these observations imply that LSTMs have a generally better grasp of the intricate underlying patterns in the data, allowing them to capture data variability and long-term dependencies with slightly greater accuracy than GRUs.

Similar conclusions can be drawn when examining specific features individually, such as ND and IA, where the improvement achieved with LSTM units as opposed to GRU units is notably more pronounced. For example, 2-5% higher R^2 coefficients when deploying LSTMs for an FC architecture. When looking at more complex data generated for the DSD bins, even though both models seems to struggle to predict some of these dependencies, LSTMs still demonstrate superiority in capturing the variability within specific bins, notably for bins B_6 and B_8.

In terms of computational requirements during tuning, surprisingly the LSTM and GRU models have similar peak memory usage but GRUs consume more time than LSTMs, particularly in FC models, taking almost twice as long to tune. Training times show, however, a different conclusion, with shorter training times for both GRU-based networks. Based on the favourable aspect raised for LSTMs in this part, relevant analysis is carried out in further detail exploring their performance and robustness.

Table 6.2: Model accuracy and computational performance metrics of all combinations between RNN architectures and units. R^2 and RMSE values presented in brackets correspond to the training, validation and testing sets, respectively.
*values marked with * and + correspond to the highest and lowest time taken for model tuning/training, repsectively.*

Metrics	LSTM-FC	LSTM-ED	GRU-FC	GRU-ED
	Model accuracy (training, validation, testing)			
Overall RMSE	(0.057, 0.071, 0.063)	(0.058, 0.048, 0.067)	(0.054, 0.070, 0.065)	(0.061, 0.049, 0.067)
Overall R^2	(0.952, 0.926, 0.942)	(0.950, 0.969, 0.935)	(0.956, 0.927, 0.938)	(0.944, 0.964, 0.934)
R^2 (ND)	(0.893, 0.627, 0.938)	(0.808, 0.873, 0.907)	(0.883, 0.723, 0.921)	(0.829, 0.825, 0.897)
R^2 (IA)	(0.684, 0.075, 0.841)	(0.728, 0.872, 0.808)	(0.740, 0.095, 0.836)	(0.554, 0.880, 0.760)
R^2 (B_3)	(-0.027, -0.176, 0.571)	(0.346, 0.158, 0.543)	(-0.386, 0.050, 0.557)	(0.361, -0.113, 0.629)
R^2 (B_5)	(-0.646, -4.663, -0.073)	(0.123, -0.155, 0.496)	(-0.515, -3.325, -0.010)	(-0.280, -1.516, -0.086)
R^2 (B_6)	(-1.188, -6.147, 0.422)	(0.247, -2.600, 0.677)	(-1.262, -2.552, 0.451)	(0.081, -2.130, 0.642)
R^2 (B_8)	(-0.022, 0.559, 0.708)	(0.530, 0.140, 0.698)	(-1.868, -0.098, 0.460)	(0.585, 0.225, 0.745)
	Computational performance			
Tuning				
time (mins)	3281.855^{+}	22367.724^{*}	5708.065	20574.498
peak memory (MB)	254.931	305.009	252.107	305.013
Training				
time (mins)	143.749	1271.801^{*}	110.922^{+}	934.931
peak memory (MB)	13.441	13.441	13.441	13.441



(*a*) LSTM-FC training

(*b*) LSTM-FC validation

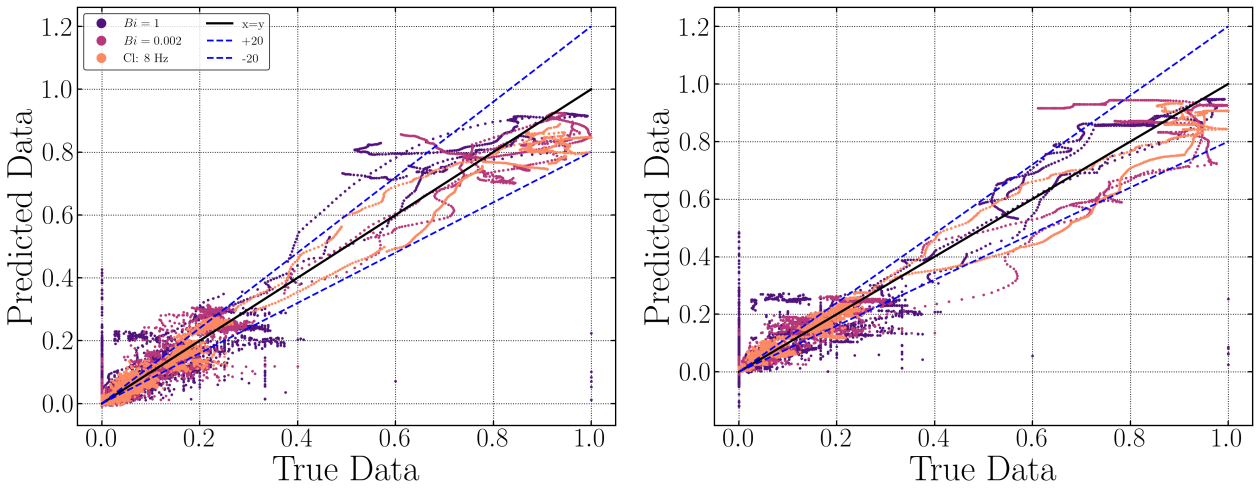
(*c*) LSTM-ED training

(*d*) LSTM-ED validation

Figure 6.1: LSTM-FC (top panel) and LSTM-ED (bottom panel) predicted vs. true data error dispersion plots for all 12 features considered in this work. A ± 20 % deviation area is included. Sub-figures to the left ((*a*), (*c*)) showcase training data, while those to the right ((*b*), (*d*)) illustrate validation data for the mixer respectively.

6.1.2 Model generalisation: performance on training and validation data

Before analysing model performance using LSTM cells on the testing sets, we first compare the performance of both trained networks on the training and validation data sets, depicted in Figure 6.1. In these plots, the scattered points represent the predicted values for all the features studied. The first observation drawn from these plots is that most of the points are located at the left bottom corner. This region corresponds to a range of [0, 0.2], wherein most of the feature values associated with drop density estimation are likely to occur. Meanwhile, 10 bins have been considered as individual features which account for more than 80% of the overall 12 features, which naturally leads to the aggregation seen in this area. In addition, an evident deviation is shown in this corner, not only for training and validation but also for testing predictions (refers to Figure 6.2). Relevant discussion on this observation will be included in the next section to avoid redundancy. On the other hand, the predicted values related to both the training and validation data sets align reasonably well with the true data,



(*a*) LSTM-FC testing (*b*) LSTM-ED testing

Figure 6.2: LSTM-FC (*a*) and -ED (*b*) predicted vs true data error dispersion plots for testing datasets, with a ±20% deviation region included.

though there exhibits a slightly developing deviation between predictions and ground truth, especially when looking at the corresponding the validation set. This conclusion is supported by the RMSE and R^2 values for the training and validation sets. The consistently low RMSE values (0.057 for training and 0.071 for validation), coupled with the marginal increase in the validation RMSE relative to the one for the training set, suggest that the trained LSTM-FC model adeptly captures the underlying patterns in the dispersion dynamics and can generalise this knowledge to new data. This indicates the model's robustness against overfitting and its capability to make reliable predictions on unseen data. A similar performance can be seen from the RMSE values for the LSTM-ED, which also finds its support in the corresponding values of R^2. From the dispersion clouds displayed in Figure 6.1, the LSTM-ED appears to provide a better-trained state, as most of the sequences above 20% deviation are eliminated, especially for the clean and low Bi (<0.1) cases. This observation holds for the validation set, where the encoder-decoder structure only exhibits slight over-prediction, with a small section deviating beyond 20%; in contrast, the LSTM-FC model seems to encounter difficulties in accurately predicting behaviours in the surfactant-laden scenario, particularly towards the later stages of studied time frame.

6.1.3 Model performance: prediction via rollout

This section presents the model rollout predictions on the testing data sets for both LSTM architectures. Similar to what we have shown for the training and validation data sets, Figure 6.2 presents error dispersion plots for the testing cases, which contain all 12 target scaled features (ND, IA and 10 bins). This figure offers a broad overview of each model's performance for all testing cases. However, it falls short when pinpointing the specific features associated with a particular error cloud or region. This association can only be achieved by correlating it with the subsequent Figure 6.3 demonstrating the rollout predictions for each feature.

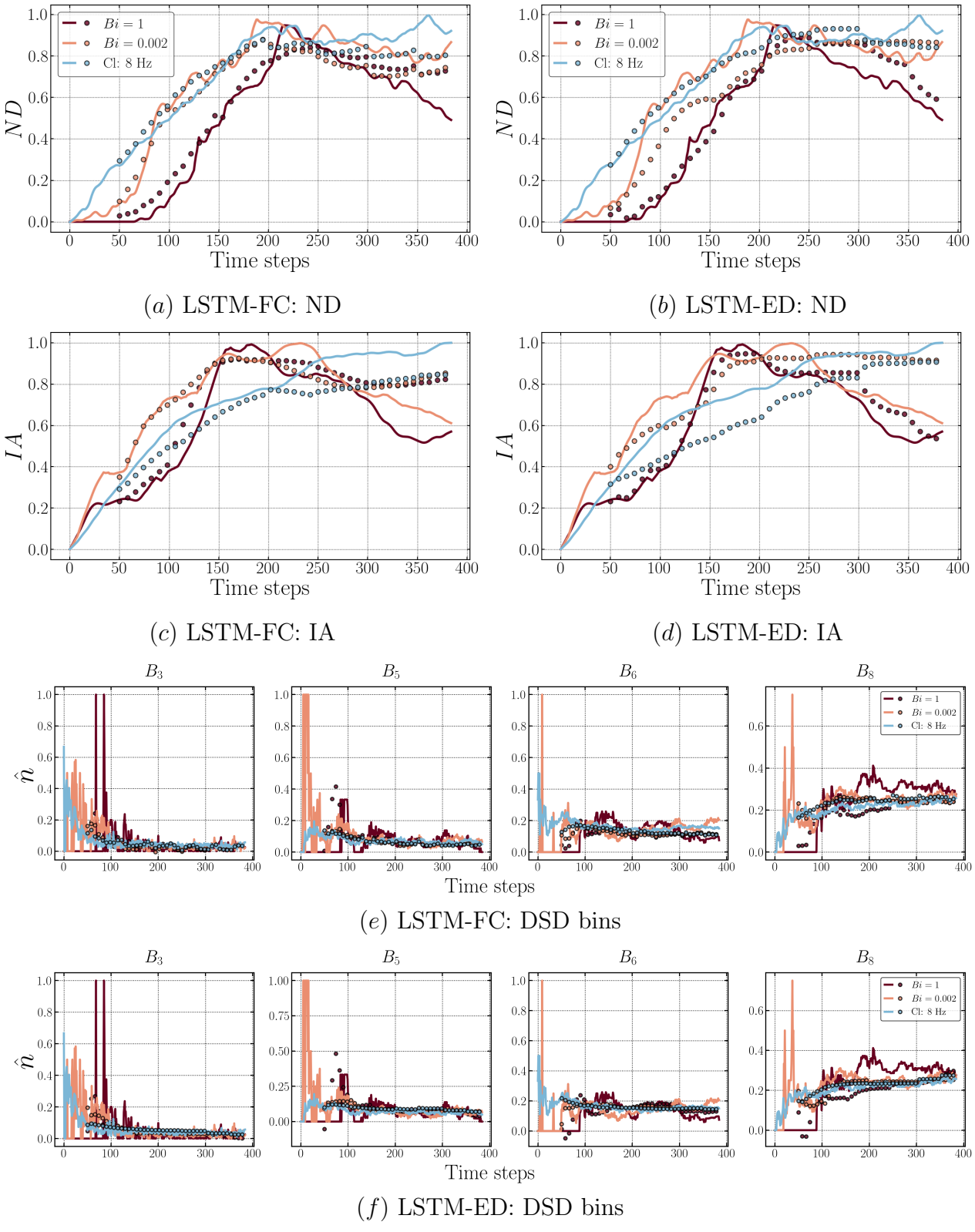
Starting with the LSTM-FC model in Figure 6.2*a*, the dots corresponding to the high Bi case (coloured by dark purple) are mostly found above the black solid parity line ($y = x$). This implies that the model is inclined to overestimate the dispersion metrics for this particular setup, predicting a larger interfacial area, and more dispersed drops overall. A possible explanation for the overestimation could be that the trained LSTM fails to learn the relationship between the highly soluble surfactant and the distribution of ND and IA. This type of surfactant typically leads to notably smaller ND and IA values due to higher interfacial tension when compared to other surfactant cases. This effect is linked to the rapid departure of surfatcant species from the interface, resulting in a dispersion performance similar to that seen in the surfactant-free case. In contrast, the predicted values via LSTM-FC for the other two testing cases and those via LSTM-ED (see Figure 6.2) are distributed over both sides of the parity line, implying that there is no defined biases in the model predictions. Recall that both Figure 6.1 and 6.2 present noticeable variations beyond ±20% at low true data values (data point <0.3). These discrepancies predominantly align with early time-step predictions for any feature. Figure 6.3 offers a detailed perspective on the rollout predictions concerning each feature. From this figure, the described deviation is most likely due to the sensitivity of DSD to perturbations in the total drop count during the early stages of dispersion formation, especially at the edges of the distribution (i.e., small or large drops). More discussion relevant to this will be presented along with subsequent figures.

As mentioned earlier, Figure 6.3 compares the target and predicted values for each feature via LSTM models. It can be seen that the predicted values for features ND and IA, especially at early times, exhibit a much better agreement with the targets compared to that seen for the selected bins exemplified herein. This corroborates our earlier assertion regarding the origin of the large deviations associated with low-value true data. Moreover, the trained LSTM-FC correctly captures the hierarchy of the testing cases for all features (see Figure 6.3*a*, *c*), particularly at the early time-steps of the predicted sequence. Taking ND as an example, the order, Cl: 8Hz > $Bi = 0.002$ > $Bi = 1$, is reproduced for time steps $\sim 50 - 200$. However, the trained LSTM-FC is unable to predict this ranking further down the time range, as displayed in Figure 6.3*a*: the predicted ND for $Bi = 1$ is overlapping with that for $Bi = 0.002$. This can be attributed to the model's inability to extract the correct physical knowledge from the surfactant cases, failing to correlate the surfactant effect with the dispersion performance at later stages. A similar scenario can be seen for the predictions of feature IA, wherein the trained LSTM-FC is capable of recovering the hierarchy at early times, but since the gap between the prior input information and the point where it is needed becomes larger, the model starts to perform poorly. Regarding the performance of LSTM-ED (see Figure 6.3*b*, *d*), it demonstrates comparable accuracy to LSTM-FC during the early times. However, unlike LSTM-FC, LSTM-ED successfully reproduces ND and IA behaviours in later dispersion stages. For instance, it correctly captures the descending trend in ND for $Bi = 1$ and predicts similar ND levels for $Bi = 0.002$ and Cl: 8 Hz. Likewise, it accurately predicts the decrease in IA for $Bi = 1$ and the increase for Cl: 8 Hz.

The superiority of LSTM-ED over LSTM-FC comes from their distinct training methods, as described in Section 3.2.2.3: LSTM-FC is trained to map an entire output sequence with its input, while LSTM-ED learns to progressively generate the output sequence. This guarantees a better performance for LSTM-ED when dealing with sequence generation, i.e., prediction via rollout herein, as it is trained to utilise previous predictions for generating subsequent sequences, a capability not explicitly developed in LSTM-FC. Nonetheless, additional observation from Figure 6.3*b*, *d* reveals that LSTM-ED struggles in certain cases, such as replicating the decrease in IA for $Bi = 0.002$. This suggest that there is room for improvement in the trained LSTM-ED to enhance its understanding of the features and the underlying mechanisms presented in this study. This improvement could be achieved by training on larger data sets and further tuning the hyperparameters. In summary, while training an LSTM-FC may be relatively straightforward due to its simply mapping between input and output sequences, its performance would be globally inferior to that of a well-trained and finely-tuned LSTM-ED; this is due to the feature evolution embedded in the sequence in the latter, which is absent in LSTM-FC.

Figure 6.4*a*, *c* present examples of the predictions of the DSD in the form of histograms for time-step $t = 280$, containing all the bins involved in the predictions. This figure, along with the rollout predictions relevant to bins presented in Figure 6.3*e*, *f*, forms an integrated visualisation of model performance concerning DSD prediction. Take Cl: 8 Hz as an example, LSTM-FC consistently overestimates the values of B_8 throughout most of the time steps (see Figure 6.3*e*), aligning with the observation in Figure 6.4*a* wherein the predicted B_8 lies above its target. Likewise, for LSTM-ED, a good agreement between target and predicted distribution for Cl: 8 Hz is presented in Figure 6.4*c*, compared to the other two cases; this is also evidently indicated by the close alignment of target and predicted values shown in Figure 6.3*f*.

Additionally, to give an overview of the difference between the targeted and predicted distributions, we computed the Wasserstein distance using the built-in functions from SciPy library in Python, which is a measure originating from studying optimal transport problem. Intuitively, if each distribution is treated as piles of soils, this metric quantifies the masses and corresponding distance that must be moved around to turn one distribution into the other; hence this metric is also known as earth mover's distance (EMD). Consequently, lower values of this score indicate higher similarity between the two concerned distributions. Temporal plots with regard to EMD is given in Figure 6.4*b*, *d* for LSTM-FC and LSTM-ED, respectively. From this figure, the predicted DSDs via both network architectures tend to significantly deviate from the target at the early times. This is consistent with the observations in the rollout predictions displayed in Figure 6.3*e*, *f*, where evident deviation is seen for all bins during $t \sim 50 - 100$. Moreover, the statistical instability could be inherently linked to the grid resolution of the simulations, which indicates that nonphysical drops are appearing or disappearing from the domain, causing stochastic irregularity in the data. As a result, with an increase in drop count, the trained



(a) LSTM-FC: ND

(b) LSTM-ED: ND

(c) LSTM-FC: IA

(d) LSTM-ED: IA

(e) LSTM-FC: DSD bins

(f) LSTM-ED: DSD bins

Figure 6.3: Plots comparing the model target sequences (lines) and predicted sequences via rollout procedure (dots) of LSTM-FC ((*a*), (*c*)) and LSTM-ED ((*b*), (*d*)), with features ND and IA in the top and bottom, respectively. The results of predicted drop size distribution are exemplified using B_3, B_5, B_6 and B_8 for both network architectures ((*e*), (*f*)).

models capture the DSD more faithfully with a low level of dissimilarity as reflected by the EMD scores (< 0.2).

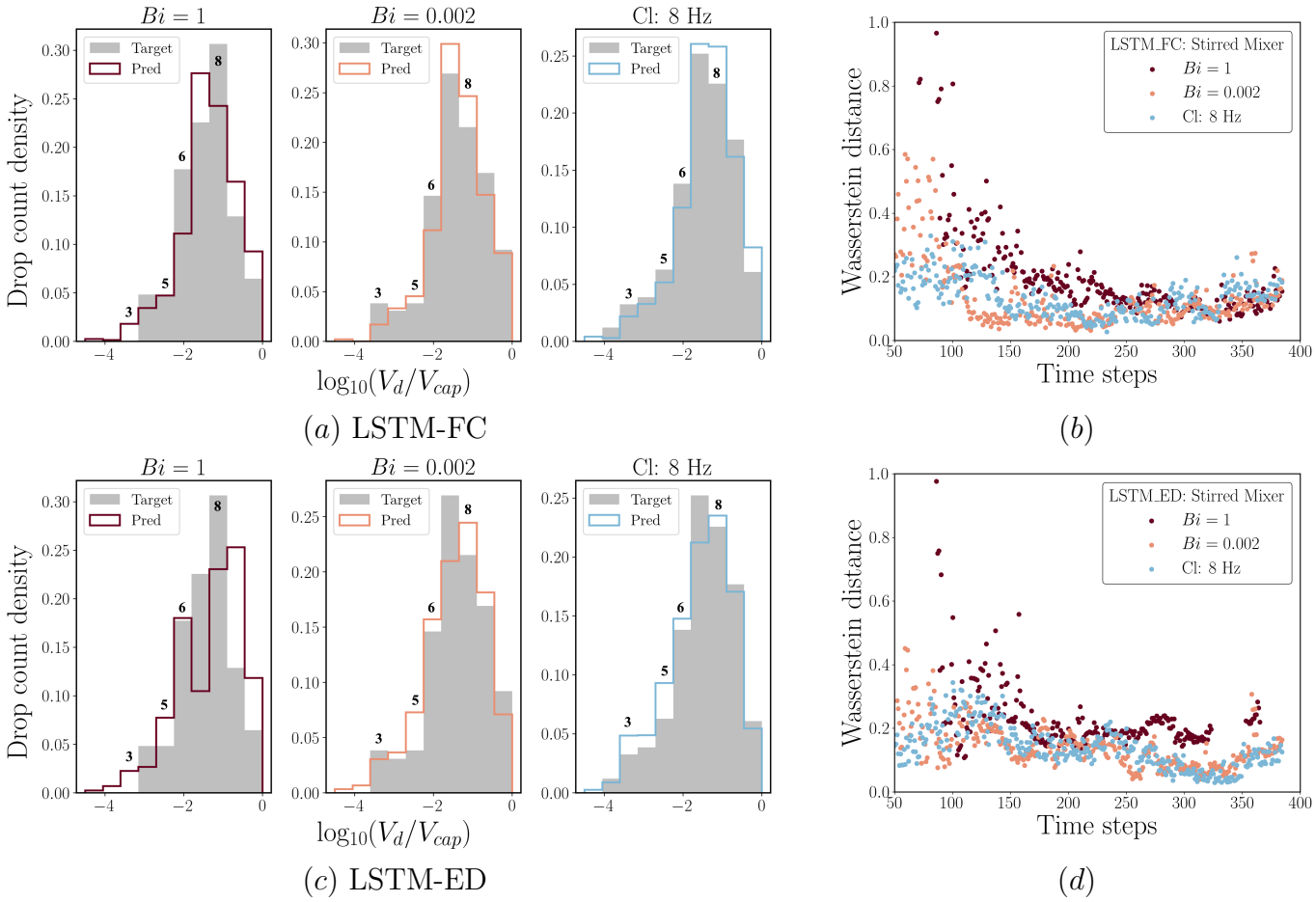


Figure 6.4: $(a), (c)$: Exemplified histograms presenting the predicted drop size distribution via LSTM-FC and LSTM-ED; three test cases are shown for time-step $t = 280$: $Bi = 1, Bi = 0.002$ and Cl: 8 Hz, with the numeric labels in the figure denoting the corresponding bins (B_3, B_5, B_6, and B_8). $(b), (d)$: Temporal plots presenting the divergence between targeted and predicted drop size distribution via LSTM-FC and LSTM-ED, using metrics, Wasserstein distance.

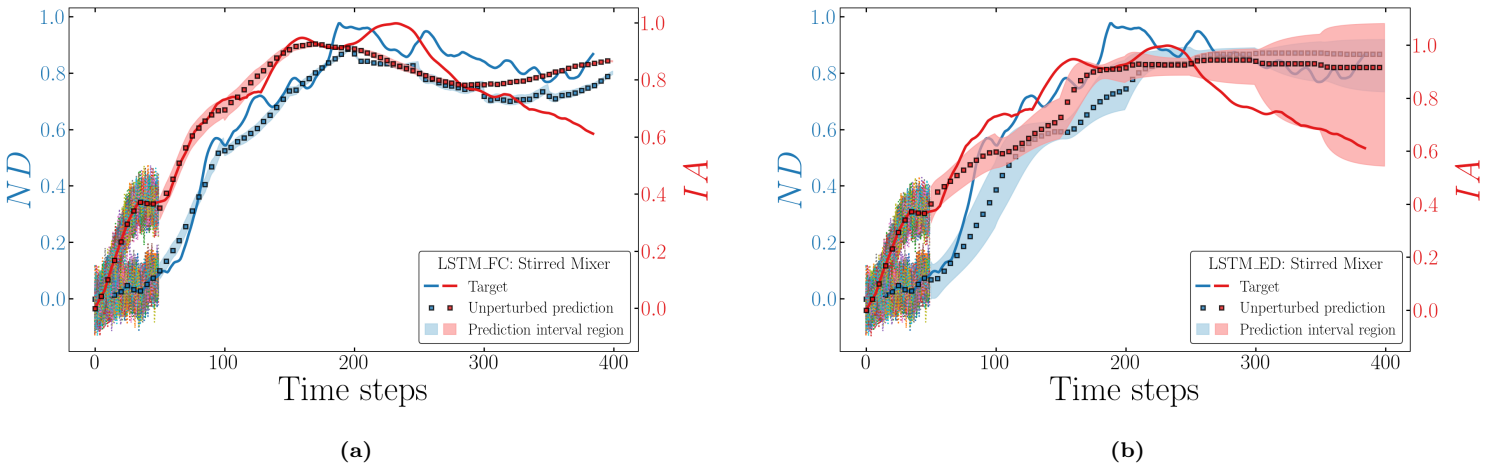


Figure 6.5: Uncertainty quantification plots, comparing the model target (represented by solid lines), model predictions from unperturbed input (dotted line) and the ensemble prediction interval region (coloured bands), for LSTM-FC (a) and LSTM-ED (b). The dots cloud displayed at the early times represents the ensemble of perturbed input sequences.

6.1.4 Uncertainty quantification

In this section, the uncertainty quantification of LSTM-FC and LSTM-ED is demonstrated using two features ND and IA of the test case $Bi = 0.002$. To remind the reader, an ensemble-based scheme is proposed in this study to address the iterative nature of the trained model, which repeatedly processes its output to generate a sequence of predetermined length. As illustrated in Figure 6.5, this method involves generating an ensemble of perturbed input sequence (denoted by dots cloud), which the trained model uses to produce an ensemble of corresponding predicted sequences. Based on these predictions, a prediction interval is calculated to give an overview of the range wherein the model prediction is likely to occur, which is represented by a coloured band indicating the prediction interval region.

The first observation from the figure is the difference in the spread sizes of the interval region associated with the two models. As demonstrated previously, perturbation noise is drawn from the distribution $\mathcal{N}(0, 0.04^2)$, resulting in a spread of the input ensemble with corresponding standard deviation of $\sigma_{s.d.} \approx 0.04$. However, the spread, or the band width, of the prediction ensemble via LSTM-FC is noticeably narrower than that of the input ensemble. This suggests a low level of sensitivity of the LSTM-FC to the input noise, which is expected given that LSTM-FC learns to map the entire output sequence based on its input. Moreover, a close alignment between the interval region and target sequence is presented for $t = 50 - 150$, particularly for the prediction of ND where the model target is covered within the ensemble region. This indicates that the trained model exhibits high precision for predictions within this time frame. It is worth noting that the band width vanishes when $t > 150$, implying that consistent predictions are generated regardless of previous observations. On the one hand, this suggests a stable convergence of LSTM-FC within the specific range of input noise. On the other hand, it indicates that the LSTM-FC struggles to account for the impact of modified initial observations on the evolution of dispersion performance, especially as the gap between the predicting time-step and the input observation increases.

In contrast, the trained LSTM-ED presents a wider prediction interval region, which reflects a higher sensitivity to the added noise. This can be attributed to the sequential procedure of the LSTM-ED when generating an output sequence. The model is trained to learn the evolution step-by-step, making it particularly susceptible to fluctuations in feature values, which have a profound effect on the model's prediction for the next time step. Furthermore, we investigate the correlation between the spread size and model performance along the time axis for LSTM-ED. Model performance is expressed by the divergence of the prediction from its corresponding target at each time-step, i.e., $|\widehat{y}_t - y_t|$. Pearson's correlation coefficient (PCC) [Pearson, 1901] is computed to offer an overview of the direction and strength of the relationship between the predictions and their associated targets. The corresponding result is presented in Figure 6.6. As shown, the spread size generated by the trained LSTM-ED model for both features exhibits a fairly strong positive correlation with the model performance indicated by a PCC larger than 0.5. However, related studies have suggested that researchers should not rely solely on the

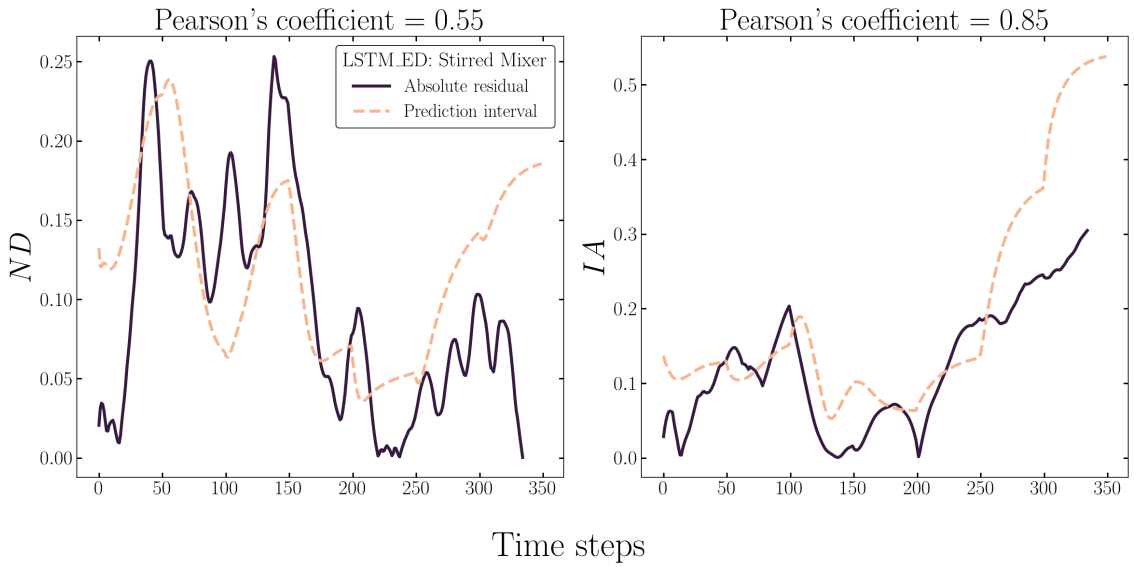


Figure 6.6: Plots comparing the evolution of spread size and model performance (i.e., absolute residual between model prediction and target at each time-step, $|\widehat{y}_t - y_t|$) for LSTM-ED.

correlation coefficients for identifying the relation between data sets [Armstrong, 2019, Derrick et al., 1994]; instead, it is essential to plot the data for visual inspection [Asuero et al., 2006, Anscombe, 1973]. From this perspective, plots presented in Figure 6.6 offers insight into the temporal similarity between the spread size and model performance. Although the spread size does not precisely mirror the exact trend and amplitude of the model performance, it effectively captures the local extrema that signify large deviations of the model predictions from their targets. This is beneficial when performing sequential prediction since the spread size could help identify the point where the accuracy of the model prediction begins to deteriorate.

From the above analysis, the spread size of the prediction interval generated by the LSTM-ED serves as a reliable indicator of model performance and reliability along the sequence generation. This is particularly valid in the case where the trained model is deployed to predict mixing systems that were not included in the training data set and for which the actual target, or "truth", is inaccessible.

6.2 Concluding remarks

This chapter has demonstrated the application of the RNN to predict the temporal behaviour of key dispersion performance metrics for complex multiphase mixing systems. Specifically, two network architectures, FC and ED, with two types of RNN units, LSTM and GRU, have been finely trained and deployed to predict interfacial area growth, dispersed entity count, and their size distribution for future time-steps. The RNN models have been trained with data obtained from high-fidelity, three-dimensional, CFD simulations carried out for stirred mixers, as presented in previous chapters. In particular, the RNN model has been assigned the task of learning and capturing the influence of varying physiochemical properties and operational conditions on dispersion performance. Concerning the network architecture, the RNN-FC has been

taught to map a single long output sequence from the input sequence alone, while RNN-ED has learned to progressively generate feature output sequences based on its previous predictions. The comparison between GRU and LSTM has shown their similar performances in prediction accuracy and computational resource consumption, although a slight edge was observed for LSTMs.

Hence, this chapter is focused on LSTM-based networks, presenting model performance in terms of the prediction of each dispersion metric. Both model architectures exhibits high prediction accuracy at early time-steps. However, for longer time frames, the trained LSTM-ED outperforms the LSTM-FC, demonstrating superior capability in accurately recovering dispersion dynamics that the LSTM-FC fails to predict correctly. This distinction is attributed to the fact that the feature evolution embedded in the sequence is absent in the LSTM-FC. In particular, we have presented different methods to visualise the model performance in the drop size distribution. These methods include the temporal drop counts in each bin representing a specific drop size range and the histogram of all bins at one time-step. Additionally, Wasserstain distances have been computed to track the similarity between the predicted and target distributions. Based on this score, we have shown that the evident discrepancies occur at early times, where the corresponding DSD is sensitive to the perturbation in the total drop count due to its small value initially; hence, the deviation gradually diminishes with the increase in drop numbers. Lastly, we have proposed an ensemble-based procedure to quantify the model uncertainty and have illustrated the high sensitivity of the LSTM-ED when concerning the added noise drawn from the same Gaussian distribution as LSTM-FC. Furthermore, the correlation between the spread size of the prediction interval generated by LSTM-ED and the model performance has investigated. We have demonstrated that the spread size serves as a reliable indicator of the evolution of model reliability through the rollout.

Throughout this work, we have delineated a baseline procedure for data preprocessing, reconditioning, and RNN deployment (detailed in the Methodology, Chapter 3) in the field of complex multiphase mixing. More importantly, we have implemented a system-agnostic framework capable of seamlessly handling any time-series data with similar structures from other applications, regardless of their origin (i.e., numerical data or experimental measurements), and performing analogous temporal evolution predictions of key metrics. Thus, this study could significantly benefit the chemical engineering academic community and industrial practitioners by introducing a cost-effective yet robust alternative to computationally demanding or high-fidelity CFD modelling frameworks, such as those presented in previous chapters, intended to provide an accurate representation of complex interfacial metrics as the ones studied herein.

Chapter 7

Conclusions and future work

7.1 Conclusions

Understanding the physical mechanisms underlying liquid-liquid dispersion is crucial in modern industries due to its extensive application across various fields. However, the inherent complexity of this process has hindered comprehensive understanding. With advancements in computational power, the multiphase mixing research community has increasingly applied high-fidelity numerical simulations to uncover the mechanisms governing liquid-liquid mixing process. The literature review provided here has shown that information regarding interfacial behaviours subjected to complex flow conditions is rarely accessible, though fundamentals of single drop dynamics in the absence and presence of surfactant have been well established through numerous experimental investigation.

In this respect, this thesis has carried out high-fidelity CFD simulations to bridge the gap in the understanding of all the stages of the emulsification process, especially within a practical operational unit, namely a stirred vessel equipped with a pitched blade turbine. Firstly, the effect of impeller speed on the dispersion performance is investigated. The coupling between interfacial evolution and vortical structures generated by the rotating mixer has been detailed from the onset of the impeller rotation throughout to a dynamic steady state. Additionally, comprehensive analysis regarding the drop size distribution has been performed across a range of impeller speeds, examining the temporal evolution of dispersed drop number and their size distribution. Corresponding results demonstrate the possibility of selecting an optimal impeller rotation frequency depending on the specific requirements of the application at hand.

This work has been extended to surfactant-laden systems in agitated vessels, elucidating the impact of surfactants on interfacial evolution and dispersion performance. The study has investigated the effects of varying surfactant properties such as surfactant elasticity and desorption rate from the interface toward the bulk. It is found that the decrease in interfacial tension facilitates interface deformation and fragmentation in the studied system, particularly promoting a drop breakup mechanism called tip-streaming, which is absent in surfactant-free systems. Additionally, the surfactant concentration gradient at the interface has been shown to retard interfacial elongation and thereby drop formation, especially via tip streaming, while

simultaneously encouraging drop breakup events through capillary instability. These combined effects result in a negligible change in drop size in surfactant-laden systems compared to their surfactant-free counterparts.

Meanwhile, recent advancements in ML techniques have opened new possibilities for further elucidating the physics embedded in liquid dispersion processes. This thesis has examined the applicability of ML-based time-series forecasting models to reproduce the temporal dispersion performance when trained with its initial observation from CFD simulations. Two network architectures, RNN with one fully connected layer, RNN-FC, and encoder-decoder architecture, RNN-ED, with two types of RNN units, LSTM and GRU, have been finely trained and deployed to predict interfacial area growth, dispersed entity count and their size distribution for future time-steps. Concerning the network architecture, the RNN-FC has been taught to map a single long output sequence from the input sequence alone, while RNN-ED has learned to progressively generate feature output sequences based on its previous predictions. The comparison between GRU and LSTM has shown their similar performances in prediction accuracy and computational resource consumption, although a slight edge was observed for LSTMs. Based on this finding, model performance for LSTM networks has been discussed in depth. Furthermore, the uncertainty with regard to model predictions has been quantified using an ensemble-based scheme, demonstrating the high sensitivity of LSTM-ED when concerning the added noise drawn from the same Gaussian distribution as LSTM-FC. This work has implemented a system-agnostic framework capable of seamlessly handling any time-series data with similar structures from other applications, regardless of their origin (i.e., numerical data or experimental measurements), and performing analogous temporal evolution predictions of key metrics. Hence, it could significantly benefit the chemical engineering academic community and industrial practitioners by introducing a cost-effective yet robust alternative to computationally demanding modelling frameworks which are intended to provide an accurate representation of complex interfacial metrics.

In summary, this thesis has provided detailed insights into interfacial dynamics of liquid dispersion within stirred vessels; moreover, it has examined the applicability of several popular machine learning techniques in the field of multiphase flow mixing, serving as a benchmark for future ML applications in this area.

7.2 Future Work

As demonstrated, high-fidelity simulations allow for other studies of various surfactant properties and mixer configurations in the future due to the flexibility of the CFD code used in this thesis. For example, the high-fidelity simulations can be employed to construct correlations of the drop size distribution with the dimensionless parameters that characterise the surfactant systems. In addition, based on the findings relevant to the surfactant-free system (Chapter 4), a map in (Re, We) space can be constructed, in which the region of limited mixing is demarcated,

through a framework that focuses on the detection of vortex breakdown (whether it occurs or not). Another crucial aspect in the study of mixing system lies in the energy consumption of agitators, which can be represented using the Power number and approximated by correlating it with variables from simulated mixing vessels, e.g., shear rate. From an industrial point of view, energy consumption is another key performance factor for the mixer in addition to the dispersion performance. This area holds significant research potential, particularly when coupling sophisticated physical mechanisms uncovered with the Power number calculation.

However, a more promising direction for future work lies in the application of ML techniques in the field of multiphase flow mixing. In the work of RNN, exploring additional hyperparameters, such as the number of LSTM layers, could be significantly enhance model performance. There is ample room for improvements in RNN performance. In addition, the uncertainty quantification can be expanded to include various types of uncertainties, thus testing the model's capability of filtering noises from different sources.

Furthermore, ML presents potential for addressing several challenges in CFD, particularly at the interface where various dynamics of phases intersect. One main challenge currently, as indicated from this thesis, is the modelling of complex surfactant behaviours and their effects on fluid interfaces. Traditional CFD methods often struggle with accurately resolving these dynamic interfaces due to their intricate, multi-scale nature. ML algorithms, however, with their ability to learn from large datasets and identify patterns, can enhance the resolution and prediction of surfactant dynamics by improving interface tracking behaviour modelling. This integration can lead to more precise simulations of phenomena such as those illustrated already. Furthermore, ML can accelerate convergence in large-scale industrial CFD simulations by optimising computational resources and providing adaptive mesh refinement. By bridging the gap between detailed, small-scale models and industrial-scale applications, ML facilitates more efficient and accurate simulations, ultimately enabling more robust and scalable solutions in industrial scenarios.

Bibliography

[1] Shuichi Aiba. Flow patterns of liquids in agitated vessels. *AIChE Journal*, 4:485–489, 1958. ISSN 15475905. doi: 10.1002/AIC.690040419.

[2] Raul Alcamo, Giorgio Micale, Franco Grisafi, Alberto Brucato, and Michele Ciofalo. Large-eddy simulation of turbulent flow in an unbaffled stirred tank driven by a rushton turbine. *Chemical Engineering Science*, 60:2303–2316, 4 2005. ISSN 0009-2509. doi: 10.1016/J.CES.2004.11.017.

[3] Gustavo A Padron Aldana and Richard V Calabrese. Effect of surfactants on drop size distribution in a batch, rotor-stator mixer. 2005.

[4] Houari Ameur, Youcef Kamla, and Djamel Sahel. Optimization of the operating and design conditions to reduce the power consumption in a vessel stirred by a paddle impeller. *Periodica Polytechnica Mechanical Engineering*, 62:312–319, 9 2018. ISSN 1587-379X. doi: 10.3311/PPME.12372. URL https://pp.bme.hu/me/article/view/12372.

[5] Theodore W Anderson and Donald A Darling. A test of goodness of fit. *Journal of the American statistical association*, 49(268):765–769, 1954.

[6] Bengt Andersson, Ronnie Andersson, Love Håkansson, Mikael Mortensen, Rahman Sudiyo, and Berend Van Wachem. *Computational fluid dynamics for engineers*. Cambridge university press, 2011.

[7] Ronnie Andersson and Bengt Andersson. On the breakup of fluid particles in turbulent flows. *AIChE Journal*, 52:2020–2030, 6 2006. ISSN 00011541. doi: 10.1002/AIC.10831.

[8] Francis J Anscombe. Graphs in statistical analysis. *The american statistician*, 27(1): 17–21, 1973.

[9] Richard A Armstrong. Should pearson's correlation coefficient be avoided? *Ophthalmic and Physiological Optics*, 39(5):316–327, 2019.

[10] Kartik Arora, Radhakrishna Sureshkumar, Matthew P. Scheiner, and Justin L. Piper. Surfactant-induced effects on turbulent swirling flows. *Rheologica acta*, 41:25–34, 2002.

[11] Agustin Garcia Asuero, Ana Sayago, and AG González. The correlation coefficient: An overview. *Critical reviews in analytical chemistry*, 36(1):41–59, 2006.

[12] J. Aubin, P. Mavros, D. F. Fletcher, J. Bertrand, and C. Xuereb. Effect of axial agitator configuration (up-pumping, down-pumping, reverse rotation) on flow patterns generated in stirred vessels. *Chemical Engineering Research and Design*, 79:845–856, 11 2001. ISSN 0263-8762. doi: 10.1205/02638760152721046.

[13] Néstor Balcázar, Lluís Jofre, Oriol Lehmkuhl, Jesús Castro, and Joaquim Rigola. A finite-volume/level-set method for simulating two-phase flows on unstructured grids. *International Journal of Multiphase Flow*, 64:55–72, 9 2014. ISSN 0301-9322. doi: 10.1016/J.IJMULTIPHASEFLOW.2014.04.008.

[14] A. Barker, R. D. Laroche, M. H. Wang, and R. V. Calabrese. Sliding mesh simulation of laminar flow in stirred reactors. *Chemical Engineering Research and Design*, 75:42–44, 1 1997. ISSN 0263-8762. doi: 10.1205/026387697523372.

[15] Manjunath Basavarajappa, Teri Draper, Pal Toth, Terry A. Ring, and Sanja Miskovic. Numerical and experimental investigation of single phase flow characteristics in stirred tanks using rushton turbine and flotation impeller. *Minerals Engineering*, 83:156–167, 11 2015. ISSN 0892-6875. doi: 10.1016/J.MINENG.2015.08.018.

[16] Nausheen Basha, Rossella Arcucci, Panagiota Angeli, Charitos Anastasiou, Thomas Abadie, César Quilodrán Casas, Jianhua Chen, Sibo Cheng, Loïc Chagot, Federico Galvanin, et al. Machine learning and physics-driven modelling and simulation of multiphase systems. *International Journal of Multiphase Flow*, 179:104936, 2024.

[17] G. K. (George Keith) Batchelor. *An introduction to fluid dynamics*. Cambridge University Press, 1999. ISBN 0521663962.

[18] George Keith Batchelor. *An introduction to fluid dynamics*. Cambridge university press, 1967.

[19] Assen Batchvarov, Lyes Kahouadji, Cristian R. Constante-Amores, Gabriel Farah Norões Gonçalves, Seungwon Shin, Jalel Chergui, Damir Juric, Richard V. Craster, and Omar K. Matar. Three-dimensional dynamics of falling films in the presence of insoluble surfactants. *Journal of Fluid Mechanics*, 2020. ISSN 14697645. doi: 10.1017/jfm.2020.796.

[20] Assen Batchvarov, Lyes Kahouadji, Mirco Magnini, Cristian R. Constante-Amores, Richard V . Craster, Seungwon Shin, Jalel Chergui, Damir Juric, and Omar K. Matar. Effect of surfactant on elongated bubbles in capillary tubes at high reynolds number. 5 2020. URL http://arxiv.org/abs/2005.12269.

[21] Ivan B Bazhlekov, Patrick D Anderson, and Han E H Meijer. Numerical investigation of the effect of insoluble surfactants on drop deformation and breakup in simple shear flow. *Journal of Colloid and Interface Science*, 298:369–394, 2006. doi: 10.1016/j.jcis.2005.12.017. URL www.elsevier.com/locate/jcis.

[22] BJ Bentley and L Gary Leal. An experimental investigation of drop deformation and breakup in steady, two-dimensional linear flows. *Journal of Fluid Mechanics*, 167:241–283, 1986.

[23] D I Bigio, C R Marks, and R V Calabrese. Predicting drop breakup in complex flows from model flow experiments. *International Polymer Processing*, 13:192–198, 1998.

[24] Sougata Biswas and Jiten C. Kalita. Moffatt vortices in the lid-driven cavity flow. volume 759. Institute of Physics Publishing, 11 2016. doi: 10.1088/1742-6596/759/1/012081.

[25] Alexander Lewis Bowler, Serafim Bakalis, and Nicholas James Watson. A review of in-line and on-line measurement techniques to monitor industrial mixing processes. *Chemical Engineering Research and Design*, 153:463–495, 1 2020. ISSN 0263-8762. doi: 10.1016/J.CHERD.2019.10.045.

[26] John A. Boxall, Carolyn A. Koh, E. Dendy Sloan, Amadeu K. Sum, and David T. Wu. Measurement and calibration of droplet size distributions in water-in-oil emulsions by particle video microscope and a focused beam reflectance method. *Industrial and Engineering Chemistry Research*, 49:1412–1418, 2010. ISSN 08885885. doi: 10.1021/ie901228e.

[27] A. M. Boye, M. Y.A. Lo, and P. Ayazi Shamlou. The effect of two-liquid phase rheology on drop breakage in mechanically stirred vessels. *Chemical Engineering Communications*, 143:149–167, 1 1996. ISSN 00986445. doi: 10.1080/00986449608936439. URL https://www.tandfonline.com/doi/abs/10.1080/00986449608936439.

[28] P Bradshaw. Possible origin of prandt's mixing-length theory. *Nature*, 249(5453):135–136, 1974.

[29] B. J. Briscoe, C. J. Lawrence, and W. G.P. Mietus. A review of immiscible fluid mixing. *Advances in Colloid and Interface Science*, 81:1–17, 6 1999. ISSN 0001-8686. doi: 10.1016/S0001-8686(99)00002-0.

[30] Alberto Brucato, Michele Ciofalo, Franco Grisafi, and Giorgio Micale. Numerical prediction of flow fields in baffled stirred vessels: A comparison of alternative modelling approaches. *Chemical Engineering Science*, 53:3653–3684, 1998. ISSN 00092509. doi: 10.1016/S0009-2509(98)00149-3.

[31] R A De Bruijn. Tipstreaming of drops in simple shear flows, 1993.

[32] R. V. Calabrese, C. Y. Wang, and N. P. Bryner. Drop breakup in turbulent stirred-tank contactors. part iii: Correlations for mean size and drop size distribution. *AIChE Journal*, 32:677–681, 1986. ISSN 15475905. doi: 10.1002/AIC.690320418.

[33] Chien Hsiang Chang and Elias I. Franses. Adsorption dynamics of surfactants at the air/water interface: a critical review of mathematical models, data, and mechanisms. *Colloids and Surfaces A: Physicochemical and Engineering Aspects*, 100:1–45, 7 1995. ISSN 09277757. doi: 10.1016/0927-7757(94)03061-4.

[34] D. Chapple, S. M. Kresta, A. Wall, and A. Afacan. The effect of impeller and tank geometry on power number for a pitched blade turbine. *Chemical Engineering Research and Design*, 80:364–372, 5 2002. ISSN 0263-8762. doi: 10.1205/026387602317446407.

[35] E. G. Chatzi and C. Kiparssides. Steady-state drop-size distributions in high holup fraction dispersion systems. *AIChE Journal*, 41:1640–1652, 1995. ISSN 15475905. doi: 10.1002/aic.690410705.

[36] Eleni G. Chatzi, Costas J. Boutris, and Costas Kiparissides. On-line monitoring of drop size distributions in agitated vessels. 2. effect of stabilizer concentration. *Industrial and Engineering Chemistry Research*, 30:1307–1313, 1991. ISSN 15205045. doi: 10.1021/ie00054a035.

[37] Jinnan Chen and Kathleen J. Stebe. Marangoni retardation of the terminal velocity of a settling droplet: The role of surfactant physico-chemistry. *Journal of Colloid and Interface Science*, 178:144–155, 3 1996. ISSN 00219797. doi: 10.1006/JCIS.1996.0102.

[38] Shun Chen and Lei Ge. Exploring the attention mechanism in lstm-based hong kong stock price movement prediction. *Quantitative Finance*, 19(9):1507–1515, 2019.

[39] Sibo Cheng, I. Colin Prentice, Yuhan Huang, Yufang Jin, Yi Ke Guo, and Rossella Arcucci. Data-driven surrogate model with latent data assimilation: Application to wildfire forecasting. *Journal of Computational Physics*, 464:111302, 9 2022. ISSN 0021-9991. doi: 10.1016/J.JCP.2022.111302.

[40] Sibo Cheng, Jianhua Chen, Charitos Anastasiou, Panagiota Angeli, Omar K. Matar, Yi Ke Guo, Christopher C. Pain, and Rossella Arcucci. Generalised latent assimilation in heterogeneous reduced spaces with machine learning surrogate models. *Journal of Scientific Computing*, 94:1–37, 1 2023. ISSN 15737691. doi: 10.1007/S10915-022-02059-4/TABLES/8. URL https://link.springer.com/article/10.1007/s10915-022-02059-4.

[41] Sibo Cheng, Jianhua Chen, Charitos Anastasiou, Panagiota Angeli, Omar K Matar, Yi-Ke Guo, Christopher C Pain, and Rossella Arcucci. Generalised latent assimilation in heterogeneous reduced spaces with machine learning surrogate models. *Journal of Scientific Computing*, 94(1):11, 2023.

[42] Hong Bai Chin and Chang Dae Han. Studies on droplet deformation and breakup. ii. breakup of a droplet in nonuniform shear flow. *Journal of Rheology*, 24:1, 7 2000. ISSN 0148-6055. doi: 10.1122/1.549554. URL https://sor.scitation.org/doi/abs/10.1122/1.549554.

[43] Kyunghyun Cho, Bart van Merriënboer, Dzmitry Bahdanau, and Yoshua Bengio. On the properties of neural machine translation: Encoder-decoder approaches. *Proceedings of SSST 2014 - 8th Workshop on Syntax, Semantics and Structure in Statistical Translation*,

pages 103–111, 9 2014. doi: 10.3115/v1/w14-4012. URL https://arxiv.org/abs/1409.1259v2.

[44] Alexandre Joel Chorin. Numerical solution of the navier-stokes equations. *Mathematics of computation*, 22:745–762, 1968.

[45] C. R. Constante-Amores, A. Batchvarov, L. Kahouadji, S. Shin, J. Chergui, D. Juric, and O. K. Matar. Role of surfactant-induced marangoni stresses in drop-interface coalescence. 2021. URL http://arxiv.org/abs/2102.08071.

[46] C R Constante-Amores, L Kahouadji, A Batchvarov, S Shin, J Chergui, D Juric, and O K Matar. Dynamics of a surfactant-laden bubble bursting through an interface. *J. Fluid Mech*, 911:57, 2021. doi: 10.1017/jfm.2020.1099. URL https://doi.org/10.1017/jfm.2020.1099.

[47] C. R. Constante-Amores, L. Kahouadji, A. Batchvarov, S. Shin, J. Chergui, D. Juric, and O. K. Matar. Direct numerical simulations of transient turbulent jets: vortex-interface interactions. *Journal of Fluid Mechanics*, 922: A6, 2021. ISSN 0022-1120. doi: 10.1017/JFM.2021.519. URL https://www.cambridge.org/core/journals/journal-of-fluid-mechanics/article/direct-numerical-simulations-of-transient-turbulent-jets-vortexinterface-interacti
A419969A9C6A96FC15811EE7B04E33A8.

[48] C. R. Constante-Amores, L. Kahouadji, S. Shin, J. Chergui, D. Juric, J. R. Castrejón-Pita, O. K. Matar, and A. A. Castrejón-Pita. Impact of droplets onto surfactant-laden thin liquid films. *Journal of Fluid Mechanics*, 961:A8, 4 2023. ISSN 0022-1120. doi: 10.1017/JFM.2023.224. URL https://www.cambridge.org/core/journals/journal-of-fluid-mechanics/article/impact-of-droplets-onto-surfactantladen-thin-liquid-films/03C213289D24A7074987081D659E1DB3.

[49] Cristian R Constante-Amores, Lyes Kahouadji, Assen Batchvarov, Seungwon Shin, Jalel Chergui, Damir Juric, and Omar K Matar. Dynamics of retracting surfactant-laden ligaments at intermediate ohnesorge number. *Physical Review Fluids*, 5, 2020. doi: 10.1103/PhysRevFluids.5.084007.

[50] J. Costes and J. P. Couderc. Study by laser doppler anemometry of the turbulent flow induced by a rushton turbine in a stirred tank: Influence of the size of the units-i. mean flow and turbulence. *Chemical Engineering Science*, 43:2751–2764, 1988. ISSN 00092509. doi: 10.1016/0009-2509(88)80018-6.

[51] James W Deardorff. A numerical study of three-dimensional turbulent channel flow at large reynolds numbers. *Journal of Fluid Mechanics*, 41(2):453–480, 1970.

[52] M William Deen. *ANALYSIS OF TRANSPORT PHENOMENA*. 1998.

[53] D. A. Deglon and C. J. Meyer. Cfd modelling of stirred tanks: Numerical considerations. *Minerals Engineering*, 19:1059–1068, 8 2006. ISSN 0892-6875. doi: 10.1016/J.MINENG.2006.04.001.

[54] J J Derksen, M S Doelman, and H E A Van den Akker. Three-dimensional lda measurements in the impeller region of a turbulently stirred tank. *Experiments in Fluids*, 27: 522–532, 1999.

[55] Timothy R Derrick, Barry T Bates, and Janet S Dufek. Evaluation of time-series data sets using the pearson product-moment correlation coefficient. *Medicine and science in sports and exercise*, 26(7):919–928, 1994.

[56] C. Desnoyer, O. Masbernat, and C. Gourdon. Experimental study of drop size distributions at high phase ratio in liquid–liquid dispersions. *Chemical Engineering Science*, 58: 1353–1363, 4 2003. ISSN 0009-2509. doi: 10.1016/S0009-2509(02)00461-X.

[57] Abel Desouza and Ralph W. Pike. Fluid dynamics and flow patterns in stirred tanks with a turbine impeller. *The Canadian Journal of Chemical Engineering*, 50:15–23, 2 1972. ISSN 1939-019X. doi: 10.1002/CJCE.5450500104. URL https://onlinelibrary.wiley.com/doi/full/10.1002/cjce.5450500104https://onlinelibrary.wiley.com/doi/abs/10.1002/cjce.5450500104https://onlinelibrary.wiley.com/doi/10.1002/cjce.5450500104.

[58] Thiyam Tamphasana Devi, Bimlesh Kumar, and Ajey Kumar Patel. Detached eddy simulation of turbulent flow in stirred tank reactor. volume 127, pages 87–94. Elsevier Ltd, 2015. doi: 10.1016/j.proeng.2015.11.430.

[59] Chengdi Dong, Ching Tien Hsu, Chin Yuan Chiu, and Shi Yow Lin. Study on surfactant adsorption kinetics: effect of bulk concentration on the limiting adsorption rate constant. *Langmuir*, 16:4573–4580, 1 2000. ISSN 07437463. doi: 10.1021/LA991001B/ASSET/IMAGES/LARGE/LA991001BF00012.JPEG. URL https://pubs.acs.org/doi/full/10.1021/la991001b.

[60] Z Driss, G Bouzgarrou, W Chtourou, H Kchaou, and MS Abid. Computational studies of the pitched blade turbines design effect on the stirred tank flow characteristics. *European Journal of Mechanics B/Fluids*, 29:236–245, 2010. doi: 10.1016/j.euromechflu.2010.01.006. URL www.elsevier.com/locate/ejmflu.

[61] Olive Jean Dunn. Multiple comparisons among means. *Journal of the American statistical association*, 56(293):52–64, 1961.

[62] Olive Jean Dunn. Multiple comparisons using rank sums. *Technometrics*, 6(3):241–252, 1964.

[63] Paul A Durbin. Some recent developments in turbulence closure modeling. *Annual Review of Fluid Mechanics*, 50(1):77–103, 2018.

[64] Mahidhar Dwarampudi and NV Reddy. Effects of padding on lstms and cnns. *arXiv preprint arXiv:1903.07288*, 2019.

[65] R. E. Eckert, C. M. McLaughlin, and J. H. Rushton. Liquid-liquid interfacial areas formed by turbine impellers in baffled, cylindrical mixing tanks. *AIChE Journal*, 31:1811–1820, 1985. ISSN 15475905. doi: 10.1002/aic.690311107.

[66] Maximilian F Eggl and Peter J Schmid. Mixing by stirring: optimizing shapes and strategies. *Physical Review Fluids*, 7:073904, 2022.

[67] Charles D. Eggleton and Kathleen J. Stebe. An adsorption-desorption-controlled surfactant on a deforming droplet. *Journal of Colloid and Interface Science*, 208:68–80, 12 1998. ISSN 00219797. doi: 10.1006/JCIS.1998.5816.

[68] Charles D. Eggleton, Yashodhara P. Pawar, and Kathleen J. Stebe. Insoluble surfactants on a drop in an extensional flow: A generalization of the stagnated surface limit to deforming interfaces. *Journal of Fluid Mechanics*, 385:79–99, 1999. ISSN 00221120. doi: 10.1017/S0022112098004054.

[69] Charles D Eggleton, Tse-Min Tsai, and Kathleen J Stebe. Tip streaming from a drop in the presence of surfactants. *Physical review letters*, 87, 2001. doi: 10.1103/PhysRevLett.87.048302.

[70] Amer El-Hamouz. Effect of surfactant concentration and operating temperature on the drop size distribution of silicon oil water dispersion. *Journal of Dispersion Science and Technology*, 28:797–804, 2007. ISSN 01932691. doi: 10.1080/01932690701345893.

[71] Amer El-Hamouz. Drop size distribution in a standard twin-impeller batch mixer at high dispersed- phase volume fraction. *Chemical Engineering and Technology*, 32:1203–1210, 2009. ISSN 09307516. doi: 10.1002/ceat.200900038.

[72] Amer EL-Hamouz, Mike Cooke, Adam Kowalski, and Paul Sharratt. Dispersion of silicone oil in water surfactant solution: Effect of impeller speed, oil viscosity and addition point on drop size distribution. *Chemical Engineering and Processing: Process Intensification*, 48:633–642, 2009. ISSN 02552701. doi: 10.1016/j.cep.2008.07.008.

[73] Renaud Escudie, Alain Liné´laboratoire, and Liné Liné´. Experimental analysis of hydrodynamics in a radially agitated tank. *AIChE Journal*, 49:585–603, 2003. doi: 10.1002/aic.690490306. URL https://aiche.onlinelibrary.wiley.com/doi/10.1002/aic.690490306.

[74] Renaud Escudié, Denis Bouyer, and Alain Liné. Characterization of trailing vortices generated by a rushton turbine. *AIChE Journal*, 50:75–86, 1 2004. ISSN 1547-5905. doi: 10.1002/AIC.10007. URL https://onlinelibrary.wiley.com/doi/full/10.1002/aic.10007https://onlinelibrary.wiley.com/doi/abs/10.1002/aic.10007https://aiche.onlinelibrary.wiley.com/doi/10.1002/aic.10007.

[75] E. A. Fadlun, R. Verzicco, P. Orlandi, and J. Mohd-Yusof. Combined immersed-boundary finite-difference methods for three-dimensional complex flow simulations. *Journal of Computational Physics*, 161:35–60, 6 2000. ISSN 00219991. doi: 10.1006/jcph.2000.6484.

[76] Ying Fan, Jiao Sun, Jie Jin, Hui Zhang, and Wenyi Chen. The effect of baffle on flow structures and dynamics stirred by pitch blade turbine. *Chemical Engineering Research and Design*, 168:227–238, 4 2021. ISSN 02638762. doi: 10.1016/J.CHERD.2021.01.017.

[77] Ronald P. Fedkiw, Tariq Aslam, Barry Merriman, and Stanley Osher. A non-oscillatory eulerian approach to interfaces in multimaterial flows (the ghost fluid method). *Journal of Computational Physics*, 152:457–492, 7 1999. ISSN 0021-9991. doi: 10.1006/JCPH.1999.6236.

[78] Kathleen Feigl, David Megias-Alguacil, Peter Fischer, and Erich J. Windhab. Simulation and experiments of droplet deformation and orientation in simple shear flow with surfactants. *Chemical Engineering Science*, 62:3242–3258, 5 2007. ISSN 00092509. doi: 10.1016/j.ces.2007.02.008.

[79] Joel H Ferziger, Milovan Perić, and Robert L Street. *Computational methods for fluid dynamics*. springer, 2019.

[80] Peter Fischer and Philipp Erni. Emulsion drops in external flow fields - the role of liquid interfaces. *Current Opinion in Colloid and Interface Science*, 12:196–205, 10 2007. ISSN 13590294. doi: 10.1016/J.COCIS.2007.07.014. URL www.elsevier.com/locate/cocis.

[81] Eric M Furst and Todd M Squires. *Microrheology*. Oxford University Press, 2017.

[82] Haruki Furukawa, Yoshihito Kato, Yoshiro Inoue, Tomoho Kato, Yutaka Tada, and Shunsuke Hashimoto. Correlation of power consumption for several kinds of mixing impellers. *International Journal of Chemical Engineering*, 2012. ISSN 1687806X. doi: 10.1155/2012/106496.

[83] A. Gabriele, A. W. Nienow, and M. J.H. Simmons. Use of angle resolved piv to estimate local specific energy dissipation rates for up- and down-pumping pitched blade agitators in a stirred tank. *Chemical Engineering Science*, 64:126–143, 1 2009. ISSN 0009-2509. doi: 10.1016/J.CES.2008.09.018.

[84] S. Galinat, O. Masbernat, P. Guiraud, C. Dalmazzone, and C. Noïk. Drop break-up in turbulent pipe flow downstream of a restriction. *Chemical Engineering Science*, 60:6511–6528, 2005. ISSN 00092509. doi: 10.1016/j.ces.2005.05.012.

[85] Sophie Galinat, Frédéric Risso, Olivier Masbernat, and Pascual Guiraud. Dynamics of drop breakup in inhomogeneous turbulence at various volume fractions. *Journal of Fluid Mechanics*, 578:85–94, 2007. ISSN 00221120. doi: 10.1017/S0022112007005186.

[86] Juan Pablo Gallo-Molina, Nicolás Ratkovich, and Oscar Alvarez. The application of computational fluid dynamics to the multiscale study of oil-in-water emulsions. 2017. doi: 10.1021/acs.iecr.7b03846. URL https://pubs.acs.org/sharingguidelines.

[87] Jakob Gawlikowski, Cedrique Rovile Njieutcheu Tassi, Mohsin Ali, Jongseok Lee, Matthias Humt, Jianxiang Feng, Anna Kruspe, Rudolph Triebel, Peter Jung, Ribana Roscher, Muhammad Shahzad, Wen Yang, Richard Bamler, and Xiao Xiang Zhu. A survey of uncertainty in deep neural networks. *Artificial Intelligence Review*, 56:1513–1589, 10 2023. ISSN 15737462. doi: 10.1007/S10462-023-10562-9/FIGURES/11. URL https://link.springer.com/article/10.1007/s10462-023-10562-9.

[88] Felix A Gers, J ¨ Urgen Schmidhuber, and Fred Cummins. Learning to forget: Continual prediction with lstm. 2000. URL http://direct.mit.edu/neco/article-pdf/12/10/2451/814643/089976600300015015.pdf.

[89] Felix A Gers, Nicol N Schraudolph, and Jürgen Schmidhuber. Learning precise timing with lstm recurrent networks. *Journal of machine learning research*, 3(Aug):115–143, 2002.

[90] Reza Afshar Ghotli, Abdul A.A. Raman, Shaliza Ibrahim, and Saeid Baroutian. Liquid-liquid mixing in stirred vessels: a review. *Chemical Engineering Communications*, 200: 595–627, 2013. ISSN 00986445. doi: 10.1080/00986445.2012.717313.

[91] Reza Afshar Ghotli, Mohammad Reza Abbasi, Amir Hossein Bagheri, Abdul Aziz Abdul Raman, Shaliza Ibrahim, and Huseyin Bostanci. Experimental and modeling evaluation of droplet size in immiscible liquid-liquid stirred vessel using various impeller designs. *Journal of the Taiwan Institute of Chemical Engineers*, 100:26–36, 2019. ISSN 18761070. doi: 10.1016/j.jtice.2019.04.005. URL https://doi.org/10.1016/j.jtice.2019.04.005.

[92] A. Giapos, C. Pachatouridis, and M. Stamatoudis. Effect of the number of impeller blades on the drop sizes in agitated dispersions. *Chemical Engineering Research and Design*, 83:1425–1430, 12 2005. ISSN 0263-8762. doi: 10.1205/CHERD.04167. URL https://linkinghub.elsevier.com/retrieve/pii/S0263876205728495.

[93] J. J.J. Gillissen and H. E.A. Van den Akker. Direct numerical simulation of the turbulent flow in a baffled tank driven by a rushton turbine. *AIChE Journal*, 58:3878–3890, 12 2012. ISSN 00011541. doi: 10.1002/AIC.13762.

[94] J. Gimbun, C. D. Rielly, Z. K. Nagy, and J. J. Derksen. Detached eddy simulation on the turbulent flow in a stirred tank. *AIChE Journal*, 58:3224–3241, 10 2012. ISSN 1547-5905. doi: 10.1002/AIC.12807. URL https://onlinelibrary.wiley.com/doi/full/10.1002/aic.12807https://onlinelibrary.wiley.com/doi/abs/10.1002/aic.12807https://aiche.onlinelibrary.wiley.com/doi/10.1002/aic.12807.

[95] Tanya Goloub and Robert J Pugh. The role of the surfactant head group in the emulsification process: Single surfactant systems. *Journal of Colloid and Interface Science*, 257: 337–343, 2003. URL www.elsevier.com/locate/jcis.

[96] Harold P. Grace. Dispersion phenomena in high viscosity immiscible fluid systems and application of static mixers as dispersion devices in such systems. *Chemical Engineering Communications*, 14:225–277, 3 1982. ISSN 15635201. doi: 10.1080/00986448208911047/ASSET//CMS/ASSET/E19E915D-6140-4CBC-8F71-F6847525914E/00986448208911047.FP.PNG. URL https://www.tandfonline.com/doi/abs/10.1080/00986448208911047.

[97] Klaus Greff, Rupesh K. Srivastava, Jan Koutnik, Bas R. Steunebrink, and Jurgen Schmidhuber. Lstm: A search space odyssey. *IEEE Transactions on Neural Networks and Learning Systems*, 28:2222–2232, 10 2017. ISSN 21622388. doi: 10.1109/TNNLS.2016.2582924.

[98] F. Groeneweg, F. van Dieren, and W. G.M. Agterof. Droplet break-up in a stirred water-in-oil emulsion in the presence of emulsifiers. *Colloids and Surfaces A: Physicochemical and Engineering Aspects*, 91:207–214, 11 1994. ISSN 0927-7757. doi: 10.1016/0927-7757(94)02913-X.

[99] Andreas Håkansson, Peyman Olad, and Fredrik Innings. Identification and mapping of three distinct breakup morphologies in the turbulent inertial regime of emulsification—effect of weber number and viscosity ratio. *Processes*, 10(11):2204, 2022.

[100] M G Hall. Vortex breakdown. *Annual Review of Fluid Mechanics*, 4:195–218, 1972. ISSN 0066-4189. doi: 10.1146/annurev.fl.04.010172.001211.

[101] S. Hansen, G. W.M. Peters, and H. E.H. Meijer. The effect of surfactant on the stability of a fluid filament embedded in a viscous fluid. *Journal of Fluid Mechanics*, 382:331–349, 1999. ISSN 00221120. doi: 10.1017/S0022112098003991.

[102] Vladislav Hančil and Vladimír Rod. Break-up of a drop in a stirred tank. *Chemical Engineering and Processing*, 23:189–193, 1988. ISSN 02552701. doi: 10.1016/0255-2701(88)80015-1.

[103] Francis H Harlow, J Eddie Welch, et al. Numerical calculation of time-dependent viscous incompressible flow of fluid with free surface. *Physics of fluids*, 8(12):2182, 1965.

[104] H. Hartmann, J. J. Derksen, and H. E.A. Van Den Akker. Macroinstability uncovered in a rushton turbine stirred tank by means of les. *AIChE Journal*, 50:2383–2393, 10 2004. ISSN 1547-5905. doi: 10.1002/AIC.10211. URL https://onlinelibrary.wiley.com/doi/full/10.1002/aic.10211https://onlinelibrary.wiley.com/doi/abs/10.1002/aic.10211https://aiche.onlinelibrary.wiley.com/doi/10.1002/aic.10211.

[105] Albert D. Harvey, Cassian K. Lee, and Stuart E. Rogers. Steady-state modeling and experimental measurement of a baffled impeller stirred tank. *AIChE Journal*, 41:2177–2186, 10 1995. ISSN 1547-5905. doi: 10.1002/AIC.690411002. URL

https://onlinelibrary.wiley.com/doi/full/10.1002/aic.690411002https://onlinelibrary.wiley.com/doi/abs/10.1002/aic.690411002https://aiche.onlinelibrary.wiley.com/doi/10.1002/aic.690411002.

[106] Basim O. Hasan. Breakage of drops and bubbles in a stirred tank: A review of experimental studies. *Chinese Journal of Chemical Engineering*, 25:698–711, 2017. ISSN 10049541. doi: 10.1016/j.cjche.2017.03.008. URL http://dx.doi.org/10.1016/j.cjche.2017.03.008.

[107] Yunfei He, Pavel Yazhgur, Anniina Salonen, and Dominique Langevin. Adsorption–desorption kinetics of surfactants at liquid surfaces. *Advances in Colloid and Interface Science*, 222:377–384, 8 2015. ISSN 0001-8686. doi: 10.1016/J.CIS.2014.09.002.

[108] Stephanie Hermann, Sebastian Maaß, Daniel Zedel, Astrid Walle, Michael Schäfer, and Matthias Kraume. Experimental and numerical investigations of drop breakage mechanism. *1st International Symposium on Multiscale Multiphase Process Engineering (MMPE)*, pages 1–7, 2011. URL www.mmpe.jp.

[109] M A Herrada, A Ponce-Torres, M Rubio, J Eggers, and J M Montanero. Stability and tip streaming of a surfactant-loaded drop in an extensional flow. influence of surface viscosity. *J. Fluid Mech*, 934:26, 2022. doi: 10.1017/jfm.2021.1118. URL https://doi.org/10.1017/jfm.2021.1118.

[110] Paul C. Hiemenz and Ra] Rajagopalan. Principles of colloid and surface chemistry: Third edition, revised and expanded. *Principles of Colloid and Surface Chemistry: Third Edition, Revised and Expanded*, pages 1–650, 1 2016. doi: 10.1201/9781315274287/PRINCIPLES-COLLOID-SURFACE-CHEMISTRY-REVISED-EXPANDED-PAUL-HIEMENZ-RA URL https://www.taylorfrancis.com/books/mono/10.1201/9781315274287/principles-colloid-surface-chemistry-revised-expanded-paul-hiemenz-raj-rajagopalan

[111] J. O. Hinze. Fundamentals of the hydrodynamic mechanism of splitting in dispersion processes. *AIChE Journal*, 1:289–295, 1955. ISSN 15475905. doi: 10.1002/aic.690010303.

[112] C. W. Hirt and B. D. Nichols. Volume of fluid (vof) method for the dynamics of free boundaries. *Journal of Computational Physics*, 39:201–225, 1 1981. ISSN 0021-9991. doi: 10.1016/0021-9991(81)90145-5.

[113] C. W. Hirt, J. L. Cook, and T. D. Butler. A lagrangian method for calculating the dynamics of an incompressible fluid with free surface. *Journal of Computational Physics*, 5:103–124, 2 1970. ISSN 0021-9991. doi: 10.1016/0021-9991(70)90055-0.

[114] C. W. Hirt, A. A. Amsden, and J. L. Cook. An arbitrary lagrangian-eulerian computing method for all flow speeds. *Journal of Computational Physics*, 14:227–253, 3 1974. ISSN 0021-9991. doi: 10.1016/0021-9991(74)90051-5.

[115] Sepp Hochreiter. The vanishing gradient problem during learning recurrent neural nets and problem solutions. *International Journal of Uncertainty, Fuzziness and Knowledge-Based Systems*, 6(02):107–116, 1998.

[116] Sepp Hochreiter and J ¨ Urgen Schmidhuber. Long short-term memory. 1997. URL http://direct.mit.edu/neco/article-pdf/9/8/1735/813796/neco.1997.9.8.1735.pdf.

[117] R. M. Hockey and J. M. Nouri. Turbulent flow in a baffled vessel stirred by a 60° pitched blade impeller. *Chemical Engineering Science*, 51:4405–4421, 10 1996. ISSN 0009-2509. doi: 10.1016/0009-2509(96)00267-9.

[118] L W Holm, V A Josendal, K M Watson, and R A Ragatz. On-line monitoring of drop size distribution in agitated vessels. 1. effect of temperature and impeller speed. *Industrial & engineering chemistry research*, 30:536–543, 1991. URL https://pubs.acs.org/sharingguidelines.

[119] Yuqing Hou, Hui Li, Hong Chen, Wei Wei, Jiayue Wang, and Yicang Huang. A novel deep u-net-lstm framework for time-sequenced hydrodynamics prediction of the suboff aff-8. *Engineering Applications of Computational Fluid Mechanics*, 16:630–645, 12 2022. ISSN 1997003X. doi: 10.1080/19942060.2022.2030802. URL https://www.tandfonline.com/doi/abs/10.1080/19942060.2022.2030802.

[120] Y T Hu and A Lips. Estimating surfactant surface coverage and decomposing its effect on drop deformation. *Physical review letters*, 91, 2003. doi: 10.1103/PhysRevLett.91.044501.

[121] Thomas J.R. Hughes, Wing Kam Liu, and Thomas K. Zimmermann. Lagrangian-eulerian finite element formulation for incompressible viscous flows. *Computer Methods in Applied Mechanics and Engineering*, 29:329–349, 12 1981. ISSN 0045-7825. doi: 10.1016/0045-7825(81)90049-9.

[122] David Jacqmin. Calculation of two-phase navier–stokes flows using phase-field modeling. *Journal of Computational Physics*, 155:96–127, 10 1999. ISSN 0021-9991. doi: 10.1006/JCPH.1999.6332.

[123] J J M Janssen, A Boon, and W G M Agterof. Influence of dynamic interfacial properties on droplet breakup in simple shear flow. *AIChE journal*, 40:1929–1939, 1994.

[124] J. J.M. Janssen, A. Boon, and W. G.M. Agterof. Droplet break-up in simple shear flow in the presence of emulsifiers. *Colloids and Surfaces A: Physicochemical and Engineering Aspects*, 91:141–148, 11 1994. ISSN 0927-7757. doi: 10.1016/0927-7757(94)02859-1.

[125] J M H Janssen and H E H Meijer. Droplet breakup mechanisms: Stepwise equilibrium versus transient dispersion. *Journal of Rheology*, 37:597–608, 1993. doi: 10.1122/1.550385. URL https://doi.org/10.1122/1.550385.

[126] Thomas R N Jansson, Martin P Haspang, Kåre H Jensen, Pascal Hersen, and Tomas Bohr. Polygons on a rotating fluid surface. 2006. doi: 10.1103/PhysRevLett.96.174502. URL http://www.physics.dtu.dk/~tbohr/RotatingPolygon.

[127] Marek Jaszczur and Anna Młynarczykowska. A general review of the current development of mechanically agitated vessels. *Processes 2020, Vol. 8, Page 982*, 8:982, 8 2020. ISSN 2227-9717. doi: 10.3390/PR8080982. URL https://www.mdpi.com/2227-9717/8/8/982/htmhttps://www.mdpi.com/2227-9717/8/8/982.

[128] Z. Jaworski, K. N. Dyster, and A. W. Nienow. The effect of size, location and pumping direction of pitched blade turbine impellers on flow patterns: Lda measurements and cfd predictions. *Chemical Engineering Research and Design*, 79:887–894, 11 2001. ISSN 0263-8762. doi: 10.1205/02638760152721406.

[129] Chao Jiang, Ricardo Vinuesa, Ruilin Chen, Junyi Mi, Shujin Laima, and Hui Li. An interpretable framework of data-driven turbulence modeling using deep neural networks. *Physics of Fluids*, 33(5), 2021.

[130] Fang Jin and J. Kathleen Stebe. The effects of a diffusion controlled surfactant on a viscous drop injected into a viscous medium. *Physics of Fluids*, 19, 11 2007. ISSN 1070-6631. doi: 10.1063/1.2775055. URL https://aip.scitation.org/doi/abs/10.1063/1.2775055.

[131] Fang Jin, Nivedita R. Gupta, and Kathleen J. Stebe. The detachment of a viscous drop in a viscous solution in the presence of a soluble surfactant. *Physics of Fluids*, 18, 2 2006. ISSN 10706631. doi: 10.1063/1.2172003/1.2172003.MM.ORIGINAL.V4.WMV. URL https://aip.scitation.org/doi/abs/10.1063/1.2172003.

[132] Michael I Jordan. Attractor dynamics and parallelism in a connectionist sequential machine. In *Artificial neural networks: concept learning*, pages 112–127. 1990.

[133] L. Kahouadji and L. Martin Witkowski. Free surface due to a flow driven by a rotating disk inside a vertical cylindrical tank: Axisymmetric configuration. *Physics of Fluids*, 26, 2014. ISSN 10897666. doi: 10.1063/1.4890209. URL http://dx.doi.org/10.1063/1.4890209.

[134] Lyes Kahouadji, Emilia Nowak, Nina Kovalchuk, Jalel Chergui, Damir Juric, Seungwon Shin, Mark J.H. Simmons, Richard V. Craster, and Omar K. Matar. Simulation of immiscible liquid–liquid flows in complex microchannel geometries using a front-tracking scheme. *Microfluidics and Nanofluidics*, 22:1–12, 11 2018. ISSN 16134990. doi: 10.1007/S10404-018-2149-Y/FIGURES/13. URL https://link.springer.com/article/10.1007/s10404-018-2149-y.

[135] Lyes Kahouadji, Assen Batchvarov, Cristian R Constante Amores, Seungwon Shin, Jalel Chergui, Damir Juric, Richard V Craster, and Omar K Matar. The transition to aeration in two-phase mixing in stirred vessels, 2020.

[136] Pritish M Kamat, Brayden W Wagoner, Sumeet S Thete, and Osman A Basaran. Role of marangoni stress during breakup of surfactant-covered liquid threads: Reduced rates of thinning and microthread cascades. *Physical Review Fluids*, 3, 2018. doi: 10.1103/PhysRevFluids.3.043602.

[137] Johannes Kamp, Jörn Villwock, and Matthias Kraume. Drop coalescence in technical liquid/liquid applications: a review on experimental techniques and modeling approaches. *Reviews in Chemical Engineering*, 33:1–47, 2 2017. ISSN 0167-8299. doi: 10.1515/revce-2015-0071.

[138] Abir Khalil, François Puel, Yves Chevalier, Jean-Marc Galvan, Alain Rivoire, and Jean-Paul Klein. Study of droplet size distribution during an emulsification process using in situ video probe coupled with an automatic image analysis. *Chemical Engineering Journal*, 165(3):946–957, 2010.

[139] Firoz R. Khan, Chris D. Rielly, and Graham K. Hargrave. A multi-block approach to obtain angle-resolved piv measurements of the mean flow and turbulence fields in a stirred vessel. *Chemical Engineering & Technology*, 27:264–269, 3 2004. ISSN 1521-4125. doi: 10.1002/CEAT.200401998. URL https://onlinelibrary.wiley.com/doi/full/10.1002/ceat.200401998https://onlinelibrary.wiley.com/doi/abs/10.1002/ceat.200401998https://onlinelibrary.wiley.com/doi/10.1002/ceat.200401998.

[140] Siti Khotijah, Jimmy Tirtawangsa, and Arie A Suryani. Using lstm for context based approach of sarcasm detection in twitter. In *Proceedings of the 11th international conference on advances in information technology*, pages 1–7, 2020.

[141] Hyunseung Kim, Myeongnam Park, Chang Won Kim, and Dongil Shin. Source localization for hazardous material release in an outdoor chemical plant via a combination of lstm-rnn and cfd simulation. *Computers & Chemical Engineering*, 125:476–489, 6 2019. ISSN 0098-1354. doi: 10.1016/J.COMPCHEMENG.2019.03.012.

[142] Junseok Kim. Phase-field models for multi-component fluid flows. *Communications in Computational Physics*, 12:613–661, 9 2012. ISSN 1815-2406. doi: 10.4208/CICP.301110.040811A. URL https://www.cambridge.org/core/journals/communications-in-computational-physics/article/phasefield-models-for-multicomponent-fluid-flows/0672FBD318BBE2621A51AE0F2C9C2FE3.

[143] Diederik P Kingma and Jimmy Ba. Adam: A method for stochastic optimization. *arXiv preprint arXiv:1412.6980*, 2014.

[144] Dmitrii Kochkov, Jamie A Smith, Ayya Alieva, Qing Wang, Michael P Brenner, and Stephan Hoyer. Machine learning–accelerated computational fluid dynamics. *Proceedings of the National Academy of Sciences*, 118(21):e2101784118, 2021.

[145] Andrey Kolmogorov. On the breakage of drops in a turbulent flow. In *Dokl. Akad. Navk. SSSR*, volume 66, pages 825–828, 1949.

[146] Mikio Konno, Minoru Aoki, and Shozaburo Saito. Scale effect on breakup process in liquid-liquid agitated tanks. *Journal of chemical engineering of Japan*, 16(4):312–319, 1983.

[147] Abraham Koshy, T. R. Das, and R. Kumar. Effect of surfactants on drop breakage in turbulent liquid dispersions. *Chemical Engineering Science*, 43:649–654, 1 1988. ISSN 0009-2509. doi: 10.1016/0009-2509(88)87023-4.

[148] Matthias Kraume, Ansor Gäbler, and Kai Schulze. Influence of physical properties on drop size distributions of stirred liquid-liquid dispersions. *Chemical Engineering and Technology*, 27:330–334, 2004. ISSN 09307516. doi: 10.1002/ceat.200402006.

[149] Suzanne M Kresta' and Philip E Wood. The flow field produced by a pitched blade turbine: Characterization of the turbulence and estimation of the dissipation rate. *Chemical Enginering Science*, 48:1761–1774, 1993.

[150] R Krishna. Multicomponent surface diffusion of adsorbed species: a description based on the generalized maxwell—stefan equations. *Chemical Engineering Science*, 45(7):1779–1791, 1990.

[151] Y. W. Kruijt-Stegeman, F. N. van de Vosse, and H. E.H. Meijer. Droplet behavior in the presence of insoluble surfactants. *Physics of Fluids*, 16:2785–2796, 2004. ISSN 10706631. doi: 10.1063/1.1756168.

[152] William H Kruskal and W Allen Wallis. Use of ranks in one-criterion variance analysis. *Journal of the American statistical Association*, 47(260):583–621, 1952.

[153] S. Kumar, R. Kumar, and K. S. Gandhi. Alternative mechanisms of drop breakage in stirred vessels. *Chemical Engineering Science*, 46:2483–2489, 1991. ISSN 00092509. doi: 10.1016/0009-2509(91)80041-V.

[154] Sanjeev Kumar, R. Kumar, and K. S. Gandhi. A multi-stage model for drop breakage in stirred vessels. *Chemical Engineering Science*, 47:971–980, 4 1992. ISSN 0009-2509. doi: 10.1016/0009-2509(92)80224-Z.

[155] Sanjeev Kumar, Vivek Ganvir, C. Satyanand, R. Kumar, and K. S. Gandhi. Alternative mechanisms of drop breakup in stirred vessels. *Chemical Engineering Science*, 53:3269–3280, 1998. ISSN 00092509. doi: 10.1016/S0009-2509(98)00139-0.

[156] T. Kumaresan and Jyeshtharaj B. Joshi. Effect of impeller design on the flow pattern and mixing in stirred tanks. *Chemical Engineering Journal*, 115:173–193, 1 2006. ISSN 1385-8947. doi: 10.1016/J.CEJ.2005.10.002.

[157] Masafumi Kuriyama, Minobu Ono, Hideki Tokanai, and Hirotaka Konno. The number of daughter drops formed per breakup of a highly viscous mother-drop in turbulent flow. *Journal of chemical engineering of Japan*, 28(4):477–479, 1995.

[158] Do Y. Kwak and Jun S. Lee. Multigrid algorithm for the cell-centered finite difference method ii: discontinuous coefficient case. *Numerical Methods for Partial Differential Equations*, 20:742–764, 9 2004. ISSN 1098-2426. doi: 10.1002/NUM.20001. URL https://onlinelibrary.wiley.com/doi/full/10.1002/num.20001https://onlinelibrary.wiley.com/doi/abs/10.1002/num.20001https://onlinelibrary.wiley.com/doi/10.1002/num.20001.

[159] Marko Laakkonen, Pasi Moilanen, and Juhani Aittamaa. Local bubble size distributions in agitated vessels. *Chemical Engineering Journal*, 106(2):133–143, 2005.

[160] Ronald Laymon. Newton's bucket experiment. *Journal of the History of Philosophy*, 16 (4):399–413, 1978.

[161] L. G. Leal and Howard . A . Stone. The effect of surfactant on drop deformation and breakup, 1990.

[162] L Gary Leal. *Advanced transport phenomena: fluid mechanics and convective transport processes*, volume 7. Cambridge university press, 2007.

[163] James M Lee and Yee Soong. Effect of surfactants on the liquid-liquid dispersions in agitated vessels, 1985. URL https://pubs.acs.org/sharingguidelines.

[164] K C Lee and M Yianneskis. Turbulence properties of of a rushton the impeller stream turbine. *AIChE Journal*, 44:13–24, 1998. doi: 10.1002/aic.690440104. URL https://aiche.onlinelibrary.wiley.com/doi/10.1002/aic.690440104.

[165] T. Lemenand, P. Dupont, D. Della Valle, and H. Peerhossaini. Comparative efficiency of shear, elongation and turbulent droplet breakup mechanisms: Review and application. *Chemical Engineering Research and Design*, 91:2587–2600, 2013. ISSN 02638762. doi: 10.1016/j.cherd.2013.03.017. URL http://dx.doi.org/10.1016/j.cherd.2013.03.017.

[166] DE Leng and GJ Quarderer. Drop dispersion in suspension polymerization. *Chemical Engineering Communications*, 14(3-6):177–201, 1982.

[167] Martin Leutbecher and Tim N Palmer. Ensemble forecasting. *Journal of computational physics*, 227(7):3515–3539, 2008.

[168] Liangchao Li, Jiajun Wang, Lianfang Feng, and Xueping Gu. Computational fluid dynamics simulation of hydrodynamics in an uncovered unbaffled tank agitated by pitched blade turbines. *Korean J. Chem. Eng*, 34:2811–2822, 2017. ISSN 1975-7220. doi: 10.1007/s11814-017-0208-9.

[169] Wencheng Li, Xiumin Gao, and Haojie Liu. Efficient prediction of transonic flutter boundaries for varying mach number and angle of attack via lstm network. *Aerospace Science and Technology*, 110:106451, 3 2021. ISSN 1270-9638. doi: 10.1016/J.AST.2020.106451.

[170] X. Li and C. Pozrikidis. The effect of surfactants on drop deformation and on the rheology of dilute emulsions in stokes flow. *J. Fluid Mech*, 341:165–194, 1997. doi: 10.1017/S0022112097005508. URL https://doi.org/10.1017/S0022112097005508.

[171] Yibao Li, Ana Yun, Dongsun Lee, Jaemin Shin, Darae Jeong, and Junseok Kim. Three-dimensional volume-conserving immersed boundary model for two-phase fluid flows. *Computer Methods in Applied Mechanics and Engineering*, 257:36–46, 4 2013. ISSN 0045-7825. doi: 10.1016/J.CMA.2013.01.009.

[172] Yunfei Li, Juntao Chang, Chen Kong, and Wen Bao. Recent progress of machine learning in flow modeling and active flow control. *Chinese Journal of Aeronautics*, 35(4):14–44, 2022.

[173] Fuyue Liang, Lyes Kahouadji, Juan Pablo Valdes, Seungwon Shin, Jalel Chergui, Damir Juric, and Omar K Matar. Numerical study of oil–water emulsion formation in stirred vessels: effect of impeller speed. *Flow*, 2:E34, 2022.

[174] Fuyue Liang, Lyes Kahouadji, Juan Pablo Valdes, Seungwon Shin, Jalel Chergui, Damir Juric, and Omar K Matar. Numerical simulation of surfactant-laden emulsion formation in an un-baffled stirred vessel. *Chemical Engineering Journal*, 472:144807, 2023.

[175] Fuyue Liang, Juan P Valdes, Sibo Cheng, Lyes Kahouadji, Seungwon Shin, Jalel Chergui, Damir Juric, Rossella Arcucci, and Omar K Matar. Liquid–liquid dispersion performance prediction and uncertainty quantification using recurrent neural networks. *Industrial & Engineering Chemistry Research*, 63(17):7853–7875, 2024.

[176] Yixiang Liao and Dirk Lucas. A literature review of theoretical models for drop and bubble breakup in turbulent dispersions. *Chemical Engineering Science*, 64:3389–3406, 2009. ISSN 00092509. doi: 10.1016/j.ces.2009.04.026.

[177] Yixiang Liao and Dirk Lucas. A literature review on mechanisms and models for the coalescence process of fluid particles. *Chemical Engineering Science*, 65:2851–2864, 5 2010. ISSN 0009-2509. doi: 10.1016/J.CES.2010.02.020.

[178] Douglas K Lilly. The representation of small-scale turbulence in numerical simulation experiments. *IBM Form*, pages 195–210, 1967.

[179] Douglas Keith Lilly. On the application of the eddy viscosity concept in the inertial sub-range of turbulence. *NCAR manuscript*, 123, 1966.

[180] Chenwei Liu, Mingzhong Li, Chen Liang, and Weiyang Wang. Measurement and analysis of bimodal drop size distribution in a rotor–stator homogenizer. *Chemical Engineering Science*, 102:622–631, 2013. ISSN 0009-2509. doi: https://doi.org/10.1016/j.ces.2013.08.030. URL https://www.sciencedirect.com/science/article/pii/S0009250913005733.

[181] Nannan Liu, Wei Wang, Yunya Tian, Changchun Wu, and Jing Gong. Experimental and numerical study for drop size distribution in oil-water dispersions with nonionic surfactant tween 80. *Experimental Thermal and Fluid Science*, 89:153–165, 12 2017. ISSN 0894-1777. doi: 10.1016/J.EXPTHERMFLUSCI.2017.08.007.

[182] J. Lovick, A. A. Mouza, S. V. Paras, G. J. Lye, and P. Angeli. Drop size distribution in highly concentrated liquid-liquid dispersions using a light back scattering method. *Journal of Chemical Technology and Biotechnology*, 80:545–552, 5 2005. ISSN 02682575. doi: 10.1002/JCTB.1205.

[183] E. H. Lucassen-Reynders and K. A. Kuijpers. The role of interfacial properties in emulsification. *Colloids and Surfaces*, 65:175–184, 1992. ISSN 01666622. doi: 10.1016/0166-6622(92)80272-4.

[184] Hean Luo and Hallvard F. Svendsen. Theoretical model for drop and bubble breakup in turbulent dispersions. *AIChE Journal*, 42:1225–1233, 1996. ISSN 00011541. doi: 10.1002/AIC.690420505.

[185] S. Maaß, S. Wollny, R. Sperling, and M. Kraume. Numerical and experimental analysis of particle strain and breakage in turbulent dispersions. *Chemical Engineering Research and Design*, 87:565–572, 2009. ISSN 02638762. doi: 10.1016/j.cherd.2009.01.002.

[186] Sebastian Maaß and Matthias Kraume. Determination of breakage rates using single drop experiments. *Chemical Engineering Science*, 70:146–164, 2012. ISSN 00092509. doi: 10.1016/j.ces.2011.08.027. URL http://dx.doi.org/10.1016/j.ces.2011.08.027.

[187] Sebastian Maaß, A. Gäbler, A. Zaccone, A. R. Paschedag, and M. Kraume. Experimental investigations and modelling of breakage phenomena in stirred liquid/liquid systems. *Chemical Engineering Research and Design*, 85:703–709, 2007. ISSN 02638762. doi: 10.1205/cherd06187.

[188] Sebastian Maaß, Niklas Paul, and Matthias Kraume. Influence of the dispersed phase fraction on experimental and predicted drop size distributions in breakage dominated stirred systems. *Chemical Engineering Science*, 76:140–153, 2012. ISSN 00092509. doi: 10.1016/j.ces.2012.03.050. URL http://dx.doi.org/10.1016/j.ces.2012.03.050.

[189] Prafulli A Mahakal, Hatim T Rangwala, and Ashwin W Patwardhan. Drop size distribution in batch stirred tank at high organic to aqueous phase ratios. *Chemical Engineering Research and Design*, 193:843–861, 2023. doi: 10.1016/j.cherd.2023.04.024. URL www.sciencedirect.com.

[190] Marta Major-Godlewska and Joanna Karcz. Power consumption for an agitated vessel equipped with pitched blade turbine and short baffles. *Chemical Papers*, 72:1081–1088, 5 2018. ISSN 13369075. doi: 10.1007/S11696-017-0346-X/TABLES/2. URL https://link.springer.com/article/10.1007/s11696-017-0346-x.

[191] Shubhadeep Mandal, Sayan Das, and Suman Chakraborty. Effect of marangoni stress on the bulk rheology of a dilute emulsion of surfactant-laden deformable droplets in linear flows. *PHYSICAL REVIEW FLUIDS*, 2:113604, 2017. doi: 10.1103/PhysRevFluids.2.113604.

[192] Harishankar Manikantan and Todd M. Squires. Surfactant dynamics: Hidden variables controlling fluid flows. *Journal of Fluid Mechanics*, 892:1–115, 2020. ISSN 14697645. doi: 10.1017/jfm.2020.170.

[193] Frank J Massey Jr. The kolmogorov-smirnov test for goodness of fit. *Journal of the American statistical Association*, 46(253):68–78, 1951.

[194] Bertrand Maury and Olivier Pironneau. Characteristics ale method for unsteady free surface flows with surface tension. *Zeitschrift für angewandte Mathematik und Mechanik*, 76:613–614, 1996.

[195] Paul Mavros, Alain Ricard, Catherine Xuereb, and Joël Bertrand. A study of the effect of drag-reducing surfactants on flow patterns in stirred vessels. *Chemical Engineering Research and Design*, 89:94–106, 2011. ISSN 02638762. doi: 10.1016/j.cherd.2010.04.016. URL http://dx.doi.org/10.1016/j.cherd.2010.04.016.

[196] Caroline M McFarlane and Alvin W Nienow. Studies of high solidity ratio hydrofoil impellers for aerated bioreactors. 1. review. *Biotechnology progress*, 11(6):601–607, 1995.

[197] Oden J McMillan and Joel H Ferziger. Direct testing of subgrid-scale models. *Aiaa Journal*, 17(12):1340–1346, 1979.

[198] W J Milliken, H A Stone, and L G Leal. The effect of surfactant on the transient motion of newtonian drops. *Physics of Fluids A: Fluid Dynamics*, 5:69–79, 1993. doi: 10.1063/1.858790. URL https://doi.org/10.1063/1.858790. gamma: ratio of the surface Pe and the capillary number;¡br/¿beta: the same definition but with initial Gamma¡br/¿¡br/¿Important: surfactant accumulates along those regions of the interface where the flow converges, lowers the local interfacial tension, and thus requires a high degree of curvature in order to maintain the normal stress boundary condition.

[199] William J. Milliken and L. Gary Leal. The influence of surfactant on the deformation and breakup of a viscous drop: The effect of surfactant solubility. *Journal of Colloid And Interface Science*, 166:275–285, 1994. ISSN 00219797. doi: 10.1006/JCIS.1994.1296.

[200] V. P. Mishra, P. Kumar, and J. B. Joshi. Flow generated by a disc turbine in aqueous solutions of polyacrylamide. *Chemical Engineering Journal*, 71:11–21, 11 1998. ISSN 1385-8947. doi: 10.1016/S1385-8947(98)00112-0.

[201] Arvind T Mohan and Datta V Gaitonde. A deep learning based approach to reduced order modeling for turbulent flow control using lstm neural networks. *arXiv preprint arXiv:1804.09269*, 2018.

[202] G. Montante, K. C. Lee, A. Brucato, and M. Yianneskis. An experimental study of double-to-single-loop transition in stirred vessels. *The Canadian Journal of Chemical Engineering*, 77:649–659, 8 1999. ISSN 1939-019X. doi: 10.1002/CJCE.5450770405. URL https://onlinelibrary.wiley.com/doi/full/10.1002/cjce.5450770405https://onlinelibrary.wiley.com/doi/abs/10.1002/cjce.5450770405https://onlinelibrary.wiley.com/doi/10.1002/cjce.5450770405.

[203] Giuseppina Montante, Fabio Laurenzi, Alessandro Paglianti, and Franco Magelli. A study on some effects of a drag-reducing agent on the performance of a stirred vessel. *Chemical Engineering Research and Design*, 89:2262–2267, 11 2011. ISSN 0263-8762. doi: 10.1016/J.CHERD.2011.03.013.

[204] Metin Muradoglu and Gretar Tryggvason. Simulations of soluble surfactants in 3d multiphase flow. *Journal of Computational Physics*, 274:737–757, 10 2014. ISSN 0021-9991. doi: 10.1016/J.JCP.2014.06.024.

[205] JY Murphy. Cfd simulation of flows in stirred tank reactors using a sliding mesh technique. In *Instn. Chem. Engng. Symp. Ser.*, volume 136, pages 341–348, 1994.

[206] M Musgrove and S Ruszkowski. Influence of impeller type and agitation conditions on the drop size of immiscible liquid dispersions. In *10th European Conference on Mixing*, pages 165–172. Elsevier, 2000.

[207] S Nachtigall, D Zedel, A Walle, and M Kraume. Determination of drop breakage mechanisms by experimental and numerical investigations of single drop breakages. *14th European Conference on Mixing*, pages 10–13, 2012.

[208] Stephanie Nachtigall, Daniel Zedel, and Matthias Kraume. Analysis of drop deformation dynamics in turbulent flow. *Chinese Journal of Chemical Engineering*, 24:264–277, 2 2016. ISSN 10049541. doi: 10.1016/J.CJCHE.2015.06.003.

[209] Sepehr Khajeh Naeeni and Leila Pakzad. Experimental and numerical investigation on mixing of dilute oil in water dispersions in a stirred tank. *Chemical Engineering Research and Design*, 147:493–509, 7 2019. ISSN 0263-8762. doi: 10.1016/J.CHERD.2019.05.024.

[210] Tsukasa Nakayama and Mine0 Mori. An eulerian finite element method for time-dependent free surface problems in hydrodynamics. *INTERNATIONAL JOURNAL FOR NUMERICAL METHODS IN FLUIDS*, 22:996, 1996. doi: 10.1002/(SICI)1097-0363(19960215)22:3. URL https://onlinelibrary.wiley.com/terms-and-conditions.

[211] D. K.R. Nambiar, R. Kumar, and K. S. Gandhi. Breakage and coalescence of drops in turbulent stirred dispersions. *Sadhana*, 15:73–103, 1990. ISSN 02562499. doi: 10.1007/BF02760469.

[212] Isabelle Naude, Catherine Xuereb, and Joël Bertrand. Direct prediction of the flows induced by a propeller in an agitated vessel using an unstructured mesh. *The Canadian Journal of Chemical Engineering*, 76:631–640, 6 1998. ISSN 1939-019X. doi: 10.1002/CJCE.5450760335. URL https://onlinelibrary.wiley.com/doi/full/10.1002/cjce.5450760335https://onlinelibrary.wiley.com/doi/abs/10.1002/cjce.5450760335https://onlinelibrary.wiley.com/doi/10.1002/cjce.5450760335.

[213] A. W. Nienow, M. F. EDWARDS, and N. Harnby. *Mixing in the Process Industries: Second Edition*. 1997. URL https://books.google.co.uk/books?hl=en&lr=&id=LxdFnHQcXhgC&oi=fnd&pg=PP1&dq=impeller+classification+mixing&ots=IcBz9KmAWD&sig=ELVvHqFcdMOAIP6vKGcV37jmi_I&redir_esc=y#v=onepage&q=impeller%20classification%20mixing&f=false.

[214] K. Niranjan, D. L.O. Smith, C. D. Rielly, J. A. Lindley, and V. R. Phillips. Mixing processes for agricultural and food materials: Part 5, review of mixer types. *Journal of Agricultural Engineering Research*, 59:145–161, 11 1994. ISSN 0021-8634. doi: 10.1006/JAER.1994.1072.

[215] Masabumi Nishikawa, Yukimichi Okamoto, Kenji Hashimoto, and Shinji Nagata. Turbulence energy spectra in baffled mixing vessels. *Journal of Chemical Engineering of Japan*, 9:489–494, 1976. ISSN 00219592. doi: 10.1252/jcej.9.489.

[216] Masabumi Nishikawa, Fuyuhiko Mori, and Shigeo Fujieda. Average drop size in a liquid-liquid phase mixing vessel. *Journal of Chemical Engineering of Japan*, 20:82–88, 1987. ISSN 00219592. doi: 10.1252/jcej.20.82.

[217] Guido Novati, Hugues Lascombes de Laroussilhe, and Petros Koumoutsakos. Automating turbulence modelling by multi-agent reinforcement learning. *Nature Machine Intelligence*, 3(1):87–96, 2021.

[218] Cheolhwan Oh, Seungmin Han, and Jongpil Jeong. Time-series data augmentation based on interpolation. *Procedia Computer Science*, 175:64–71, 1 2020. ISSN 1877-0509. doi: 10.1016/J.PROCS.2020.07.012.

[219] Takashi Okamoto and Mutsuto Kawahara. Two-dimensional sloshing analysis by lagrangian finite element method. *International Journal for Numerical Methods in Fluids*, 11:453–477, 10 1990. ISSN 1097-0363. doi: 10.1002/FLD.1650110502. URL https://onlinelibrary.wiley.com/doi/full/10.1002/fld.1650110502https://onlinelibrary.wiley.com/doi/abs/10.1002/fld.1650110502https://onlinelibrary.wiley.com/doi/10.1002/fld.1650110502.

[220] Alan M. O'Rourke and P. F. MacLoughlin. A comparison of measurement techniques used in the analysis of evolving liquid–liquid dispersions. *Chemical Engineering and Processing: Process Intensification*, 44:885–894, 8 2005. ISSN 0255-2701. doi: 10.1016/J.CEP.2004.10.001.

[221] Ronald Osher and Stanley Fedkiw. *Level Set Methods and Dynamic Implicit Surfaces*. Springer, 2002.

[222] A. W. Pacek, C. C. Man, and A. W. Nienow. On the sauter mean diameter and size distributions in turbulent liquid/liquid dispersions in a stirred vessel. *Chemical Engineering Science*, 53:2005–2011, 1998. ISSN 00092509. doi: 10.1016/S0009-2509(98)00068-2.

[223] A.W. Pacek, S. Chamsart, A.W. Nienow, and A. Bakker. The influence of impeller type on mean drop size and drop size distribution in an agitated vessel. *Chemical Engineering Science*, 54:4211–4222, 10 1999. ISSN 00092509. doi: 10.1016/S0009-2509(99)00156-6. URL https://doi.org/10.1016/S0009-2509(99)00156-6https://linkinghub.elsevier.com/retrieve/pii/S0009250999001566.

[224] Rennan Pan, John Green, and Charles Maldarelli. Theory and experiment on the measurement of kinetic rate constants for surfactant exchange at an air/water interface. *Journal of Colloid and Interface Science*, 205:213–230, 9 1998. ISSN 0021-9797. doi: 10.1006/JCIS.1998.5559.

[225] Wendy S Parker. Ensemble modeling, uncertainty and robust predictions. *Wiley interdisciplinary reviews: Climate change*, 4(3):213–223, 2013.

[226] Pramod Patil and Sanjeev Kumar. Breakup of drops around the edges of rushton turbine. *The Canadian Journal of Chemical Engineering*, 88(6):912–918, 2010.

[227] Pramod D Patil and Sanjeev Kumar. Continued self-similar breakup of drops in viscous continuous phase in agitated vessels. *Chemical engineering science*, 66(20):4932–4935, 2011.

[228] Ashwin W. Patwardhan and Jyeshtharaj B. Joshi. Relation between flow pattern and blending in stirred tanks. *Industrial and Engineering Chemistry Research*, 38:3131–3143, 1999. ISSN 08885885. doi: 10.1021/IE980772S/ASSET/IMAGES/LARGE/IE980772SF00007.JPEG. URL https://pubs.acs.org/doi/full/10.1021/ie980772s.

[229] Edward L Paul, Victor A Atiemo-obeng, and Suzanne M Kresta. *HANDBOOK OF INDUSTRIAL MIXING Edited by*. 2003. ISBN 3175723993.

[230] Yashodhara Pawar and Kathleen J. Stebe. Marangoni effects on drop deformation in an extensional flow: The role of surfactant physical chemistry. i. insoluble surfactants. *Physics of Fluids*, 8:1738–1751, 1996. ISSN 10706631. doi: 10.1063/1.868958.

[231] Karl Pearson. Liii. on lines and planes of closest fit to systems of points in space. *The London, Edinburgh, and Dublin Philosophical Magazine and Journal of Science*, 2:559–572, 11 1901. ISSN 1941-5982. doi: 10.1080/14786440109462720.

[232] A E Perry and M S Chong. A description of eddying motions and flow patterns using critical-point concepts. *Ann. Rev. Fluid Mech*, 19:125–55, 1987. URL www.annualreviews.org.

[233] Charles S. Peskin. Numerical analysis of blood flow in the heart. *Journal of Computational Physics*, 25:220–252, 11 1977. ISSN 0021-9991. doi: 10.1016/0021-9991(77)90100-0.

[234] Charles S. Peskin. The immersed boundary method. *Acta Numerica*, 11:479–517, 1 2002. ISSN 1474-0508. doi: 10.1017/S0962492902000077. URL https://www.cambridge.org/core/journals/acta-numerica/article/immersed-boundary-method/95ECDAC5D1824285563270D6DD70DA9A.

[235] Charles S Peskin and David M McQueen. A general method for the computer simulation of biological systems interacting with fluids. In *Symposia of the society for Experimental Biology*, volume 49, pages 265–276, 1995.

[236] M. Piva and E. Meiburg. Steady axisymmetric flow in an open cylindrical container with a partially rotating bottom wall. *Physics of Fluids*, 17:1–12, 2005. ISSN 10706631. doi: 10.1063/1.1932664.

[237] W Podgórska. Influence of the impeller type on drop size in liquid-liquid dispersions. In *Proceedings of the 13 European Conference on Mixing, London, UK*, pages 14–17, 2009.

[238] Stephen B Pope. Ten questions concerning the large-eddy simulation of turbulent flows. *New journal of Physics*, 6(1):35, 2004.

[239] Paulo A. Quadros and Cristina M.S.G. Baptista. Effective interfacial area in agitated liquid-liquid continuous reactors. *Chemical Engineering Science*, 58:3935–3945, 2003. ISSN 00092509. doi: 10.1016/S0009-2509(03)00302-6.

[240] Doraiswami Ramkrishna and Meenesh R Singh. Population balance modeling: Current status and future prospects. *Annu. Rev. Chem. Biomol. Eng*, 5:123–169, 2014. doi: 10.1146/annurev-chembioeng-060713-040241. URL www.annualreviews.org.

[241] V. V. Ranade and H. E.A. Van den Akker. A computational snapshot of gas—liquid flow in baffled stirred reactors. *Chemical Engineering Science*, 49:5175–5192, 12 1994. ISSN 0009-2509. doi: 10.1016/0009-2509(94)00318-1.

[242] V. V. Ranade and S. M S Dommeti. Computational snapshot of flow generated by axial impellers in baffled stirred vessels. *Chemical Engineering Research and Design*, 74:476–484, 1996. ISSN 0263-8762. URL https://pure.qub.ac.uk/en/publications/computational-snapshot-of-flow-generated-by-axial-impellers-in-ba.

[243] Khandakar M Rashid and Joseph Louis. Window-warping: A time series data augmentation of imu data for construction equipment activity identification. In *ISARC. Proceedings of the international symposium on automation and robotics in construction*, volume 36, pages 651–657. IAARC Publications, 2019.

[244] J Ratulowski and H-C Chang. Marangoni effects of trace impurities on the motion of long gas bubbles in capillaries. *Journal of Fluid Mechanics*, 210:303–328, 1990.

[245] Frédéric Risso. The mechanisms of deformation and breakup of drops and bubbles. *Multiphase science and technology*, 12(1), 2000.

[246] Paul E. Rueger and Richard V. Calabrese. Dispersion of water into oil in a rotor–stator mixer. part 1: Drop breakup in dilute systems. *Chemical Engineering Research and Design*, 91:2122–2133, 11 2013. ISSN 0263-8762. doi: 10.1016/J.CHERD.2013.05.018.

[247] P.E. Rueger and R.V. Calabrese. Dispersion of water into oil in a rotor-stator mixer. part 2: Effect of phase fraction. *Chemical Engineering Research and Design*, 91:2134–2141, 2013. doi: 10.1016/j.cherd.2013.06.010.

[248] M. C. Ruiz, P. Lermanda, and R. Padilla. Drop size distribution in a batch mixer under breakage conditions. *Hydrometallurgy*, 63:65–74, 2002. ISSN 0304386X. doi: 10.1016/S0304-386X(01)00223-7.

[249] PG Saffman and M Delbrück. Brownian motion in biological membranes. *Proceedings of the National Academy of Sciences*, 72(8):3111–3113, 1975.

[250] René Sanjuan-Galindo, Enrique Soto, Roberto Zenit, and Gabriel Ascanio. Viscous filament fragmentation in a turbulent flow inside a stirred tank. *Chemical Engineering Communications*, 202(9):1251–1260, 2015.

[251] A. N. Sathyagal, D. Ramkrishna, and G. Narsimhan. Droplet breakage in stirred dispersions. breakage functions from experimental drop-size distributions. *Chemical Engineering Science*, 51:1377–1391, 1996. ISSN 00092509. doi: 10.1016/0009-2509(95)00311-8.

[252] M Schafer, M Yianneskis, P Wachter, and F Durst. Trailing vortices around a 45" pitched-blade impeller. 1998.

[253] Hermann Schlichting and Joseph Kestin. *Boundary layer theory*, volume 121. Springer, 1961.

[254] Laurier L Schramm. *Emulsions, foams, and suspensions: fundamentals and applications*. John Wiley & Sons, 2006.

[255] M. Schäfer, M. Höfken, and F. Durst. Detailed ldv measurements for visualization of the flow field within a stirred-tank reactor equipped with a rushton turbine. *Chemical Engineering Research and Design*, 75:729–736, 11 1997. ISSN 0263-8762. doi: 10.1205/026387697524399.

[256] André Zamith Selvaggio, Felipe Matheus, Mota Sousa, Flávio Vasconcelos Da Silva, and Sávio S V Vianna. Application of long short-term memory recurrent neural networks for localisation of leak source using 3d computational fluid dynamics. *Process safety and Environmental Protection*, 159:757–767, 2022. doi: 10.1016/j.psep.2022.01.021. URL https://doi.org/10.1016/j.psep.2022.01.021.

[257] J. A. Sethian. Evolution, implementation, and application of level set and fast marching methods for advancing fronts. *Journal of Computational Physics*, 169:503–555, 5 2001. ISSN 00219991. doi: 10.1006/jcph.2000.6657.

[258] K V Sharp and R J Adrian. Piv study of small-scale flow structure around a rushton turbine. *AIChE Journal*, 47:766–778, 2001. doi: 10.1002/aic.690470403. URL https://aiche.onlinelibrary.wiley.com/doi/10.1002/aic.690470403.

[259] K. Shimizu, K. Minekawa, T. Hirose, and Y. Kawase. Drop breakage in stirred tanks with newtonian and non-newtonian fluid systems. *Chemical Engineering Journal*, 72:117–124, 1999. ISSN 13858947. doi: 10.1016/S1385-8947(98)00150-8.

[260] Seungwon Shin and Beomjoon Choi. Numerical simulation of a rising bubble with phase change. *Applied Thermal Engineering*, 100:256–266, 5 2016. ISSN 1359-4311. doi: 10.1016/J.APPLTHERMALENG.2016.02.025.

[261] Seungwon Shin and Damir Juric. Modeling three-dimensional multiphase flow using a level contour reconstruction method for front tracking without connectivity. *Journal of Computational Physics*, 180:427–470, 2002. ISSN 00219991. doi: 10.1006/jcph.2002.7086.

[262] Seungwon Shin and Damir Juric. High order level contour reconstruction method. *Journal of Mechanical Science and Technology*, 21:311–326, 2007. ISSN 1738494X. doi: 10.1007/BF02916292.

[263] Seungwon Shin, S. I. Abdel-Khalik, Virginie Daru, and Damir Juric. Accurate representation of surface tension using the level contour reconstruction method. *Journal of Computational Physics*, 203:493–516, 2005. ISSN 00219991. doi: 10.1016/j.jcp.2004.09.003.

[264] Seungwon Shin, Damir Juric, S Shin, and D Juric. A hybrid interface method for three-dimensional multiphase flows based on front tracking and level set techniques. *International Journal for Numerical Methods in Fluids*, 60:753–778, 7 2009. ISSN 1097-0363. doi: 10.1002/FLD.1912. URL https://onlinelibrary.wiley.com/doi/full/10.1002/fld.1912https://onlinelibrary.wiley.com/doi/abs/10.1002/fld.1912https://onlinelibrary.wiley.com/doi/10.1002/fld.1912.

[265] Seungwon Shin, Ikroh Yoon, and Damir Juric. The local front reconstruction method for direct simulation of two- and three-dimensional multiphase flows. *Journal of Computational Physics*, 230:6605–6646, 2011. ISSN 10902716. doi: 10.1016/j.jcp.2011.04.040. URL http://dx.doi.org/10.1016/j.jcp.2011.04.040.

[266] Seungwon Shin, Jalel Chergui, and Damir Juric. A solver for massively parallel direct numerical simulation of three-dimensional multiphase flows. *Journal of Mechanical Science and Technology*, 31:1739–1751, 2017. ISSN 1738494X. doi: 10.1007/s12206-017-0322-y.

[267] Seungwon Shin, Jalel Chergui, Damir Juric, Lyes Kahouadji, Omar K. Matar, and Richard V. Craster. A hybrid interface tracking – level set technique for multiphase flow with soluble surfactant. *Journal of Computational Physics*, 359:409–435, 2018. ISSN 10902716. doi: 10.1016/j.jcp.2018.01.010. URL https://doi.org/10.1016/j.jcp.2018.01.010. Q1: Why the negative source term in [17] is dropped?¡br/¿Q2: Without the negative source term as in the interfacial concentration equation, how to make sure surfactant in the bulk is conserved? Is te sharp boundary condition?¡br/¿.

[268] Chi-Wang Shu and Stanley Oshers. Efficient implementation of essentially non-oscillatory shock-capturing schemes, ii, 1989.

[269] Shuli Shu and Ning Yang. Gpu-accelerated large eddy simulation of stirred tanks. *Chemical Engineering Science*, 181:132–145, 5 2018. ISSN 00092509. doi: 10.1016/j.ces.2018.02.011.

[270] Harminder Singh, David F. Fletcher, and Justin J. Nijdam. An assessment of different turbulence models for predicting flow in a baffled tank stirred with a rushton turbine. *Chemical Engineering Science*, 66:5976–5988, 12 2011. ISSN 0009-2509. doi: 10.1016/J.CES.2011.08.018.

[271] Joseph Smagorinsky. General circulation experiments with the primitive equations: I. the basic experiment. *Monthly weather review*, 91:99–164, 1963. ISSN 00368075. doi: 10.1126/science.26.653.25.

[272] Anton Smolianski. Finite-element/level-set/operator-splitting (felsos) approach for computing two-fluid unsteady flows with free moving interfaces. *INTERNATIONAL JOURNAL FOR NUMERICAL METHODS IN FLUIDS Int. J. Numer. Meth. Fluids*, 48:231–269, 2005. doi: 10.1002/fld.823. URL https://onlinelibrary.wiley.com/doi/10.1002/fld.823.

[273] Giovanni Soligo, Alessio Roccon, and Alfredo Soldati. Breakage, coalescence and size distribution of surfactant-laden droplets in turbulent flow. *Journal of Fluid Mechanics*, 881:244–282, 2019. ISSN 14697645. doi: 10.1017/jfm.2019.772.

[274] Giovanni Soligo, Alessio Roccon, and Alfredo Soldati. Effect of surfactant-laden droplets on turbulent flow topology. *Physical Review Fluids*, 5, 2020. doi: 10.1103/PhysRevFluids.5.073606.

[275] Jannike Solsvik and Hugo A. Jakobsen. Single drop breakup experiments in stirred liquid-liquid tank. *Chemical Engineering Science*, 131:219–234, 2015. ISSN 00092509. doi: 10.1016/j.ces.2015.03.059. URL http://dx.doi.org/10.1016/j.ces.2015.03.059.

[276] R. S. Spencer and R. M. Wiley. The mixing of very viscous liquids. *Journal of Colloid Science*, 6:133–145, 1951. ISSN 00958522. doi: 10.1016/0095-8522(51)90033-5.

[277] A. Spohn, M. Mory, and E. J. Hopfinger. Observations of vortex breakdown in an open cylindrical container with a rotating bottom. *Experiments in Fluids: Experimental Methods and their Applications to Fluid Flow*, 14:70–77, 1993. ISSN 14321114. doi: 10.1007/BF00196990.

[278] A. Spohn, M. Mory, and E. J. Hopfinger. Experiments on vortex breakdown in a confined flow generated by a rotating disc. *Journal of Fluid Mechanics*, 370:73–99, 1998. ISSN 00221120. doi: 10.1017/S0022112098002092.

[279] F. B. Sprow. Distribution of drop sizes produced in turbulent liquid-liquid dispersion. *Chemical Engineering Science*, 22:435–442, 1967. ISSN 00092509. doi: 10.1016/0009-2509(67)80130-1.

[280] Michael Stamatoudlsr. Effect of continuous-phase viscosity on the drop sizes of liquid-liquid dispersions in agitated vessels. *Industrial & Engineering Chemistry Process Design and Development*, 24:1175–1181, 1985.

[281] Ralf C Staudemeyer and Eric Rothstein Morris. Understanding lstm–a tutorial into long short-term memory recurrent neural networks. *arXiv preprint arXiv:1909.09586*, 2019.

[282] Carl M Stoots and Richard V Calabrese. Mean velocity field relative to a rushton turbine blade. *AIChE Journal*, 41:1–11, 1995. doi: 10.1002/aic.690410102. URL https://aiche.onlinelibrary.wiley.com/doi/10.1002/aic.690410102.

[283] M. Sussman, K. M. Smith, M. Y. Hussaini, M. Ohta, and R. Zhi-Wei. A sharp interface method for incompressible two-phase flows. *Journal of Computational Physics*, 221:469–505, 2 2007. ISSN 0021-9991. doi: 10.1016/J.JCP.2006.06.020.

[284] Mark Sussman and Elbridge Gerry Puckett. A coupled level set and volume-of-fluid method for computing 3d and axisymmetric incompressible two-phase flows. *Journal of computational physics*, 162(2):301–337, 2000.

[285] Mark Sussman, Peter Smereka, and Stanley Osher. A level set approach for computing solutions to incompressible two-phase flow. *Journal of Computational physics*, 114(1):146–159, 1994.

[286] Mark Sussman, Emad Fatemi, Peter Smereka, and Stanley Osher. An improved level set method for incompressible two-phase flows. *Computers & Fluids*, 27(5-6):663–680, 1998.

[287] K. Suzukawa, S. Mochizuki, and H. Osaka. Effect of the attack angle on the roll and trailing vortex structures in an agitated vessel with a paddle impeller. *Chemical Engineering Science*, 61:2791–2798, 5 2006. ISSN 0009-2509. doi: 10.1016/J.CES.2005.10.063.

[288] A Tamburini, G Gagliano, G Micale, A Brucato, F Scargiali, and M Ciofalo. Direct numerical simulations of creeping to early turbulent flow in unbaffled and baffled stirred tanks. *Chemical Engineering Science*, 192:161–175, 2018. doi: 10.1016/j.ces.2018.07.023. URL https://doi.org/10.1016/j.ces.2018.07.023.

[289] G. Tryggvason, B. Bunner, A. Esmaeeli, D. Juric, N. Al-Rawahi, W. Tauber, J. Han, S. Nas, and Y. J. Jan. A front-tracking method for the computations of multiphase flow. *Journal of Computational Physics*, 169:708–759, 2001. ISSN 00219991. doi: 10.1006/jcph.2001.6726.

[290] G. Tryggvason, A. Fernández, A. Esmaeeli, and B. Bunner. *Direct numerical simulations of gas-liquid multiphase flows*. Cambridge University Press, 2011. ISBN 1402005237. doi: 10.1007/0-306-48421-8_9.

[291] Yeng Yung Tsui and Yu Chang Hu. Flow characteristics in mixers agitated by helical ribbon blade impeller. *Engineering Applications of Computational Fluid Mechanics*, 5:416–429, 2011. ISSN 1997003X. doi: 10.1080/19942060.2011.11015383. URL https://www.tandfonline.com/action/journalInformation?journalCode=tcfm20.

[292] Yeng-Yung Tsui, Jian-Ren Chou, Graduate Student, and Yu-Chang Hu. Blade angle effects on the flow in a tank agitated by the pitched-blade turbine. 2006. doi: 10.1115/1.2201636. URL http://asmedigitalcollection.asme.org/fluidsengineering/article-pdf/128/4/774/5593811/774_1.pdf.

[293] Paul G Tucker. *Unsteady computational fluid dynamics in aeronautics*, volume 104. Springer Science & Business Media, 2013.

[294] H. S. Udaykumar, R. Mittel, and Wei Shyy. Computation of solid–liquid phase fronts in the sharp interface limit on fixed grids. *Journal of Computational Physics*, 153:535–574, 8 1999. ISSN 0021-9991. doi: 10.1006/JCPH.1999.6294.

[295] Salih Ozen Unverdi and Grétar Tryggvason. A front-tracking method for viscous, incompressible, multi-fluid flows. *Journal of Computational Physics*, 100:25–37, 5 1992. ISSN 0021-9991. doi: 10.1016/0021-9991(92)90307-K.

[296] K Van't Riet and John M Smith. The trailing vortex system produced by rushton turbine agitators. *Chemical Engineering Science*, 30:109–1105, 1975.

[297] Georgios H. Vatistas. A note on liquid vortex sloshing and kelvin's equilibria. *Journal of Fluid Mechanics*, 217:241–248, 1990. ISSN 14697645. doi: 10.1017/S0022112090000702.

[298] H K Versteeg and W Malalasekera. *An Introduction to Computational Fluid Dynamics Second Edition*. 2007. URL www.pearsoned.co.uk/versteeg.

[299] Pieter Walstra. Physical chemistry of foods. *Physical Chemistry of Foods*, 10 2002. doi: 10.1201/9780203910436. URL https://www.taylorfrancis.com/books/mono/10.1201/9780203910436/physical-chemistry-foods-pieter-walstra.

[300] C. Y. Wang and R. V. Calabrese. Drop breakup in turbulent stirred-tank contactors. part ii: Relative influence of viscosity and interfacial tension. *AIChE Journal*, 32:667–676, 4 1986. ISSN 1547-5905. doi: 10.1002/AIC.690320417. URL https://onlinelibrary.wiley.com/doi/full/10.1002/aic.690320417https://onlinelibrary.wiley.com/doi/abs/10.1002/aic.690320417https://aiche.onlinelibrary.wiley.com/doi/10.1002/aic.690320417.

[301] Jianyou Wang, Michael Xue, Ryan Culhane, Enmao Diao, Jie Ding, and Vahid Tarokh. Speech emotion recognition with dual-sequence lstm architecture. In *ICASSP 2020-2020 IEEE International Conference on Acoustics, Speech and Signal Processing (ICASSP)*, pages 6474–6478. IEEE, 2020.

[302] Qiming Wang, Michael Siegel, and Michael R Booty. Numerical simulation of drop and bubble dynamics with soluble surfactant. *Physics of Fluids*, 26:52102, 2014. doi: 10.1063/1.4872174. URL https://doi.org/10.1063/1.4872174.

[303] K. Wechsler, M. Breuer, and F. Durst. Steady and unsteady computations of turbulent flows induced by a 4/45° pitched-blade impeller. *Journal of Fluids Engineering*, 121:318–329, 6 1999. ISSN 0098-2202. doi: 10.1115/1.2822210. URL https://dx.doi.org/10.1115/1.2822210.

[304] Bruce Weinstein and Robert E. Treybal. Liquid-liquid contacting in unbaffled, agitated vessels. *AIChE Journal*, 19:304–312, 1973. ISSN 15475905. doi: 10.1002/AIC.690190215.

[305] Qingsong Wen, Liang Sun, Fan Yang, Xiaomin Song, Jingkun Gao, Xue Wang, and Huan Xu. Time series data augmentation for deep learning: A survey. *arXiv preprint arXiv:2002.12478*, 2020.

[306] Kamil Wichterle. Drop breakup by impellers. *Chemical Engineering Science*, 50:3581–3586, 1995.

[307] H. Wu and G. K. Patterson. Laser-doppler measurements of turbulent-flow parameters in a stirred mixer. *Chemical Engineering Science*, 44:2207–2221, 1989. ISSN 00092509. doi: 10.1016/0009-2509(89)85155-3.

[308] Yuteng Xiao, Hongsheng Yin, Yudong Zhang, Honggang Qi, Yundong Zhang, and Zhaoyang Liu. A dual-stage attention-based conv-lstm network for spatio-temporal correlation and multivariate time series prediction. *International Journal of Intelligent Systems*, 36(5):2036–2057, 2021.

[309] Zhiming Xu, Zhimin Han, and Hongwei Qu. Comparison between lagrangian and eulerian approaches for prediction of particle deposition in turbulent flows. *Powder Technology*, 360:141–150, 1 2020. ISSN 0032-5910. doi: 10.1016/J.POWTEC.2019.09.084.

[310] Kerim Yapici, Bulent Karasozen, Michael Schäfer, and Yusuf Uludag. Numerical investigation of the effect of the rushton type turbine design factors on agitated tank flow

characteristics. *Chemical Engineering and Processing: Process Intensification*, 47:1340–1349, 8 2008. ISSN 0255-2701. doi: 10.1016/J.CEP.2007.05.002.

[311] M Yianneskis, Z Popiolek, and J H Whitelaw. An experimental study of the steady and unsteady flow characteristics of stirred reactors. *J. Fluid Mech*, 175:537–555, 1987. doi: 10.1017/S002211208700051X. URL https://doi.org/10.1017/S002211208700051X.

[312] H. S. Yoon, K. V. Sharp, D. F. Hill, R. J. Adrian, S. Balachandar, M. Y. Ha, and K. Kar. Integrated experimental and computational approach to simulation of flow in a stirred tank. *Chemical Engineering Science*, 56:6635–6649, 2001. ISSN 00092509. doi: 10.1016/S0009-2509(01)00315-3.

[313] Masanori Yoshida, Yuma Wakura, Kazuaki Yamagiwa, Akira Ohkawa, and Shuichi Tezura. Effect of impeller clearance on liquid flow within an unbaffled vessel agitated with a forward-reverse rotating impeller. *Canadian Journal of Chemical Engineering*, 87: 832–838, 12 2009. ISSN 00084034. doi: 10.1002/CJCE.20235.

[314] Yong Yu, Xiaosheng Si, Changhua Hu, and Jianxun Zhang. A review of recurrent neural networks: Lstm cells and network architectures. *Neural Computation*, 31:1235–1270, 7 2019. ISSN 0899-7667. doi: 10.1162/NECO_A_01199. URL https://dx.doi.org/10.1162/neco_a_01199.

[315] Alessio Zaccone, Ansor Gäbler, Sebastian Maaß, Daniele Marchisio, and Matthias Kraume. Drop breakage in liquid-liquid stirred dispersions: Modelling of single drop breakage. *Chemical Engineering Science*, 62:6297–6307, 2007. ISSN 00092509. doi: 10.1016/j.ces.2007.07.026.

[316] Jinli Zhang, Shuangqing Xu, and Wei Li. High shear mixers: A review of typical applications and studies on power draw, flow pattern, energy dissipation and transfer properties. *Chemical Engineering and Processing*, 57:25–41, 2012. doi: 10.1016/j.cep.2012.04.004. URL http://dx.doi.org/10.1016/j.cep.2012.04.004.

[317] Yanhong Zhang, Chao Yang, and Zai Sha Mao. Large eddy simulation of the gas–liquid flow in a stirred tank. *AIChE Journal*, 54:1963–1974, 8 2008. ISSN 1547-5905. doi: 10.1002/AIC.11516. URL https://onlinelibrary.wiley.com/doi/full/10.1002/aic.11516https://onlinelibrary.wiley.com/doi/abs/10.1002/aic.11516https://aiche.onlinelibrary.wiley.com/doi/10.1002/aic.11516.

[318] Jing Zhao, Zhengming Gao, and Yuyun Bao. Effects of the blade shape on the trailing vortices in liquid flow generated by disc turbines. *Chinese Journal of Chemical Engineering*, 19:232–242, 4 2011. ISSN 1004-9541. doi: 10.1016/S1004-9541(11)60160-2.

[319] Lingxiao Zhao, Zhiyang Li, Leilei Qu, Junsheng Zhang, and Bin Teng. A hybrid vmd-lstm/gru model to predict non-stationary and irregular waves on the east coast of china. *Ocean Engineering*, pages 114–136, 2023. doi: 10.1016/j.oceaneng.2023.114136. URL https://doi.org/10.1016/j.oceaneng.2023.114136.

[320] Hanbin Zhong, Zhenyu Wei, Yi Man, Shaowei Pan, Juntao Zhang, Ben Niu, Xi Yu, Yi Ouyang, and Qingang Xiong. Prediction of instantaneous yield of bio-oil in fluidized biomass pyrolysis using long short-term memory network based on computational fluid dynamics data. *Journal of Cleaner Production*, 391:136192, 2023. doi: 10.1016/j.jclepro.2023.136192. URL https://doi.org/10.1016/j.jclepro.2023.136192.

[321] Genwen Zhou and Suzanne M. Kresta. Correlation of mean drop size and minimum drop size with the turbulence energy dissipation and the flow in an agitated tank. *Chemical Engineering Science*, 53:2063–2079, 1998. ISSN 00092509. doi: 10.1016/S0009-2509(97)00438-7.

[322] Genwen Zhou and Suzanne M. Kresta. Evolution of drop size distribution in liquid-liquid dispersions for various impellers. *Chemical Engineering Science*, 53:2099–2113, 1998. ISSN 00092509. doi: 10.1016/S0009-2509(97)00437-5.

[323] Han Zhou, Xiong Yu, Bo Wang, Shan Jing, Wenjie Lan, and Shaowei Li. Experimental study on drop breakup time and breakup rate with drop swarms in a stirred tank. *AIChE Journal*, 67:1–16, 2021. ISSN 15475905. doi: 10.1002/aic.17065.

[324] Li-Tao Zhu, Xi-Zhong Chen, Bo Ouyang, Wei-Cheng Yan, He Lei, Zhe Chen, and Zheng-Hong Luo. Review of machine learning for hydrodynamics, transport, and reactions in multiphase flows and reactors. *Industrial & Engineering Chemistry Research*, 61(28): 9901–9949, 2022.

[325] Yuejian Zhu. Ensemble forecast: A new approach to uncertainty and predictability. *Advances in atmospheric sciences*, 22:781–788, 2005.

[326] Zhaoyou Zhu, Bin Qin, Shuhua Li, Yigang Liu, Xin Li, Peizhe Cui, Yinglong Wang, and Jun Gao. Multi-dimensional analysis of turbulence models for immiscible liquid-liquid mixing in stirred tank based on numerical simulation. *Separation Science and Technology (Philadelphia)*, 56:411–424, 2021. ISSN 15205754. doi: 10.1080/01496395.2020.1715436. URL https://doi.org/10.1080/01496395.2020.1715436.